Transactions of the ASME
Journal of Turbomachinery

Published Quarterly by The American Society of Mechanical Engineers

VOLUME 108 • NUMBER 2 • OCTOBER 1986

TECHNICAL PAPERS

Technical Editor
ARTHUR J. WENNERSTROM
Senior Associate Editor
G. K. SEROVY
Associate Editors
Advanced Energy Systems
S. I. FREEDMAN
Environmental Control
H. E. HESKETH
Fuels and Combustion Technologies
R. E. BARRETT
Gas Turbine
S. KUO
Internal Combustion Engine
K. J. SPRINGER
Nuclear Engineering
S. M. CHO
Power
R. W. PORTER

BOARD ON COMMUNICATIONS
Chairman and Vice-President
K. N. REID, JR.

Members-at-Large
W. BEGELL
J. T. COKONIS
W. G. GOTTENBERG
M. KUTZ
J. R. LLOYD
T. C. MIN
R. E. NICKELL
C. F. PHILLIPS
R. E. REDER
F. W. SCHMIDT

President, **N. D. FITZROY**
Executive Director,
PAUL ALLMENDINGER
Treasurer, **ROBERT A. BENNETT**

PUBLISHING STAFF
Mng. Dir., Publ., **J. J. FREY**
Dep. Mng. Dir., Pub.,
JOS. SANSONE
Managing Editor,
CORNELIA MONAHAN
Sr. Production Editor,
VALERIE WINTERS
Editorial Prod. Asst.,
MARISOL ANDINO

The Transactions of the ASME, Journal of Turbomachinery (ISSN 0889-504X) is published quarterly (Jan., Apr., July, Oct.) for $85 per year by The American Society of Mechanical Engineers, 345 East 47th Street, New York, NY 10017. Second class postage permission pending at New York, NY and additional mailing offices. POSTMASTER: Send address change to The Journal of Turbomachinery, c/o The AMERICAN SOCIETY OF MECHANICAL ENGINEERS, 22 Law Drive, Box 2300, Fairfield, NJ 07007-2300."

CHANGES OF ADDRESS must be received at Society headquarters seven weeks before they are to be effective. Please send old label and new address.

PRICES: To members, $24.00, annually; to nonmembers, $85.00.
Add $6.00 for postage to countries outside the United States and Canada.

STATEMENT from By-Laws. The Society shall not be responsible for statements or opinions advanced in papers or ... printed in its publications (B 7.1, para. 3).

COPYRIGHT © **1986** by the American Society of Mechanical Engineers. Reprints from this publication may be made on condition that full credit be given the TRANSACTIONS OF THE ASME – JOURNAL OF TURBOMACHINERY, and the author, and date of publication be stated.

INDEXED by Engineering Information

Downloaded 01 Jun 2010 to 171.66.16.52. Redistribution subject to ASME license or copyright; see http://www.asme.org/terms/Terms_Use.cfm

T. Sato
Manager.

S. Aoki
Senior Research Engineer.

Turbomachinery Research & Promotion Laboratory,
Takasago Technical Institute

T. Nagayama
Senior Research Engineer,
Turbomachinery Research Laboratory,
Nagasaki Technical Institute

Mitsubishi Heavy Industries, Ltd.,
Japan

Extensive Verification of the Denton New Scheme From the User's Point of View: Part I—Calibration of Code Control Variables

Recently, a computer-aided interactive design system has been used for turbine design. The blade-to-blade flow program incorporated in the system is required to have short run times, robustness, and no limitations. The Denton time-marching code is attractive as it is fast and can handle mixed subsonic–supersonic flows. The Denton new scheme was published in 1982 and improvements were achieved in run times and entropy conservation. In this paper, code control variables are calibrated from the user's point of view. Factors affecting computing costs and accuracy are investigated, and the "know-how" necessary to operate the code efficiently is discussed. Comparisons of calculated and experimental results are presented in part II.

Introduction

Recently, a computer-aided interactive design system has been introduced in turbine design. A highly developed computer-aided design system enables design engineers to achieve better designs in a very short time [1, 2]. In this efficient design tool, a blade-to-blade flow calculation program is incorporated, and has made significant contributions to high-performance blade design. The blade-to-blade flow calculation program adopted for design is required to have short computer run times, robustness, and no limitations, as well as a high degree of accuracy. This is because the blade-to-blade flow program is used several hundred times in the blade design of a multistage turbine, and cascade design conditions vary significantly from the first-stage nozzle to the last-stage rotating blade. In addition, turbine designers are not usually specialists in numerical analysis and are not familiar with details of numerical procedures.

There are several well-tested and established methods for calculation of inviscid blade-to-blade flow fields. The well-known methods are streamline curvature, finite difference, finite element methods, and time-marching methods. Among these methods, the time-marching methods seem to be the most promising for turbine cascade flow problems. The main attraction of these methods arises from their ability to handle mixed subsonic–supersonic flows, as turbines often operate in the transonic regime. One disadvantage of the time-marching methods is their comparatively long computer run times. Such long run times are undesirable for the design jobs in which the computer-aided interactive design system is used. But reduction in computer costs and improvements in numerical methods have made time-marching methods usable as design tools.

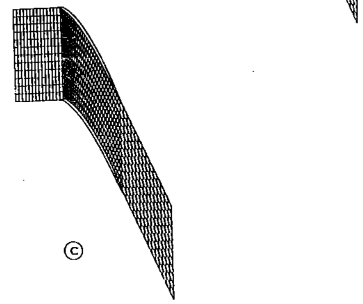

Fig. 1 Cascade configurations and mesh arrangements

The Denton time-marching methods are the most practical and fastest among the various time-marching methods. The Denton original scheme was published in 1975 [3], and verified

---

Contributed by the Gas Turbine Division of The American Society of Mechanical Engineers and presented at the 31st International Gas Turbine Conference and Exhibit, Düsseldorf, Federal Republic of Germany, June 8–12, 1986. Manuscript received at ASME Headquarters January 10, 1986. Paper No. 86-GT-57.

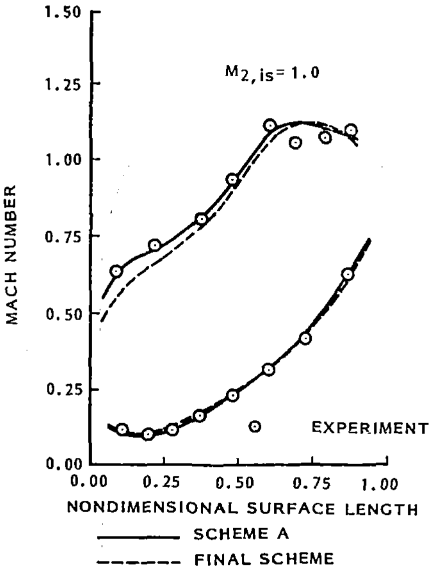

Fig. 2 Comparison of calculated surface Mach number distribution with experimental data for cascade Ⓑ

Table 1 Comparison of convergence behavior of scheme A with final scheme

TIME STEP MULTIPLIER	CONVERGENCE			
	M2,is = 0.8		M2,is = 1.0	
	SCHEME A (TIME STEPS)	FINAL SCHEME (TIME STEPS)	SCHEME A (TIME STEPS)	FINAL SCHEME (TIME STEPS)
0.4	YES (235)	NO (FAILED)	YES (226)	NO (FAILED)
0.3		YES (301)		NO (FAILED)
0.2				YES (344)

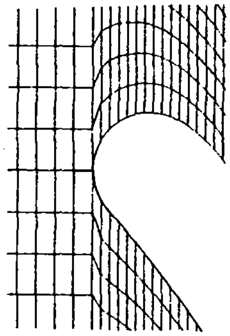

Fig. 3 A leading edge model for cascade Ⓐ

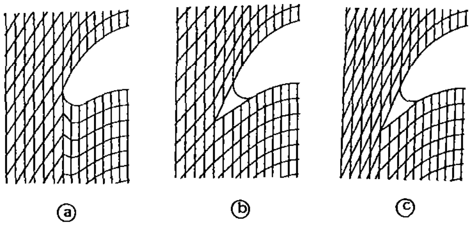

Fig. 4 Leading edge models for cascade Ⓑ

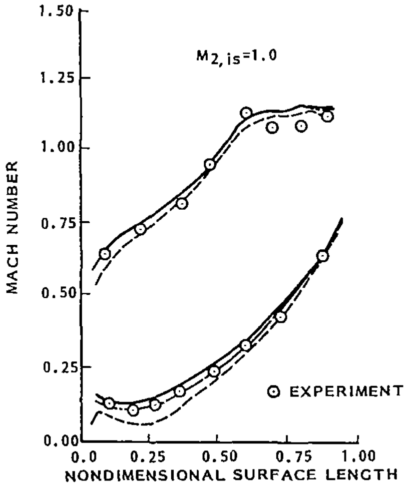

MARKS	LEADING EDGE MODELS	CONVERGENCE TIME STEPS	CPU TIME (SEC)
– – –	ⓐ	491	34
——	ⓑ	488	34
–·–·–	ⓒ	476	33

Fig. 5 Effect of leading edge models on calculated surface Mach number distributions for cascade Ⓑ

by Bryce and Litchfield [4]. The scheme was improved in 1982 [5]. The new scheme uses a new type of grid consisting of quadrilateral elements which do not overlap and have nodes at their corners. The use of the new grid reduces the finite differencing error and helps to improve entropy conservation. Computer run times are considerably reduced by using a simple multigrid method.

In the authors' company, the Denton blade-to-blade flow calculation code based on the new scheme has been used for the design of industrial gas turbines and satisfactory results have been obtained.

In order to operate the computer code efficiently, the code control variables should be calibrated to provide accurate solutions with minimum costs. In this paper, factors affecting computing costs and accuracy are investigated from the practical point of view and the "know-how" necessary to operate the code efficiently is discussed.

Factors Affecting Computing Costs and Accuracy

It is very important to check the computational limitations and the behavior of solutions before new computer methods are introduced to the design process. The codes used in design jobs are required to provide accurate solutions with minimum costs for a wide range of cascade configurations which cover all design sections of an industrial gas turbine. The following factors affecting computing costs and accuracy are investigated in this paper:

- difference scheme
- leading edge and trailing edge models
- multigrid block size
- time step multiplier
- mesh size and arrangements
- smoothing factor
- convergence tolerance

Selection of Cascade Configurations. The three cascade configurations shown in Fig. 1 were selected from the various cascade configurations of industrial gas turbines to investigate the above factors because they have some particular geometrical features. Cascade Ⓐ is a typical first-stage air-cooled nozzle of a high-temperature gas turbine and has a blunt leading edge. Cascade Ⓑ is an air-cooled blade with a high deflection angle. Both cascades Ⓐ and Ⓑ have large

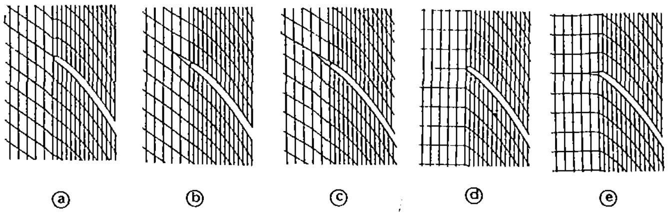

Fig. 6 Leading edge models for cascade Ⓒ

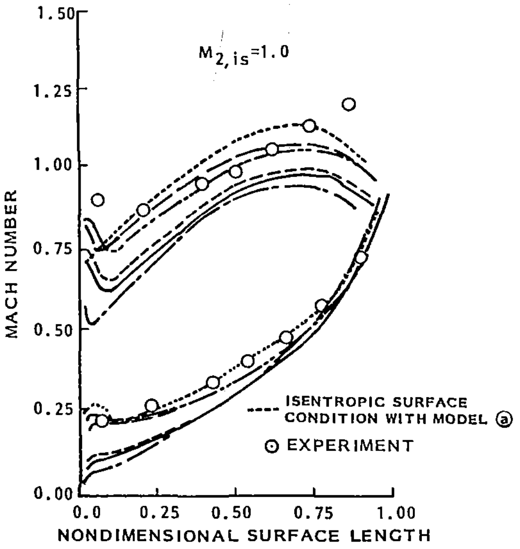

MARKS	LEADING EDGE MODELS	CONVERGENCE (TIME STEPS)	CPU TIME (SEC)
----	ⓐ	436	30
———	ⓑ	465	32
—-—	ⓒ	474	33
—··—	ⓓ	427	30
— —	ⓔ	435	30

Fig. 7 Effect of leading edge models on calculated surface Mach number distributions for cascade Ⓒ

blade and trailing edge thicknesses. Cascade Ⓒ is a blade tip section of a low-hub-ratio, last-stage turbine and has small blade and trailing edge thicknesses, and a small deflection angle. Pitch chord ratios of each cascade are 0.906, 0.808, and 0.845, respectively. Since these three cascade configurations are considered to be representative of all design sections of industrial gas turbines, the "know-how" required to operate the code obtained from the investigation can be applied to all cascade configurations. As the turbine cascades of industrial gas turbines usually operate at an exit Mach number range of 0.7-1.1, the calculations are performed at isentropic exit Mach numbers ($M_{2,is}$) of 0.8 and 1.0. The cascade flow is fully subsonic at $M_{2,is}=0.8$ and there exist local supersonic regions on the suction surface at $M_{2,is}=1.0$.

Difference Scheme. In [5], four difference schemes were discussed. Among the schemes, a linear combination of schemes B and C was adopted as final because it would have good shock-capturing properties and permit reverse flow.

However, for a blade-to-blade flow calculation code used in blade design of industrial gas turbines, faster schemes with good stability properties are more desirable, rather than shock-capturing properties or tolerance of reverse flow. This is because the turbines usually operate at high subsonic exit Mach number, and cusps may be placed in regions where reverse flow would occur. Thus, both the final scheme and scheme A, which has the same stability mechanism as the original opposed difference scheme, are investigated here.

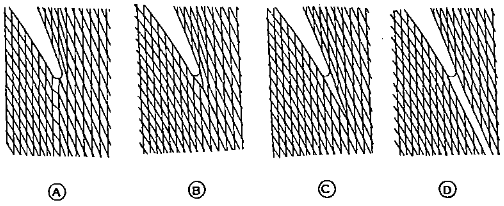

Fig. 8 Trailing edge models

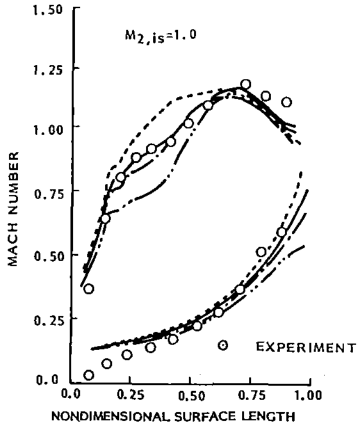

MARKS	TRAILING EDGE MODELS	CONVERGENCE (TIME STEPS)	CPU TIME (SEC)
- - -	Ⓐ	459	32
———	Ⓑ	452	32
—·—	Ⓒ	451	31
—··—	Ⓓ	471	31

Fig. 9 Effect of trailing edge models on calculated surface Mach number distributions for cascade Ⓐ

Table 1 shows the rate of convergence of both schemes for cascade Ⓑ. Scheme A is more stable and faster than the final scheme. It permits about 30 percent fewer time steps than the final scheme. Calculated blade surface Mach number distributions of cascade Ⓑ are compared with experimental data in Fig. 2. Trends were similar at Mach 0.8. Scheme A brings better agreement than the final scheme. From the results of this investigation, scheme A was chosen for design jobs and further investigations. In this calculation, a mesh of 13×61 grid points and a 3×3 multigrid block size were used. Convergence tolerance was a maximum change in axial velocity of 0.05 percent per iteration.

Leading Edge and Trailing Edge Models. Numerical errors in the finite difference approximation are expected to be significant in the leading edge and trailing edge regions due to large surface curvatures. The rate of change of fluid properties is greatest around the leading edge. Since the numerical errors are convected downstream, the whole downstream flow is influenced. On the other hand, the trailing edge flow affects the suction surface velocities with which the designers are mostly concerned.

In this section, several leading edge and trailing edge models are investigated. A mesh of 13×61 grid points and a 3×3 multigrid block size were used. The convergence tolerance was a maximum change in axial velocity of 0.01 percent per iteration.

Leading Edge Models. In the Denton scheme, the computational grid is formed by a series of quasi-streamlines and pitchwise lines. The quasi-streamlines upstream of the cascade are usually chosen to be roughly in line with the blade metal angle.

The nozzle cascades represented by cascade Ⓐ are usually

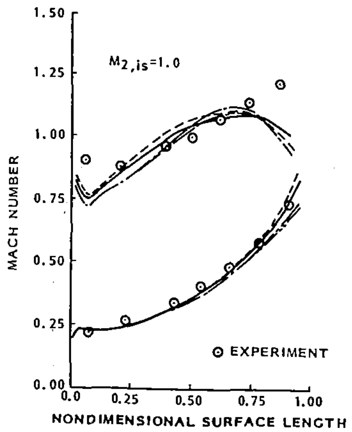

MARKS	TRAILING EDGE MODELS	CONVER-GENCE (TIME STEPS)	CPU TIME (SEC)
- - -	Ⓐ	429	30
———	Ⓑ	435	30
— - —	Ⓒ	436	31
-·-·-	Ⓓ	437	31

Fig. 10 Effect of trailing edge models on calculated surface Mach number distributions for cascade Ⓒ

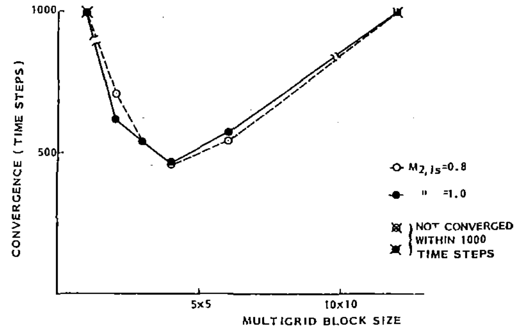

Fig. 11 Effect of multigrid block sizes on convergence for cascade Ⓐ

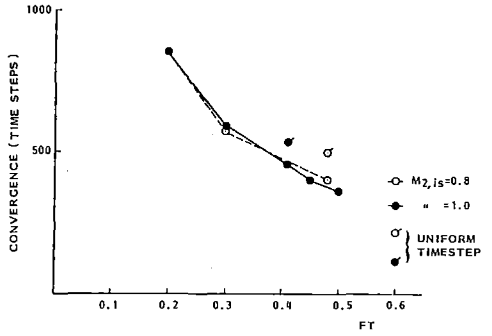

Fig. 12 Effect of FT on convergence for cascade Ⓐ

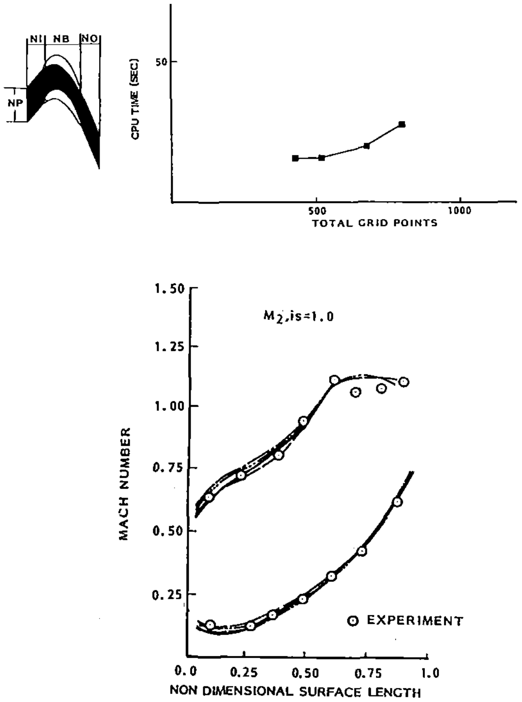

MARKS	GRID SIZE					CONVERGENCE (TIME STEPS)
	TOTAL	NI	NB	NO	NP	
	217	6	19	6	7	NOT CONVERGED WITHIN 1000 ITERATIONS
	403	6	19	6	13	NO(FAILED)
—·—	520	10	20	10	13	YES(375)
—··—	676	12	28	12	13	YES(336)
——-	427	15	32	14	7	YES(439)
———	793	15	32	14	13	YES(413)
	1159	15	32	14	9	NOT CONVERGED WITHIN 1000 ITERATIONS

Fig. 13 Effect of grid size on calculated surface Mach number distributions and CPU time for cascade Ⓑ

air cooled and have film-cooling holes at the leading edge and on both suction and pressure surfaces. An accurate prediction of the pressure distribution around the nozzle is required to obtain the design cooling flow rates for each of the cooling holes. Therefore the leading edge model without a cusp is adopted for the cascade Ⓐ, as shown in Fig. 3.

Three leading edge models are considered for cascade Ⓑ, as shown in Fig. 4. Model ⓐ has no cusp at the leading edge. Model ⓑ has a cusp, and the quasi-streamlines upstream of the cascade are in line with the blade metal angle. Model ⓒ has the cusp and the quasi-streamlines upstream of the cascade are chosen in line with the tangent to the suction surface of the blade.

The surface Mach number distributions of the cascade Ⓑ, calculated with the three leading edge models, are shown in Fig. 5. Trends were similar at Mach 0.8. A typical calculation (mesh size 13 × 61) consumes approximately 30 s CPU time on an IBM 3081. The suction surface Mach number distributions calculated with models ⓑand ⓒare almost equal. Close agreements between calculated and measured data are obtained with both models ⓑand ⓒ. The pressure surface Mach number distributions calculated with the model ⓐ are lower than those of the other models, and do not agree with the experimental results. The lower velocities calculated with model ⓑ are due to stagnation pressure losses around the leading edge. It is considered that these results come from the numerical errors due to sudden change of the direction of the grid in the leading edge region. From these results, it is concluded that the use of the grid having no sudden change of its direction is required in the leading edge region.

For cascade Ⓒ which has a small leading edge, the models ⓐ, ⓑ, and ⓒ, shown in Fig. 6, were tried initially. But good agreement was not obtained as shown in Fig. 7. Both the suction and pressure surface velocities are lower than those of the experiment. Trends were similar at Mach 0.8. No improvement was obtained with a nonuniform grid arrangement, in which grid spacing was reduced in both the axial and pitchwise directions, in the leading edge region. Better agreement was obtained by using an upstream grid consisting of axial quasi-streamlines and uniform pitchwise lines, shown in Fig. 7 as models ⓓ and ⓔ. Similar improvement was obtained by using isentropic surface conditions.

As the results show, a cusp may be placed at the leading edge and any sudden change of the grid directions in the leading edge region should be avoided to reduce the numerical errors. For a turbine blade which has a highly loaded leading

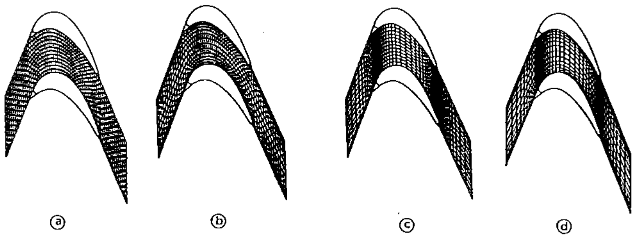

Fig. 14 Mesh arrangements

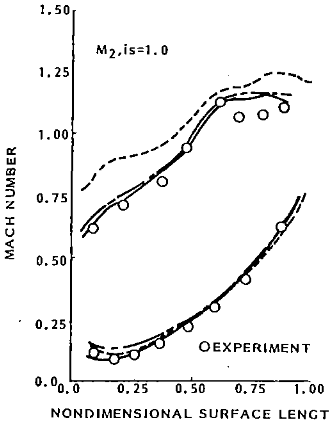

MARKS	MESH ARRANGEMENTS	CONVERGENCE (TIME STEPS)
——	ⓐ	YES(403)
– – –	ⓑ	YES(430)
- - -	ⓒ	YES(527)
	ⓓ	NO(FAILED)

Fig. 15 Effect of mesh arrangement on convergence and calculated surface Mach number distribution for cascade Ⓑ

edge, the isentropic surface conditions should be applied, or an upstream grid, whose direction is axial, should be used.

Trailing Edge Models. It is reasonable to set the grid in line with blade outlet metal angle in the downstream region. Four trailing edge models, shown in Fig. 8, were tested. Model Ⓐ has no cusp. Model Ⓑ has a cusp with a streamwise length taken from that of the stagnation region of the turbine blade, as observed in two-dimensional cascade tests. The streamwise length behind the trailing edge is 1.5 times that of the trailing edge thickness. The cusp of model Ⓒ is formed by drawing tangents to both suction and pressure surfaces. Model Ⓓ simulates the wake blockage and gradually decreases its width toward the downstream boundary.

In the investigation, no cusp was placed at the leading edge for cascade Ⓐ. The model ⓒ for cascade Ⓑ and the model ⓓfor cascade Ⓒ were adopted as the leading edge models, respectively.

Figure 9 shows the surface Mach number distributions and convergences of cascade Ⓐ with four trailing edge models. It is clearly shown that the choice of trailing edge model has a significant influence on the surface Mach number distributions of cascade Ⓐ. The same trends occurred for cascade Ⓑ. The suction surface Mach number distributions of cascades Ⓐ and Ⓑ are significantly influenced by the trailing edge models. This results from the difference in the simulated pressure surface flow boundaries around the trailing edge. Hence it is reasonable that the model Ⓑ, which simulates the real stagnation region of the turbine blade, produces the best solutions. The difference between the calculated surface Mach number distributions with model Ⓑ, and those with model Ⓒ, is relatively small. The suction surface Mach number distribution, calculated with the model Ⓒ, is lower than that with model Ⓑ. Model Ⓓ, which simulates wake blockage, does not produce good results.

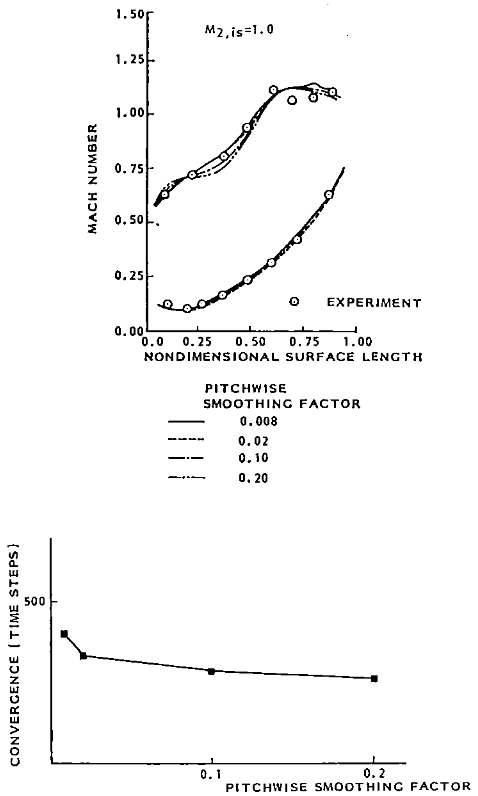

Fig. 16 Effect of smoothing factor on convergence and calculated surface Mach number distribution for cascade Ⓑ

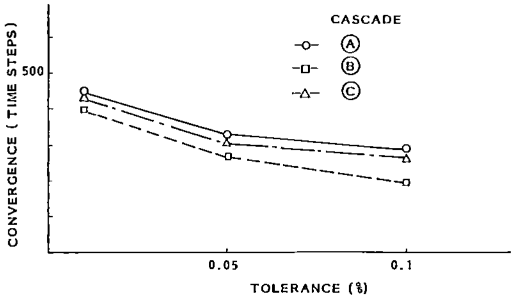

Fig. 17 Effect of tolerances on convergence

Table 2 Relation between cascade total pressure loss coefficients and smoothing factors

CASCADE	Y_P		(P_{02}/P_{01}) EXPERIMENT		SMOOTHING FACTOR REQUIRED TO ACHIEVE (P_{02}/P_{01}) EXPERIMENT
	$M_{2,is}$		$M_{2,is}$		
	0.8	1.0	0.8	1.0	
Ⓐ	0.028	0.048	0.991	0.978	< 0.01
Ⓑ	0.040	0.062	0.986	0.972	≤ 0.02
Ⓒ	0.028	0.030	0.991	0.986	∿ 0

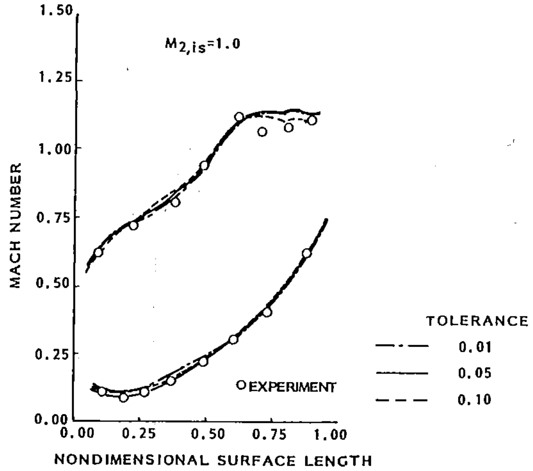

Fig. 18 Effect of convergence tolerances on calculated surface Mach number distribution for cascade Ⓑ

Figure 10 shows the surface Mach number distributions, and convergences of cascade Ⓒ, with the trailing edge models. For cascade Ⓒ, trailing edge models do not have significant effects on the flow field. The ratio of trailing edge thickness to throat width for cascades Ⓐ, Ⓑ, and Ⓒ are 0.116, 0.132, and 0.033, respectively. Therefore, it may be concluded that attention must be paid to cascades with large values of trailing edge thickness/throat width. By using the model Ⓑ, both cascades Ⓐ and Ⓑ agree well with experimental data at Mach numbers of 0.8 and 1.0. However, in the case of cascade Ⓒ, the prediction does not agree with experiment at $M_{2,is} = 1.0$, though good agreements are obtained at $M_{2,is} = 0.8$. Further investigation will be required for the trailing edge model of cascade Ⓒ.

As the results of the investigation show, it is obvious that a trailing edge model which simulates effective pressure surface flow boundaries should be used.

Multigrid Block Size. One weakness of the time-marching methods is their relatively long computer run times. The Denton original scheme was the fastest of the time-marching methods, but required much longer times than other methods, such as the finite difference or streamline curvature methods. This problem is partly overcome by adopting the multigrid method. A study on an optimum block size was performed for the three cascades. A mesh of 13×61 grid points was used, and the following single level multigrid block sizes were compared: 1×1 (without multigrid); 2×2; 3×3; 4×4; 6×6; and 12×12.

Figure 11 shows the effect of multigrid block size on convergence for cascade Ⓐ. An optimum block size is not affected by Mach number level. Since an optimum block size exists between 2×2 and 4×4 for all three cascades, it is reasonable to use a block size of 3×3 in the calculations. Considerable savings in run times are obtained by the multigrid method. The required time steps for convergence are about half of those without the multigrid method. It is not effective to use multigrid blocks which have different size in the streamwise and pitchwise directions. This is shown by the following results, which were obtained for cascade Ⓑ at $M_{2,is} = 1.0$ by changing the block size:

3×3	408 time steps
3×6	430 time steps
6×3	435 time steps

Therefore the multigrid block size of 3×3 is recommended.

Time Step Multiplier FT. This is the main factor controlling the stability of the Denton method which is an explicit approach. The time step used in the successive iterations is a fraction (FT) of that obtained by dividing the smallest distance increment in the axial direction by the speed of sound based on inlet stagnation conditions. Figure 12 shows the influence of FT on convergence for cascade Ⓐ. The highest stable FT value changes with cascade configurations, but an FT of 0.55 causes failure of the calculations for all three cascades. The Mach number level has little effect on the optimum value of FT. As the results show, the optimum value lies between 0.4 and 0.45 for these test cases.

Spatial variation of time step is a powerful means of reducing computer run times, and was adopted in the present investigation. The effectiveness of spatial variation of time steps is shown in Fig. 12. The method is quite effective for highly varied mesh arrangements and a 15–40 percent reduction in CPU time was obtained for cascades Ⓐ and Ⓒ. On the other hand, it is not effective for a grid which has constant axial mesh spacing.

Mesh Size and Arrangements. The mesh size has great influence on the computing cost and the accuracy. The finer the mesh the more accurate the solution, but the greater the computing cost. Hence, it is very important to use the smallest number of grid points, without any loss of accuracy, as the code is used several hundred times in each design job. Figure 13 shows the influence of the mesh size on the accuracy, and the computing time, for cascade Ⓑ. As the results of the investigation show, it appears that 500–600 grid points give satisfactory solutions for most blade rows. A typical CPU time with a mesh size of 10×50 is about 20 s on an IBM 3081. The method seems to be less stable with too few grid points, and also with too many grid points. This stability problem seems to be related to the grid aspect ratio defined by dividing the axial grid spacing by the pitchwise grid spacing.

An alternative method of obtaining accurate solutions, without increasing the number of grid points, is to reduce the grid spacing in regions where the flow properties change most rapidly. Spatially varied mesh arrangements were tested for the three cascades. In the investigation, the axial spacing of grid points was reduced in the leading and trailing edge regions, by 10 percent, and also 20 percent. The relative spacing of the quasi-streamlines was also changed across the pitch to reduce the spacing close to the blade surface. Figure 14 illustrates the following mesh arrangements for cascade Ⓑ:

Mesh arrangement	Axial	Pitchwise
ⓐ	uniform	uniform
ⓑ	uniform	nonuniform
ⓒ	nonuniform	uniform
ⓓ	nonuniform	nonuniform

Figure 15 shows the calculated surface Mach number distributions, and the convergence, for each mesh arrangement of cascade Ⓑ. No improvement was obtained for the cascade Ⓑ with spatially varied mesh arrangements.

A slight improvement is obtained for the pressure surface Mach numbers of cascade Ⓐ, but for cascade Ⓒ, no improvements are achieved. The calculations become less stable with increasing nonuniformity of the mesh arrangement. Therefore, in design jobs, it is sufficient to use a uniform arrangement of grid points for both pitchwise and streamwise directions.

Smoothing Factor. Some smoothing is necessary to stabilize the calculations. Smoothing of the dependent variables in the pitchwise direction is used to prevent decoupling of the solutions on odd and even-numbered grid points. Smoothing should be kept to a minimum since it influences the accuracy of the solution.

Thus it is very important to use the largest smoothing factor which does not affect the accuracy of the solution. Figure 16 shows the effect of pitchwise smoothing factors on the solution and convergence for cascade Ⓑ. Smoothing factors of less than 0.02 have no influence on the solution. Convergence is improved with an increase in the smoothing factor. Increasing the smoothing factor beyond 0.02 causes a decrease in accuracy, but convergence is not much improved. Hence it is preferable to use a smoothing factor less than 0.02.

One good indicator for the permissible smoothing factor is the total pressure deficit across the computational region. The ratio of the downstream total pressure (P_{02}) to the upstream value (P_{01}) decreases with an increase of the smoothing factor. The total pressure ratios (P_{02}/P_{01}) calculated from the total pressure loss coefficients ($Y_p = (P_{01} - P_{02})/(P_{02} - P_2)$, where P_2 = downstream static pressure) obtained from the two-dimensional cascade test, and the smoothing factors to achieve the same values of total pressure ratio, are also shown in Table 2.

In the case of cascade Ⓒ, the total pressure ratio obtained from the experiment is not achieved even by using a zero smoothing factor. This large total pressure deficit results from numerical errors around the leading edge.

Since well-designed blades of modern turbines have total pressure loss coefficients of 0.03–0.04 in the high subsonic regime, it is recommended that a smoothing factor of about 0.01 be used.

Convergence Criterion. Convergence is taken to occur when the maximum specified change in axial velocity per step anywhere in the flow field is less than some specified value. It is a practical approach to relax the tolerance to save run times. Figure 17 shows the relationship between convergence tolerances and time steps. Relaxing the tolerance from 0.01 percent to 0.05 percent results in about a 30 percent reduction in time steps. Thus a typical CPU time with a mesh size of 10×50 is reduced to about 15 s on an IBM 3081. However, further relaxing of tolerance does not bring as large a reduction in the number of time steps.

Solutions obtained using tolerances of 0.01 and 0.05 percent agree quite well with each other as shown in Fig. 18. The same trend occurred in all cases. From the study, it is recommended that a maximum change in axial velocity of 0.05 percent per iteration be used as a convergence criterion.

Conclusion

The code control variables of the Denton new scheme are calibrated from the user's point of view. From the results of the investigation using three cascade configurations, which are considered to be representative of all design sections of an industrial gas turbine, the following conclusions are obtained:

1 Scheme A is preferable as it is faster and more stable than the final scheme.

2 The accuracy of the solution is significantly influenced by both leading edge and trailing edge models. It is recommended that a trailing edge cusp with streamwise length 1.5 times that of the trailing edge thickness should be used. No leading edge cusp is preferable for a first-stage nozzle. For the blade, it is recommended to place a cusp at the leading edge to reduce the numerical errors produced around the leading edge. For thin blades with a small leading edge, it is necessary to adopt the isentropic surface condition, or to use an upstream grid whose direction is axial.

3 The multigrid method reduces run times by over 50 percent. A 3×3 block size appears to be optimal.

4 A mesh size of 500-600 grid points gives satisfactory results.

5 An optimum time step multiplier exists between 0.4 and 0.45. Use of a spatially varied time step is quite effective for highly varied mesh arrangements.

6 It is recommended that a smoothing factor of about 0.01 be used.

7 For the convergence criterion, it is recommended that a maximum change in the axial velocity of 0.05 percent per iteration be used.

Acknowledgments

The authors wish to express their indebtedness to Mitsubishi Heavy Industries, Ltd. for permission to publish this paper. The authors also wish to express their gratitude to Dr. J. D. Denton of Cambridge University for his valuable advice, and to Mr. Yamachika for his assistance in preparing this paper.

References

1 Aoki, S., Mase, M., and Murai, T., "Gas Turbine Interactive Design System (TDSYS)," *Mitsubishi Technical Review*, June 1981, pp. 96–101.

2 Sato, T., Aoki, S., and Mori, H., "A Gas Turbine Interactive Design System – TDSYS – for Advanced Gas Turbine," ASME Paper No. 85-JPGC-GT-11.

3 Denton, J. D., "A Time Marching Method for Two and Three Dimensional Blade to Blade Flow," ARC R. & M.3775, 1975.

4 Bryce, J. D., and Litchfield, M., "Experience of the Denton Blade-to-Blade Time Marching Programs," NGTE Note 1050, Oct. 1976.

5 Denton, J. D., "An Improved Time Marching Method for Turbomachinery Flow Calculation," ASME Paper No. 82-GT-239.

APPENDIX

Airfoil Coordinates of the Cascades

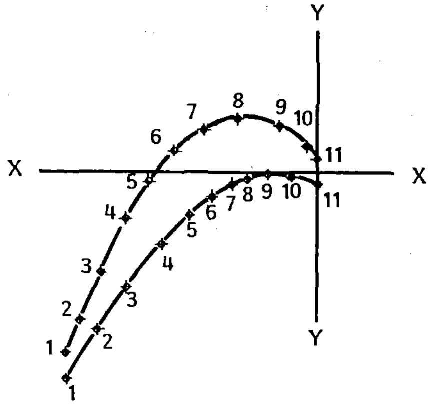

Fig. 19 Locations and point numbers of coordinates

Table 3 Airfoil coordinates of cascade Ⓐ

POINT NO.	SUCTION SURFACE		PRESSURE SURFACE	
	X	Y	X	Y
1	-16.78	-38.02	-16.78	-42.75
2	-13.40	-21.89	-13.40	-34.43
3	-10.02	- 8.50	-10.02	-26.88
4	- 6.66	1.99	- 6.66	-20.15
5	- 3.30	9.82	- 3.30	-14.09
6	0.05	15.73	0.05	- 8.58
7	3.40	19.76	3.40	- 3.51
8	6.74	22.06	6.74	1.19
9	10.08	23.44	10.08	5.56
10	13.42	24.00	13.42	9.50
11	16.75	23.91	16.75	13.14

Table 4 Airfoil coordinates of cascade Ⓑ

POINT NO.	SUCTION SURFACE		PRESSURE SURFACE	
	X	Y	X	Y
1	-38.94	-26.12	-38.94	-29.89
2	-34.33	-13.27	-30.56	-15.38
3	-28.51	- 0.97	-22.72	- 5.77
4	-23.69	5.78	-17.78	- 1.41
5	-17.93	10.55	-13.78	1.02
6	-12.52	12.11	-11.39	1.82
7	- 8.25	11.48	- 9.80	2.04
8	- 4.35	9.29	- 7.85	1.94
9	- 1.24	5.81	- 5.11	1.17
10	0.62	2.23	- 2.23	- 0.21
11	0.71	2.02	0.71	- 2.13

Table 5 Airfoil coordinates of cascade Ⓒ

POINT NO.	SUCTION SURFACE		PRESSURE SURFACE	
	X	Y	X	Y
1	-16.72	-29.51	-16.83	-31.62
2	-13.35	-21.32	-13.50	-24.25
3	- 9.97	-13.48	-10.15	-16.91
4	- 6.57	- 6.12	- 6.76	- 9.76
5	- 3.17	0.74	- 3.36	- 2.92
6	0.24	7.00	0.05	3.45
7	3.65	12.57	3.47	9.24
8	7.05	17.38	6.90	14.33
9	10.45	21.30	10.31	18.68
10	13.83	24.32	13.72	22.27
11	17.20	26.52	17.13	25.07

Extensive Verification of the Denton New Scheme From the User's Point of View: Part II—Comparison of Calculated and Experimental Results

T. Sato
Manager.

S. Aoki
Senior Research Engineer.

Turbomachinery Research &
Promotion Laboratory,
Takasago Technical Institute

T. Nagayama
Senior Research Engineer,
Turbomachinery Research Laboratory,
Nagasaki Technical Institute

Mitsubishi Heavy Industries, Ltd., Japan

A blade-to-blade flow program incorporated in the computer-aided turbine design system is required to have short run times, robustness, and no limitations. The Denton time-marching method published in 1982 is attractive as it is fast and can handle mixed subsonic-supersonic flows. Calibration of code control variables is discussed in part I. In this paper, the scheme is extensively verified by comparing calculated surface Mach number distributions with experimental data obtained from two-dimensional cascade tests for 23 cascades. For the nozzles, excellent agreement is obtained if the flows are fully subsonic, or transonic with weak shock-boundary layer interaction. For the blades, very good agreement is also obtained if the blades have moderate blade reaction and viscous effects are small. Satisfactory results are obtained for suction surface diffusion, even at off-design inlet conditions, if absolute values of incidence angle are less than 10 deg.

Introduction

Recently, a computer-aided interactive design system has been introduced in turbine design. A highly developed computer-aided design system enables design engineers to achieve better designs in a very short time [1, 2]. In this efficient design tool, a blade-to-blade flow calculation program is incorporated, and has made significant contributions to high-performance blade design. The blade-to-blade flow calculation program adopted for design is required to have short computer run times, robustness, and no limitations, as well as a high degree of accuracy. This is because the blade-to-blade flow program is used several hundred times in the blade design of a multistage turbine, and cascade design conditions vary significantly from the first-stage nozzle to the last-stage rotating blade. In addition, turbine designers are not usually specialists in numerical analysis and are not familiar with details of numerical procedures.

There are several well-tested and established methods for calculation of inviscid blade-to-blade flow fields. The well-known methods are streamline curvature, finite difference, finite element methods, and time-marching methods. Among these methods, the time-marching methods seem to be the most promising for turbine cascade flow problems. The main attraction of these methods arises from their ability to handle mixed subsonic–supersonic flows, as turbines often operate in the transonic regime. One disadvantage of the time-marching methods is their comparatively long computer run times. Such long run times are undesirable for the design jobs in which the computer-aided interactive design system is used. But the reduction in computer costs and improvements in the numerical methods have made time-marching methods usable as design tools. The Denton time-marching methods are the most practical and fastest among the various time-marching methods. The Denton original scheme was published in 1975

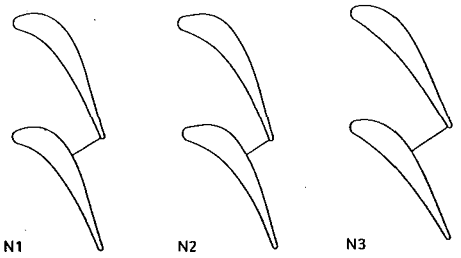

NAME	β_{1M} deg.	$\sin^{-1}(O/S)$ deg.	S/C	$d_{T.E.}/O$	S/e
N1	90.0	17.8	0.762	0.129	0.214
N2	90.0	15.5	0.715	0.155	0.290
N3	90.0	23.7	0.734	0.095	0.202

Fig. 1 Cascade configurations and geometric data for N1, N2, and N3

Contributed by the Gas Turbine Division of THE AMERICAN SOCIETY OF MECHANICAL ENGINEERS and presented at the 31st International Gas Turbine Conference and Exhibit, Düsseldorf, Federal Republic of Germany, June 8–12, 1986. Manuscript received at ASME Headquarters January 10, 1986. Paper No. 86-GT-58.

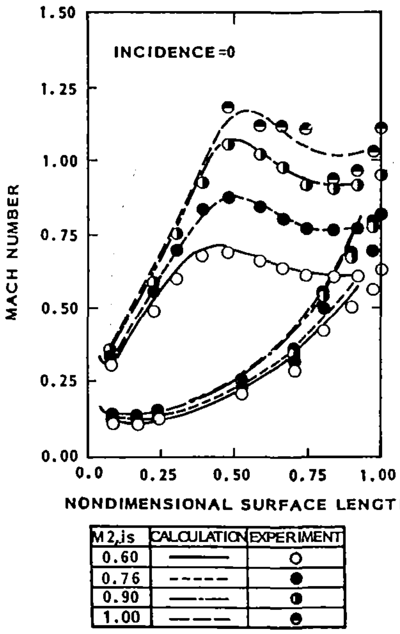

Fig. 2 Comparison of calculated surface Mach number distributions and experimental data for cascade N1

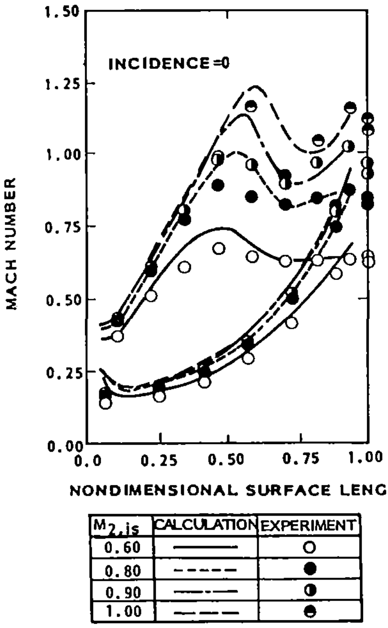

Fig. 4 Comparison of calculated surface Mach number distributions and experimental data for cascade N4

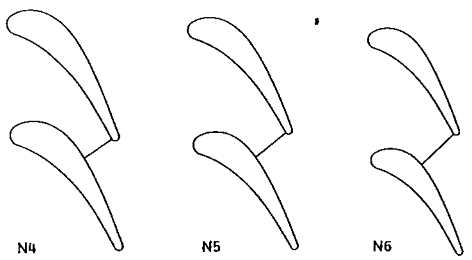

NAME	β_{1M}	$\sin^{-1}(O/S)$	S/C	$d_{T.E.}/O$	S/e
N4	90.0	18.8	0.675	0.237	0.210
N5	90.0	20.5	0.775	0.190	0.276
N6	90.0	22.7	0.900	0.148	0.386

Fig. 3 Cascade configurations and geometric data for N4, N5, and N6

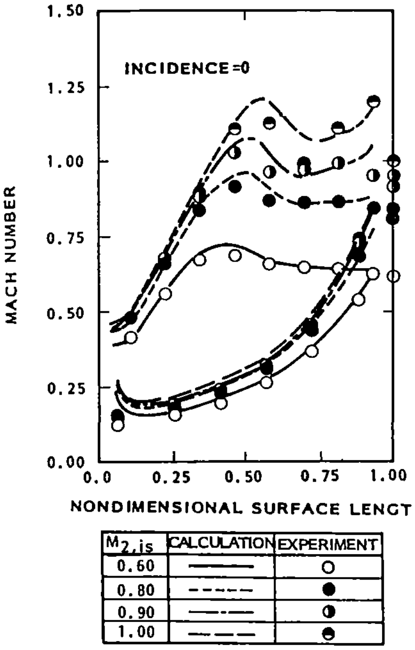

Fig. 5 Comparison of calculated surface Mach number distributions and experimental data for cascade N5

[3], and verified by Bryce and Litchfield [4]. The scheme was improved in 1982 [5].

In the authors' company, the Denton blade-to-blade flow calculation code based on the new scheme has been used for the design of industrial gas turbines and satisfactory results have been obtained. In this paper, the Denton new scheme is

Nomenclature

β_{1M} = metal inlet angle
O = throat width
S = pitch
C = chord
d_{TE} = trailing edge thickness
e = mean radius of curvature of suction surface between throat and trailing edge

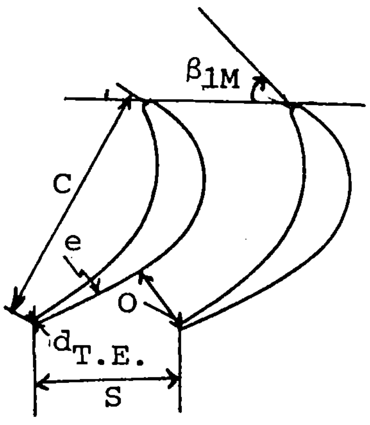

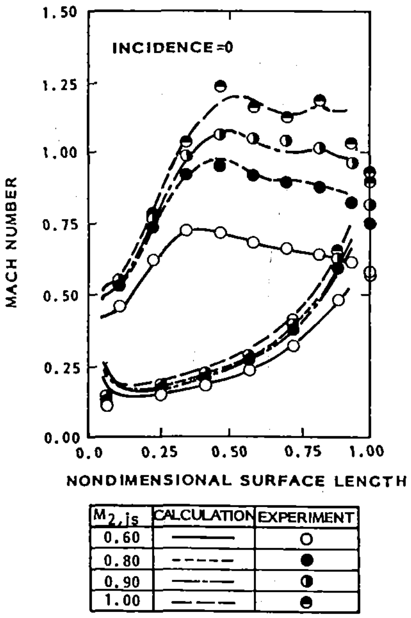

Fig. 6 Comparison of calculated surface Mach number distributions and experimental data for cascade N6

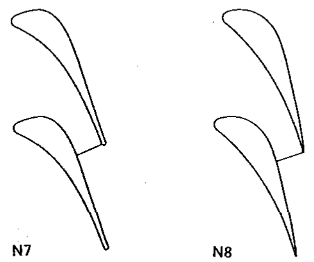

NAME	β_{1M}	$\sin^{-1}(O/S)$	S/C	$d_{T.E.}/O$	S/e
N7	90.0	16.4	0.668	0.141	0.021
N8	90.0	16.6	0.658	0.040	0.142

Fig. 7 Cascade configurations and geometric data of N7 and N8

extensively verified by comparing calculated blade surface Mach number distributions with experimental data obtained from two-dimensional cascade tests for 23 cascades.

Comparison of Calculated Results With Experimental Results

Calculated surface Mach number distributions are compared with measured data obtained from two-dimensional high-speed cascade tests. Twenty-three cascades which cover all typical design sections of industrial gas turbines are tested. These cascades are grouped into the following classes:

ⓐ	Mean section of first-stage nozzle	N1-N8
ⓑ	Mean section of first-stage blade	B1-B6
ⓒ	Mean section of intermediate-stage nozzle and blade	B7, B8
ⓓ	Hub section of last-stage blade	B9, B10
ⓔ	Mean section of last-stage nozzle and blade	B11-B13
ⓕ	Tip section of last-stage blade	B14, B15

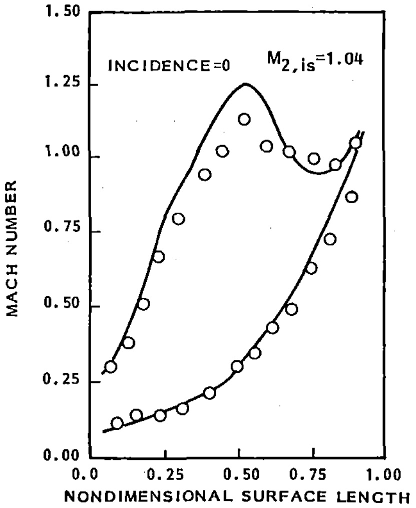

Fig. 8 Comparison of calculated surface Mach number distributions and experimental data for cascade N7

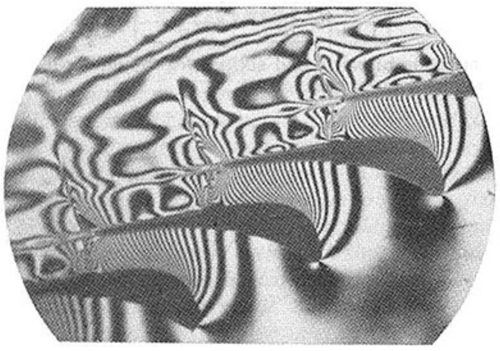

Fig. 9 Interferogram of N7 at $M_{2,is}$ = 1.04

Comparisons are performed for various isentropic exit Mach numbers and incidence angles. The leading edge and trailing edge models and factors affecting computations are those obtained in part I. For example, a mesh of 10×50 grid points and a 3×3 multigrid block size are used. Convergence tolerance is a maximum change in axial velocity of 0.05 percent.

Mean Section of First Stage Nozzle: N1-N8. Figure 1 shows cascade configurations and geometric features of N1, N2, and N3. These are all air-cooled nozzles whose design exit Mach numbers are between 0.7 and 0.8. Very good agreements are obtained for the three nozzles at subsonic exit Mach numbers as typically shown in Fig. 2. Under these conditions, the cascade flow is fully subsonic, or transonic with a local supersonic region, but the interaction between the shock wave and boundary layer is weak. Even at higher exit Mach numbers where the strong interaction between trailing edge shock and boundary layer occurs, the surface Mach numbers in the front part of both suction and pressure surfaces agree well with measured data. This is very important for the design of the cooled nozzle because film-cooling holes are usually located in these regions. The discrepancy on the aft part of the suction surface results from strong viscous effects due to the shock–boundary layer interaction, which is beyond an inviscid flow calculation. For better agreement, it is necessary to combine a surface boundary layer calculation, which includes shock–boundary layer interaction, with the inviscid calculation.

Figure 3 shows cascade configurations and geometric features of N4, N5, and N6. N4, N5, and N6 have a similar profile, but different pitch chord ratios of 0.675, 0.775, and

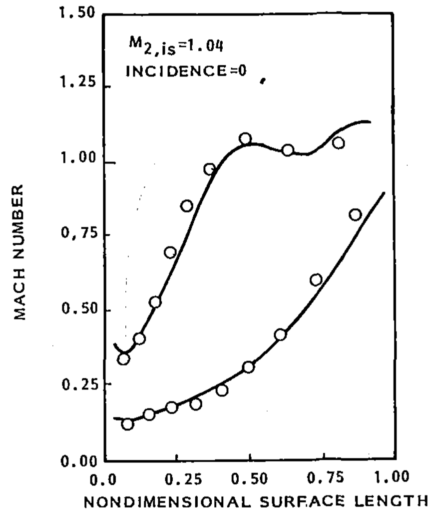

Fig. 10 Comparison of calculated surface Mach number distributions and experimental data for cascade N8

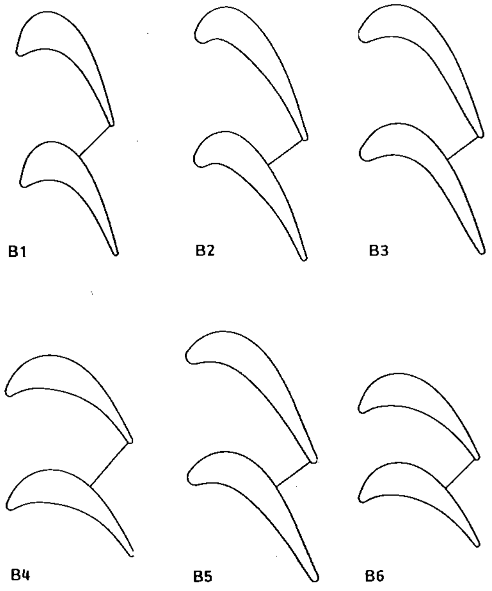

NAME	β_{1M}	$\sin^{-1}(O/S)$	S/C	$d_{T.E.}/O$	S/e
B1	40.6	20.4	1.068	0.104	0.534
B2	42.0	21.7	0.807	0.133	0.382
B3	53.8	19.8	0.728	0.155	0.320
B4	41.6	31.2	0.844	0.096	0.555
B5	57.9	21.5	0.710	0.182	0.206
B6	41.9	29.4	0.657	0.124	0.365

Fig. 11 Cascade configurations and geometric data of B1-B6

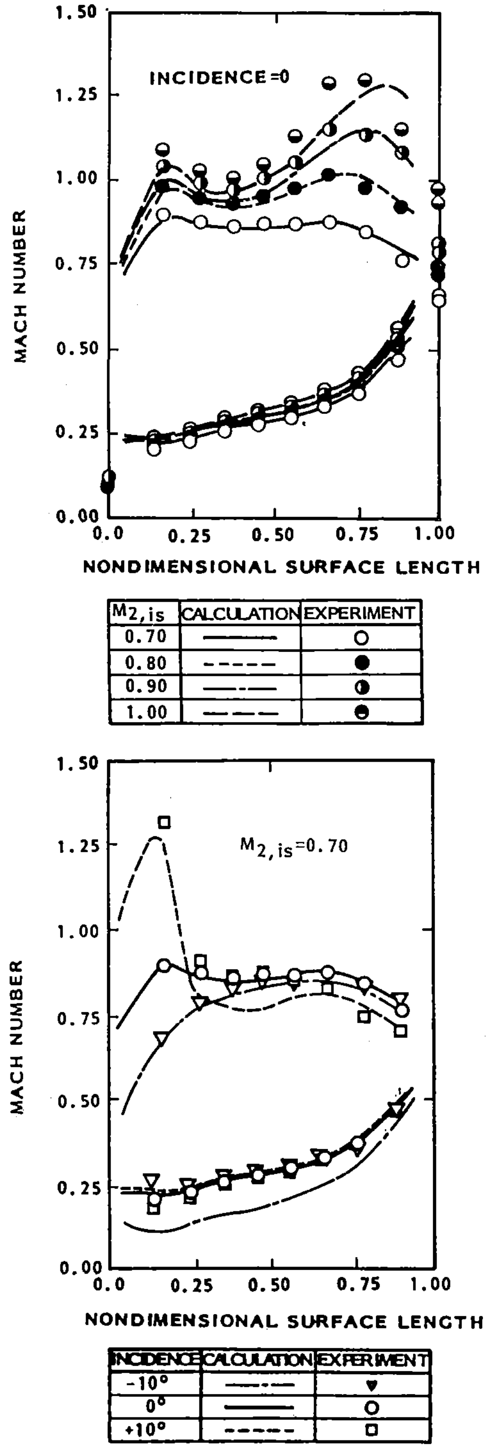

$M_{2,is}$	CALCULATION	EXPERIMENT
0.70	———	○
0.80	-----	●
0.90	—·—	◑
1.00	— — —	⊖

INCIDENCE	CALCULATION	EXPERIMENT
-10°	—·—	▼
0°	———	○
+10°	-----	□

Fig. 12 Comparison of calculated surface Mach number distributions and experimental data for cascade B4

0.900, respectively. The design pitch chord ratio is 0.775. As the profile is designed to investigate the effect of the trailing edge thickness on the aerodynamic performance, it has a large trailing edge thickness.

Hence values of trailing edge thickness/throat width are, with the exception of N6, much larger than for an ordinary air-cooled nozzle. However, ratios of pitch to mean radius of curvature of the unguided suction surface are not large.

As shown in Fig. 4, the agreement is not good for N4, which has a pitch chord ratio of 0.675. There seem to be two reasons for the discrepancy. The first one is that the inviscid calculation predicts high-velocity diffusion on the suction surface due to the convergent-slightly divergent passage of N4, but in the real flow, viscous effects improve the passage convergence. The second reason is that the trailing edge model is not valid for this cascade configuration, which has a large value of trailing edge thickness/throat width. Better agreement is obtained with an increased pitch chord ratio, as shown in Fig. 5 and Fig. 6. The predictions for N6, which has a pitch chord ratio of 0.9, agree well with the experimental results.

As the results clearly show, it is very important to choose a valid trailing edge model for cascades with large trailing edge thickness/throat width.

Figure 7 shows cascade configurations and geometric features of N7 and N8. N7 and N8 are so-called "flat back" nozzles. The profiles of both nozzles are similar to each other except in the trailing edge region. The pitch chord ratios and the gaugings (opening/pitch) of both nozzles are almost the same.

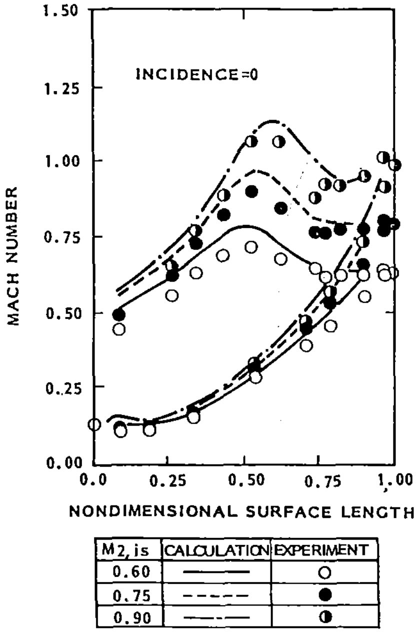

Fig. 13 Comparison of calculated surface Mach number distributions and experimental data for cascade B5

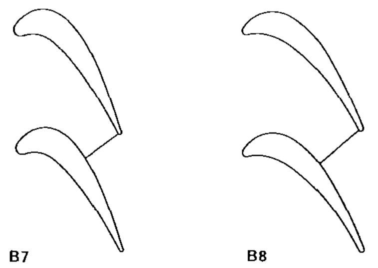

NAME	β_{1M}	$\sin^{-1}(O/S)$	S/C	$d_{T.E.}/O$	S/e
B7	53.3	21.0	0.786	0.084	0.320
B8	54.4	26.4	0.763	0.104	0.331

Fig. 14 Cascade configurations and geometric data of B7 and B8

Figure 8 shows the comparison of calculated result and measured result for N7. The isentropic exit Mach number is 1.04.

Some discrepancy is observed in the suction surface Mach number distribution of N7. At this isentropic exit Mach number, sudden thickening of the suction surface boundary layer, due to strong shock-boundary layer interaction, was observed in the interferograms obtained from the cascade test, as shown in Fig. 9. Good agreement is obtained at the same isentropic exit Mach number for N8, which has a thin trailing edge, as shown in Fig. 10.

By comparing these figures, it is obvious that by reducing the trailing edge thickness, the suction surface diffusion is much improved. This results from weakening of the trailing edge shock by narrowing of the trailing edge.

Mean Section of First-Stage Blade: B1-B6. Figure 11 shows cascade configurations and geometric features of B1-B6. B1-B6 are all air-cooled blades. The geometric features of the cascades are a large deflection angle, a large blade thickness, and a large trailing edge thickness. The blades have a wide range of geometric parameters. Pitch chord ratios vary from 0.657 to 1.068. Trailing edge thickness/throat widths are be-

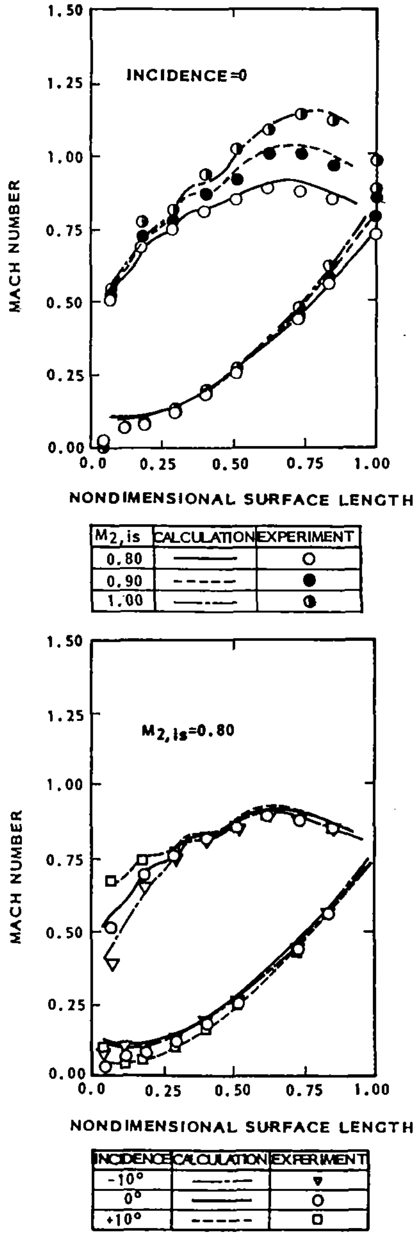

Fig. 15 Comparison of calculated surface Mach number distributions and experimental data for cascade B7

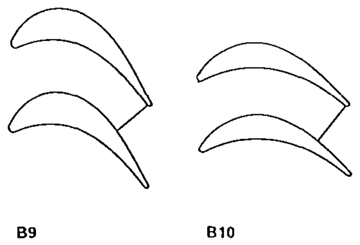

NAME	β_{1M}	$\sin^{-1}(O/S)$	S/C	$d_{T.E.}/O$	S/e
B9	48.7	30.2	0.523	0.096	0.232
B10	53.7	39.6	0.445	0.096	0.230

Fig. 16 Cascade configurations and geometric data of B9 and B10

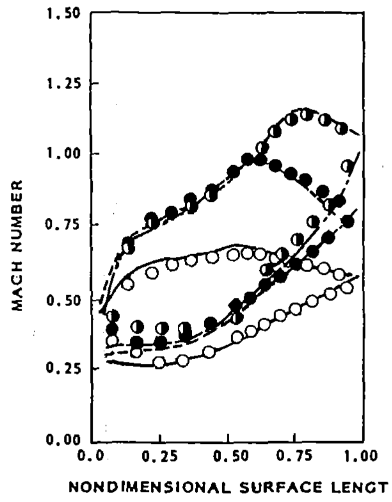

$M_{2,is}$	CALCULATION	EXPERIMENT
0.58	———	○
0.82	- - - - -	●
1.07	—·—	◑

Fig. 17 Comparison of calculated surface Mach number distributions and experimental data for cascade B9

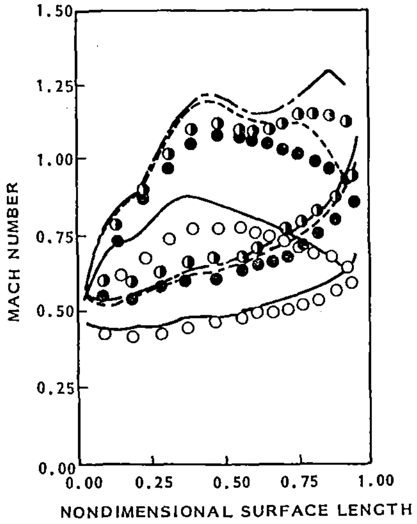

$M_{2,is}$	CALCULATION	EXPERIMENT
0.65	———	○
0.93	- - - - -	●
1.11	—·—	◑

Fig. 18 Comparison of calculated surface Mach number distributions and experimental data for cascade B10

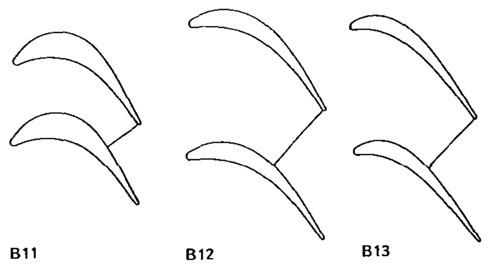

NAME	β_{1M}	$\sin^{-1}(O/S)$	S/C	$d_{T.E.}/O$	S/e
B11	48.9	29.2	0.558	0.076	0.173
B12	73.5	35.3	0.786	0.048	0.424
B13	73.7	34.2	0.766	0.040	0.261

Fig. 19 Cascade configuration and geometric data of B11, B12, and B13

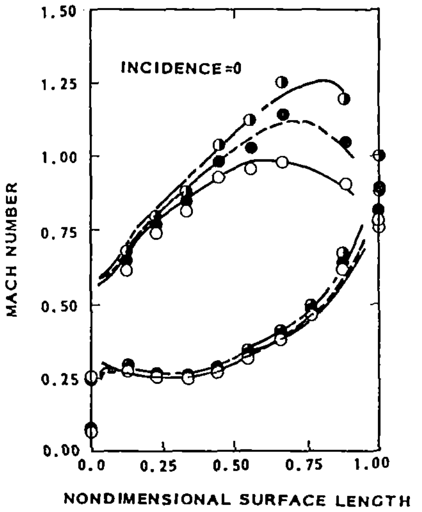

$M_{2,is}$	CALCULATION	EXPERIMENT
0.80	———	○
0.90	- - - - -	●
1.00	—·—	◑

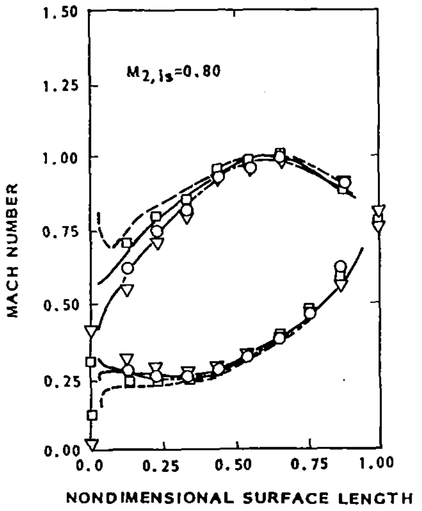

INCIDENCE	CALCULATION	EXPERIMENT
-10°	—·—	▼
0°	———	○
+10°	- - - - -	□

Fig. 20 Comparison of calculated surface Mach number distributions and experimental data for cascade B12

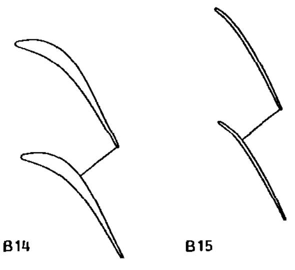

NAME	β_{1M}	$\sin^{-1}(O/S)$	S/C	$d_{T.E.}/O$	S/e
B14	96.1	25.2	0.764	0.046	0.227
B15	124.5	26.4	0.931	0.041	0.271

Fig. 21 Cascade configuration and geometric data of B14 and B15

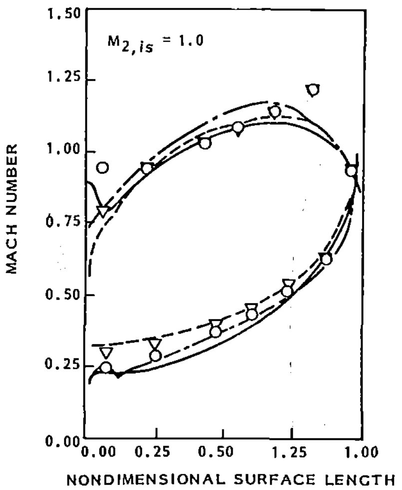

INCIDENCE	CALCULATION	EXPERIMENT
-10°	----	▽
0°	——— —·— ISENTROPIC SURFACE CONDITION	○

Fig. 22 Comparison of calculated surface Mach number distributions and experimental data for cascade B15

tween 0.096 and 0.182. As the design exit Mach numbers of the blades are about 0.8, ratios of pitch to mean radius of curvature of unguided suction surface are relatively large. As shown in Fig. 12, for the blade which has a moderate value of trailing edge thickness/throat width, the calculated results at zero incidence angle agree well with the experimental results at subsonic exit Mach numbers.

At off-design inlet conditions, there exists some discrepancy between the calculations and the experiments, but the suction surface diffusions, which are the important aerodynamic parameter, are satisfactorily predicted for absolute values of the incidence angle of less than 10 deg.

Good agreement is not obtained for B5, which has a large value of trailing edge thickness/throat width, as shown in Fig. 13.

Mean Section of Intermediate Stage Nozzle and Blade: B7, B8. Figure 14 shows cascade configurations and geometric features of B7 and B8. Comparison of the calculation for B7 and the experiments is shown in Fig. 15; good agreement is also obtained for B8. As B7 and B8 have moderate blade reaction and deflection angles, viscous effects are small if the flow is fully subsonic, or transonic with weak shock-boundary layer interaction. Then good agreement is obtained at subsonic exit conditions with absolute values of incidence angle less than 10 deg.

Hub Section of Last Stage Blade: B9, B10. Figure 16 shows cascade configurations and geometric features of B9 and B10. The geometric features of the cascade classified into this group are a low pitch chord ratio and a large gauging. Blade reaction is low.

Figures 17 and 18 show the comparison of the calculations for B9 and B10 with the experiments. The agreement is good for B9, but not good for B10. This result comes from the difference of the blade reactions. The blade reaction of B9 is higher than that of B10, and the blade passage contraction of B9 is better than that of B10. In the case of B10, the blade passage area change is so small that the boundary layer on both blade surfaces has much influence on the flow through the cascade.

Mean Section of Last Stage Nozzle and Blade: B11-B13. Figure 19 shows cascade configurations and geometric features of B11, B12, and B13. As typically shown in Fig. 20, good results are obtained for B11, B12, and B13 as the cascades classified in this group have high blade reactions and moderate deflection angles.

Tip Section of Last Stage Blade: B14, B15. Figure 21 shows cascade configurations and geometric features of B14 and B15. Figure 22 shows the comparison of the calculated data for B15 and the measured data. B15 is similar to the cascade C discussed in part I, hence the isentropic surface condition and an axial upstream grid are applied. B14 is a tip section of a shrouded blade and it has relatively large blade thickness. The configuration of the blade is similar to that of the cascade grouped in ⓔ. Hence good results are obtained.

For the calculations described above, a typical CPU time is approximately 15 s on an IBM 3081, and about 5-6 s on an IBM 3090.

Conclusion

The Denton new scheme is extensively verified from the user's point of view.

By using the "know-how" of operating the program (presented in part I) the surface Mach number distributions of 23 cascades, which cover all typical design sections of industrial gas turbines, are calculated and compared with the experimental data. A typical CPU time on an IBM 3090 is about 5-6 s with a mesh of 10×50. The following results are obtained:

1 For nozzle cascades, very good agreement is obtained if the flow is fully subsonic, or if it has a local supersonic region with a weak shock-boundary layer interaction.

2 For blade cascades, very good agreement is also obtained if the blade has sufficient blade reaction and viscous effects are small. Satisfactory results are obtained for the suction surface diffusion if the absolute value of incidence angle is less than 10 deg.

3 Calculated surface Mach number distributions do not agree well with experimental data if the cascades have large values of trailing edge thickness/throat width. For these cascades, further improvement will be required for the trailing edge model.

Acknowledgments

The authors wish to express their indebtedness to Mitsubishi Heavy Industries, Ltd. for permission to publish this paper. The authors also wish to express their gratitude to Dr. J. D. Denton of Cambridge University for his valuable advice, and to Mr. Yamachika for his assistance in preparing this paper.

References

1 Aoki, S., Mase, M., and Murai, T., "Gas Turbine Interactive Design System (TDSYS)," *Mitsubishi Technical Review*, June 1981, pp. 96-101.

2 Sato, T., Aoki, S., and Mori, H., "A Gas Turbine Interactive Design System – TDSYS – for Advanced Gas Turbine," ASME Paper No. 85-JPGC-GT-11.

3 Denton, J. D., "A Time Marching Method for Two and Three Dimensional Blade to Blade Flow," ARC R. & M. 3775, 1975.

4 Bryce, J. D., and Litchfield, M., "Experience of the Denton Blade-to-Blade Time Marching Programs," NGTE Note 1050, Oct. 1976.

5 Denton, J. D., "An Improved Time Marching Method for Turbomachinery Flow Calculation," ASME Paper No. 82-GT-239.

APPENDIX

Airfoil Coordinates of the Typical Cascades

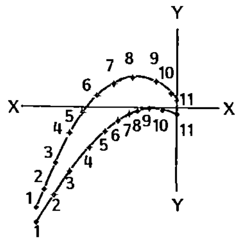

Fig. 23 Locations and point number of coordinates

Table 1 Airfoil coordinates of cascade N4

POINT NO.	SUCTION SURFACE		PRESSURE SURFACE	
	XU	YU	XL	YL
1	-10.546	-15.142	-10.546	-18.388
2	- 8.231	- 8.816	- 8.231	-14.036
3	- 6.175	- 4.001	- 6.175	-10.384
4	- 4.118	0.173	- 4.118	- 7.101
5	- 2.057	3.447	- 2.057	- 4.362
6	0.0	5.801	0.0	- 2.090
7	2.126	7.346	2.126	- 0.103
8	4.259	8.156	4.259	1.523
9	6.385	8.381	6.385	2.792
10	8.517	8.019	8.517	3.766
11	10.644	6.990	10.644	4.456

Table 2 Airfoil coordinates of cascade B4

POINT NO.	SUCTION SURFACE		PRESSURE SURFACE	
	XU	YU	XL	YL
1	-90.356	-32.629	-90.356	-39.560
2	-78.746	-10.245	-72.056	-15.557
3	-66.487	7.383	-56.803	- 4.275
4	-52.512	20.302	-43.267	1.366
5	-41.729	25.721	-35.709	3.181
6	-29.825	27.486	-29.272	4.186
7	-17.694	24.623	-23.061	4.672
8	- 9.491	19.260	-17.509	4.326
9	- 4.871	14.224	-12.958	3.365
10	0.500	4.676	- 4.573	0.102
11	1.111	3.128	1.111	- 3.130

Table 3 Airfoil coordinates of cascade B7

POINT NO.	SUCTION SURFACE		PRESSURE SURFACE	
	XU	YU	XL	YL
1	-54.920	-50.007	-54.920	-53.600
2	-47.606	-28.182	-41.971	-31.045
3	-40.850	-12.420	-32.630	-17.699
4	-33.141	0.081	-24.171	- 8.050
5	-27.146	6.926	-19.248	- 3.845
6	-20.143	11.180	-15.115	- 1.452
7	-12.120	12.134	-11.803	- 0.418
8	- 6.331	10.089	- 9.256	- 0.101
9	- 1.603	6.353	- 5.829	- 0.402
10	0.703	3.342	- 3.074	- 1.169
11	0.759	3.250	0.759	- 2.893

Table 4 Airfoil coordinates of cascade B9

POINT NO.	SUCTION SURFACE		PRESSURE SURFACE	
	XU	YU	XL	YL
1	-36.114	-12.574	-36.114	-14.026
2	-33.045	- 7.307	-31.362	- 8.622
3	-29.801	- 2.420	-27.227	- 4.818
4	-26.434	1.823	-23.215	- 1.934
5	-22.793	5.324	-19.476	0.056
6	-18.744	7.912	-16.146	1.236
7	-14.261	9.319	-13.251	1.769
8	- 9.553	9.223	-10.578	1.857
9	- 5.115	7.415	- 7.637	1.572
10	- 1.462	3.970	- 3.911	0.686
11	0.322	1.111	0.322	- 1.031

Table 5 Airfoil coordinates of cascade B12

POINT NO.	SUCTION SURFACE		PRESSURE SURFACE	
	XU	YU	XL	YL
1	-48.246	-26.594	-48.246	-28.641
2	-41.471	-15.762	-39.547	-17.239
3	-34.546	- 6.645	-31.753	- 9.495
4	-27.219	0.132	-24.359	- 4.428
5	-21.973	3.125	-19.791	- 2.418
6	-16.498	4.754	-15.452	- 1.281
7	-11.005	4.958	-11.132	- 0.768
8	- 8.336	4.541	- 8.894	- 0.671
9	- 4.500	3.356	- 5.370	- 0.689
10	- 2.062	2.275	- 2.901	- 0.809
11	0.058	1.171	0.058	- 1.063

Table 6 Airfoil coordinates of cascade B15

POINT NO.	SUCTION SURFACE		PRESSURE SURFACE	
	XU	YU	XL	YL
1	-14.333	-23.673	-14.333	-26.089
2	-11.179	-16.229	-11.187	-19.168
3	- 8.026	- 9.207	- 8.041	-12.431
4	- 4.872	- 2.624	- 4.895	- 5.955
5	- 1.719	3.480	- 1.749	0.155
6	1.435	9.032	1.397	5.799
7	4.589	13.981	4.543	10.909
8	7.742	18.248	7.689	15.410
9	10.896	21.747	10.835	19.283
10	14.049	24.481	13.981	22.512
11	17.203	26.524	17.127	25.069

APPENDIX

Airfoil Coordinates of the Typical Cascades

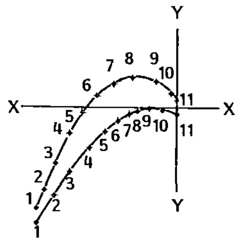

Fig. 23 Locations and point number of coordinates

Table 1 Airfoil coordinates of cascade N4

POINT NO.	SUCTION SURFACE		PRESSURE SURFACE	
	XU	YU	XL	YL
1	-10.546	-15.142	-10.546	-18.388
2	- 8.231	- 8.816	- 8.231	-14.036
3	- 6.175	- 4.001	- 6.175	-10.384
4	- 4.118	0.173	- 4.118	- 7.101
5	- 2.057	3.447	- 2.057	- 4.362
6	0.0	5.801	0.0	- 2.090
7	2.126	7.346	2.126	- 0.103
8	4.259	8.156	4.259	1.523
9	6.385	8.381	6.385	2.792
10	8.517	8.019	8.517	3.766
11	10.644	6.990	10.644	4.456

Table 2 Airfoil coordinates of cascade B4

POINT NO.	SUCTION SURFACE		PRESSURE SURFACE	
	XU	YU	XL	YL
1	-90.356	-32.629	-90.356	-39.560
2	-78.746	-10.245	-72.056	-15.557
3	-66.487	7.383	-56.803	- 4.275
4	-52.512	20.302	-43.267	1.366
5	-41.729	25.721	-35.709	3.181
6	-29.825	27.486	-29.272	4.186
7	-17.694	24.623	-23.061	4.672
8	- 9.491	19.260	-17.509	4.326
9	- 4.871	14.224	-12.958	3.365
10	0.500	4.676	- 4.573	0.102
11	1.111	3.128	1.111	- 3.130

Table 3 Airfoil coordinates of cascade B7

POINT NO.	SUCTION SURFACE		PRESSURE SURFACE	
	XU	YU	XL	YL
1	-54.920	-50.007	-54.920	-53.600
2	-47.606	-28.182	-41.971	-31.045
3	-40.850	-12.420	-32.630	-17.699
4	-33.141	0.081	-24.171	- 8.050
5	-27.146	6.926	-19.248	- 3.845
6	-20.143	11.180	-15.115	- 1.452
7	-12.120	12.134	-11.803	- 0.418
8	- 6.331	10.089	- 9.256	- 0.101
9	- 1.603	6.353	- 5.829	- 0.402
10	0.703	3.342	- 3.074	- 1.169
11	0.759	3.250	0.759	- 2.893

Table 4 Airfoil coordinates of cascade B9

POINT NO.	SUCTION SURFACE		PRESSURE SURFACE	
	XU	YU	XL	YL
1	-36.114	-12.574	-36.114	-14.026
2	-33.045	- 7.307	-31.362	- 8.622
3	-29.801	- 2.420	-27.227	- 4.818
4	-26.434	1.823	-23.215	- 1.934
5	-22.793	5.324	-19.476	0.056
6	-18.744	7.912	-16.146	1.236
7	-14.261	9.319	-13.251	1.769
8	- 9.553	9.223	-10.578	1.857
9	- 5.115	7.415	- 7.637	1.572
10	- 1.462	3.970	- 3.911	0.686
11	0.322	1.111	0.322	- 1.031

Table 5 Airfoil coordinates of cascade B12

POINT NO.	SUCTION SURFACE		PRESSURE SURFACE	
	XU	YU	XL	YL
1	-48.246	-26.594	-48.246	-28.641
2	-41.471	-15.762	-39.547	-17.239
3	-34.546	- 6.645	-31.753	- 9.495
4	-27.219	0.132	-24.359	- 4.428
5	-21.973	3.125	-19.791	- 2.418
6	-16.498	4.754	-15.452	- 1.281
7	-11.005	4.958	-11.132	- 0.768
8	- 8.336	4.541	- 8.894	- 0.671
9	- 4.500	3.356	- 5.370	- 0.689
10	- 2.062	2.275	- 2.901	- 0.809
11	0.058	1.171	0.058	- 1.063

Table 6 Airfoil coordinates of cascade B15

POINT NO.	SUCTION SURFACE		PRESSURE SURFACE	
	XU	YU	XL	YL
1	-14.333	-23.673	-14.333	-26.089
2	-11.179	-16.229	-11.187	-19.168
3	- 8.026	- 9.207	- 8.041	-12.431
4	- 4.872	- 2.624	- 4.895	- 5.955
5	- 1.719	3.480	- 1.749	0.155
6	1.435	9.032	1.397	5.799
7	4.589	13.981	4.543	10.909
8	7.742	18.248	7.689	15.410
9	10.896	21.747	10.835	19.283
10	14.049	24.481	13.981	22.512
11	17.203	26.524	17.127	25.069

DISCUSSION

J. D. Denton[1]

As it is now some six years since the numerical scheme discussed in these papers was developed it may be worth comparing my own experiences of it with those of the authors.

Comparatively little development of the two-dimensional scheme has taken place since [5] was written and most emphasis has been placed on developing the three-dimensional versions of the scheme which are described in [6]. The most significant change has been the development of a method of allowing scheme "A" [5] to work with limited regions of backflow, such as occur around the leading edge of a turbine blade. As a result of this development my own preference is now for scheme "A" rather than for the combination of schemes "B" and "C" which was originally recommended.

---

[1] Whittle Laboratory, Cambridge University, United Kingdom.

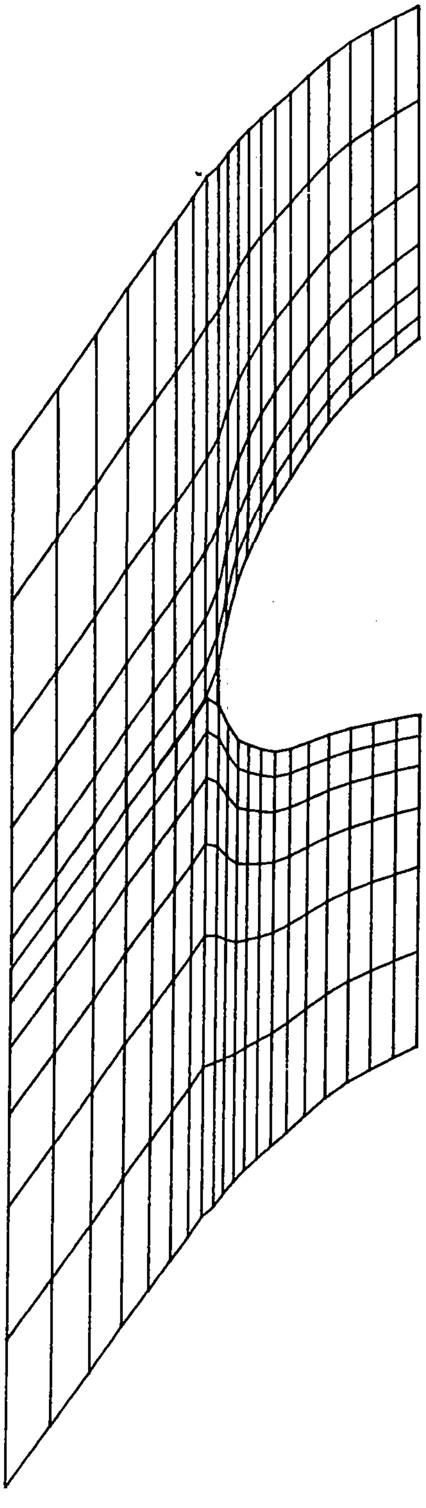

Fig. 25 Detail of suitable grid around a leading edge

This is in agreement with the findings of the present authors. Such a scheme is simpler, faster, and more stable than the alternative schemes described in [5].

I would nowadays always tend to use more mesh points than are used by the authors, who suggest that 500-600 points are sufficient. Such a coarse grid is inadequate to resolve details of the flow around a leading edge and good results can only be obtained by judicious use of a cusp as described in the paper. However, the optimum cusp shape is highly dependent on the type of blading and so I now feel that it is preferable to try to resolve the details of the leading edge flow. The poor results shown for cascade C in Fig. 7 are due to the use of a grid which is far too coarse to resolve the steep gradients of flow properties around the sharp leading edge. My preference would be to use about 1000 grid points with the points nonuniformly spaced in both the axial and the pitchwise directions as shown by grid "D" of the first paper. With such a grid, I would not use any cusp at the leading edge except for that caused by a small "flat" at the first point on the blade as illustrated in the attached figure. For a blunt leading edge I would try to locate about five grid points on the leading edge circle and to vary the pitchwise grid spacing so that, near the blade surface, it is of the same order as the axial spacing. With such a grid the leading edge stagnation point and subsequent acceleration can be accurately captured as shown by Hodson in [7].

The instability which the authors found when using such a nonuniform grid arises because the time step needed for stability becomes limited by the perpendicular spacing between the bladewise faces of an element when this spacing is much smaller than the axial spacing between the pitchwise faces. No method of reducing the local time step when this occurred was included in the original coding but such a reduction is now regarded as essential.

There is no doubt that the form of the trailing edge cusp influences the solution for turbine blades with supersonic exit flow. A smooth cusp (Fig. 8*c*), which is optimum for subsonic flow, can completely lose all details of the trailing edge shock-expansion system in supersonic flow. Hence it will also give incorrect results for the rear part of the suction surface which is strongly influenced by the waves generated at the trailing edge. My preference for supersonic trailing edge flow would be to terminate the blade with a wedge, as in Fig. 8(*b*), but with the wedge treated as a part of the blade, i.e., as a solid boundary. The shape of the wedge should be chosen to match the base flow region of a real supersonic flow and several grid points should be located on it. Even a simple guess of the shape of this region is better than using a smooth cusp, but the process of choosing the shape can be automated by incorporating a base pressure correlation as described by Singh in [8].

In most other respects I agree with the conclusions reached by the authors. I am, however, surprised by the emphasis that they place on saving computer time. My feeling is that, since the cost of a two-dimensional solution is now only a few dollars, more emphasis should be placed on obtaining better accuracy by the use of more grid points. If saving of computer time is really important then significant savings could easily be made by incorporating further levels of multigrid, as is done in the three-dimensional versions of the code.

References

6 Denton, J. D., "The Calculation of Fully Three-Dimensional Flow Through Any Type of Turbomachine Blade Row," in: *Three-Dimensional Computation Techniques Applied to Internal Flows in Propulsion Systems*, AGARD LS140, 1985.

7 Hodson, H. P., "Boundary-Layer Transition and Separation Near the Leading Edge of a High-Speed Turbine Blade," ASME JOURNAL OF ENGINEERING FOR GAS TURBINES AND POWER, Vol. 107, 1985, pp. 127-134.

8 Singh, U. K., "Computation of Transonic Flows in and About Turbine Cascades With Viscous Effects," ASME Paper No. 84-GT-18, 1984.

Authors' Closure

The authors would like to thank Dr. Denton very much for his useful discussion.

The blade-to-blade flow calculation code based on scheme A has been used successfully in both gas and steam turbine designs in the authors' company.

It is necessary to use more mesh points, as pointed out by Dr. Denton, to resolve details of the flow around a leading edge. However, details of the flow around the leading edge are

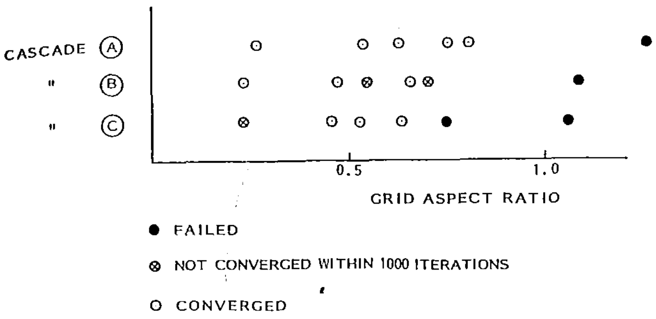

Fig. 26 Grid aspect ratio and convergence

not very important in blade design of industrial gas turbines because a blade has moderate reactions and the blade inlet Mach number is not high. A main concern of designers is a suction surface diffusion of the blade. Hence it is suggested to use 500 ~ 600 mesh points with judicious use of a leading edge model in the blade design of industrial gas turbines.

The grid aspect ratio really does have some effects on stability. Figure 26 shows the effect of the grid aspect ratios on convergence for the three cascades tested in the first paper. The grid aspect ratio is defined by dividing axial grid spacing by pitchwise grid spacing. From the figure, an aspect ratio less than 0.7 is desirable for the three cascades.

Selection of a trailing edge model is quite important to get valid solutions. The authors agree with Dr. Denton on the point that, for turbine blades with supersonic exit flow, a different shape is required for the cusp. The process of forming the cusp shape should be automated in order to use the blade-to-blade program in an interactive design system. Incorporating a base pressure correlation is a reasonable method for automatic formation of the cusp. One problem is that it is difficult to make a general base pressure correlation which can be applied to cascades with various geometric conditions, especially for low supersonic exit flow conditions.

The computing cost for one calculation is really inexpensive. The typical CPU time is 5 ~ 6 s on an IBM 3090, if the program based on scheme A and the "know how" to operate the code are used, as described in the second paper. According to the authors' experiences, the other time-marching Euler codes require much longer run times for the same calculation (over 60 s). The longer CPU time also brings a longer elapse or waiting time under time-sharing computing systems. For these reasons a short computing time is stressed in the papers.

J. J. Adamczyk
NASA Lewis Research Center,
Cleveland, OH 44135

R. A. Mulac

M. L. Celestina

Sverdrup Technology, Inc.,
Middleburg Heights, OH

A Model for Closing the Inviscid Form of the Average-Passage Equation System

A mathematical model is proposed for closing or mathematically completing the system of equations which describes the time-averaged flow field through the blade passages of multistage turbomachinery. These equations, referred to as the average-passage equation system, govern a conceptual model which has proven useful in turbomachinery aerodynamic design and analysis. The closure model is developed so as to insure a consistency between these equations and the axisymmetric through-flow equations. The closure model was incorporated into a computer code for use in simulating the flow field about a high-speed counterrotating propeller and a high-speed fan stage. Results from these simulations are presented.

Introduction

Engineers have long recognized the difficulty associated with adopting a "First Principle" approach based on directly solving the Navier–Stokes equations for the purpose of designing (or analyzing) vehicles which operate in high Reynolds number turbulent flows. However, numerous examples exist, such as turbomachinery blading, aircraft wings and bodies, inlets and nozzles, which clearly show that models which describe an "averaged" flow state can be used to design aerodynamic vehicles and provide answers to many aerodynamic problems. In both external and internal aerodynamics, the "averaged" state most often modeled is one in which the flow appears steady. In general, the number of equations associated with this averaged flow representation does not equal the number of unknowns. The problem of mathematically completing this system of equations so that they may be solved is referred to as the closure problem. The flow models associated with the completed system of equations must be considered semi-empirical for they rely heavily on empirical correlations to introduce the effects of turbulent motion and, in the case of turbomachinery, the additional effects of unsteadiness and spatial nonuniformities into these averaged flow representations. For nonturbomachinery application, the equation governing such a flow is the familiar Reynolds-averaged Navier–Stokes equation. In general, the length scales associated with this equation are sufficiently restricted so as to make them amenable to numerical simulation. Indeed there is considerable activity these days in the external aerodynamic community to develop numerical simulators based on these equations for flow over an entire aircraft.

For turbomachinery involving more than one blade row, the Reynolds-averaged form of the Navier–Stokes equations does not describe a flow which is steady in time. On the contrary, they describe a flow which is highly unsteady in which blade rows are moving relative to one another, generating disturbances whose time scales range from a fraction of wheel speed to many times that of blade passing frequency and whose length scales range from the circumference of the machine to the thickness of the laminar sublayer region of the turbulent boundary layers. Simulations based on the Reynolds-averaged Navier–Stokes equations are well beyond the capabilities of today's computers for all but the simplest of multistage geometries. They also do not govern the conceptual flow model traditionally used to design multistage turbomachinery. As noted above, multistage designs are based on flow models in which the flow appears steady within each blade row. In addition, with respect to a given blade row, these models assume the flow to be spatially periodic from one blade passage to another. In [1], a mathematical derivation of the equations governing this flow was presented. These equations were referred to as the average-passage equation system. This derivation was carried out for arbitrary configurations and clearly showed the relationship between the Navier–Stokes equations, their Reynolds-averaged form, and their average-passage form. The closure problem associated with the average-passage form of the Navier–Stokes equations was also identified. This work put the average-passage model on a sound mathematical base equivalent to that of the Reynolds-averaged Navier–Stokes model. A brief summary of that work is presented in the next section. The purpose of the present work is to elaborate further on the issue of closure for the average-passage equation system and to propose a closure model for the inviscid form of this equation system. This closure model was used to obtain the results presented in [2]. Those results and the ones to be presented in this work show that the present model appears applicable to configurations in

---

Contributed by the Gas Turbine Division of The American Society of Mechanical Engineers and presented at the 31st International Gas Turbine Conference and Exhibit, Düsseldorf, Federal Republic of Germany, June 8–12, 1986. Manuscript received at ASME Headquarters Feburary 14, 1986. Paper No. 86-GT-227.

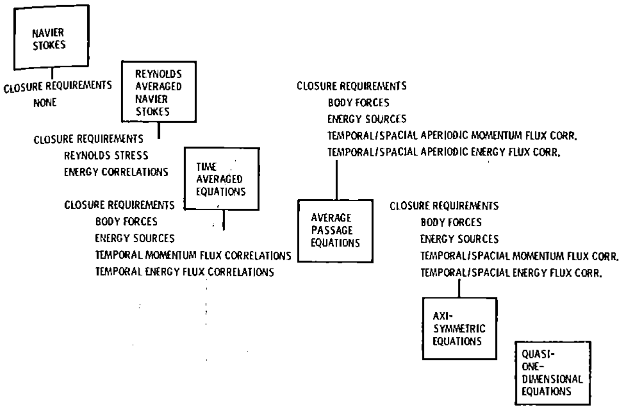

Fig. 1 Flow models for use in turbomachinery design/analysis

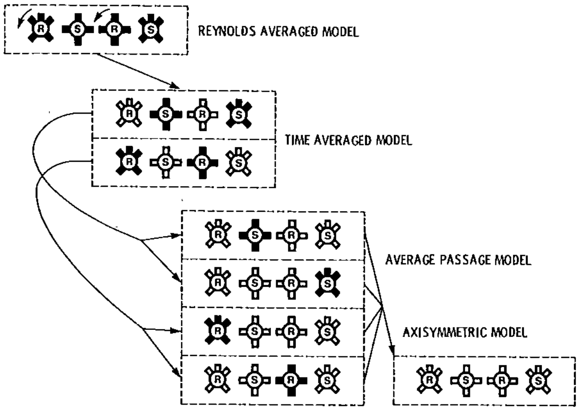

Fig. 2 Two-stage flow models

which the average-passage flow field is nearly irrotational between blade rows.

Model Equation Hierarchy

Figure 1 shows a hierarchy of equations which can be used to analyze turbomachinery flows. The Navier-Stokes equations appear at the upper left-hand corner of this figure. These equations are assumed to provide a complete description of the flow field, including a complete description of turbulent motions. To use these equations as a basis for simulating turbomachinery flows requires sufficient computer capacity to resolve all of the time and length scales associated with high Reynolds number flows. In addition, since turbomachinery flow are statistically nonstationary, a sufficient number of computations would have to be performed over a range of randomly chosen initial conditions to insure a statistical steady-state description of the flow. Such simulations are clearly beyond the capacity of today's most advanced computers. The next box (i.e., Fig. 1) contains the Reynolds-averaged form of the Navier-Stokes equations. They are derived by ensemble averaging the Navier-Stokes equations and hence govern a deterministic description of the flow field. An illustration of this description for a two-stage configuration in which the first and second rotors have five and four blades, respectively, while the first and second-stage stators have four and five blades, is presented in Fig. 2. The rotors rotate relative to the stators, and, therefore, the flow will be unsteady in either the rotor or stator frame of reference. As noted previously, the time scales associated with this unsteady flow are quite diverse, which makes simulation of all but the most simple of geometries beyond the capabilities of today's computers. The closure problem associated with these equations requires the modeling of the familiar Reynolds stress and energy correlations. It is by means of these correlations that the "average" effects of random fluctuations in momentum and energy of a fluid particle are introduced in the equations governing the deterministic flow field.

The third box from the left in Fig. 1 represents the time-averaged form of the Reynolds-averaged Navier-Stokes equations. These equations govern the time-averaged flow field as viewed by an observer whose frame of reference is fixed to a given blade row. An illustration of this description for the two-stage configuration used to illustrate the Reynolds-averaged flow model is also presented in Fig. 2. All rotating blade rows have a unique time-averaged flow field associated with them. In a similar fashion, all nonrotating blade rows have their own time-averaged flow field representation. These two flow fields are not the same. For both flow fields, the blade rows which rotate relative to the stationary blade rows (i.e., with respect to one another) appear smeared. Their physical appearance is very similar to what one observes when viewing a high-speed propeller. Within the context of the time-averaged flow description, these smeared blade rows are replaced by actuator ducts (i.e., actuator ducts of finite thickness). These ducts are represented by a body-force distribution which can add or extract energy from the flow. In addition, the time-averaged flow equations contain correlations between time-varying flow variables. These correlations arise because the Reynolds-averaged Navier-Stokes equation is nonlinear. These correlations represent the time average of the fluctuating density field and products of the fluctuating velocity field as well as the time average of the fluctuating density, fluctuating velocity, and fluctuating total enthalpy field. It is through these correlations that the averaged effect of the relevant unsteady physical phenomena is introduced into the time-averaged representation. The modeling of the body forces and energy sources associated with the smeared blade rows and the temporal correlations, plus the modeling of the time-averaged Reynolds stresses, forms the closure problem associated with the time-averaged equations. Finally, it should be noted that, for a single-stage configuration, the time-averaged flow field associated with either blade row will be spatially periodic over the pitch of that blade row. Thus, if the closure issue associated with the time-averaged representation can be addressed without overdue complexity, it should be feasible to conduct a simulation based on this flow model for a single stage.

For a multistage configuration in which the number of rotor blades differs from rotor to rotor, or for which the number of stator blades differs from stator to stator, the time-averaged flow field will not, in general, be spatially periodic over the pitch of any given blade row. An averaging procedure may be introduced which transforms this spatially aperiodic flow field into one that is periodic over the pitch of a given blade row. The resulting flow field is referred to as the average-passage flow and appears in the fourth box from the left in Fig. 1. Each blade row in a multistage machine has associated with it an average-passage flow field. An illustration of this description is shown in Fig. 2. For the two-stage machine under consideration there exist four average-passage flow descriptions due to the number of blades assigned to each wheel. The geometry of neighboring blade rows (rotating and stationary) for which the blade count is not an integral multiple of the blade row of interest, and which are stationary relative to this blade row, appear smeared in this flow description. Their appearance is similar to that of the rotating blade rows in the time-averaged flow description. It should be noted that all of the blade rows which rotate relative to the blade row of interest appear smeared, since the average-passage description is also a time-averaged description. The four average-passage flows illustrated in Fig. 2 are coupled to one another through a system of body forces, energy sources, and temporal and spatial correlations. The closure problem associated with this flow description consists of developing mathematical expressions for the spatial and temporal correlations in addition to the body forces and energy sources. These correlations introduce the transport on the average of momentum and energy between the time-averaged representation and the average-passage representation.

Many analyses currently used to analyze multiblade row turbomachinery involve iteration between a meridional flow analysis and a blade-to-blade analysis. Within the context of the present discussion, these analyses may be viewed in one of two ways. They may be thought of as attempting to describe the average-passage flow field. If one gives these analyses this interpretation, then one immediately notes that their derivation lacks mathematical rigor. As a result, the closure problem associated with the average-passage representation is never addressed, for it is completely overlooked. On the other hand, one may interpret these as axisymmetric analyses in which the blade-to-blade solution, along with some empirical correlations, is used to close the meridional flow equations. In this case, these analyses are rigorous because the closure problem, i.e., the closure of the axisymmetric representation, is generally clearly defined. However one wishes to interpret these analyses, one must be impressed with the degree of accuracy with which they predict the axisymmetric flow field in the neighborhood of design conditions. As one moves away from the neighborhood of the design point, however, the validity of these analyses appears to degenerate quickly. This disagreement is thought to be due to the inability of the blade-to-blade model to properly account for large spanwise migration of flow which occurs at these off-design conditions. To analyze such situations, a true three-dimensional analysis is needed. The average-passage model provides a framework for developing such an analysis, as illustrated by the work presented in [2]. The accuracy of such simulation will, of course, depend upon the validity of the closure model used in the simulation.

The next box in Fig. 1 represents the axisymmetric flow model, which is the mainstay of many turbomachinery design systems. The field equations for this model can be derived by tangentially averaging the average-passage equation system. An illustration of the geometry associated with this representation is also provided in Fig 2. Each average-passage flow model can be related to an axisymmetric model. The equations governing these four axisymmetric models must be equal to one another, for there can only be one axisymmetric or through-flow representation of the flow field within a multiblade row configuration. The average-passage equations thus define the three-dimensional passage flows having a common axisymmetric flow description. All of the blade rows within the axisymmetric description appear smeared and are mathematically replaced by actuator ducts. These ducts exert a force on the fluid which may add or extract energy from the flow. There may also be energy sources or sinks within the ducts which are associated with blade heat transfer. Over the years, numerous publications have appeared which dealt with modeling these forces and the energy sources. Quite often they are estimated from cascade or blade-to-blade analyses tempered by empirical correlations. In addition, the axisymmetric or through-flow equations contain correlations between temporal varying flow variables as well as correlations between spatial varying flow variables. These correlations introduce on the average the effect of radial transport of momentum and energy from the average-passage representation. Only very recently have models for these correlations appeared in the open literature. Sehra [3] was one of the first to attempt to incorporate these correlations into a through-flow code. His correlation model was based on data obtained from a high-speed isolated rotor test. Jennions [4] modeled these correlations using results from an inviscid blade-to-blade analysis. He was able to develop an iterative procedure for incorporating these correlations into a through-flow analysis. Finally, the Adkins and Smith [5] model for accounting for the effects of the spanwise mixing in multistage machinery may be thought of as an attempt at modeling the correlations which appear in the axisymmetric model. The last box in Fig. 1 represents a quasi-one-dimensional equation system. These equations result from averaging the axisymmetric equation over the span of the flow annulus. This equation system is often used in engine stability studies and in preliminary design to estabish the flow properties along the pitch-line of a machine. Closure of this system of equations can be quite involved. It requires models for the blade forces, energy sources, spatial and temporal correlations associated with the blade-to-blade flow field, as well as a model for the force exerted by the casing on the flow.

The flow models identified in Fig. 1 are by no means complete, nor were they ever intended to be complete. The purpose of this figure was to illustrate symbolically the connection between a hierarchy of equations associated with turbomachinery aerodynamics. It is hoped that the rational derivation of the average-passage equation system will ultimately lead to the development of three-dimensional viscous computer codes for multistage configurations. Such codes will enhance our ability to analyze turbomachinery flows, especially at off-design conditions. Our inability to accurately predict off-design performance of multistage machinery is often the major contributor to their high development costs, rather than problems associated with poor design performance. In the next section, the closure model associated with the inviscid form of the average-passage equations system will be developed.

The Closure Problem

For simplicity we shall only address the closure problem associated with solving the inviscid form of the average-passage equation system as it pertains to a single stage. A solution to the corresponding multistage problem can be obtained by a direct extension of the analysis which follows. For a single-stage configuration, each blade row has associated with it an average-passage equation system. As noted in the previous section, the dependence of the flow through the first blade row upon that through the second is introduced by means of a body force, energy source, and time-averaged correlations between fluctuating flow variables. Likewise, a corresponding dependency exists between the flow through the second blade row and that through the first. In [1], the body force and energy source which appear in the inviscid form of the average-passage equation system were shown to depend upon the ensemble-averaged pressure. This averaged pressure was estimated from samples of the pressure field taken over a period of one revolution of the wheel recorded at the instant a blade passes an observer whose frame of reference is fixed to that of the blade row of interest. If one assumes the average-passage flows of the two blade rows to be nearly irrotational outside of the blade passage region, then this ensemble-averaged pressure is nearly equal to the average-passage pressure distribution on the surface of the neighboring blade row. Hence, from the solution for the first blade row, one can estimate the body force and energy source which appear in the equations for the second blade row. In a similar fashion, one may estimate the body force and energy source which appear in the equations for the first blade row from a solution to the corresponding equations for the second blade row.

The remaining terms which must be estimated are the temporal correlations associated with the time-varying flow field. The origin and nature of these correlations were discussed in the previous section. To develop a model for these correlations, we decompose the absolute velocity field $\mathbf{v}$ according to the equation

$$
\begin{aligned}
\mathbf{v}(r,\theta,z,t) &= \mathbf{v}^{(AX)}(r,z) \\
&+ [\mathbf{v}^{(1)}(r,\theta-\Omega_1 t,z) = v^{(AX)}(r,z)] \\
&+ [\mathbf{v}^{(2)}(r,\theta-\Omega_2 t,z) - \mathbf{v}^{(AX)}(r,z)] \\
&+ \mathbf{v}^{(3)}(r,\theta,z,t)
\end{aligned}
\tag{1}
$$

where $\mathbf{v}^{(AX)}$ represents the axisymmetric velocity component, $\mathbf{v}^{(1)}$, the time-averaged absolute velocity field as observed in a frame of reference fixed to the first blade row, $\mathbf{v}^{(2)}$, the corresponding velocity field observed in a frame of reference fixed to the second blade row, and $\mathbf{v}^{(3)}$, the component of velocity which is unsteady in either frame of reference. The remaining variables which appear in equation (1) are the cylindrical coordinates r, θ, z, time t, and the rotational speed of the first and second blade rows Ω_1, Ω_2. In similar fashion, the total enthalpy H, measured in the absolute frame of reference, can be decomposed according to the equation

$$
\begin{aligned}
H(r,\theta,z,t) &= H^{(AX)}(r,z) \\
&+ [H^{(1)}(r,\theta-\Omega_1 t,z) - H^{(AX)}(r,z)] \\
&+ [H^{(2)}(r,\theta-\Omega_2 t,z) - H^{(AX)}(r,z)] \\
&+ H^{(3)}(r,\theta,z,t)
\end{aligned}
\tag{2}
$$

Fixed in the frame of reference of the first blade row, the velocity field $\mathbf{v}^{(1)}$ will appear steady in time, while the components $\mathbf{v}^{(2)}$ and $\mathbf{v}^{(3)}$ will appear to be unsteady. If we define the velocity component $\mathbf{v}''(r, \theta, z, t)$ as

$$
\mathbf{v}''(r,\theta,z,t) \equiv \mathbf{v}^{(2)}(r,\theta-\Omega_2 t,z) - \mathbf{v}^{(AX)}(r,z) \tag{3}
$$

the correlations which appear in the average-passage momentum equations associated with the first blade row are obtained by forming the time average of the product of the fluid density and $(\mathbf{v}'' + \mathbf{v}^{(3)})^2$ [1]. The result is

$$
R_{ij} = \overline{\rho v_i'' v_j''} + \overline{\rho v_i'' v_j^{(3)}} + \overline{\rho v_i^{(3)} v_j''} + \overline{\rho v_i^{(3)} v_j^{(3)}} \tag{4}
$$

where the subscripts i, j take on the values of 1, 2, and 3. On the right-hand side of equation (4), these subscripts are used to denote the axial, tangential, and radial velocity components, respectively. The variable ρ is the fluid density, and the overbar represents the time average of the variables which appear beneath it. Thus for $i = 1$ and $j = 2$, R_{12} denotes the temporal correlation between the density ρ, and the product of the axial and tangential components of the fluctuating velocity field. For low Mach number flows in which the density may be assumed constant, the correlation $\overline{\rho v_i'' v_j''}$ will be independent of tangential position θ, since v_i'' is spatially periodic over the pitch of the second blade row. This correlation is thus associated with the transport on the average of momentum across the axisymmetric stream surfaces. The remaining correlations which appear in equation (4), however, will be functions of θ if $v^{(3)}$ is spatially aperiodic over the pitch of the second blade row. In general this will be the case.

Based on the arguments used to derive equation (4) and the analysis presented in [1], the correlations which appear in the energy equation are obtained by forming the time average of the product of ρ, $H'' + H^{(3)}$ and $v'' + v^{(3)}$. The result is

$$
Q_i = \overline{\rho H'' v_i''} + \overline{\rho H'' v_i^{(3)}} + \overline{\rho H^{(3)} v_i''} + \overline{\rho H^{(3)} v_i^{(3)}} \tag{5}
$$

where

$$
H''(r,\theta,z,t) \equiv H^{(2)}(r,\theta-\Omega_2 t,z) - H^{(AX)}(r,z) \tag{6}
$$

The first correlation in equation (5) is independent of θ if the fluid density is constant. This is the result of H'' and v_i'' being spatially periodic over the pitch of the second blade row. In general, the remaining correlations will not exhibit this behavior. As a result, the total enthalpy associated with the average-passage flow field for a multiblade row configuration will be nonuniform in the tangential direction. Kerrebrock and Mikolajczak [6] were the first to attempt to analyze the fluid mechanics associated with this phenomenon. They attributed it to the transport of excess total temperature of a fluid particle in a rotor wake across the stator passage. Their analysis of this process was based on kinematics. Although the present work makes no attempt at developing an alternative model of this phenomenon, it does suggest that it is associated with the dynamics of stator-blade rotor-wake interaction.

For an inviscid nearly irrotational flow, the magnitude of the unsteady component $\mathbf{v}^{(3)}$ will be comparable to or less than the magnitude of $\mathbf{v}''$, except for regions near blade leading edges. In particular, in regions where the body force and the energy source are finite, the correlation associated with $\mathbf{v}''$ (i.e., equations (4) and (5)) will be significantly larger than those associated with $\mathbf{v}^{(3)}$. For this reason we assume that the correlations in equations (4) and (5) associated with the unsteady velocity component $\mathbf{v}^{(3)}$ can be neglected. As a result, the correlations R_{ij} and the correlation Q_i can be directly evaluated from the average-passage solutions. For a stage, this implies that the flow field through both blade rows must be evaluated simultaneously.

To incorporate the suggested closure model into a numerical simulation, one may envision a two-tier iteration procedure as depicted in Fig. 3. In the inner loop, the body forces, energy sources, and correlations are frozen. An average-passage flow field is evaluated based on the value of these quantities and the imposed boundary conditions. In the outer loop, the body forces, energy sources, and correlations are updated based on the converged inner loop solutions. We must update these terms, as previously noted, in a manner which yields a unique axisymmetric representation of the flow field through the machine. This will insure that the average-passage representation of the flow is consistent with the axisymmetric representation.

The equations to be solved in the outer loop may be derived starting from the equations of motion expressed in the vector form [2]

$$
L(U_n) + \int K(U_n)dV + \int S_{n-1}dV = 0 \tag{7}
$$

The operator $L(U_n)$ in this equation represents the net flux of mass (i.e., continuity of flow through a control volume), axial and radial momentum, angular momentum, and energy through a differential volume of fluid, while $K(U_n)$ represents the added contribution of the pressure field and centrifugal acceleration to the balance of radial momentum. The components of the vector U_n are density, axial and radial momentum, angular momentum, and total inertial energy. The symbol S_{n-1} represents the sum of the contribution of the body force, energy source, and temporal correlations to the momentum and energy equations, while the subscript n denotes the

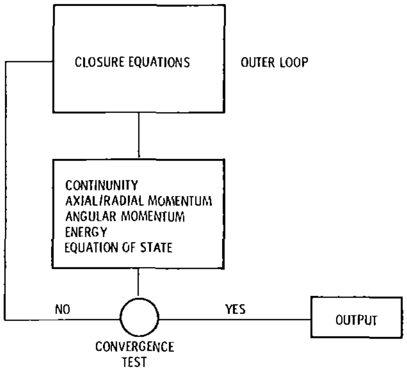

Fig. 3 Solution strategy

iteration index of the outer loop. The remaining symbol, dv, denotes the volume of a differential volume of fluid. Based on the discussion presented earlier, the temporal correlations which are embedded in S_{n-1} are simply a function of average-passage flow field associated with the neighboring blade row. Thus, for a single-stage configuration, the field equation for the first blade row can be written as

$$L(U_n^{(1)})+\int K(U_n^{(1)})dv+\int S(U_{n-1}^{(2)})dv=0 \tag{8}$$

while the corresponding equation for the second blade row is

$$L(U_n^{(2)})+\int K(U_n^{(2)})dv+\int S(U_{n-1}^{(1)})dv=0 \tag{9}$$

The superscripts (1) and (2), respectively, denote the variables associated with the first and second blade row passage flow fields. Next we multiply both equations (8) and (9) by an operator A, which forms the axisymmetric average of its argument. This is equivalent to averaging the three-dimensional equations of motion (i.e., equations (8) and (9)) over the tangential direction. For the first blade row, the axisymmetric average of the operator L is

$$AL(U_n^{(1)})=L^{(AX)}(AU_n^{(1)})+\int S(U_n^{(1)})Adv \tag{10}$$

while for the second row

$$AL(U_n^{(2)})=L^{(AX)}(AU_n^{(2)})+\int S(U_n^{(2)})Adv \tag{11}$$

In both of these expressions, the operator $L^{(AX)}$ denotes the axisymmetric counterpart of L. The axisymmetric average of the combined integrals which appear in equation (8) is

$$A[\int K(U_n^{(1)})dv+\int S(U_{n-1}^{(2)})dv]=\int A[K(U_n^{(1)})dv]+\int S(U_{n-1}^{(2)})Adv \tag{12}$$

Similarly, the axisymmetric average of the combined integrals in equation (9) is

$$A[\int K(U_n^{(2)})dv+\int S(U_{n-1}^{(2)})dv]=\int A[K(U_n^{(2)})dv]+\int S(U_{n-1}^{(1)})Adv \tag{13}$$

These last results follow because S is independent of tangential position. Based on the above equations, the axisymmetric average of equations (8) and (9) may be expressed as

$$L^{(AX)}(AU_n^{(1)})+\int A[K(U_n^{(1)})dv]+\int[S(U_n^{(1)})+S(U_{n-1}^{(2)})]Adv=0 \tag{14}$$

$$L^{(AX)}(AU_n^{(2)})+\int A[K(U_n^{(2)})dv]+\int[S(U_n^{(2)})+S(U_{n-1}^{(1)})]Adv=0 \tag{15}$$

Upon convergence of the outer loop, equations (14) and (15) yield identical solutions for the axisymmetric flow field. In addition, these equations provide a means of updating the variables $\int(U_n^1)$ and $\int(U_n^2)$ without evaluating the body forces, energy sources, and correlations directly. This becomes apparent as soon as one notes that the vectors U_n^1 and U_n^2 are known having been evaluated in the inner iteration loop, while the quantities $\int S(U_{n-1}^{(1)})$ and $S(U_{n-1}^{(2)})$ are known from the previous outer iteration loop.

This simple strategy for incorporating the closure model into a numerical simulation has been implemented into the computer code outlined in [2]. That code has been used successfully to simulate the flow about high-speed counterrotating propellers as illustrated by the results presented in [2]. We shall present additional results from that simulation as well as that for a high-speed fan stage.

Results

The model proposed for closing the inviscid form of the average-passage equation system was based on the assumption that, within the confined region of a blade row, the correlations associated with the blade row interaction velocity field are small relative to those associated with the steady aerodynamic blade loading. The justification for this assumption can be based on the argument that the unsteady airload, which is an indication of the magnitude for the velocity component associated with blade row interaction, is generally smaller than its time-averaged counterpart which serves as a measure of the magnitude of the nonaxisymmetric component of the average-passage velocity field. Data presented in a recent publication by Dring et al. [7] show this to be the case in the midspan region of a turbine stage. Outside of the confines of a blade row, the magnitude of both of these velocity fields should be comparable; however, their magnitude is small compared to the magnitude of the axisymmetric velocity field. As an illustration that hardware does exist in which one may find regions in which such flows exist, we present the circulation as a function of radius at a number of axial locations generated by a high-speed counterrotating propeller. These results are for a flight Mach number of 0.72 and an advance ratio for both propellers of 2.8. The circulation is defined as the integral over a blade pitch of the product of nondimensional radius and nondimensional tangential velocity. The tangential velocity is nondimensionalized by the far-field speed of sound, while the radius is rendered nondimensional by the tip diameter of the first propeller. The results presented in Figs. 4(*a–d*) are for an axial location slightly forward of the first propeller, aft of the trailing edge of the first propeller, slightly forward of the second propeller, and aft of the trailing edge of the second propeller, respectively. For each axial location, two plots are drawn. The first (solid line) represents the axisymmetric flow field obtained from the average-passage simulation of the first propeller. The second (dashed line) corresponds to the axisymmetric flow field obtained from the average-passage simulation of the second propeller. It is quite apparent that both results agree with each other to within plotting accuracy and hence are more than adequate for assessing blade row performance. Upstream of the first propeller the circulation must be zero since there is no swirl present in the incoming flow. At the trailing edge of the first propeller, the circulation is nearly constant over the inboard portion, decreasing in a smooth monotonic fashion toward zero as the tip is approached (i.e., r = 0.5). Thus the aerodynamic loading of the inboard region is nearly independent of radius, which implies a near-free vortex design. The flow between the two propellers would therefore be nearly irrotational. The reduction in circulation with radius in the outboard region produces a weak tip vortex which convects downsteam. In the axisymmetric flow representation, this tip vortex is smeared into a ring vortex. At the leading edge of the second propeller,

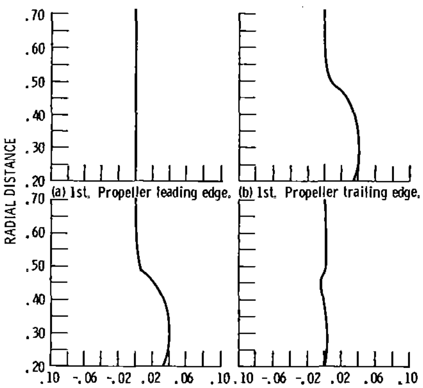

(a) 1st. Propeller leading edge. (b) 1st. Propeller trailing edge.

(c) 2nd Propeller leading edge. (d) 2nd Propeller trailing edge.

Fig. 4 Circulation distribution

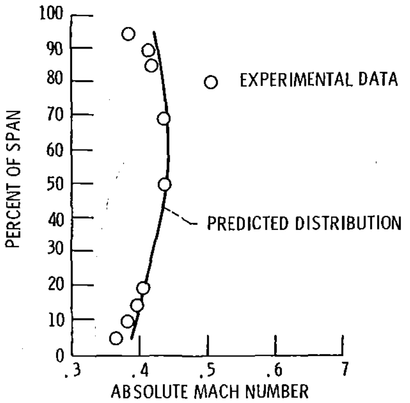

Fig. 5 Absolute Mach distribution (rotor inlet)

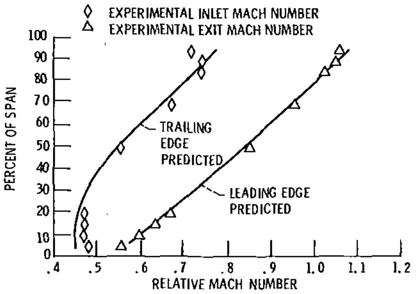

Fig. 6 Relative Mach number distribution (rotor)

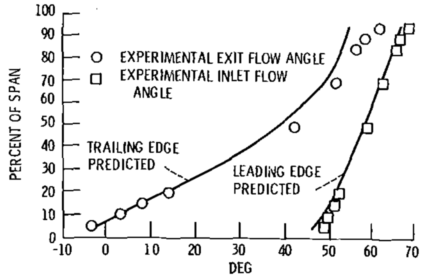

Fig. 7 Relative flow angle distribution (rotor)

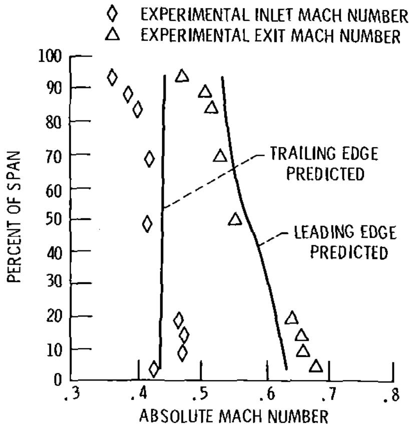

Fig. 8 Absolute Mach number distribution (stator)

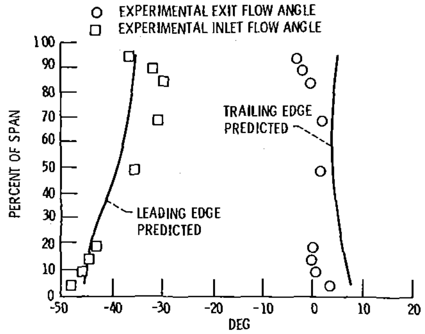

Fig. 9 Absolute flow angle distribution (stator)

the circulation distribution is seen to be nearly identical to the distribution at the trailing edge of the first propeller. This result further substantiates that the flow field between the two propellers is nearly irrotational, for in an irrotational unsteady flow the time-averaged circulation (or angular momentum) is conserved along the axisymmetric stream lines. The slight redistribution of circulation that one observes in the outboard region is attributed to spanwise mixing of angular momentum due to the tip vortex. Figure 4(*d*) show the distribution of circulation at the trailing edge of the second propeller. The second propeller appears to take out almost all of the swirl produced by the first propeller. The change in the swirl distribution across the second propeller implies that the spanwise aerodynamic loading is nearly uniform over the inboard region of the second propeller. The inboard region is behaving as a free-vortex design. The results shown in Fig. 4 strongly suggest that the closure model developed in this work should be applicable to this and similar high-speed counterrotating propellers. This is confirmed by the comparison between the measured and predicted nacelle pressure distribution presented in [2]. Further comparisons are planned as shown as experimental data become available.

An attempt was also made to predict the average-passage flow fields generated by a high-speed fan stage. The stage chosen was the first of a two-stage machine designed and tested at NASA Lewis [8]. The computation was performed for an operating point near maximum efficiency of the first stage. This point was chosen to minimize the effect of viscosity on the measured flow variables. The rotor's rotational speed was 80 percent of design and the stage pressure ratio and adiabatic efficiency were 1.352 and 0.891, respectively. The inferred velocity field between the blade rows resembled that induced by a free-vortex design in the midspan region. The inlet boundary conditions in the computation were chosen to produce an inlet absolute Mach number and flow angle distribution which approximated the measured distributions. At the downsteam boundary the nondimensional pressure at the hub at the exit of the stator was set equal to the measured value. The absolute Mach number distribution at the inlet to the rotor is shown in Fig. 5, while the relative Mach number distribution across the rotor is shown in Fig. 6. The measured results at the inlet to the rotor agree very well with the predicted results, as they should, due to the choice of inlet conditions. The predicted exit relative Mach number distribution appears to be in good agreement with the measured results, especially in the midspan region. It should also be noted that the predicted relative Mach number is less than measured over most of the rotor span. This result is to be expected since the blade boundary layers restrict the flow area, thus reducing the diffusion capabilities of the rotor. The measured distribution also shows the existence of an end-wall casing boundary layer which obviously cannot be predicted by the present inviscid analysis.

The relative flow angle distribution at the leading and trailing edge of the rotor was also computed and is shown in Fig. 7 alomg with the measured distribution. This angle is defined as the angle between the relative circumferential velocity component and the meridional component. At both stations the predicted results appear to be in reasonable agreement with the measurements inboard of the tip region. The discrepancy in the tip end-wall region is caused by the inability of the present inviscid analysis to properly simulate the three-dimensional end-wall flow. Over the region inboard of the tip, the neglect of the influence of viscosity on the simulated axisymmetric flow field produces more turning of the flow then experimentally measured. By introducing the effect of viscosity into the current average-passage model (which includes the outlined closure model), the agreement between prediction and experiment should improve in the midspan region.

The next series of results is for the stator. The absolute Mach number entering and leaving the stator is plotted as a function of blade span in Fig. 8. The corresponding plot for the absolute flow angle is shown in Fig. 9. This angle is defined as the angle between the absolute tangential velocity component and the meridional component. The agreement between the predicted results and measurements appears to have deteriorated from that for the rotor. This illustrates the difficulty in predicting multiblade row flows. A small error in predicting the performance of the first blade row can escalate very quickly into a large error in predicted performance of later blade rows. This problem becomes particularly acute whenever there are appreciable regions of flow separation in the end-wall region, as appears to be the case in the stator hub region. The poor agreement in the stator tip region is attributed to the end-wall wall flow induced by the rotor. To analyze these flow regions requires a model which incorporates the proper end-wall flow physics. A step in this direction might be made by including the effects of viscosity into the current average-passage flow solver. An additional issue is the development of a closure model for the average-passage model applicable to highly rotational flows. Research in both of these areas is currently underway.

Conclusion

A model was formulated to close the inviscid form of the system of equations governing the average-passage flow fields for a stage. This model was developed so as to insure consistency between the average-passage equation system and the axisymmetric flow equations. This closure model was used successfully to simulate the average-passage flow fields associated with a high-speed counterrotating propeller. The model was also used in a simulation of a high-speed fan stage operating near measured peak efficiency. This simulation showed the rotor results to be in reasonable agreement with measurements outside of the end-wall region. For the stator the simulation yielded results which were only qualitatively correct. The lack of quantitative agreement was attributed to neglect of viscosity and the questionable applicability of the present closure model to the end-wall regions where the flow is known to be highly rotational. Research directed at overcoming these shortcomings is currently underway.

Acknowledgments

The authors wish to express their appreciation to Professor E. M. Greitzer and Dr. C. Tan for their many helpful suggestions and comments. We hope that we have incorporated them correctly into the manuscript. The authors would also like to express their gratitude to Dr. L. D. Nichols, Dr. M. E. Goldstein, and Mr. M. J. Hartmann for their support and encouragement during the course of this research effort.

References

1 Adamczyk, J. J., "Model Equation for Simulating Flows in Multistage Turbomachinery," ASME Paper No. 85-GT-226, Mar. 1985.

2 Celestina, M. L., Mulac, R. A., and Adamczyk, J. J., "A Numerical Simulation of the Inviscid Flow Through a Counterrotating Propeller," ASME JOURNAL OF TURBOMACHINERY, this issue.

3 Sehra, A. K., "Boundary Layer and Wake Modifications to Compressor Design Systems: the Effect of Blade-to-Blade Flow Variations on the Mean Flow Field of a Transonic Rotor," GT/PLD-144, MIT Gas Turbne and Plasma Dynamics Lab., Cambridge, MA, 1979 (AFAPL-TR-79-2010, AD-A076204).

4 Jennions, I. K., and Stow, P., "The Importance of Circumferential Non-uniformities in a Passage-Averaged Quasi-Three-Dimensional Turbomachinery Design System," ASME JOURNAL OF ENGINEERING FOR GAS TURBINES AND POWER, Vol. 108, 1986, pp. 240-245.

5 Adkins, G. G., Jr., and Smith, L. H., Jr., "Spanwise Mixing in Axial-Flow Turbomachines," ASME JOURNAL OF ENGINEERING FOR POWER, Vol. 104, No. 1, Jan. 1982, pp. 97-110.

6 Kerrebrock, J. L., and Mikolajczak, A. A., "Intra-Stator Transport of Rotor Wakes and Its Effect on Compressor Performance," ASME JOURNAL OF ENGINEERING FOR POWER, Vol. 92, 1970, pp. 359-368.

M. L. Celestina

R. A. Mulac

Sverdrup Technology, Inc.

J. J. Adamczyk

NASA Lewis Research Center,
Cleveland, OH 44135

A Numerical Simulation of the Inviscid Flow Through a Counterrotating Propeller

This paper presents the results of a numerical simulation of the time-averaged inviscid flow field through the blade rows of a multiblade row turboprop configuration. The governing equations are outlined along with a discussion of the solution procedure and coding strategy. Numerical results obtained from a simulation of the flow field through a modern high-speed turboprop will be shown.

Introduction

Solving the flow field of a multiblade row machine is very difficult considering the time and length scales involved. The numerical simulation of a general configuration remains formidable even for a machine much larger and faster than today's Class VI computers. However, by mathematically modeling the flow field in the spirit of Reynolds-averaged modeling of turbulent flows, much of the physics relevant to design can be deduced [1]. The objective of this paper is to describe a procedure for simulating the inviscid, time-averaged flow through a multiblade row geometry and present results for a counterrotating propeller configuration designed to operate at transonic speeds.

Three-dimensional, inviscid codes have been developed for isolated propellers using a variety of algorithms. Bober et al. [2] and Barton et al. [3] used the Beam and Warming algorithm and obtained good comparisons to experimental results. Clark [4] used Denton's finite volume code modified for propellers to obtain solutions for acoustic analyses. Holmes and Tong [5] applied Jameson's Runge-Kutta procedure [6] formulated in terms of Cartesian velocity components to a turbine, compressor, and propeller blade row. Celestina and Adamczyk [7] presented results applying Jameson's technique formulated in terms of cylindrical velocity components to a turbine and propeller blade row.

A procedure for extending isolated blade row analyses to multiblade row configurations was suggested by Denton [8]. His method as applied to a stage involved circumferentially averaging the flow properties at a given axial location between the two blade rows. By doing so, the downstream boundary condition to the first blade row and upstream boundary condition to the second blade row are circumferentially uniform.

Adamczyk [1] developed a first principles procedure for analyzing multiblade row flows in which a sequence of averaging operators is used to derive a set of equations that describes an "averaged" three-dimensional representation of the flow field through each blade row of a multiblade row machine. This flow field is steady in time in a reference frame fixed to each blade row and spatially periodic from passage to passage. The field equations associated with this model are referred to as the average-passage equation system. The present work is therefore unique in that it outlines a procedure to solve a set of equations which govern a three-dimensional multiblade row flow field that is directly traceable to the Navier-Stokes equations. However, this average-passage description has associated with it a well-known difficulty. Averaged equations of motion always lead to situations in which there are more unknowns than equations – this is the "closure" problem which requires assumptions or empirical information to make the number of equations equal to the number of unknowns. The closure problem is addressed for the inviscid form of the equations by Adamczyk [9].

The procedure for solving the average-passage equation system requires a mesh for each blade row. The axial and radial location of each grid point is identical for each mesh, but varies in the circumferential direction due to relative blade row locations and unequal blade numbers. A solution is generated for each blade row on its own mesh with the effect of the neighboring blade row contained in source terms in the governing equations. The source terms are sequentially updated using information provided by the neighboring blade row simulation.

Governing Equations

The three-dimensional average-passage equation system for simulating the flow through multiblade rows can be written in cylindrical (r, θ, z) coordinates as

$$(\lambda \mathbf{u})_t + L(\lambda \mathbf{u}) + \int \lambda \mathbf{S} d\text{Vol} = \int \lambda \mathbf{K} d\text{Vol} \quad (1)$$

The vector $\mathbf{u}$ contains the flow variables density, axial and radial momenta, angular momentum, and total internal energy, and λ is the neighboring blade row blockage factor. The value of this parameter ranges between zero and unity, unity being the value associated with zero blade thickness (see [1] for details). The operator $L(\lambda \mathbf{u})$ balances the mass, axial and radial momenta, angular momentum, and energy through a control volume, $\int \lambda \mathbf{K} d\text{Vol}$ is a source term due to the cylin-

---

Contributed by the Gas Turbine Division of THE AMERICAN SOCIETY OF MECHANICAL ENGINEERS and presented at the 31st International Gas Turbine Conference and Exhibit, Düsseldorf, Federal Republic of Germany, June 8–12, 1986. Manuscript received at ASME Headquarters January 27, 1986. Paper No. 86-GT-138.

drical coordinate system, and $\int \mathbf{S}d\mathrm{Vol}$ contains the body forces, energy sources, momentum, and energy temporal mixing correlations associated with the neighboring blade row(s). The details for computing these terms are given in a companion paper [9]. The vector $\mathbf{u}$ and the operator $L(\lambda\mathbf{u})$ are defined by the following expressions

$$\mathbf{u} = [\rho, \rho v_r, r\rho v_\theta, \rho v_z, \rho e_0]$$

$$L(\lambda\mathbf{u}) = \int_{dA} [\lambda\mathbf{F}\cdot d\mathbf{A}_r + \lambda\mathbf{G}\cdot d\mathbf{A}_\theta + \lambda\mathbf{H}\cdot d\mathbf{A}_z] \tag{2}$$

where

$$\mathbf{F}^T = [\rho v_r, \rho v_r^2 + p, r\rho v_\theta v_r, \rho v_z v_r, \rho H v_r]$$

$$\mathbf{G}^T = [\rho v_\theta, \rho v_r v_\theta, r(\rho v_\theta^2 + p), \rho v_z v_\theta, \rho H v_\theta]$$

$$\mathbf{H}^T = [\rho v_z, \rho v_r v_z, r\rho v_\theta v_z, \rho v_z^2 + p, \rho H v_z]$$

$$\mathbf{K}^T = \left[0, \frac{\rho v_\theta^2 + p}{r}, 0, 0, 0\right]$$

In the above equations ρ represents the density, v_r, v_θ, and v_z are the radial, tangential, and axial absolute velocities, and p is the pressure. From the equation of state the total internal energy is related to the pressure as follows

$$e_0 = \frac{p}{\rho(\gamma - 1)} + \frac{1}{2}(v_r^2 + v_\theta^2 + v_z^2)$$

and the total enthalpy is related to e_0, p by the equation

$$H = e_0 + \frac{p}{\rho}$$

In the above equations all lengths are nondimensionalized by the diameter of the largest blade row. The velocity components are nondimensionalized by the reference speed of sound, $a_{\mathrm{ref}}/\sqrt{\gamma}$, pressure and density by their respective reference values, and γ is the ratio of specific heats.

For rotating flows, the absolute (fixed) reference frame is transformed to the relative (rotating) frame by the transformation

$$\theta_{\mathrm{abs}} = \theta_{\mathrm{rel}} + \Omega t \tag{3}$$

where Ω is the rotational wheel speed (positive with θ). Introducing equation (3) into equation (1) yields

$$L(\lambda\mathbf{u}) = \int_{dA} \lambda\mathbf{F}\cdot d\mathbf{A}_r + \lambda(\mathbf{G} - r\Omega\mathbf{u})\cdot d\mathbf{A}_\theta + \lambda\mathbf{H}\cdot d\mathbf{A}_z \tag{4}$$

The term $(\mathbf{G} - r\Omega\mathbf{u})\cdot d\mathbf{A}_\theta$ represents the relative flux of $\mathbf{u}$ in the tangential direction.

Equation (1) is discretized in space for a cell volume (Fig. 1) by approximating the surface integrals by the midpoint rule. The result is a system of ordinary differential equations of the form

$$\frac{d}{dt}(\lambda\mathbf{u}) + \sum [\lambda\mathbf{F}d\mathbf{A}_r + \lambda(G - r\Omega\mathbf{u})d\mathbf{A}_\theta + \lambda\mathbf{H}d\mathbf{A}_z]$$

$$+ \int \lambda\mathbf{S}d\mathrm{Vol} = \int \lambda\mathbf{K}d\mathrm{Vol} \tag{5}$$

The surface areas, $d\mathbf{A}_r$, $d\mathbf{A}_\theta$, $d\mathbf{A}_z$ are calculated using the cross product of the diagonals of a cell face and the volume is determined using the formula described by Holmes and Tong [5]. Since all the flow quantities are cell-centered, a simple averaging procedure is used to determine the value of a variable at any surface, excluding solid boundaries. This is equivalent to second-order accurate central differencing for a uniform mesh.

Runge-Kutta Integration. To advance the equations in time, a four-stage Runge-Kutta scheme is used. The scheme employed has been patterned after the work of Jameson et al. [6]. Given information at time level n, the steps to advance to the next level, $n+1$, are

$$\left.\begin{aligned} \mathbf{u}^\alpha &= \mathbf{u}^n - \alpha\Delta t L(\mathbf{u}^n) \\ \mathbf{u}^\beta &= \mathbf{u}^n - \beta\Delta t L(\mathbf{u}^\alpha) \\ \mathbf{u}^\gamma &= \mathbf{u}^n - \gamma\Delta t L(\mathbf{u}^\beta) \\ \mathbf{u}^* &= \mathbf{u}^n - \Delta t L(\mathbf{u}^\gamma) \\ \mathbf{u}^{n+1} &= \mathbf{u}^* + D(u^*) \end{aligned}\right\} \tag{6}$$

where $\alpha = 1/4$, $\beta = 1/3$, $\gamma = 1/2$, and $D(\mathbf{u})$ is the dissipation operator. The maximum permissible time step for this scheme is restricted by the CFL stability limit. Jameson has determined the limit for the above four-stage scheme to be $2\sqrt{2}$ based on a one-dimensional model problem. To enhance the convergence rate of this scheme, a local time step is chosen based on the maximum CFL number commensurate with stability. An advantage of using the present Runge-Kutta scheme is that it minimizes storage requirements.

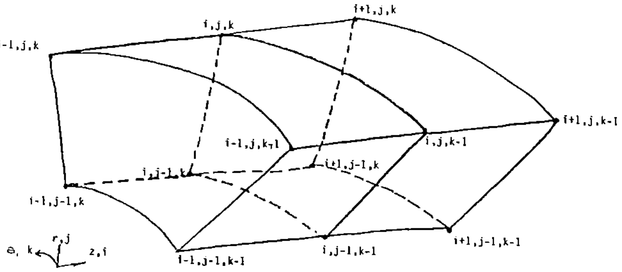

Fig. 1 Typical cell in cylindrical coordinate system

Artificial Dissipation. To suppress odd-even point decoupling in the solution, dissipative terms are added to the equations. Jameson [6], via numerical experiments, developed a blend of second and forth difference smoothing operators. The operator $D(\mathbf{u})$ in equation (6) can be decomposed into three spatial operators

$$D(\mathbf{u}) = (D_r + D_\theta + D_z)(\mathbf{u})$$

such that the dissipation in each direction can be evaluated separately. The dissipation in the axial direction $D_z(\mathbf{u})$ is expressed as follows

$$D_z(\mathbf{u}) = d_{i+1/2,j,k} - d_{i-1/2,j,k} \tag{7}$$

where

$$d_{i+1/2,j,k} = \frac{\mathrm{Vol}_{i+1/2,j,k}}{\Delta t_{i+1/2,j,k}} [\epsilon^2_{i+1/2,j,k}\Delta_z\mathbf{u}_{i,j,k} - \epsilon^4_{i+1/2,j,k}\Delta_z^3\mathbf{u}_{i,j,k}] \tag{8}$$

and the coefficients ϵ^2 and ϵ^4 are evaluated as follows

$$\epsilon^2_{i+1/2,j,k} = \kappa^2 \max(\nu_{i+1,j,k}, \nu_{i,j,k})$$

$$\epsilon^4_{i+1/2,j,k} = \max(0, \kappa^4_{i+1/2,j,k} - \epsilon^2_{i+1/2,j,k})$$

κ^2 and κ^4 are constants typically set at 1/2 and 1/64, respectively. To capture shocks sharply and retain second-order accuracy away from shocks, Jameson defined the coefficient $\nu_{i,j,k}$ as

$$\nu_{i,j,k} = \mathrm{abs}\left[\frac{P_{i+1,j,k} - {}^2P_{i,j,k} + P_{i-1,j,k}}{P_{i+1,j,k} + {}^2P_{i,j,k} + P_{i-1,j,k}}\right] \tag{9}$$

The variable $\nu_{i,j,k}$ is proportional to the square of the mesh spacing in smooth regions of flow and linear in mesh spacing

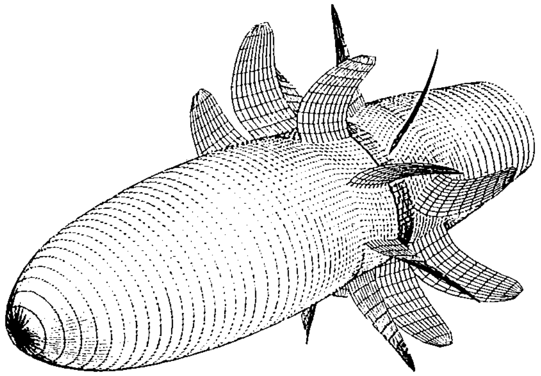

Fig. 2 General Electric unducted fan configuration

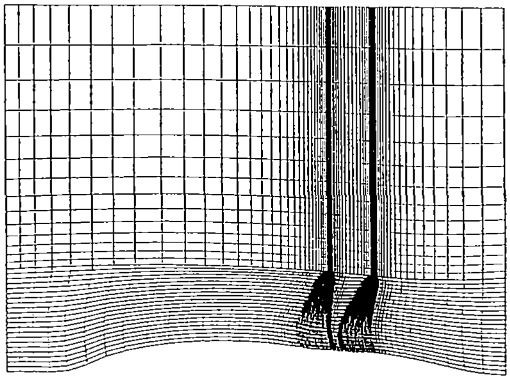

(a) Constant ζ cut for forward and aft propellers.

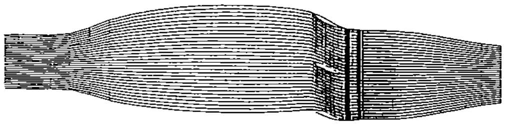

(b) Constant η cut for forward propeller.

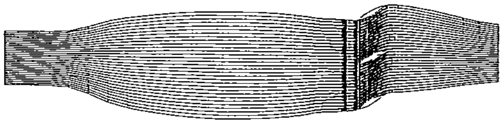

(c) Constant η cut for aft propeller.

Fig. 3 GE unducted fan grid (99 × 36 × 16)

in regions of large pressure gradients. The pressure sensitive switch was applied only in the axial and circumferential directions. For the radial direction, it was found that setting $\nu_{i,j,k}$ to a constant (0.05) and ϵ^4 to zero enhanced the stability of the scheme.

Boundary Conditions. The mathematical form of the field equations solved in the present work closely resembles that of the Euler equations. Therefore, the known mathematical properties of the Euler equations will be used as a guide to develop the boundary conditions of the present system of equations. It is assumed that the absolute flow field approaching and leaving the propeller is subsonic. This implies that four conditions must be specified at the upstream boundary and only one at the downstream boundary.

The axial velocity component and the flow properties at the upstream boundary are updated based on a local unsteady one-dimensional flow model in which the entropy is assumed constant with time and uniform in space. The equations associated with this model are

$$\frac{dC^-}{dt} + (v_z - a)\frac{\partial C^-}{\partial z} = 0 \qquad (10a)$$

$$\frac{dC^+}{dt} + (v_z - a)\frac{\partial C^+}{\partial z} = 0 \qquad (10b)$$

in which C^+ and C^- are the well-known Riemann invariants. They are related to the axial velocity v_z and speed of sound a by the equations

$$v_z + \frac{2a}{\gamma - 1} = C^+, \qquad v_z - \frac{2a}{\gamma - 1} = C^-$$

The invariant C^+ is associated with information coming from outside the computational domain and thus it is specified based on the farfield flow conditions. The C^- invariant is updated by solving equation (10*b*) in time using the Runge-Kutta integration procedure outlined earlier. The axial derivative is approximated by a backward difference operator. The Riemann invariants determine the speed of sound and the axial velocity component. The pressure, density, and temperature are updated based on the known value of the incoming entropy. The values of the velocity components parallel to the upstream boundary are assumed known.

At the downstream boundary, simple radial equilibrium is enforced

$$\frac{\partial p}{\partial r} = \frac{\rho v_r^2}{r} \qquad (11)$$

The pressure is specified at the free-stream farfield boundary and equation (11) is integrated radially using the trapezoidal rule toward the spinner-nacelle. The remaining flow variables are extrapolated from the interior.

Boundary conditions at the farfield boundary are derived based on a one-dimensional unsteady flow model identical to the one employed at the upstream boundary. In this model, the axial velocity component is replaced by the radial component. The value of C^+ is fixed by the farfield condition and C^- is extrapolated from the interior.

At periodic flow boundaries we require the flow to exhibit a spatial periodicity equal to the pitch of the blade row. Thus, any information required from a cell which lies adjacent to a periodic boundary but outside the computational domain is obtained from a cell which also lies adjacent to a periodic boundary but is inside the computational domain.

Since the flux is zero on solid surfaces only the pressure need be known. This can be extrapolated from the interior or determined from an adaptation to the present system of equations of a normal pressure gradient condition developed by Rizzi [6]. The present work uses the adapted Rizzi condition on the hub and extrapolation for the blade surfaces.

Mesh Generation. To solve the average-passage equation system through a multiblade row machine, a mesh is needed for each blade row which contains the axial and radial coordinates of all blade rows. Thus, for a two-stage machine, four grids would be generated and each assigned the thickness and period of one of the four blade rows. However, each mesh must also conform axisymmetrically to the coordinates of the other blade rows. To do this efficiently, the geometry is separated into blade and nonblade sections from inlet to exit. An axisymmetric algebraic mesh is generated using one-dimensional spline fits and the axial and radial coordinates are common to all the grids in the meridional plane. To complete the grids, the tangential mesh lines are generated using spline fits and taking into account blade thickness and blade count.

Solution Procedure. A nested iteration procedure using an inner and outer loop was presented in [9] to solve the average-passage equation system through each blade row of a multiblade row machine. Within the inner loop the three-dimensional "average" flow variables are evaluated for a given distribution of body forces, energy sources, and correla-

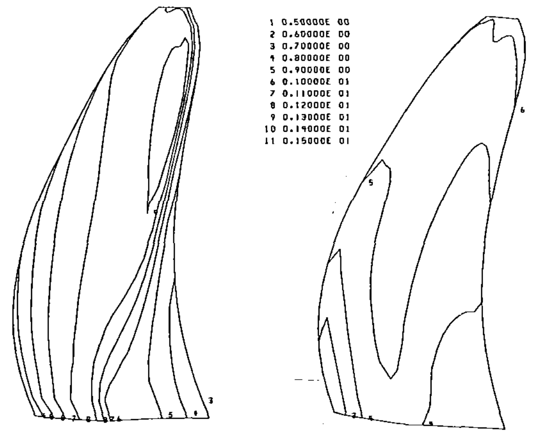

(a) Suction side. (b) Pressure side.

Fig. 4 Contour of constant relative Mach number for forward propeller; $M_\infty = 0.72$, $J = 2.80$

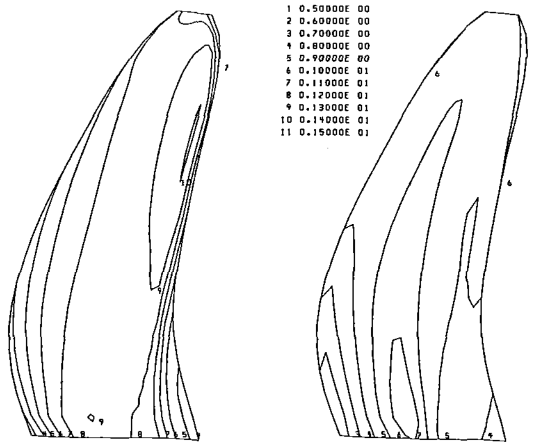

Fig. 5 Contours of constant relative Mach number for aft propeller; $M_\infty = 0.72$, $J = -2.80$

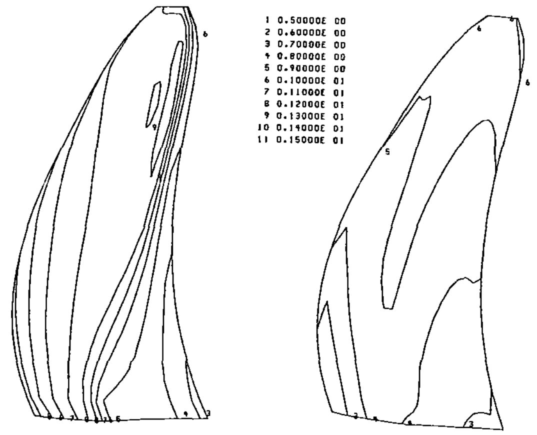

Fig. 6 Contours of constant relative Mach number for forward propeller in isolation, $M_\infty = 0.72$, $J = 2.80$

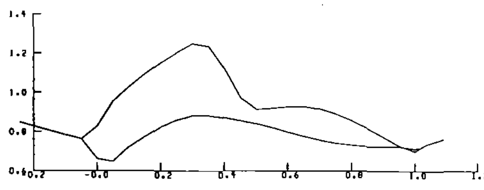

(a) 10% span.

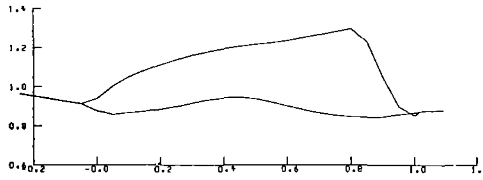

(b) 50% span.

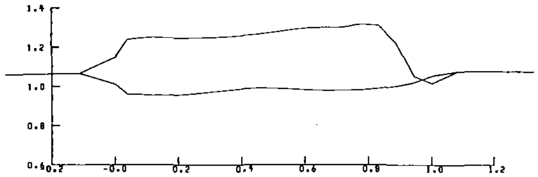

(c) 90% span.

Fig. 7 Relative Mach number versus axial distance on blade surface; forward propeller

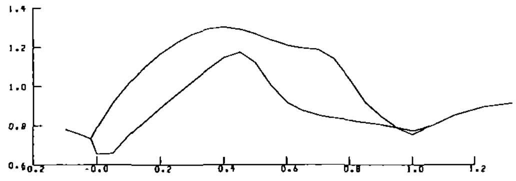

(a) 10% span.

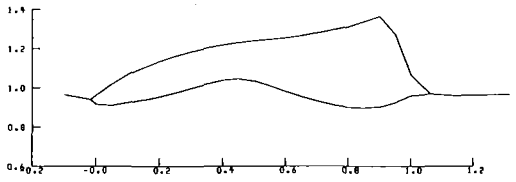

(b) 50% span.

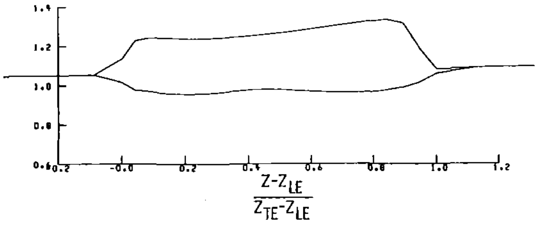

(c) 90% span.

Fig. 8 Relative Mach number versus axial distance on blade surface; aft propeller

tions. These terms are denoted as S in equation (5). The inner loop uses the Runge-Kutta integration procedure outlined earlier for solving the Euler-like equations. The outer loop updates the body forces, energy sources, and correlations based on the axisymmetric average of the converged inner loop solution. An outline for updating the above terms can be found in [9]. Global or outer loop convergence is obtained when the difference between the axisymmetric average of the time-averaged flow variables on each blade row is below a given tolerance.

Results and Discussion

A General Electric counterrotating unducted fan configuration was simulated on a Cray 1-S. The geometry contains two, eight-bladed fans (Fig. 2) designed to operate at a free-stream Mach number of 0.72 and advance ratio of 2.80. The grid (Fig. 3) contains 99 axial, 36 radial, and 16 circumferential points with 28 points lying forward of the front blade, 20 points axially on both blades, 15 points between blades, and 15 points aft of the rear blade. Both blades contain 22 equally spaced points in the radial direction with the remaining 14 spaced from the blade tip to the free stream. No mesh cluster-

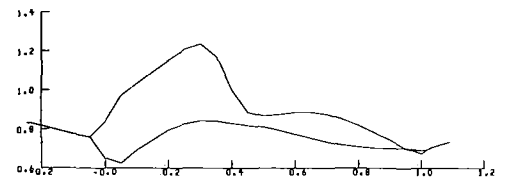

(a) 10% span.

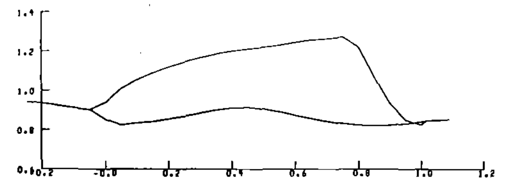

(b) 50% span.

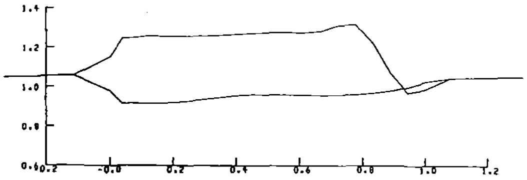

(c) 90% span.

Fig. 9 Relative Mach number versus axial distance on blade surface; forward propeller in isolation

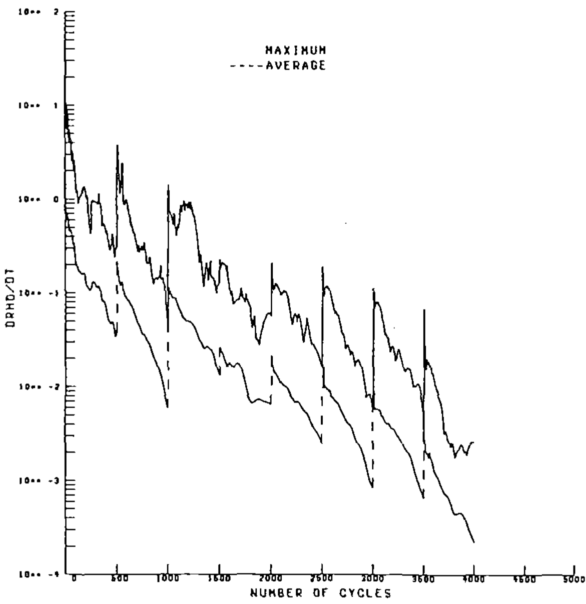

(a) Forward propeller solution.

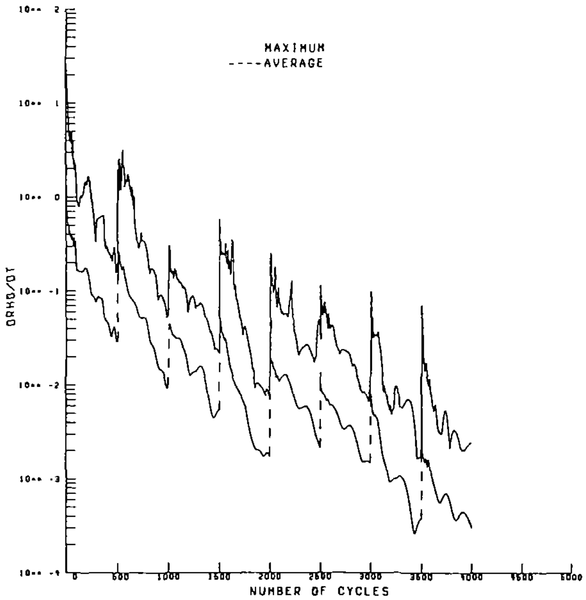

(b) Aft propeller solution.

Fig. 10 Convergence history for forward and aft propeller

ing was used in the angular direction. A sting whose diameter was equal to the sting at the hub exit was affixed to the front of the nacelle.

Figures 4 and 5 show contours of constant relative Mach number on the pressure and suction side of the forward and aft blade rows. The shock locations on the suction side of both blades (Figs. 4(*a*) and 5(*a*)) run along the trailing edge of the blade terminating at about 30 percent of span on the first propeller. One would expect to observe this shock structure given the high inlet Mach number and blade geometry. There also appears to be a shock in the vicinity of the nacelle/suction surface interface for the forward propeller. Figure 5(*b*) shows the presence of a supersonic bubble at the junction of the nacelle surface on the pressure side of the aft blade. This bubble seems to extend across the passage to the suction surface indicating that the flow in the hub region is choked.

The forward blade was also run in isolation using the same spinner-nacelle geometry. The inlet Mach number and rotational speed were identical to those for the counterrotating configuration. The relative Mach number contours are illustrated in Fig. 6 for the suction and pressure surfaces. Note that the Mach numbers in general are lower than those which appear on the forward propeller of the counterrotating configuration. This is attributed to the "induction" effect of the second blade row. More fluid passes through the counterrotating configuration than through the isolated configuration. This can be seen more readily in plots of relative Mach number versus axial distance. Three radial stations are shown in Figs. 7-9. It is seen that the relative Mach number forward and aft of the first blade row is higher for the counterrotating configuration than it is for the isolated configuration. The shock strength for both configurations appears to be the same; however, for the counterrotating configuration the shock location is nearer the blade trailing edge.

There are a number of ways to determine convergence of the above simulations. Jameson typically computes the time derivative of the density (i.e., $\partial\rho/\partial t$), and the number of supersonic points. Figures 10 show plots of $\partial\rho/\partial t$ versus the number of cycles for the first and second blade row simulation. The solid line indicates the maximum absolute value of the derivative and the dashed line the average value of the derivative. The average value is determined by evaluating the sum of the absolute value of the time derivative at each point in the field divided by the number of points. The peaks at every 500 cycles are attributed to updating the body forces, energy sources, and correlations. It is seen that the present solution strategy for solving the inner loop equations converges as indicated by the reduction in both the maximum and average levels of $\partial\rho/\partial t$. Figure 11 shows the number of supersonic points based on the absolute Mach number versus the number of calculation cycles. Again, the number of supersonic points for both simulations converges to a constant value further indicating convergence. Finally, Fig. 12 measures the L_2 norm of the difference of the axisymmetrically averaged solutions calculated at the end of each outer loop. The L_2 norm shows a drop of two orders of magnitude. This reduction was judged sufficient to consider the computations converged.

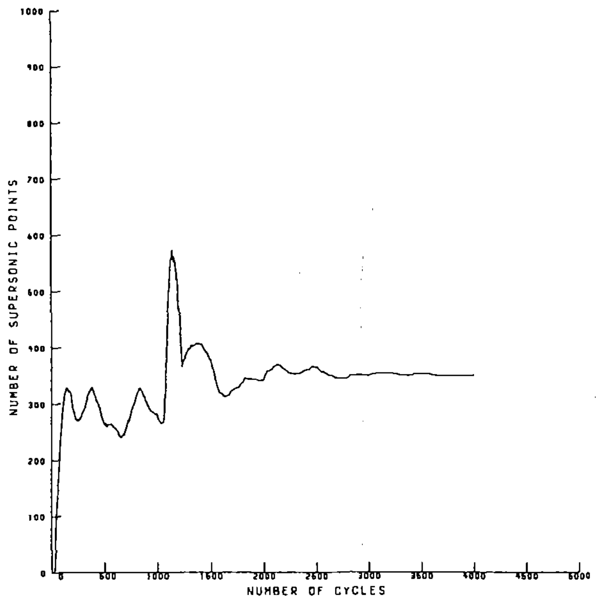

(a) Forward propeller solution.

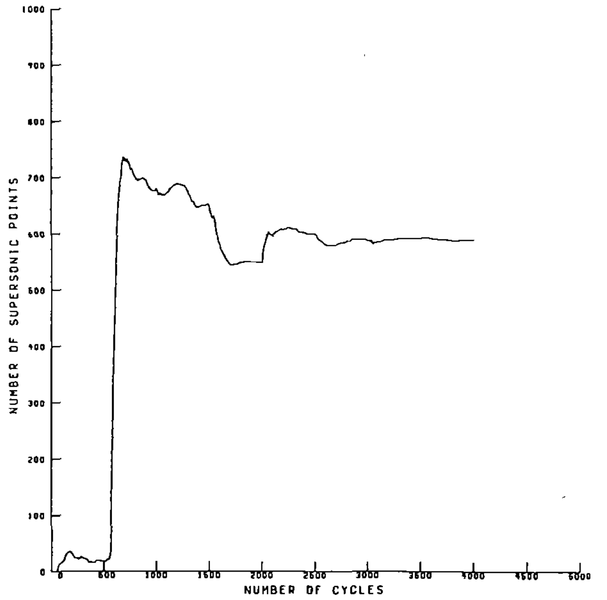

(b) Aft propeller solution.

Fig. 11 Convergence based on number of supersonic points

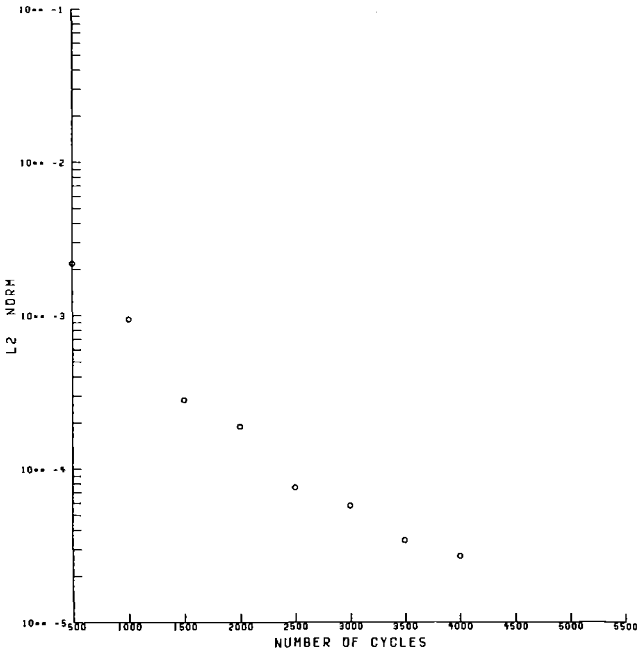

Fig. 12 L_2 norm of difference between axisymmetrically averaged solutions

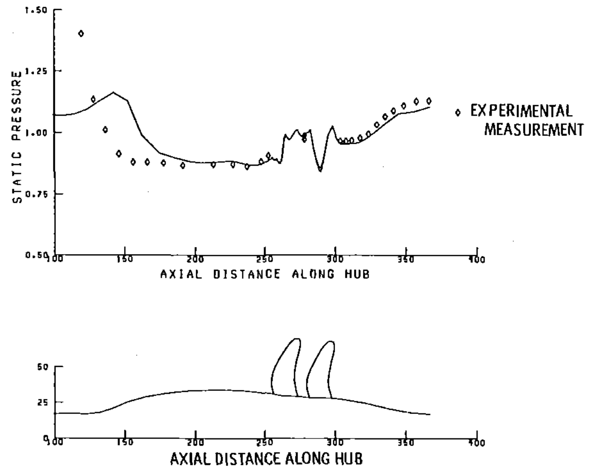

Fig. 13 Spinner-nacelle axisymmetric static pressure distribution

As a final check on the solutions described above, they were compared to experimental measurement taken in the NASA Lewis 8 by 6 Tunnel [10]. This comparison is shown in Fig. 13. The solid and dashed line is a plot of the axisymmetrically averaged static pressure along the nacelle obtained from the first and second blade row simulations, respectively. The diamonds represent the experimental data. There is good agreement between the prediction and measurement aft of the maximum nacelle diameter. The discrepancy at the spinner-nacelle nose was expected since the physical domain did not conform to the true nacelle geometry in this region. The grid conformed to a sting having the same diameter as the sting attachment at the end of the model.

Since the above computations required large memory and CPU time, some code enhancements are being pursued. These include multitasking and minimization of in-core storage. The first attempt at multitasking required the resources of a Cray X-MP multiprocessor computer. This effort involved assigning the flow field simulation associated with each blade row to a processor. This step alone decreased run time by a factor of two for a two blade row configuration. Also, due to the advanced architecture of the Cray X-MP compared to the Cray 1-S, an additional speedup was obtained. The net result was a reduction in CPU time by a factor of three over a comparable simulation on the Cray 1-S. To minimize in-core storage, the three-dimensional solutions will be stored in two-dimensional planes on secondary storage. To minimize I/0 overhead, the use of a high-speed mass storage device will be needed. By implementing these two enhancements, the capabilities of the code can be extended to solve multistage problems.

Conclusions

A numerical procedure based on a finite volume formulation was developed to solve the average-passage equation system for a multiblade row configuration. This procedure employed a four-stage Runge–Kutta integration scheme to march the equations forward in time toward the time asymptotic limit. A computer code based on this procedure was successfully used to simulate the average-passage flow fields associated with a high-speed counterrotating propeller. The results of this simulation yielded information which proved useful in evaluating aerodynamic design.

Acknowledgments

The authors would like to express their thanks to Mr. Tom Sullivan of GE Evandale and Dr. Larry Bober and Mr. Bob Jeracki of NASA Lewis for their helpful comments, suggestions, and assistance in developing the results pertaining to these computations.

References

1 Adamczyk, J. J., "Model Equation for Simulating Flows in Multistage Turbomachinery," NASA TM-86869 and ASME Paper No. 85-GT-226, Nov. 1984.

2 Bober, L. J., Chaussee, D. S., and Kutler, P., "Prediction of High-Speed Propeller Flow Fields Using a Three-Dimensional Euler Analysis," NASA TM-83065 and AIAA-83-0188, Jan. 1983.

3 Barton, J. M., Yamamoto, O., and Bober, L. J., "Inviscid Analysis of Advanced Turboprop Propeller Flow Fields," AIAA-85-1263, July 1985.

4 Clark, B. J., and Scott, J. R., "Coupled Aerodynamic and Acoustical Prediction for Turboprops," 107th Meeting of the Acoustical Society of America, Norfolk, VA, May 7-10, 1984.

5 Holmes, D. G., and Tong, S. S., "A Three-Dimensional Euler Solver for Turbomachinery Blade Rows," ASME JOURNAL OF ENGINEERING FOR GAS TURBINES AND POWER, Vol. 107, 1985, pp. 258-264.

6 Jameson, A., Schmidt, W., and Turkel, E., "Numerical Solutions of the Euler Equations by Finite Volume Methods Using Runge-Kutta Time-Stepping Schemes," AIAA-81-1259, June 1981.

7 Celestina, M. L., and Adamczyk, J. J., "Three-Dimensional Euler Solver for Turbomachinery," presented at NASA Marshall SSME CFD Workshop, Huntsville, AL, Nov. 1984.

8 Denton, J. D., and Singh, U. K., "Time Marching Methods for Turbomachinery Flow Calculations," VKI Lecture Series 1979-7, Rhodes-Saint-Genèse, Belgium, Apr. 1979.

9 Adamczyk, J. J., Mulac, R. A., and Celestina, M. L., "A Model for Closing the Inviscid Form of the Average-Passage Equation System," ASME JOURNAL OF TURBOMACHINERY, this issue.

10 Jeracki, B., private communications.

An Inverse (Design) Problem Solution Method for the Blade Cascade Flow on Streamsurface of Revolution[1]

Chen Naixing
Zhang Fengxian
Li Weihong
Institute of Engineering Thermophysics,
Chinese Academy of Sciences,
Beijing, People's Republic of China

On the basis of the fundamental equations of aerothermodynamics a method for solving the inverse (design) problem of blade cascade flow on the blade-to-blade streamsurface of revolution is suggested in the present paper. For this kind of inverse problem the inlet and outlet flow angles, the aerothermodynamic parameters at the inlet, and the other constraint conditions are given. Two approaches are proposed in the present paper: the suction-pressure-surface alternative calculation method (SSAC) and the prescribed streamline method (PSLM). In the first method the metric tensor (blade channel width) is obtained by alternately fixing either the suction or pressure side and by revising the geometric form of the other side from one iteration to the next. The first step of the second method is to give the geometric form of one of the streamlines. The velocity distribution or the mass flow rate per unit area on that given streamline is estimated approximately by satisfying the blade thickness distribution requirement. The stream function in the blade cascade channel is calculated by assuming initial suction and pressure surfaces and solving the governing differential equations. Then, the distribution of metric tensor on the given streamline is specified by the stream function definition. It is evident that the square root of the metric tensor is a circumferential width of the blade cascade channel for the special nonorthogonal coordinate system adopted in the present paper. The iteration procedure for calculating the stream function is repeated until the convergence criterion of the metric tensor is reached. A comparison between the solutions with and without consideration of viscous effects is also made in the present paper.

Introduction

The inverse problem is an aerothermodynamics solution problem for designing a blade cascade profile for given inlet and outlet flow angles and other constraint conditions, such as the blade thickness required by structural stresses or blade internal cooling. In industry, the blade cascade is usually designed by the designer's experiences and the design process is carried on with graphic methods. The primary designed blade cascade finally is tested in the wind tunnel and on rotating facilities to satisfy the aerodynamic requirements.

During 1983–1984 an aerodynamics hybrid solution method was developed by the authors [1]. It is successful for modifying turbine and compressor blade cascades of outdated design. An aerodynamically qualified profile geometry is formed by continuously revising the unreasonable velocity distribution and the geometry of blade surfaces. The method suggested in [1] is not an inverse problem solution method because it is impossible to obtain the full geometry of the blade profile.

In the fourth decade of this century people paid attention to the inverse problem. A series of inverse (design) methods for incompressible fluid flow and low Mach number flow has been suggested, such as a conformal mapping method, a singularity method, and a hodograph method (see Döge's review paper [2]). During the sixth decade the hodograph method was developed and applied successfully to the design of transonic turbine blade cascades [4–6]. At the end of the last decade a critical blade cascade flow problem was solved by German scientists employing potential and stream functions [7]. We would point out that the mean-streamline method, as an inverse solution method, suggested by Wu [8–9] and Cai [10], has played an important role in designing turbine and compressor blade cascades. Recently some good new studies of the inverse problem have appeared in China and abroad [11–17].

On the basis of solving aerothermodynamics equations and of employing the stream function definition the procedure for specifying the square root of metric tensor g_{22}, or the angular width of the blade channel, is discussed in the present paper.

Governing Equations

For a relatively steady flow on the blade-to-blade steamsurface of revolution, the continuity equation, dynamic equa-

---

[1] Projects supported by the Science Fund of the Chinese Academy of Sciences.

Contributed by the Gas Turbine Division of The American Society of Mechanical Engineers and presented at the 31st International Gas Turbine Conference and Exhibit, Düsseldorf, Federal Republic of Germany, June 8–12, 1986. Manuscript received at ASME Headquarters February 7, 1986. Paper No. 86-GT-159.

tions on the $\mathbf{e}^2$ and $\mathbf{e}^3$ directions, energy equation, and entropy equation can be expressed as follows [20–22]

$$\frac{\partial}{\partial x^2}\,(\rho\sqrt{g}w^2)+\frac{\partial}{\partial x^3}\,(\rho\sqrt{g}w^3)=0 \tag{1}$$

$$w^3\left(\frac{\partial w_3}{\partial x^2}-\frac{\partial w_2}{\partial x^3}\right)+2\sqrt{g}w^3\omega^1=\frac{\partial I}{\partial x^2}-T\frac{\partial s}{\partial x^2}-\frac{1}{\rho}\,(f_{\rm vis})_2 \tag{2a}$$

$$w^2\left(\frac{\partial w_2}{\partial x^3}-\frac{\partial w_3}{\partial x^2}\right)-2\sqrt{g}w^2\omega^1=\frac{\partial I}{\partial x^3}-T\frac{\partial s}{\partial x^3}-\frac{1}{\rho}\,(f_{\rm vis})_3 \tag{2b}$$

$$w^2\,\frac{\partial I}{\partial x^2}+w^3\,\frac{\partial I}{\partial x^3}=\dot{q}+\frac{1}{\rho}\,\mathbf{W}\cdot\mathbf{F}_{\rm vis}+\frac{\Phi}{\rho} \tag{3}$$

$$T\left(w^2\,\frac{\partial s}{\partial x^2}+w^3\frac{\partial s}{\partial x^3}\right)=\dot{q}+\frac{\Phi}{\rho} \tag{4}$$

Substituting a dimensionless stream function $\bar{\psi}=\psi/G_0$ satisfying the following definition

$$w^2=-\frac{1}{\rho g}\,\frac{\partial\bar{\psi}}{\partial x^3}\,G_0 \tag{5a}$$

$$w^3=\frac{1}{\rho g}\,\frac{\partial\bar{\psi}}{\partial x^2}\,G_0 \tag{5b}$$

into equation (2*a*), employing a special "constant ratio" nonorthogonal coordinate system [1], we have:

$$A_{10}\,\frac{\partial^2\bar{\psi}}{\partial(x^2)^2}+A_{20}\,\frac{\partial^2\bar{\psi}}{\partial x^2\partial x^3}+A_{30}\,\frac{\partial^2\bar{\psi}}{\partial(x^3)^2}+A_{40}\,\frac{\partial\bar{\psi}}{\partial x^2}+A_{50}\,\frac{\partial\bar{\psi}}{\partial x^3}=B_1 \tag{6}$$

where $A_{10}, A_{20}, \ldots\ldots, A_{50}$ are the coefficients of the stream-function equation (6). They can be written as

$$\left.\begin{aligned}
A_{10}&=\sqrt{g_{33}}/(\rho_1 f\sqrt{g_{22}})\\
A_{20}&=-2\cos\theta/(\rho f)\\
A_{30}&=\sqrt{g_{22}}/(\rho f\sqrt{g_{33}})\\
A_{40}&=\partial A_{10}/\partial x^2+0.5\partial A_{20}/\partial x^3\\
A_{50}&=\partial A_{30}/\partial x^3+0.5\,\partial A_{20}/\partial x^2\\
B_1&=(\partial I/\partial x^2-T\partial s/\partial x^2\\
&\quad-2w^3\Omega\sin\theta\sin\sigma-(f_{\rm vis})_2/\rho)
\end{aligned}\right\} \tag{7}$$

The heat transfer term $\dot{q}$, the viscous force components $(f_{\rm vis})_2$, $(f_{\rm vis})_3$, the work done by the viscous force $\mathbf{W}\cdot\mathbf{F}_{\rm vis}$, and the dissipation function Φ are expressed as follows

$$\dot{q}=\frac{1}{\rho}\,(\lambda g^{im}T|_m)|_i \tag{8}$$

$$(f_{\rm vis})_j=g^{im}\,(\pi_{mj}|_i) \tag{9}$$

$$\mathbf{W}\cdot\mathbf{F}_{\rm vis}=w^j g^{im}\,(\pi_{mj}|_i) \tag{10}$$

$$\Phi=g^{im}\pi_{mj}\,(w^j|_i) \tag{11}$$

Nomenclature

$A_{10}, A_{20}, \ldots\ldots, A_{50}$ = coefficients of stream-function equation
B_1 = right-hand side term of stream-function equation
f = $\sqrt{g_{11}}\sin\theta$
$\mathbf{F}_{\rm vis}$ = viscous force vector
$(f_{\rm vis})_1$, $(f_{\rm vis})_2$ = covariant components of viscous force vector
G_0 = flow rate through a blade cascade channel
g = metric tensor
g_{11} = metric tensor; $\sqrt{g_{11}}$ represents a normal thickness τ of blade-to-blade stream surface
g_{22} = metric tensor; $\sqrt{g_{22}}$ is a Lame coefficient of x^2
g_{33} = metric tensor; $\sqrt{g_{33}}$ is a Lame coefficient of x^3
g^{22}, g^{23}, g^{33} = metric tensors; $g^{22}=1/(g_{22}\sin^2\theta)$, $g^{23}=g^{32}=-\cos\theta/(\sqrt{g_{22}}\sqrt{g_{33}}\cdot\sin^2\theta)$, $g^{33}=1/(g_{33}\sin^2\theta)$
I = rothalpy
j, k = indices of grid point along x^2 and x^3 directions, respectively
k = adiabatic ratio
l = coordinate axis of meridional direction
p = static pressure
R, φ, z = axes of cylindrical coordinate system
$\mathbf{R}$ = radius vector
$\mathcal{R}$ = gas constant
T = absolute temperature
s = entropy
W^2, W^3 = physical contravariant components of relative velocity vector $\mathbf{W}$
w^2, w^3 = contravariant components of relative velocity vector $\mathbf{W}$
W_2, W_3 = physical covariant components of relative velocity vector $\mathbf{W}$
w_2, w_3 = covariant components of relative velocity vector $\mathbf{W}$: $w_2=w^2g_{22}+w^3g_{23}$, $w_3=w^2g_{23}+w^3g_{33}$
$\alpha_{\delta\varphi}$ = relaxation factor of $\delta\psi$
$\alpha_{\varphi p}$ = relaxation factor of φ_p
$\delta\varphi$ = angular width of blade channel
λ = coefficient of thermal conductivity
μ = dynamic viscosity
Ω = angular velocity
ψ = stream function, $\bar{\psi}=\psi/G_0$
ω^1 = contravariant component of angular velocity vector on $\mathbf{e}_1$ direction
Φ = dissipation function
σ = meridional flow angle of stream surface
θ = coordinate angle between x^2 and x^3 axes
τ = normal thickness of blade-to-blade streamsurface
$(\ )|_i$ = covariant derivative of ( )

Subscripts

1 = parameter of inlet flow condition
2 = parameter of outlet flow condition
G = given prescribed streamline
m = calculated streamline
p = pressure side of blade profile
s = suction side of blade profile

The relationship between the stress tensor components and covariant components of velocity is

$$\pi_{ij}=\mu\left(\frac{\partial w_j}{\partial x^i}+\frac{\partial w_i}{\partial x^j}-2w_k\Gamma_{ij}^k-\frac{2}{3}\,g_{ij}\mathrm{div}\mathbf{W}\right) \tag{12}$$

The covariant derivative of the stress tensor is

$$\pi_{mj}|_i=\frac{\partial\pi_{mj}}{\partial x^i}-\Gamma_{ij}^h\pi_{mh}-\Gamma_{im}^h\pi_{hj} \tag{13}$$

where

$$\Gamma_{ij}^m=\frac{1}{2}\left(\frac{\partial g_{ki}}{\partial x^j}+\frac{\partial g_{kj}}{\partial x^i}-\frac{\partial g_{ij}}{\partial x^k}\right)g^{km} \tag{14}$$

Both thermal conductivity λ and dynamic viscosity μ are known functions of temperature:

$$\left.\begin{array}{l}\lambda=f_\lambda(T)\\ \mu=f_\mu(T)\end{array}\right\} \tag{15}$$

The simplified expressions of the viscous terms were suggested by [22]. These simplified formulae agree with the full expressions well. Therefore, in this case these formulae also can be used.

Besides the above equations the following equations are also employed:

The definition of rothalpy

$$I=c_pT+\frac{(W)^2}{2}-\frac{(\Omega R)^2}{2} \tag{16}$$

Equation of perfect gas

$$p=\rho\Re T \tag{17}$$

Formulae for calculating density

$$\rho=\rho_1(T/T_1)^{\frac{1}{k-1}}/\exp[(s-s_1)/\Re] \tag{18}$$

With the boundary conditions, equations (3), (4), (5*a*), (5*b*), (6), (16), (17), (18) and the auxiliary relations (8)-(15), involving eight variables $\bar{\psi}$, ρ, p, T, I, s, w^2, w^3, can be solved. The same solution procedure of direct problem, as shown in [1, 21, 22], is used for the present inverse problem solution methods.

Inverse Problem Solution Methods

It is clear from the definition of stream function that the metric tensor g is connected with the first derivative of stream function $\partial\bar{\psi}/\partial x^2$ and mass flow rate past through a unit area ρw^3 by the following expression:

$$\sqrt{g}=\frac{\partial\bar{\psi}}{\partial x^2}\,G_0/(\rho w^3) \tag{19}$$

The metric tensor g depends on the coordinate system which we adopt. The "constant ratio" nonorthogonal coordinate system is chosen for the present method. Because each x^3 coordinate line is formed by keeping

$$(\varphi-\varphi_p)/\delta\varphi=\mathrm{const} \tag{20}$$

the metric tensors would be

$$\sqrt{g_{22}}=\sqrt{\left(\frac{\partial(R\varphi)}{\partial x^2}\right)^2+\left(\frac{\partial l}{\partial x^2}\right)^2}=R\delta\varphi \tag{21}$$

$$\sqrt{g_{33}}=\sqrt{\left(\frac{\partial(R\varphi)}{\partial x^3}\right)^2+\left(\frac{\partial l}{\partial x^3}\right)^2}=\sqrt{\tan^2\theta_3+1}=\sec\theta_3 \tag{22}$$

and

$$\sqrt{g}=\sqrt{g_{11}g_{22}g_{33}}\sin\theta=\tau R\delta\varphi \tag{23}$$

Substituting abovementioned formulae into equation (19), the result is

$$\delta\varphi=\frac{1}{R\tau}\,\frac{\partial\bar{\psi}}{\partial x^2}\,G_0/(\rho w^3) \tag{24}$$

Equation (24) shows that if the values of R, τ, ρ, w^3 are known, and $\partial\bar{\psi}/\partial x^2$ is obtained from the solution of the stream function equation in the last iteration, the angular width of the blade cascade channel, $\delta\varphi=\varphi_s-\varphi_p$, can be determined.

For the hybrid problem the shape of a portion of the blade profile is unknown and the remainder is determined by a given prescribed velocity distribution. For the inverse problem all the geometric shapes of both suction and pressure surfaces are unknown and must be calculated from the given conditions, such as inlet and outlet flow angles, the aerothermodynamic parameters at the inlet, etc.

Two programs of inverse problem solution are selected in the present paper.

Surface-to-Surface Alternative Calculation (SSAC) Method. In this program the velocity distributions of both suction and pressure surfaces, the positions of both leading and trailing edges, and the inlet parameters are given. From these leading and trailing edges the primary shapes of the suction and pressure surfaces are formed arbitrarily. For an arbitrary described velocity distribution a solution exists when the following circulation constraint is satisfied

$$\oint_{p+s}WdL=t(W_1\sin\beta_1-W_2\sin\beta_2) \tag{25}$$

Simultaneously, the formulation of an optimal suction surface velocity distribution requires a boundary layer nonseparation constraint [16]. Then, the direct solution is carried on and the geometry of one of two surfaces (for example, the suction surface) is determined from equation (24) assuming that the geometry of the other surface is known, that is

$$\varphi_p=\varphi_s-\delta\varphi=\varphi_s-\alpha_{\delta\varphi}\,\frac{1}{R\tau}\left(\frac{\partial\bar{\psi}}{\partial x^2}\right)_s G_0/(\rho w^3)_s \tag{26}$$

where $\alpha_{\delta\varphi}$ is the relaxation factor.

In the next iteration the direct problem solution is made for the new profile formed by the suction and pressure surfaces, where one of these two surfaces has been calculated from the last iteration. Then the geometry of the other surface can be obtained as

$$\varphi_s=\varphi_p+\delta\varphi=\varphi_p-\alpha_{\delta\varphi}\,\frac{1}{R\tau}\left(\frac{\partial\bar{\psi}}{\partial x^2}\right)_p G/(\rho w^3)_p \tag{27}$$

The iteration procedure is done until the convergence criterion is reached.

Prescribed Streamline Method (PSLM). In this program the geometry of a streamline with the value of $\bar{\psi}_G$ and the velocity distribution on it are given. These data can be specified by the designer's experience. The mean-streamline [8] method inspired us to give the geometric form of a streamline and according to the blade thickness to specify its flow rate through unit area ρW_z, approximately. This is the first step of the calculation.

The next step is to solve the direct problem by assuming the primary geometric form of the suction and pressure surfaces.

The third step is to calculate the angular width of the blade cascade

$$\delta\varphi=\frac{1}{R\tau}\left(\frac{\partial\bar{\psi}}{\partial x^2}\right)_m G_0(\rho w^3)_G \tag{28}$$

where $(\partial\bar{\psi}/\partial x^2)_m$ is the first derivative of the stream function calculated from the direct problem solution and $(\rho w^3)_G$ can be calculated from the prescribed distribution of $(\rho W)_G$ on a given streamline. It is impossible from calculation to obtain the streamline whose coordinate position φ_m agrees with the given one φ_G in the first iteration. So, for the next iteration the

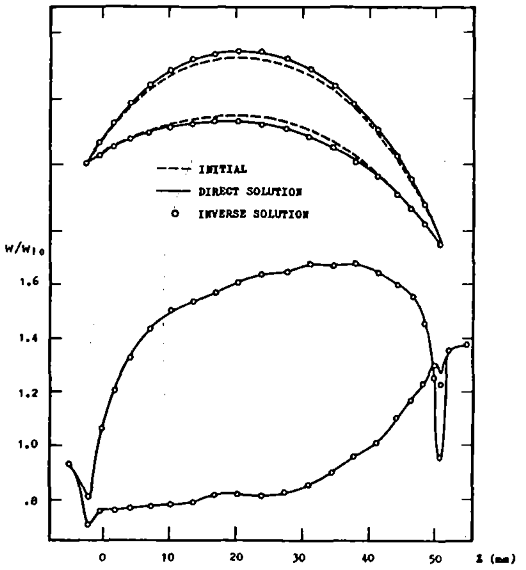

Fig. 1 Comparison between the results of inverse solution (SSAC) and of direct solution

pressure and suction surface geometries can be rearranged as follows

$$\left.\begin{aligned}\varphi_p^{(\nu+1)} &= \varphi_p^{(\nu)} + \alpha_p(\varphi_G - \varphi_m^{(\nu)}),\\ \varphi_s^{(\nu+1)} &= \varphi_p^{(\nu)} + \alpha_{\delta\varphi}\,\delta\varphi^{(\nu)}\end{aligned}\right\} \tag{29}$$

where α_p and $\alpha_{\delta\varphi}$ are the relaxation factors of the suction surface and the angular width of blade cascade channel, respectively. The iteration procedure is repeated until convergence is reached. This means that the coordinate positions of the calculated streamline and the given one agree with each other.

The principal advantage of this program is that it is not necessary to give the velocity distributions of suction and pressure surfaces, and the blade thickness requirement from cooling and structural stress design conditions is satisfied. For considering the viscous effect it is difficult to use the first program because the velocity on the surface is equal to zero, and it is impossible to satisfy the boundary condition of equation (5). The second program, i.e., PSLM, can be used to solve the viscous flow problem because of any streamline except the surface the boundary condition of equation (28) is satisfied. An example considering the viscous effect is also presented below.

Examples and Comparisons

The methods decribed have been used to calculate a number of blade cascades. Some of them are presented in this paper. The inverse problem solution may be verified by the direct problem solution, having exact results and being checked by experiment with the same blade cascade.

Turbine Blade Cascade Solved by SSAC Method. The first example shown below is for a turbine blade cascade having a pitch-chord ratio of $\bar{t} = 0.595$, inlet and outlet flow angles of $\beta_1 = -44.5$ deg, $\beta_2 = 57$ deg, respectively, Mach number of $M_1 = 0.3$ at inlet. Fixing the leading and trailing edge points from beginning to end the iteration procedure is carried on. The initial geometric positions of the suction and pressure surfaces are plotted as dotted curves in Fig. 1. Alternatively using the prescribed velocity distribution of the suction or pressure surfaces plotted by dotted curves the calculation is repeated from one iteration to the next. The calculated blade profile is shown by solid curves. The profile obtained by the present inverse method is close to the blade profile, whose velocity distributions are used for the present calculation. The velocity distributions shown by the solid curves are obtained by the direct solution method.

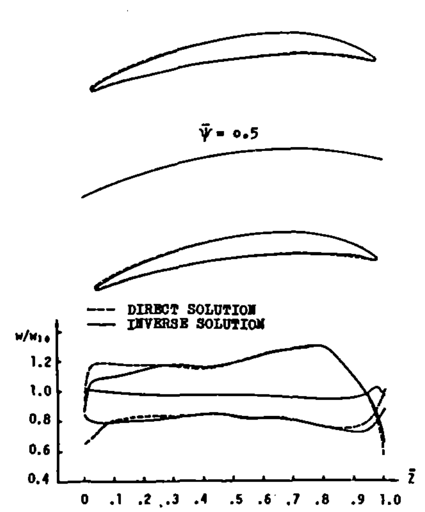

Fig. 2 Compressor blade profile obtained by inverse solution method

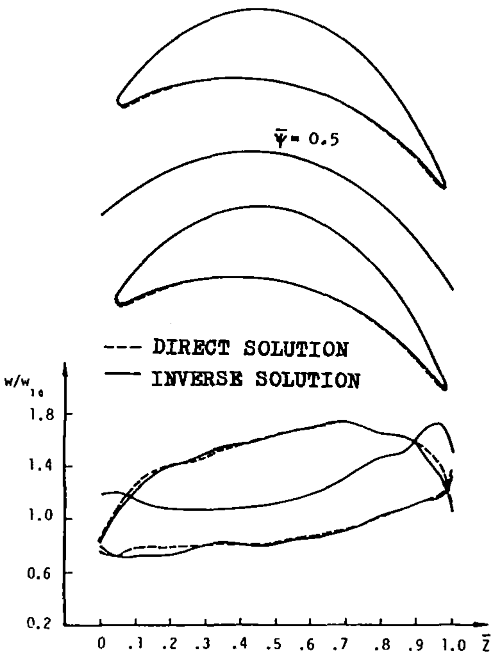

Fig. 3 Turbine blade profile obtained by inverse solution method

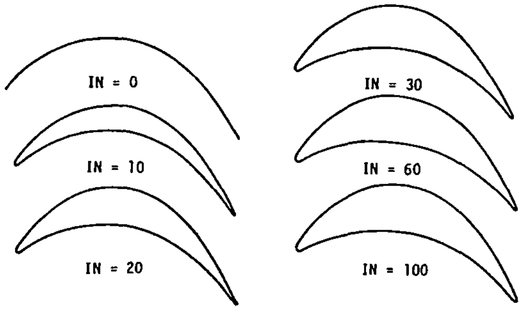

Fig. 4 Blade profiles of different iteration steps obtained by inverse solution

Compressor Blade Cascade. The prescribed streamline method (PSLM) is applied to this example. The inlet and outlet flow angles are $\beta_1 = -30$ deg and $\beta_2 = -1$ deg 8 min, respectively. The angular velocity of rotation is 1204.28 1/s. The velocity distribution of the mean streamline and its

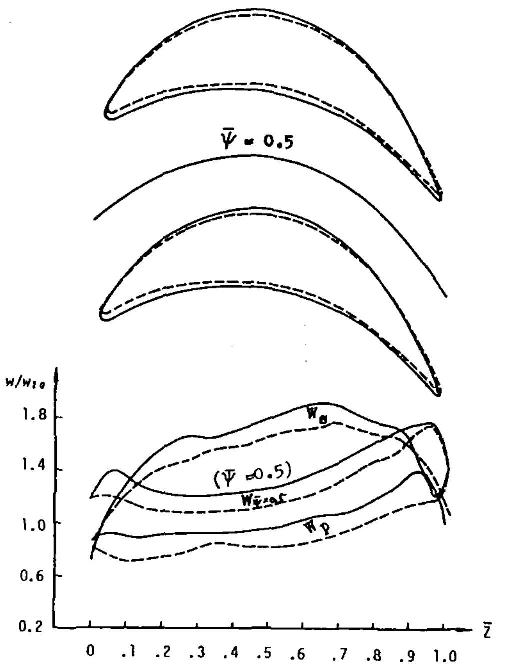

Fig. 5 Two blade profiles calculated with different prescribed velocity distribution on the streamline of $\bar{\psi} = 0.5$

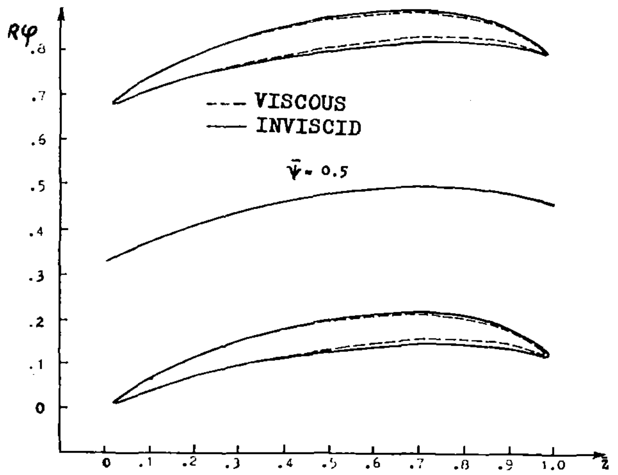

Fig. 6 Compressor blade cascade obtained by inverse solution (PSLM) with consideration of viscous effect

geometric position obtained by interpolation of direct solution of the blade cascade, which is shown by the dotted curves in Fig. 2, are employed as the given prescribed data for the present inverse solution.

The blade profile obtained by the present method is compared with the former one. Both blade profiles and their velocity distributions agree well with each other. There is a discrepancy between the two velocity distributions in the regions closing to the leading and trailing edges. The insufficient accuracy of interpolation in searching for a mean streamline and its velocity may be the reason for the abovementioned discrepancy. The proof is the result of the direct solution of the blade cascade obtained by the PSLM method.

Turbine Cascade. The same method as the latter example is adopted for this cascade. The solid curves in Fig. 3 represent the blade profile and its velocity calculated by PSLM. Different blade profiles, shown in Fig. 4, including the initial one, with its suction and pressure surfaces overlapped, describe the process of forming a blade profile by the iteration procedure. At the 100th iteration, the profile obtained is converged with $\epsilon_{\delta\varphi} = 10^{-4}$.

Effect of Velocity Distribution on the Prescribed Streamline. In Fig. 5 the dotted curves represent the former blade profile and its velocity distribution obtained from direct solution, and the solid curves represent the results calculated from the present inverse solution by making the velocity of the mean streamline higher than the former. The given prescribed geometric coordinates of the mean streamline for the inverse solution are the same as those of the direct solution. The calculated results have shown that the profile thickness is increasing. This means that the calculated channel width is decreasing when the given prescribed mean stream velocity is increasing.

Viscosity Effect. It is well known that the viscosity effect on the calculated results causes the velocity close to the wall to decrease rapidly and become zero at the wall.

The velocity distributions have the same values for both solutions, with and without consideration of viscosity. The Reynolds number has decreased to 2000 artificially to enlarge the viscosity effect. The calculated results have shown that the viscosity makes the blade thinner and the outlet geometric angle of the trailing edge greater. The blade profile obtained with consideration of viscosity is shown by the dotted curves in Fig. 6. The mean streamline is also shown in this figure.

Conclusion

The abovementioned two approaches of the numerical inverse solution method presented are general and can be directly applied to the design of the blade cascade on the stream surface of revolution. Because the blade cascade design is a very complex process, it is necessary to use the direct, inverse, and hybrid problem solution methods flexibly and alternately.

References

1 Chen Naixing and Li Weihong, "A New Method for Solving Aerodynamic Hybrid Problem of Profile Cascade on S_1 Stream Surface of Revolution by Employing Stream-Function Equation Expressed With Nonorthogonal Coordinate System," *Proceedings of International Conference on Inverse Design Concepts in Engineering Sciences (ICIDES)*, Oct. 17–18, 1984, Austin, TX.

2 Döge, R., "Über die Genauigkeit der Methoden zur Berechnung der Potentialstromung durch Schaufelgitter und ihre Brauchbarkeit in der Praxis," *Maschinenbautechnik*, No. 1, 1960.

3 Li Genshen, Chen Naixing, and Qiang Guofang, *Aero-Thermodynamics of Axial Turbomachinery of Marine Gas Turbine Engines—Principle Design and Experiment*, Vol. 1, Publishing House of Military Industry, Beijing, 1980.

4 Legendre, R., "Calcul d'un Profil Pour Ailette de Turbine à Partir d'un Hodograph," *La Recherche Aéronautique*, No. 84, 1961.

5 Legendre, R., "Traci des Ailettes Pour Fluides à Densité Legèrement Variable," *A.T.M.A.*, 1974.

6 Karadimas, G., "Increasing the Aerodynamic Loading of Axial Flow Turbines," ASME Paper No. 72-GT-78.

7 Schmidt, E., "Computation of Supercritical Compressor and Turbine Cascades With a Design Method for Transonic Flows," ASME Paper No. 79-GT-30.

8 Wu Chung-Hua and Brown, C. A., "A Theory of the Direct and Inverse Problems of Compressible Flow Past Cascade of Arbitrary Airfoils," *Journal Aero. Sci.*, Vol. 19, No. 3, Mar. 1952.

9 Wu Chung-Hua, "A Theory of the Direct and Inverse Problems of Compressible Flow Past Cascade of Arbitrary Blade Sections Lying in Arbitrary Stream Filament of Revolution in Turbomachine," *Scientia Sinica*, Vol. 8, No. 12, Dec. 1959, pp. 1529–1557.

10 Cai Ruixian, "The Analytical Solution of MSLM for 2-D Cascade," *Journal of Mechanical Engineering*, Vol. 14, No. 1, 1966.

11 Liu Gaolian and Tao Cheng, "A Generalized Solution Method for the Inverse and Hybrid Aerodynamic Problems of Airfoil Cascade on an Arbitrary Steamsheet of Revolution," *Power Engineering*, No. 2, 1981.

12 Liu Gaolian, "The Moment Function and Its Application to Inverse- & Hybrid-Aerodynamic Problems of Airfoil Cascades on a General Streamsheet of Revolution," *Journal of Engineering Thermophysics*, Vol. 3, No. 2, 1982.

13 Lu Gaolian, "New Solution Method of Some Hybrid Aerodynamic and Inverse Problems of Blade Cascade on Steamsheet of Revolution," *Journal of Engineering Thermophysics*, Vol. 4, No. 1, 1984.

14 Zou Zixiang and Gong Zhengjin, "An Inverse Problem Solution Method for Supercritical Cascade Flow and Its Extensive Application to Cascade Flow of Revolution," paper presented at 4th Conference of Society of Engineering Thermophysics, 1983.

15 Zhou Xinghai, Zhu Fangyuan, and Zhang Jin, "Finite Volume Method for Solving Inverse Problem of Transonic Cascade Flow," paper presented at 5th Conference of Society of Engineering Thermophysics, 1984.

16 Hua Yaonan and Chen Naixing, "Optimization of the Plane Compressor Blade Aerodynamic Design," *Proceeding of 6th ISABE*, Paris, France, 1983.

17 Dulikravich, G. S., *Proceedings of International Conference on Inverse Design Concepts in Engineering Sciences* (*ICIDES*), Oct. 17-18, 1984, Austin, TX.

18 Chen Naixing, "Application of Non-orthogonal Curvilinear Coordinates to Calculate the Flow in Turbomachines," *Journal of Engineering Thermophysics*, No. 2, 1981.

19 Wang Qinghuan and Chen Naixing, "Application of Non-orthogonal Curvilinear Coordinates to Calculate the Viscous Fluid Flow in Turbomachines," *Journal of Engineering Thermophysics*, No. 4, 1981.

20 Chen Naixing, "Some Problems in Viscous Gas Flow in Turbomachinery-Viscous and Heat-Transfer Terms and Methods for Solution of Basic Equations," *Scientia Sinica*, Ser. A, Nov. 1983.

21 Chen Naixing and Zhang Fengxian, "A Full Navier-Stokes Solution of Viscous Gas Flow Through Profile Cascade or S_1 Stream Surface of Revolution Employing Non-orthogonal Curvilinear Coordinates System," *Scientia Sinica*, Ser. A, No. 8, 1984.

22 Chen Naixing and Zhang Fengxian, "A Comparison Between Full and Simplified Navier-Stokes Equation Solution for Rotating Blade Cascade Flow on S_1 Stream Surface of Revolution," ASME Paper No. 85-GT-4.

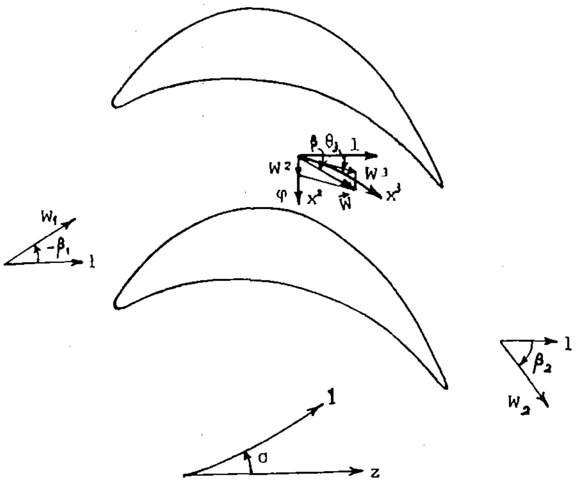

Fig. 7 Blade cascade on the blade-to-blade stream surface of revolution

APPENDIX

A blade cascade on the blade-to-blade stream surface of revolution is shown in Fig. 7. l denotes the coordinate axis of meridional direction, and it is a meridional projection of this stream surface with an angle of σ. x^2 and x^3 are noncoordinate axes. The angle between the x^3 axis and the meridional direction is denoted by θ_3. The angles θ and β_2 are coordinate angles between x^2 and x^3 axes and flow angle, respectively.

The principal schemes of computation for SSAC and PSLM methods are shown in Figs. 8 and 9.

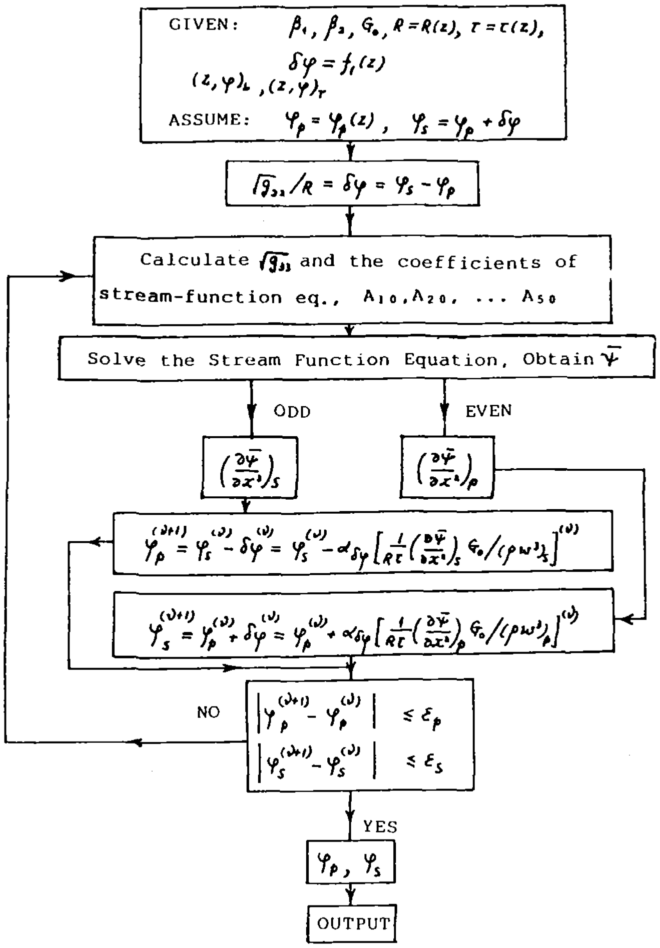

Fig. 8 Principal scheme of computation (SSAC)

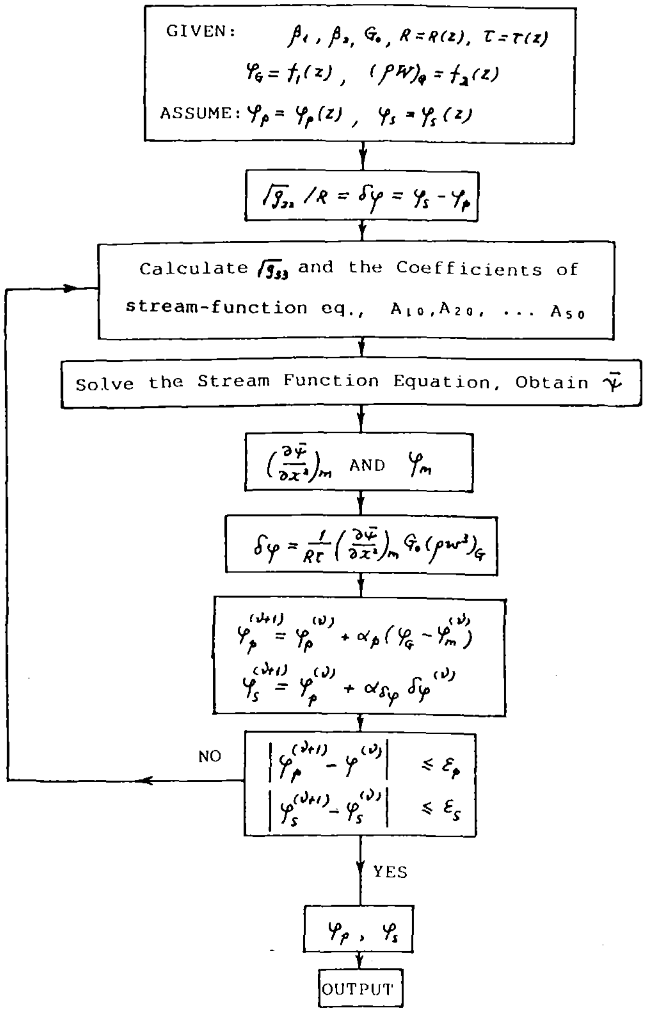

Fig. 9 Principal scheme of computation (PSLM)

A Method for Transonic Inverse Cascade Design With a Stream Function Equation

Ge Manchu

Lou Yiping

Yu Zhengti

Institute of Engineering
Thermophysics,
Academia Sinica,
Beijing, People's Republic of China

A new profile design method is developed on the basis of [1-3] *for transonic flow. The rotational dynamic stream function equation, which is expressed in functional form using calculated coordinates, is deduced. This method can be used for the calculation of cascade and S_1 stream surface of a transonic flow with a local shock wave on the blade suction surface. This method consists of two parts: an inverse method with a given velocity distribution along the suction surface and a given thickness distribution; and an inverse method with given velocity distributions on suction and pressure surfaces. Using this method it is easy to obtain a blade profile with prescribed velocity and thickness distributions. The design of optimal profile may then be done with the calculated optimal velocity distribution on the blade surface. The rotational condition is satisfied when the stream function equation is adopted with the entropy term. If the compatibility condition can be fulfilled between the S_1 and S_2 equations, the iterative calculations of two kinds of stream surfaces in three-dimensional flow will be convergent. In this paper a unique value of density can be determined from the known stream function value. The computational program is written with this method and several transonic examples have been calculated. These results are quite good.*

Introduction

With the development of high-performance turbomachines, the load-bearing capacity of the blade stage is getting higher and higher and the transonic flow begins to appear between the blades. When we design this kind of high-performance turbomachine, the design parameters must be determined carefully, so that the two basic demands of gas dynamic and strength performances must be satisfied. One of the main parameters, which determines the blade losses, is the velocity distribution on suction surface of blade. The other factor – the blade thickness – determines the strength of the blade. If these two factors are suitable, the performance of the turbomachine will be satisfactory.

In an ordinary turbomachinery design the blade profile is first selected, then the S_1 direct problem calculation is done for the given profile and the gas parameters are obtained between the blades. It is necessary to change the profile many times to get a reasonable velocity distribution on the blade suction surface, and skilled experience is necessary. It is difficult getting the prescribed velocity distribution on the blade suction surface with the above method. For this difficult problem, it is important to develop a new inverse problem solution. In the past few years, much progress has been made on the inverse problem [4-7]. The common feature of these works is that the stream and potential function coordinates were used for the dynamic equation. In [4, 5], a two-dimensional flow passage and a subsonic plane cascade have been calculated. The transonic cascade calculations are extended with these methods in [6, 7]. These papers developed the two-dimensional inverse problem method in an irrotational condition. There are some drawbacks to these methods. When the dynamic equation is solved in a three-dimensional flow design, the application of an entropy term is the common practice in the engineering design for the solution on the S_2 stream surface. In order that the compatibility condition can be satisfied between the S_1 and S_2 equations, the entropy term should be considered in the equation of the S_1 stream surface. If the compatibility condition is satisfied, the iterative calculations of two kinds of stream surfaces of three-dimensional flow will be convergent. This fact was clarified in [8, 9].

It is well known that the two main factors that affect the design performance are the velocity distribution on blade suction surface determining the gas dynamic performance and the thickness distribution, which determines the performance of the vibration and strength of blade. The main purpose of this paper is to develop a transonic solution method of the inverse problem, which is not limited by the irrotational flow condition, on plane or S_1 stream surface, so that the convergence of calculation of the three-dimensional flow field can be satisfied. For the demand of engineering design of turbomachines, it is important to develop a method by which the blade coordinates can be obtained with a given suction velocity and given thickness distributions. On the basis of this idea the partial differential equation, which is suitable to the rota-

---

Contributed by the Gas Turbine Division of The American Society of Mechanical Engineers and presented at the 31st International Gas Turbine Conference and Exhibit, Düsseldorf, Federal Republic of Germany, June 8-12, 1986. Manuscript received at ASME Headquarters February 10, 1986. Paper No. 86-GT-189.

tional flow, was developed with the main variable of the calculated coordinates. The new method used for engineering design was developed in the transonic condition. It can be simply explained as follows. Two accesses are included in it. One of them is the method which can control gas dynamic and strength performances directly with the given velocity and thickness distributions of blade. Another one is the method to obtain the profile coordinates with given velocity distributions on suction and pressure surfaces. These two methods are combined to obtain a complete calculation method of the inverse problem on plane cascade or to obtain a complete calculation method of the inverse problem on the S_1 stream surface. The velocity distributions, which satisfy prescribed gas dynamic performance, can be obtained on suction and pressure surfaces and the thickness distribution satisfying the demand of strength performance can be obtained also. Because the optimal velocity distribution can be chosen as the initial parameters known on the suction surface when the optimal velocity distribution has been calculated and a suitable thickness distribution can be obtained when the strength has been calculated, a satisfactory blade design will be obtained.

For the transonic calculation the artificial density method is used and a unique density value can be obtained for a stream function value in this paper. The program has been written for the transonic calculation of the inverse problem and several examples are calculated. Examples 1 and 3 are for turbine cascades, and the others are for compressor cascades. Compared with the calculated results of direct problem and experimental results, they are quite good. A more suitable velocity distribution of the suction surface is selected in example 3. Example 4 is the compressor blade. The non-shock wave velocity distribution is used instead of the initial distribution in which the local shock wave appeared. These calculated results show that this design method of inverse problem is successful. The blade profile can be obtained with the desired velocity and thickness distributions and this method is more time saving than the direct problem method.

Governing Equations

The main equation governing fluid flow is the dynamic equation on the plane or S_1 stream surface. The others are the continuity equation, the first law, and the second law of thermodynamics. The ordinary form of these equations can be taken from [1-3]. When the conditions of the inviscid relative steady flow, perfect gas, and adiabatic flow are satisfied, the dynamic equation can be obtained with nonorthogonal curvilinear coordinates. Using the geometric relation between tangent and normal direction vector of stream line, the relation between the velocity and normal direction vector on the stream line, and the partial derivative equation with respect to arbitrary coordinates along a stream surface, the dynamic component equations are obtained along the contravariant base vector $\mathbf{e}^i$, when the stream line coordinates are used

$$\mathbf{e}^1: w^3(\overline{w_{3,1}} - 2\omega^2\sqrt{g}) + \frac{1}{2} w_i w_k g^{ik}_{,3}\overline{x^3_{,1}} = \overline{I_{,1}} - T\overline{s_{,1}} - F_1 \tag{1a}$$

$$\mathbf{e}^2: w^3(\overline{w_{3,2}} + 2\omega^1\sqrt{g}) - w^1(\overline{w_{2,1}} - \overline{w_{1,2}} + 2\omega^3\sqrt{g}) + \frac{1}{2} w_i w_k g^{ik}_{,3}\overline{x^3_{,2}} = \overline{I_{,2}} - T\overline{s_{,2}} - F_2 \tag{1b}$$

$$\mathbf{e}^3: \frac{DW}{Dt} - 2w^1\omega^2\sqrt{g} + \frac{1}{2} w_i w_k g^{ik}_{,3} = F_3 \tag{1c}$$

where

$$\mathbf{F} = -\frac{1}{n_3}\left(\frac{1}{\rho} p_{,3} - (\omega)^2 r\cdot r_{,3}\right)\mathbf{n}$$

The dynamic equation expressed in stream function form was obtained and shown in [3] using the definition of the stream function and the continuity equation. When the definition of covariant metric tensors and the relation between the physical length of line and the arbitrary curvilinear coordinates are adopted, the dynamic component equations were

Nomenclature

$A1, A2, A3, A4, A5, A6, A1', A2', A3'$ = dynamic equation coefficients
$B2, B3, B_{jk}, C_{mj}, D_{nk}, D_{mj}, D_{nk}, E1, E2, E3$ = equation coefficients
$\mathbf{e}^i$ = contravariant base vector
$\mathbf{e}_i$ = covariant base vector
$\mathbf{F}$ = force vector of stream surface
g = determinant of metric tensors
g^{ij} = contravariant metric tensor of the three-dimensional space
g_{ij} = covariant metric tensor of the three-dimensional space
H = stagnation enthalpy
I = stagnation rothalpy
M = Mach number
$\mathbf{n}$ = stream surface unit normal vector
n_i = covariant component of vector $\mathbf{n}$
p = pressure
r = radius
s = entropy or length of line
t = time or blade pitch
T = temperature
$\mathbf{V}$ = absolute velocity vector
$\mathbf{W}$ = relative velocity vector
w^i = contravariant component of $\mathbf{W}$
w_i = covariant component of $\mathbf{W}$
x^i = arbitrary curvilinear coordinate
Z = number of blades
β = angle between direction of fluid flow and axial
δ = thickness of blade along x^2
θ = angle between coordinates x^1 and x^2
μ = coefficient
ν = iterative number
ρ = density
$\tilde{\rho}$ = artificial density
τ = normal distance between two adjacent stream surfaces
$\tilde{\tau}$ = $\tau\sqrt{g}\rho$
ϕ = angle between axial and x^i coordinate
ψ = stream function
ω^i = contravariant component of angular velocity vector

Superscripts

$\overline{}$ = on stream surface

Subscripts

$,i$ = partial derivative with respect to x^i
$;i$ = covariant derivative with respect to x^i
1 = inlet of calculated region
2 = outlet of calculated region

derived with the form of the partial derivative along a stream surface. A component equation is written along the lines of $\mathbf{e}^2$ with nonorthogonal curvilinear coordinates

$$A1\overline{(r\varphi)_{,11}}+A2\overline{(r\varphi)_{,12}}+A3\overline{(r\varphi)_{,22}}+A4\overline{(r\varphi)_{,1}} \\ +A5\overline{(r\varphi)_{,2}}=A6 \tag{2}$$

where

$$A1 = \sqrt{g_{22}}$$

$$A2 = \begin{cases} -2\sqrt{g_{11}-1}-\dfrac{n_1n_2}{n_3n_3}\dfrac{1}{\sqrt{g_{22}}} & (\theta_{12}\le 90 \text{ deg}) \\[2ex] 2\sqrt{g_{11}-1}-\dfrac{n_1n_2}{n_3n_3}\dfrac{1}{\sqrt{g_{22}}} & (\theta_{12}> 90 \text{ deg}) \end{cases}$$

$$A3 = \left[g_{11}+\left(\frac{n_1}{n_3}\right)^2\right]/\sqrt{g_{22}}$$

$$A4 = \begin{cases} \sqrt{g_{11}-1}\left[\overline{(\ln \tau\rho)_{,2}}-\dfrac{\overline{\psi_{,22}}}{\overline{\psi_{,2}}}\right] & (\theta_{12}\le 90 \text{ deg}) \\[2ex] -\sqrt{g_{11}-1}\left[\overline{(\ln \tau\rho)_{,2}}-\dfrac{\overline{\psi_{,22}}}{\overline{\psi_{,2}}}\right] & (\theta_{12}> 90 \text{ deg}) \end{cases}$$

$$A5 = \begin{cases} -\sqrt{g_{11}-1}\ \overline{(\ln \tau\rho)_{,1}} & (\theta_{12}\le 90 \text{ deg}) \\ \sqrt{g_{11}-1}\ \overline{(\ln \tau\rho)_{,1}} & (\theta_{12}> 90 \text{ deg}) \end{cases}$$

$$A6 = \Bigg\{-\bar{\tau}\Bigg[2\omega\left(\frac{n_1}{n_3}\cos\phi_1\sqrt{g_{22}}+\frac{n_2}{n_3}\cos\phi_2\sqrt{g_{11}}\right) \\ +\frac{1}{w^1}(\overline{I_{,2}}-\overline{Ts_{,2}})\Bigg]+\left[1+\left(\frac{n_1}{n_3}\right)^2\right]\overline{\psi_{,22}}\Bigg\}/\overline{\psi_{,2}} \\ -\overline{\left(\frac{n_1n_2}{n_3n_3}\right)_{,1}}+2\frac{n_1}{n_3}\overline{\left(\frac{n_1}{n_3}\right)_{,2}}+\frac{n_1n_2}{n_3n_3}\overline{(\ln \tau\rho)_{,1}} \\ -\left[1+\left(\frac{n_1}{n_3}\right)^2\right]\overline{(\ln \tau\rho)_{,2}}$$

Calculated Region, Boundary Condition, and Solution

In order that the profile calculation of blade can be used for the engineering design, a calculation method of a profile design was developed in this paper. There are two steps in this method. First step is the method which can control the gas dynamic and strength performances of blade directly and conveniently. For this purpose it should be necessary to control the velocity distribution on the suction surface of blade and to control the thickness distribution. The velocity distribution of suction surface was one of the main factors which affect the gas dynamic performance. If the selection of the profile is not suitable, the shock wave may appear and the blade losses will rise. The velocity distribution on the suction surface must be controlled so as to control the blade losses effectively. Obviously, the strength can be satisfied effectively when the thickness distribution is obtained from calculation of the strength and vibration. In the first step we wish to obtain the profile coordinates when the velocity distribution of the suction surface and the thickness distribution are given, and to obtain a satisfactory velocity distribution on the pressure surface and pressure distributions on blade surfaces. If the velocity distribution of the pressure surface does not satisfy the demand of design it is necessary to develop a calculation method of second step, that is, the profile coordinates can be obtained when the velocity distributions are given on the suction and pressure surfaces.

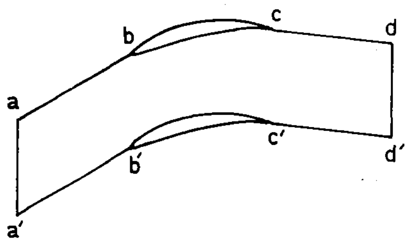

Fig. 1 Calculated region on physical surface

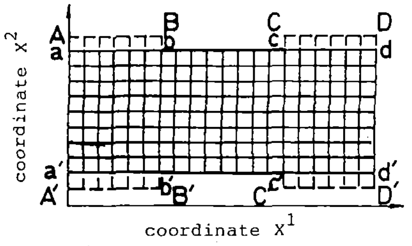

Fig. 2 Coordinates and nets on calculated surface

The calculated region is shown in Figs. 1 and 2. It includes the inlet region, blade region, and outlet region and is surrounded by lines *abcdd'c'b'a'a*. Line *aa'* is the inlet side upstream. Lines *ab* and *a'b'* are two stream lines in the inlet region. Lines *bc* and *b'c'* are solid wall boundaries, that is, pressure surface and suction surface of blade. Lines *cd* and *c'd'* are two stream lines in the outlet region. Line *dd'* is the outlet side.

Boundary Conditions. In the calculation of the first step, the boundary condition is given as follows:

On the inlet side (line *aa'*), the parameters M_1, β_1, p_1^0, and T_1^0 are given. At the outlet, on the line *dd'*, flow angle β_2 is given. The periodicity condition is used on stream lines *ab*, *a'b'*, *cd*, and *c'd'*. On the suction surface the second kind of boundary condition is adopted

$$\frac{\overline{\partial(r\varphi)}}{\partial x^2}=\frac{\dfrac{\overline{\partial\psi}}{\partial x^2}\sqrt{g_{11}}}{\bar{\tau}\sqrt{g}\,|\mathbf{W}_{sj}|} \tag{3}$$

Using a given thickness distribution the first kind of boundary condition is used

$$(r\varphi)_n=(r\varphi)_1+t-\delta_j \tag{4}$$

When the second kind of boundary condition is adopted at inlet and outlet sides, the mathematical problem is complete.

In calculating the second step, the second kind of boundary condition is used on the suction and pressure surfaces of blade. Equation (3) is applied. At all the boundaries the second kind of boundary condition is adopted except the boundary of periodicity condition on lines *ab*, *a'b'*, *cd*, and *c'd'*. This problem is also complete.

The Method of Solution. After the partial differential equation and the boundary condition are determined, the numerical calculation can be done. First the difference equation must be derived. For this reason the calculated grids are given in the calculated region, then for every grid point equation (2) is dispersed and the continuous field is changed into a dispersed field. The difference equation can be obtained using the central difference scheme for the partial derivative of variable of coordinates at every grid point. The difference equations are written as follows

$$E1_{jk}^{(n)}(r\varphi)_{j\,k-1}^{(n+1)}+E2_{jk}^{(n)}(r\varphi)_{jk}^{(n+1)}+E3_{jk}^{(n)}(r\varphi)_{j\,k+1}^{(n+1)}=B_{jk}^{(n)} \tag{5}$$

where

$$E1_{jk} = A2\bullet C_{2j}\bullet C_{1k}+A3\bullet D_{1k}+A5\bullet C_{1k}$$

$$E2_{jk} = A1\bullet D_{2j}+A2\bullet C_{2j}\bullet C_{2k}+A3\bullet D_{2k}+A4\bullet C_{2j} \\ +A5\bullet C_{2k}$$

$$E3_{jk} = A2 \bullet C_{3k} \bullet C_{2j} + A3 \bullet D_{3k} + A5 \bullet C_{3k}$$

$$\begin{aligned} B_{jk} = {} & A6 - \sum_{n=1,3} A2[C_{1j} C_{nk} (r\varphi)_{\substack{j-1 \\ k+n-2}} \\ & + C_{3j} \bullet C_{nk} (r\varphi)_{\substack{j+1 \\ k+n-2}}] - (A1 \bullet D_{1j} + A4 \bullet C_{ij})(r\varphi)_{\substack{j-1 \\ k}} \\ & - (A1 \bullet D_{3j} + A4 \bullet C_{3j})(r\varphi)_{\substack{j+1 \\ k}} \end{aligned}$$

On one of the x^2 coordinates there are N calculated points which are selected by calculating demand. Then $N-2$ tridiagonal difference equations are obtained. The other two supplemental equations are obtained using the boundary condition on the blade surfaces and the geometric relation. There are N equations for N unknown variables, so that the group of difference equations is solvable.

For first step calculation one of the supplemental equations is

$$E1_{j1}(r\varphi)_{j1} + E2_{j1}(r\varphi)_{j2} + E3_{j1}(r\varphi)_{j3} = B_{j1} \qquad (6)$$

where

$$B_{j1} = \frac{(C_{31}\psi_{j1} + C_{32}\psi_{j2} + C_{33}\psi_{j3})(\sqrt{g_{11}})_{j1}}{(\tilde{\tau}\sqrt{g}\,|\mathbf{W}_s|)_{j1}}$$

Equation (4) is another supplemental equation. For second step calculation the conditions of known velocity are used on the suction and pressure surfaces. Equation (6) is adopted on the suction surface. On the pressure surface the following equation is derived

$$E1_{jN}(r\varphi)_{jN} + E2_{jN}(r\varphi)_{jN-1} + E3_{jN}(r\varphi)_{jN-2} = B_{jN} \qquad (7)$$

where

$$B_{jN} = \frac{(C_{3N}\psi_{jN} + C_{3N-1}\psi_{jN-1} + C_{3N-2}\psi_{jN-2})(\sqrt{g_{11}})_{jN}}{(\tilde{\tau}\sqrt{g}\,|\mathbf{W}_s|)_{jN}}$$

When transonic flow appears in the calculated region the artificial density is used. The equation for artificial density is

$$\tilde{\rho}_{jK} = \rho_{jk} - \mu_{jk}\left[\left|\frac{W_1}{W}\right|(\rho_{jk} - \rho_{j-1k}) + \left|\frac{W_2}{W}\right|(\rho_{jk} - \rho_{jk-1})\right] \qquad (8)$$

where

$$\mu_{jk} = \max\{(\mathrm{M}^2 - 1)c, 0\}$$

The coordinates x^1 are selected as stream lines in this paper. Formula (8) is changed to

$$\tilde{\rho}_{jk} = \rho_{jk} - \mu_{jk}(\rho_{jk} - \rho_{j-1k}) \qquad (9)$$

Since the coordinates x^1 are stream lines and the main variable is expressed with the coordinates in the dynamic equation, the calculation of the artificial density is very easy and the central difference scheme can be used for all calculated points. The numerical calculation is as simple as in the subsonic condition.

As we know, there is a difficult problem in solution of density by the stream function. There are two values of density for one value of the stream function, as shown in [3]. It is necessary to give a known velocity value or a density value on a coordinate x^2 in order to obtain a unique value of density for a known value of the stream function when the velocity gradient form of dynamic equation is used. The velocity is given as a known value on the blade surface for the inverse problem discussed in this paper. The density can be obtained from the first law of thermodynamics and the state equation on the blade surface

$$\rho = \rho^0 \left(\frac{H - |\mathbf{V}^2|/2g_c}{H}\right)^{\frac{1}{k-1}} e^{\frac{\Delta S}{R}} \qquad (10)$$

The dynamic equation is adopted along the coordinate x^2 with the form of velocity gradient

$$A2'\overline{w^1_{,1}}/2 + A3'\overline{w^1_{,2}} + B2w^1 = B3 \qquad (11)$$

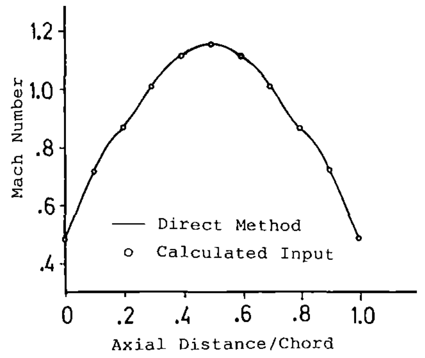

Fig. 3 Suction surface Mach number distribution (example 1)

where

$$B2 = A3'_{,2} + A2'_{,1}/2$$

$$\begin{aligned} B3 = {} & A1'\overline{w^2_{,1}} - A2'\overline{w^2_{,2}}/2 + (A1'_{,1} + A2'_{,2}/2)w^2 \\ & - 2\sqrt{g}\left[\omega^3 - \omega^1\left(\frac{n_1}{n_3}\right) - \omega^2\left(\frac{n_2}{n_3}\right)\right] + (\overline{I_{,2}} - T\overline{s_{,2}})/w^1 \end{aligned}$$

The coefficients $A1'$, $A2'$, and $A3'$ were explained in [3]. By this equation the velocity values are solved and obtained at every grid point on every x^2 line, and a unique density value is obtained for a given stream function value. Ambiguous double values of density are avoided.

Solution Procedure and Calculated Results

The following method has been developed for obtaining a suitable blade surface velocity distribution and blade thickness distribution with these equations as mentioned above. At first the inlet gas dynamic parameters p_1^0, T_1^0, M_1, and β_1 are given and β_2 is given at the outlet side in order that the requirement of circulation can be satisfied. Then the velocity (or Mach number) distribution on the suction surface, the blade thickness distribution, and the initial profile are given. The initial calculation nets are calculated. At the same time the initial density and entropy are given at every grid point. The stream filament form and thickness are given for the calculation of the S_1 stream surface. The differential coefficients, metric tensors, equation coefficients $A1$–$A6$, and the difference equation coefficients $E1$, $E2$, $E3$, and B are obtained. The tridiagonal equations give the new coordinates of the grid points. The abovementioned procedure is repeated when the coordinates and density have been relaxed. When the results converge the first step calculation is finished. In this case, when the Kutta conditions have not yet been satisfied at the trailing edge, the velocity distribution on suction surface and the thickness distribution have to be adjusted. Through the calculation of examples 1 and 2 satisfactory velocity distributions can be obtained on the suction surface and the satisfactory thickness distributions are also obtained. However, the velocity distributions are not good on the pressure surface. The detailed results are shown as follows.

In example 1 the blade is a typical impulsive turbine blade. At the inlet side $\mathrm{M}_1 = 0.575$, $\beta_1 = 46.123$ deg, $p_1^0 = 126{,}780$ N/m², $T_1^0 = 288$ K, and at the outlet side $\beta_2 = -46.123$. The solidity $b/t = 0.5259$. The velocity distribution on the suction surface and the thickness distribution are taken from [3]. They are obtained using the direct problem method. The velocity distribution is shown in Fig. 3 on the blade surfaces. In Fig. 4 the blade coordinates are expressed. The calculated results are shown in the same figure when the first step method is used.

In example 2 the T1-(18A6I46)08 blade profile is adopted. The parameters $\mathrm{M}_1 = 0.823$, $\beta_1 = 30$ deg, $p_1^0 = 126{,}780$ N/m²,

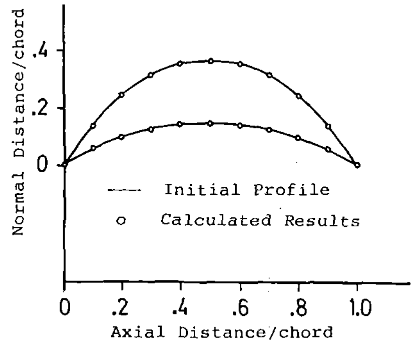

Fig. 4 Blade profile (example 1)

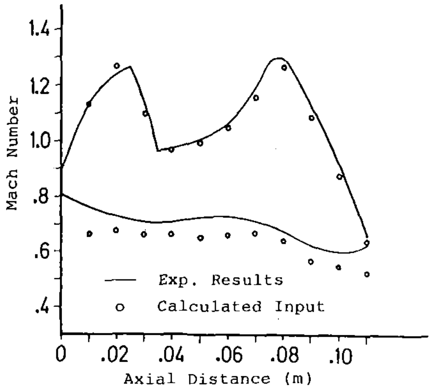

Fig. 5 Surface Mach number distribution (example 2)

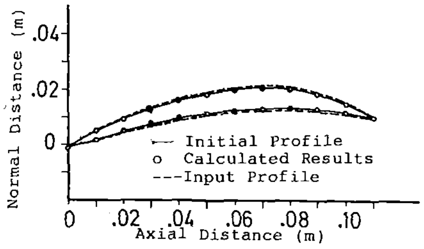

Fig. 6 Blade profile (example 2)

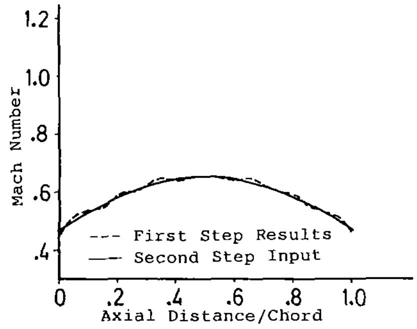

Fig. 7 Pressure surface Mach number distribution (example 1)

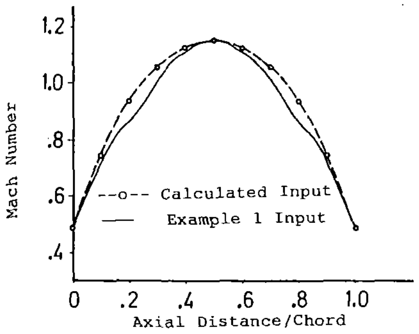

Fig. 8 Suction surface Mach number distribution (example 3)

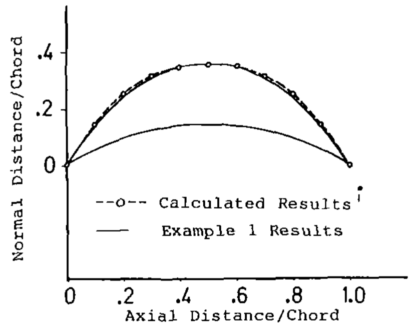

Fig. 9 Blade profile (example 3)

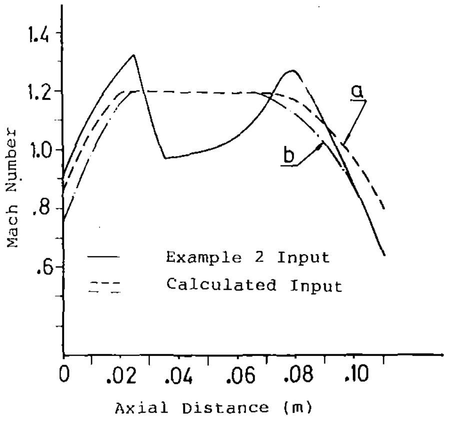

Fig. 10 Suction surface Mach number distribution (example 4)

$T_1^0 = 288$ K, and $\beta_2 = -20$ deg are given. The velocity distribution of the suction surface is shown in Fig. 5. The initial given profile and calculated results are shown in Fig. 6. In this figure, the solid lines mean the initial given profile (the blade coordinates). The dotted lines, which are the input coordinates of the blade in calculation, are the new input blade profile (considered the boundary layer). We adopted the integral equation to calculate the thickness of the boundary layer. The calculation, which is a close approximation to the real viscous flow phenomenon, offered the best result compared with experiment.

From Fig. 7 we know that the calculated velocity distribution is not good on the pressure surface for example 1. The velocity rises and falls. It is obvious that the blade thickness distribution affects the velocity distribution of the pressure surface. It is difficult to get the required velocity distribution on the suction surface when the adjustment of blade thickness distribution is used. Based on the first step calculation, for overcoming this difficulty it is necessary to continue the second step calculation. The velocity distribution on the pressure surface should be adjusted as the input datum in the calculation of the second step; this is shown in Fig. 7. The input velocity distribution on the suction surface is given and the value of it is the same as the given value in first step calculation. The new profile coordinates are obtained when the calculation of the second step is accomplished and the Kutta condition is satisfied. If the maximum change of the coordinate from the first step calculation to the second step is larger than the predetermined value $\Delta(r\phi)$, the blade thickness or velocity of pressure surface distributions must be adjusted and the above calculations must be repeated. The calculation is reiterated until satisfactory results are obtained.

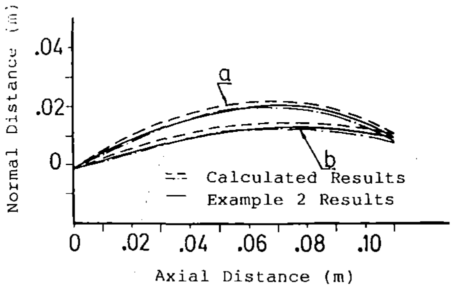

Fig. 11 Blade profile (example 4)

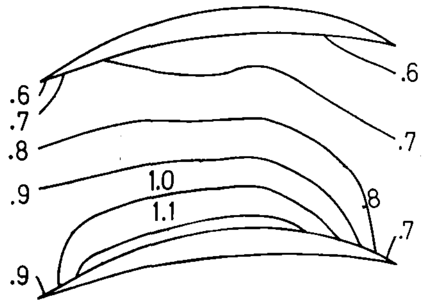

Fig. 12 Mach number contours (example 4*b*)

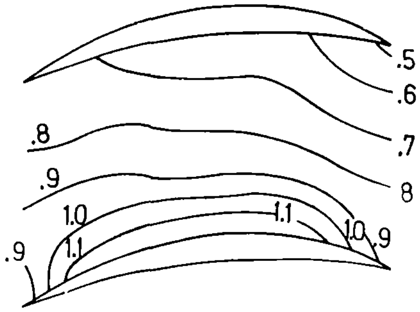

Fig. 13 Mach number contours (example 4*a*)

In example 3 the input velocity distribution of the blade suction surface is adjusted and is shown in Fig. 8. The parameters given are the same as those used in example 1. The calculated results are shown in Fig. 9. The maximum coordinate change is 0.6×10^{-5} m from the first step calculation to the second step. The results are satisfactory for the engineering design. In example 4 the velocity distributions on the suction surface are changed from a solid line into lines a and b and are shown in Fig. 10. The parameters given are the same as those used in example 2. The obtained profile coordinates are plotted in Fig. 11. The Mach number contours are presented in Figs. 12 and 13, and it is clear that the Kutta condition can be satisfied by adjusting the velocity distribution.

Conclusions

A new calculation method, suitable for engineering design, is developed in the inverse problem method. A blade profile with the prescribed velocity distribution of blade surface and the blade thickness distribution can be obtained. Therefore the design demands for the gas dynamic and strength performances can be satisfied.

This method can be used for the cascade calculation of transonic flow when there is the local shock wave on the blade suction surface.

The stream function dynamic equations are deduced with the main variable of coordinates and they are useful for obtaining the blade coordinates quickly and easily. These are general equations with nonorthogonal curvilinear coordinates and with the entropy term included.

The calculated results show quite good agreement with experiments and with results of the direct problem mode by examples 1 and 2. The method is effective and successful.

It is obvious that the velocity and thickness distributions can be controlled directly and easily with this method. In examples 3 and 4 the optimal velocity distribution can be used and the optimal blade design may be obtained.

This method can be applied to three-dimensional calculations. If the change of entropy is included, convergent results will be obtained in the iterative calculation of two kinds of stream surface. It is clear that the good results will be obtained because the compatibility is attained between the equations on S_1 and S_2 surfaces.

Ambiguous double values of density are avoided. When the velocity distribution is given on the blade surface in calculation, a unique value of density is determined from the known value of the stream function on the blade surface. Then the values of density are uniquely determined for every coordinate x^2.

References

1 Wu Chung-Hua, "A General Theory of Three-Dimensional Flow in Subsonic and Supersonic Turbomachines of Axial, Radial, and Mixed-Flow Types," *Trans. ASME*, Vol. 74, Nov. 1952; NACA TN 2604, 1952.

2 Wu Chung-Hua, "Three-Dimensional Turbomachine Flow Equations Expressed With Respect to Non-orthogonal Curvilinear Coordinates and Method of Solution," presented at the 3rd International Symposium on Air Breathing Engines, Munich, Mar. 1976.

3 Ge Manchu, "A Stream Function Relaxation Method for Solving Transonic S_1 Stream Surface With Non-orthogonal Curvilinear Coordinates," *Chinese J. of Engineering Thermophysics*, Vol. 5, No. 2, 1984.

4 Stanitz, J. D., "Design of Two-Dimensional Channels With Prescribed Velocity Distribution Along the Channel Walls," NACA Rep. 1115.

5 Silvesten, M. E., and Fitch, C. M., "Matrix Methods for the Design of Cascades to Prescribed Surface Velocity Distribution and for Fully Compressible Flow," Sp 304 N75-11174.

6 Schmidt, E., "Computation of Supercritical Compressor and Turbine Cascades With a Design Method for Transonic Flow," ASME Paper No. 79-GT-30, 1979.

7 Gong Zengjin and Zou Zixiang, "A Transonic Calculating Method of Inverse Problem in Cascades," *Chinese J. of Numerical Calculation and Computer Application*, Vol. 4, 1983.

8 Zhu Genxing, Ge Manchu, and Wu Chung-Hua, "Three-Dimensional Subsonic Flow Through a Stator by the Use of a Central S_2 Stream Surface and Several S_1 Stream Surfaces of Revolution," *Chinese J. of Engineering Thermophysics*, Vol. 4, No. 2, 1983.

9 Ge Manchu, Lou Yiping, and Yu Zhengti, "Gas Dynamic Design and 3-D Flow Computation of the Two-Stage Power Turbine," Report of Chinese Engineering Thermophysics Institute, 1983.

Navier-Stokes Solutions of Unsteady Flow in a Compressor Rotor

J. N. Scott
University of Dayton,
Dayton, OH

W. L. Hankey, Jr.
Wright State University,
Dayton, OH

In order to achieve more accurate predictions of unsteady flow in a transonic compressor rotor an existing numerical approach has been modified by incorporating a turbulence model. The computations are performed by solving the complete time-dependent compressible Navier–Stokes equations using MacCormack's explicit finite difference algorithm. These equations are solved for the flow through two adjacent rotor blades at a streamsurface near the blade tip subjected to the wakes emitted from upstream stators. At this radial location the flow enters the blade passage at an absolute Mach number of 0.66. The high blade curvature at this radial location produces a large region of separated flow on the suction surface with laminar flow. To more accurately resolve the features of this flow separation the Baldwin–Lomax algebraic eddy-viscosity turbulence model is incorporated into the numerical procedure in regions near the blade surface. The unsteady flow features are represented at the inflow boundary through the use of characteristic variables involving the upstream and downstream running Riemann invariants and the entropy variation expressed in terms of the total pressure profile. At the outflow boundary the concept of a "second throat" or choke point is implemented in conjunction with supersonic outflow conditions. The results are compared with numerical results obtained without the use of a turbulence model (laminar) for a single blade passage. Improved agreement with limited experimental data is also noted.

Introduction

Analysis of unsteady flow in turbomachinery continues to be one of the most difficult and challenging problems in internal flows. Many propulsion systems utilize a supersonic or transonic compressor in which the relative Mach number of the flow entering the blade passage is supersonic while its axial component is subsonic. As a result of the supersonic relative flow entering the blades, a complex system of shock and expansion waves is present in the blade passage. The presence of these waves along with their interaction with the viscous flow in the boundary layer results in performance degradation. In addition, these features are influenced by the unsteady flow due to the wakes from upstream stators and inlet guide vanes. In order to achieve a better understanding of the interaction between the unsteady and viscous-inviscid effects in the compressor, the use of the time-dependent compressible Navier–Stokes equations is indicated.

In recent years significant progress has been achieved in the numerical simulation of unsteady flow in turbomachinery. Recently Mitchell [1] and Hodson [2] have extended Denton's method [3] to investigate the unsteady inviscid interaction of upstream wakes on a moving blade row. To simulate the unsteady flow entering the computational domain Hodson formulated inflow boundary conditions in which he specified the stagnation temperature (assumed constant in the wake relative reference frame), the relative flow angle (α), and the mass flow per unit area (ρu). The wake is accounted for by moving a velocity profile containing the wake defect across the inflow boundary at the relative blade speed.

Janssens and Hirsch have utilized finite element methods to treat boundary conditions in developing a procedure for computing viscous-inviscid interactions in cascades, accounting for large separated boundary layer regions and correcting for Coriolis and centrifugal effects on turbulence [4]. Calvert [5] has also developed a viscous-inviscid interaction method based on Denton's time marching technique to investigate the steady flow in several transonic compressor cascades. His results show the presence of strong shock waves and regions of separated flow for certain configurations.

There has also been progress toward the solution of the time-dependent viscous flow in turbomachinery components. Patched and overlaid grids have been developed for use in conjunction with the thin-layer Navier–Stokes equations to simulate relatively low-speed unsteady flow in an axial turbine configuration [6]. In addition, there have been recent advances in the analysis of time-dependent flow in a supersonic compressor rotor [7]. This analysis accounts for the unsteady flow produced by wakes from the upstream stator and inlet guide vane by specifying the stagnation pressure profile at the inflow boundary. This stagnation pressure profile which is ob-

---

Contributed by the Gas Turbine Division of THE AMERICAN SOCIETY OF MECHANICAL ENGINEERS and presented at the 31st International Gas Turbine Conference and Exhibit, Düsseldorf, Federal Republic of Germany, June 8–12, 1986. Manuscript received at ASME Headquarters February 14, 1986. Paper No. 86-GT-226.

tained from experimental data, is used to develop boundary conditions based on characteristic variables. With this formulation the unsteady behavior occurs in the form of an entropy wave where entropy is one of the characteristic variables. This formulation also accounts for the velocity defect in the wakes from the upstream stator and inlet guide vane. The downstream boundary condition is based on the concept of a boundary region which incorporates a throat or choke point as a means of controlling the back pressure at the trailing edge of the blades. This approach permits the use of the "nonreflective" supersonic outflow boundary conditions at the outflow plane while allowing the unsteady fluctuations to occur more naturally in the subsonic flow at the trailing edge at the blades.

The primary objective of the present effort is to obtain improved resolution of the viscous-inviscid interaction and in particular to more accurately model the unsteady behavior on the suction surface of the blades. To accomplish this, the Baldwin-Lomax algebraic eddy-viscosity turbulence model is incorporated into the computational procedure in regions near the blade surfaces. The implementation of the turbulence model also required that grid refinement be performed placing more grid points in the boundary layer regions.

The computations for the present work are performed for a stream surface at approximately 90 percent of the blade span of a high-performance transonic compressor rotor being developed in the Air Force Aero Propulsion Laboratory at Wright-Patterson Air Force Base. The blade geometry for this rotor is shown in Fig. 1. The computation accounts for a streamtube contraction of about 38 percent through the blade passage. The current results are compared with those from previous computations and qualitatively with experimental observations.

Governing Equations

Since the flow in a supersonic compressor rotor contains complex viscous-inviscid interaction including shock waves, boundary layers, flow separation, and unsteady phenomena, a numerical solution of the Navier-Stokes equations is required to accurately simulate the flow behavior. Thus, the complete time-dependent compressible Navier-Stokes equations are solved using an adaptation of a computer code developed by Shang [8, 9]. Variations of this code have been applied successfully for internal flows in ducts [10], thus it seems appropriate for the present application. The governing equations are written in two-dimensional rectangular Cartesian coordinates as

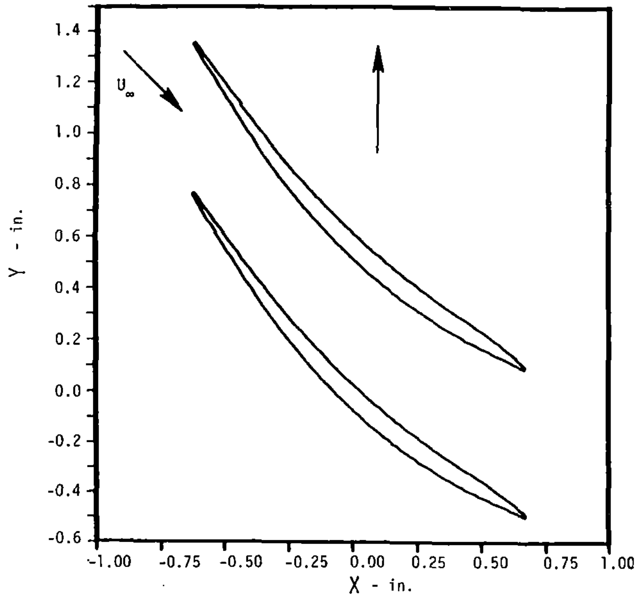

Fig. 1 Compressor rotor blade geometry

$$\mathbf{U}_t + \frac{1}{\delta}\begin{pmatrix}\zeta_x\\ \zeta_y\end{pmatrix}\left(\frac{\partial \mathbf{E}}{\partial\zeta}, \frac{\partial \mathbf{F}}{\partial\zeta}\right) + \begin{pmatrix}\eta_x\\ \eta_y\end{pmatrix}\left(\frac{\partial \mathbf{E}}{\partial\eta}, \frac{\partial \mathbf{F}}{\partial \eta}\right)=0 \qquad (1)$$

where the dependent variables are given by

$$\mathbf{U} = \begin{bmatrix}\rho\\ \rho u\\ \rho v\\ \rho e\end{bmatrix} \qquad (2)$$

The flux vectors are the Cartesian components of the continuity, momentum, and energy equations

$$\mathbf{E} = \begin{bmatrix}\delta\rho u\\ \delta\rho u^2 - \sigma_{xx}\\ \delta\rho uv - \tau_{xy}\\ \delta\rho ue - \delta u\sigma_{xx} - v\tau_{xy} - \dot{q}_x\end{bmatrix} \qquad (3)$$

Nomenclature

c = speed of sound
e = specific energy
E, F = vector fluxes in mean flow equations
i, j = indices for grid point location
k = thermal conductivity
K_i = characteristic variables
L = characteristic length (blade chord)
n = time index
p = pressure
R = gas constant, radius
t = time
T = temperature
U = dependent variable
u, v = velocity components
w = wheel speed
x = axial coordinate
y = tangential coordinate
α = stator flow angle
β = damping factor
γ = ratio of specific heats
δ = streamtube contraction factor
ζ, η = transformed coordinates
θ = azimuthal angle
λ = $-2/3\ \mu$, second viscosity coefficient
μ = molecular viscosity coefficient
ρ = density
σ_{xx}, σ_{yy} = normal stresses
τ_{xy} = shear stress
ω = vorticity

Subscripts

∞ = free-stream condition (annulus velocity)
w = wall condition
$\mathrm{JL}_{\max}$ = maximum value
$\mathrm{KL}_{\min}$ = minimum value
L = lower surface
0 = stagnation value
s = stator coordinate frame
u = upper surface

$$\mathbf{F}=\begin{bmatrix}\rho v\\ \rho uv-\tau_{xy}\\ \rho v^2-\sigma_{yy}\\ \rho ve-v\sigma_{yy}-u\tau_{xy}-\dot{q}_y\end{bmatrix} \quad (4)$$

The components of the stress tensor are given by

$$\sigma_{xx}=(2\mu+\lambda)\frac{\partial u}{\partial x}+\lambda\frac{\partial v}{\partial y}-p \quad (5)$$

$$\sigma_{yy}=(2\mu+\lambda)\frac{\partial v}{\partial y}+\lambda\frac{\partial u}{\partial x}-p \quad (6)$$

$$\tau_{yx}=\tau_{xy}=\mu\left(\frac{\partial u}{\partial y}+\frac{\partial v}{\partial x}\right) \quad (7)$$

$$\dot{q}_x=k\frac{\partial T}{\partial x} \quad (8)$$

$$\dot{q}_y=k\frac{\partial T}{\partial y} \quad (9)$$

δ = streamtube contraction factor $1-\sum_{n=1}^{4} a_n x^n$

Expressed in this form minor deviations in flow area due to contraction in the third dimension may be approximated. Sutherland's viscosity equation, the equation of state, and the Prandtl number are specified to close the system of equations.

In order to optimize numerical resolution and simplify the boundary conditions the governing equations are transformed to a body oriented coordinate system. Equation (1) is expressed in the transformed coordinates where the transformation is given by

$$\zeta=\zeta(x,y)$$

$$\eta=\eta(x,y)$$

where the transformed coordinate $\eta = 0$ line represents the upper surface of the lower blade and the η = JL line is the lower surface of the upper blade. In the streamwise direction the transformed coordinate $\zeta = 0$ line is the inflow boundary and the ζ = KL line is the outflow boundary. The two-dimensional grid is established between two adjacent rotor blades and is extended upstream to a point near the trailing edge of the upstream stator and downstream to a point well beyond the leading edge of the trailing stator. The grid boundaries extending upstream of the leading edge are tangent to the upper surface while the grid boundaries extending downstream of the trailing edge are tangent to the lower surface. The grid points are clustered adjacent to the boundaries which contain the blade surfaces in order to achieve the necessary resolution of the flowfield in the boundary layer regions. This clustering is produced by an exponential stretching function with a controlling exponent k as described in [8].

The physical finite difference mesh for the rotor cascade is shown in Fig. 2. This grid consists of 60 points in the streamwise direction and 46 points in the transverse or tangential direction.

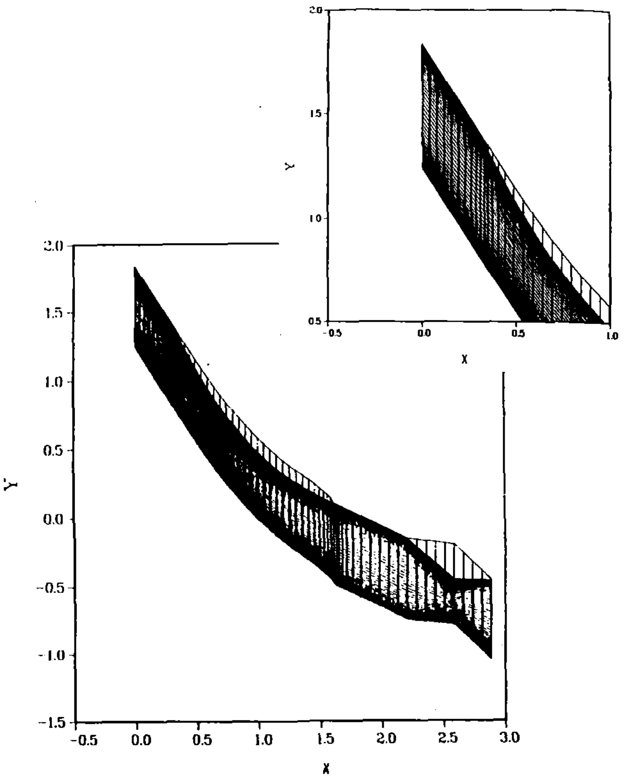

Fig. 2 Rotor mesh

Turbulence Model

The turbulence is simulated by the algebraic eddy-viscosity model developed by Baldwin and Lomax [11]. This turbulence model is incorporated into the computational procedure only in regions near the blade surfaces, since use of a steady flow turbulence model throughout the entire computational domain would tend to damp the unsteady flow oscillations unrealistically. The procedure used for the present calculations assumes the presence of two layers. The Prandtl–Van Driest formulation is used for the inner layer

$$\epsilon_i=\rho l^2|\omega| \quad (10)$$

where

$$l=ky[1-\exp(-y^+/A^+)]$$

$|\omega|$ is the magnitude of the vorticity

$$|\omega|=\left|\frac{\partial u}{\partial y}-\frac{\partial v}{\partial x}\right|$$

and

$$y^+=\frac{\sqrt{\rho_w\tau_w}}{\mu_w}y$$

y is the distance normal to the blade surface, $A^+ = 26$ is the sublayer thickness, $k = 0.40$ is the von Karman constant, and the subscript w denotes values at the blade surfaces.

The model switches from the Van Driest formulation to the formulation for the outer region at the smallest value of y for which the inner and outer values of the eddy viscosity are equal (i.e., $\epsilon_i \geq \epsilon_0$). The formulation for the outer layer is given by

$$\epsilon_0=\rho K C_{\mathrm{cp}} F_{\max} y_{\max} F_{\mathrm{KLEB}} \quad (11)$$

where $F_{\max} = y_{\max}\,|\omega|\,[1-\exp(-y^+/A^+)]$; $y_{\max}$ is the value of y at which $F_{\max}$ occurs; $F_{\mathrm{KLEB}} = [1 + 5.5\,(C_{\mathrm{KLEB}} \cdot y/y_{\max})^6]^{-1}$; $K = 0.0168$; $C_{cp} = 1.6$; and $C_{\mathrm{KLEB}} = 0.3$.

The turbulence calculation is initiated at a streamwise location just upstream from the separation point observed in the laminar computations [7]. While the incorporation of this turbulence model should give improved results, it is still inadequate for accurate prediction of the flow details. To resolve a turbulent boundary layer the first point should be within the laminar sublayer. An examination of the current results in-

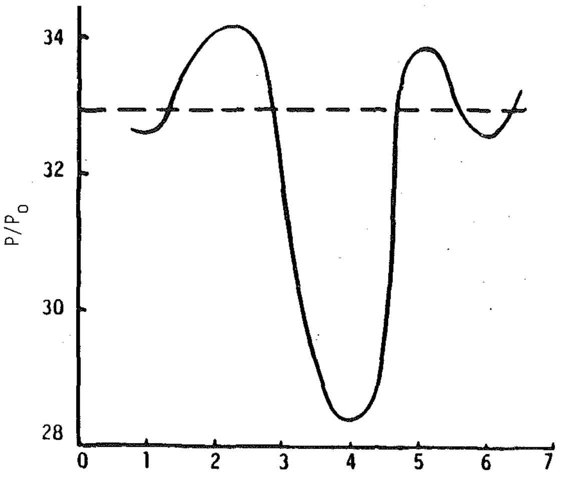

Fig. 3 Time-varying total pressure profile at leading edge of blade passage

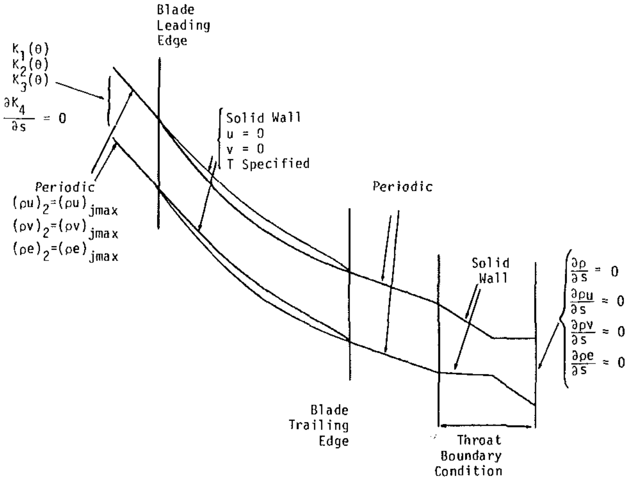

Fig. 4 Boundary conditions

dicated that the first point from the blade surface was nominally at a y^+ of 30, which marginally meets this criterion.

The Baldwin-Lomax turbulence model was developed for steady flow computations. There is still a need for an "unsteady turbulence" model which models only the fine-scale and does not suppress the large-scale fluctuations which are paramount to this case.

Numerical Procedure

The flowfield being investigated has a Reynolds number of 1.85×10^6 based on a blade chord. The dominant fluctuations in this case are due to the interaction of the rotor with the stator wakes. These fluctuations have a frequency of approximately 18.4 kHz, giving a characteristic time of 5.4×10^{-5} s. To achieve the temporal resolution for the high-frequency oscillations, MacCormack's explicit and unsplit finite difference scheme [12] is appropriate for the present study. This algorithm has been used successfully for a wide range of external and internal flows involving unsteady phenomena [8-10]. The computer code used in this program is a degenerate version of a three-dimensional code developed by Shang [8, 9] for operation on a vector processor. This algorithm requires a combination of alternating forward and backward differences for the predictor and corrector sweeps. This is accomplished by using a different indexing procedure for the predictor and corrector sweeps. These two steps are defined in general by

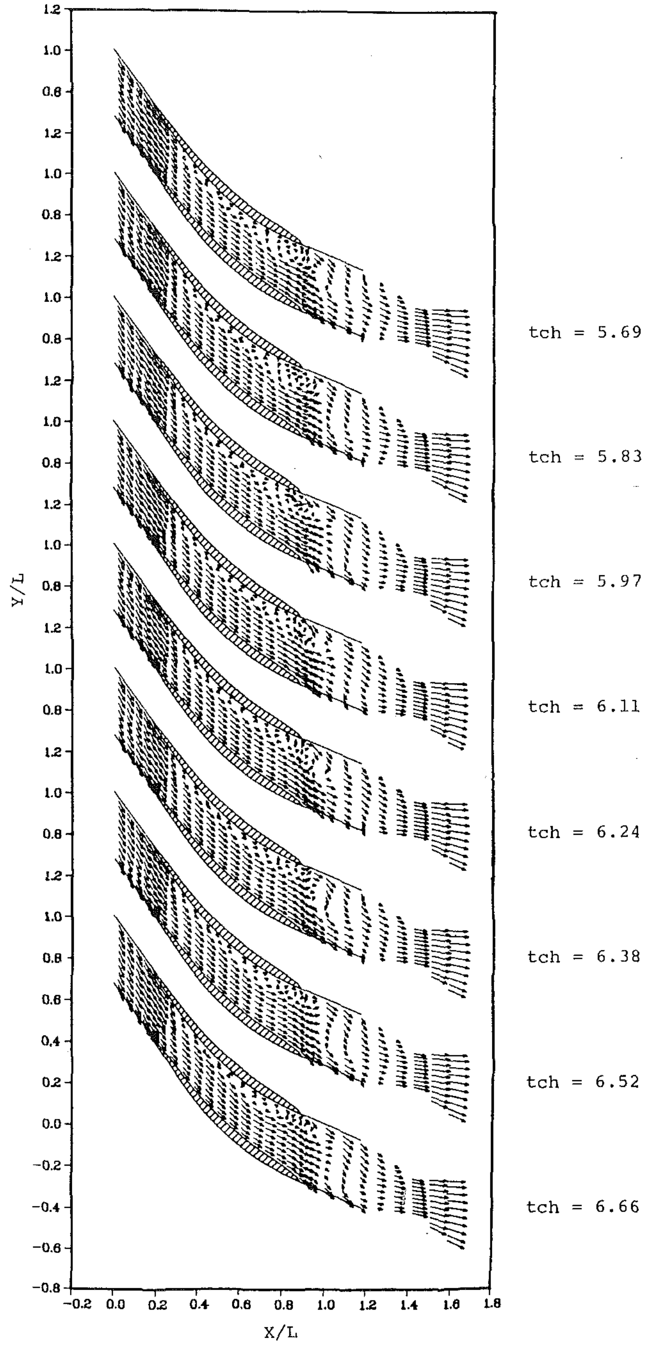

Fig. 5 Velocity vectors for laminar computation

$$U_{i,j}^{\overline{n+1}} = U_{i,j}^n - \frac{\Delta t}{\Delta x}(E_{i+1,j}^n - E_{i,j}^n) - \frac{\Delta t}{\Delta y}(F_{i,j+1}^n - F_{i,j}^n) \quad (12)$$

$$U_{i,j}^{n+1} = 1/2\Big\{U_{i,j}^n + U_{i,j}^{\overline{n+1}} - \frac{\Delta t}{\Delta x}\Big(E_{i,j}^{\overline{n+1}} - E_{i-1,j}^{\overline{n+1}}\Big) - \frac{\Delta t}{\Delta y}(F_{i,j}^{\overline{n+1}} - F_{i,j-1}^{\overline{n+1}})\Big\} \quad (13)$$

The efficiency of the code is maximized utilizing the CFL condition on allowable time increment for generalized coordinates as reported by Shang [9]

$$\Delta t_{\mathrm{CFL}} = 1/\Big\{\frac{\bar u}{\Delta\eta} + \frac{\bar v}{\Delta\zeta} + c\Big[\Big(\frac{\eta_x}{\Delta\eta} + \frac{\zeta_x}{\Delta\zeta}\Big)^2 + \Big(\frac{\eta_y}{\Delta\eta} + \frac{\zeta_y}{\Delta\zeta}\Big)^2\Big]^{1/2}\Big\} \quad (14)$$

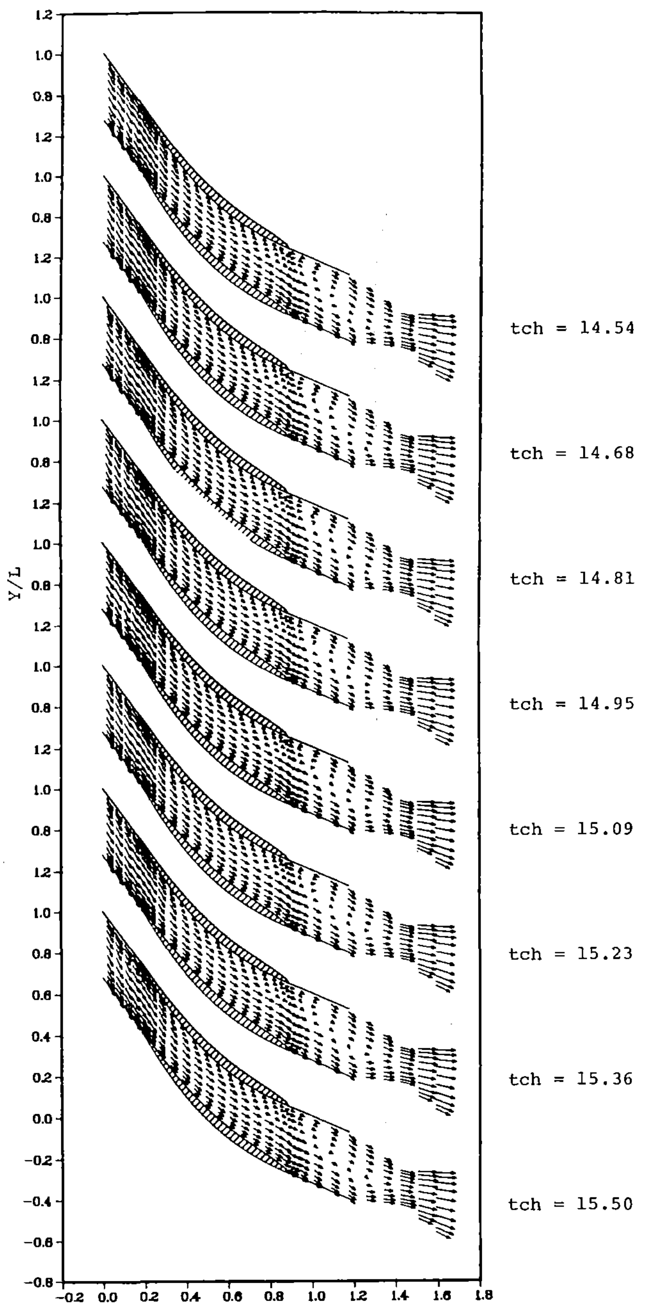

Fig. 6 Velocity vectors for turbulent computation

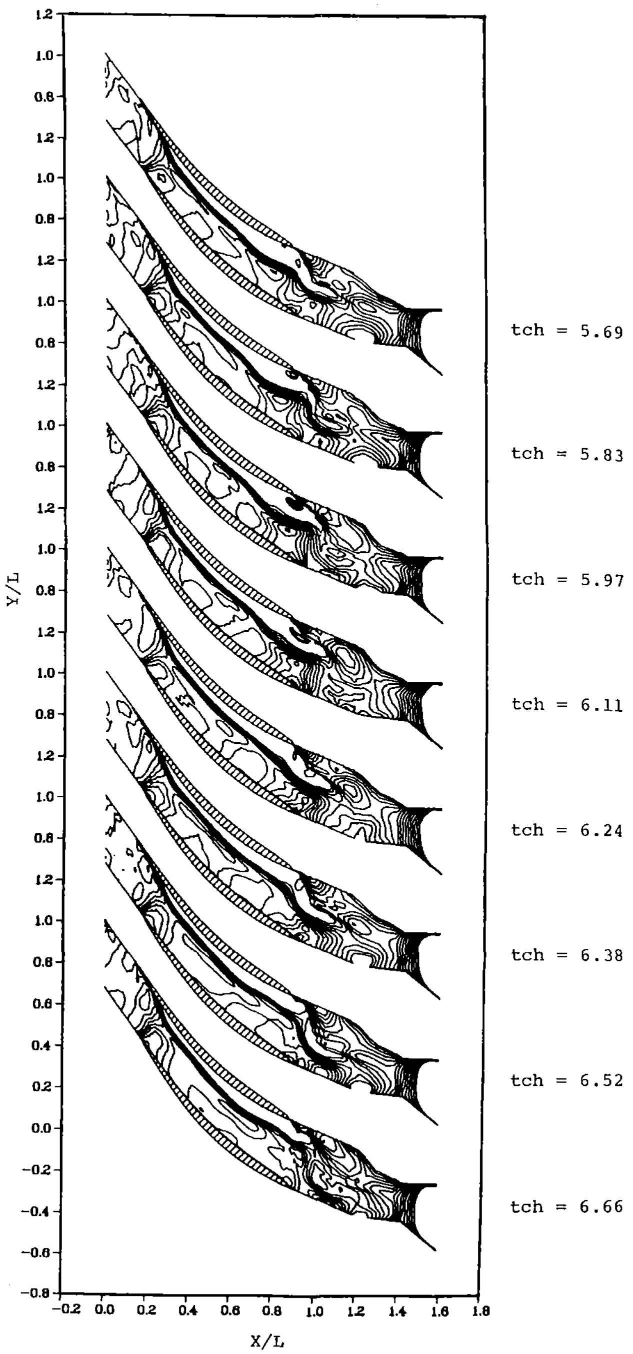

Fig. 7 Mach contours for laminar computation

with the contravariant velocity components defined as

$$\tilde{u} = \zeta_x u + \zeta_y v \tag{15}$$

$$\tilde{v} = \eta_x u + \eta_y v \tag{16}$$

The CFL numbers used in the present investigation vary from 0.15 to as high as 0.85, although most of the calculations have been made using a CFL number of 0.8. This value seems to provide stable results in a reasonable computational time.

Numerical damping is also used in the present analysis in order to suppress numerical oscillations. Again the form of the damping terms is reported by Shang [9]. These damping or artificial viscosity terms are implemented in each sweep direction. They are

$$\beta \Delta t \Delta \eta^3 \{ |\tilde{u}| + (\eta_x^2 + \eta_y^2)^{1/2} c \} \frac{1}{p} \left| \frac{\partial^2 p}{\partial \eta^2} \right| \tag{17}$$

$$\beta \Delta t \Delta \zeta^3 \{ |\tilde{v}| + (\zeta_x^2 + \zeta_y^2)^{1/2} c \} \frac{1}{p} \left| \frac{\partial^2 p}{\partial \zeta^2} \right| \tag{18}$$

In the present analysis the value of the damping constant (β) used is 2.

For steady inflow conditions the computations were performed for 6400 time steps which corresponds to about 8.9 characteristic times based on chord length L divided by the upstream free-stream velocity. This required about 3.5 hr of CYBER 845 computer time. The computations using the time-dependent inflow conditions were carried out to 6000 time steps at which point the turbulence model was implemented and the computation was continued to 11,500 time steps to ensure that a limit cycle was realized. This corresponds to about 16 characteristic times based on (L/U_∞).

Boundary Conditions

The formulation and implementation of appropriate boundary conditions for unsteady flow continues to be an area of major concern in treating internal flows. Of particular interest are the treatment of inflow and outflow boundaries. Recently, an approach has been developed which has been used successfully in computing unsteady flow in turbomachinery [7, 13]. This approach which uses characteristic variables [14] has been used in the present investigation:

(*a*) The value of $P_0(\theta)$ shown in Fig. 3 was obtained from experimental measurements made downstream of the stator and upstream of the rotor.

(*b*) The stator exit flow angle α was assumed to be constant.

(*c*) The total temperature T_0 was measured and assumed to be constant.

(*d*) The gradient of the second Riemann invariant was assumed to be zero.

From these assumptions the values of K_i may be determined

$$K_1(\theta)=\frac{P_0}{\rho_0^\gamma}=\frac{(RT_0)^\gamma}{P_0^{\gamma-1}}=\frac{p}{\rho^\gamma}=\text{entropy profile}$$

$$K_2(\theta)=u\tan\alpha=v$$

$$K_3(\theta)=\frac{p}{\rho_\infty c_\infty}+u$$

$$\frac{dK_4}{dx}(\theta)=\frac{\partial}{\partial x}\left(\frac{p}{\rho_\infty c_\infty}-u\right)=0 \tag{19}$$

where $u(\theta)=\cos\alpha\sqrt{[2\gamma/(\gamma-1)]R\;T_0}\;[(p/P_0)^{(\gamma-1/\gamma)}-1]^{1/2}$ = velocity defect, obtained using isentropic relationships.

$$\frac{P_0}{p}=\left[1+\frac{\gamma-1}{2}M^2\right]^{\gamma/\gamma-1} \tag{20}$$

$$u^2+v^2=\frac{\gamma R\;T_0}{\dfrac{\gamma-1}{2}+\dfrac{1}{M^2}} \tag{21}$$

α = stator flow angle. These four conditions may be manipulated to obtain the values of primitive variables exiting the stator: p_1, ρ_1, u_1, v_1.

The upstream values in the rotor reference frame (which is where the computation takes place) are obtained by merely adding the wheel speed to the transverse velocity: p_1, ρ_1, u_1, v_1+w.

Downstream. Great difficulty has been experienced by the CFD community in computing flows in short channels with subsonic outflow. This is especially true for unsteady flows in which it is intuitively unnatural to specify any flow quantity as being fixed at the outflow boundary unless that boundary is placed at downstream infinity. The difficulty was overcome in this study by inserting a convergent-divergent "second throat" at the exit. In this manner supersonic outflow may be achieved, which is known to produce no numerical difficulty. To obtain a desired downstream pressure the "second throat" area may be adjusted as follows:

Recall from shock relationships

$$\frac{P_{t_2}}{P_{t_1}}=\frac{A_1^*}{A_2^*} \tag{22}$$

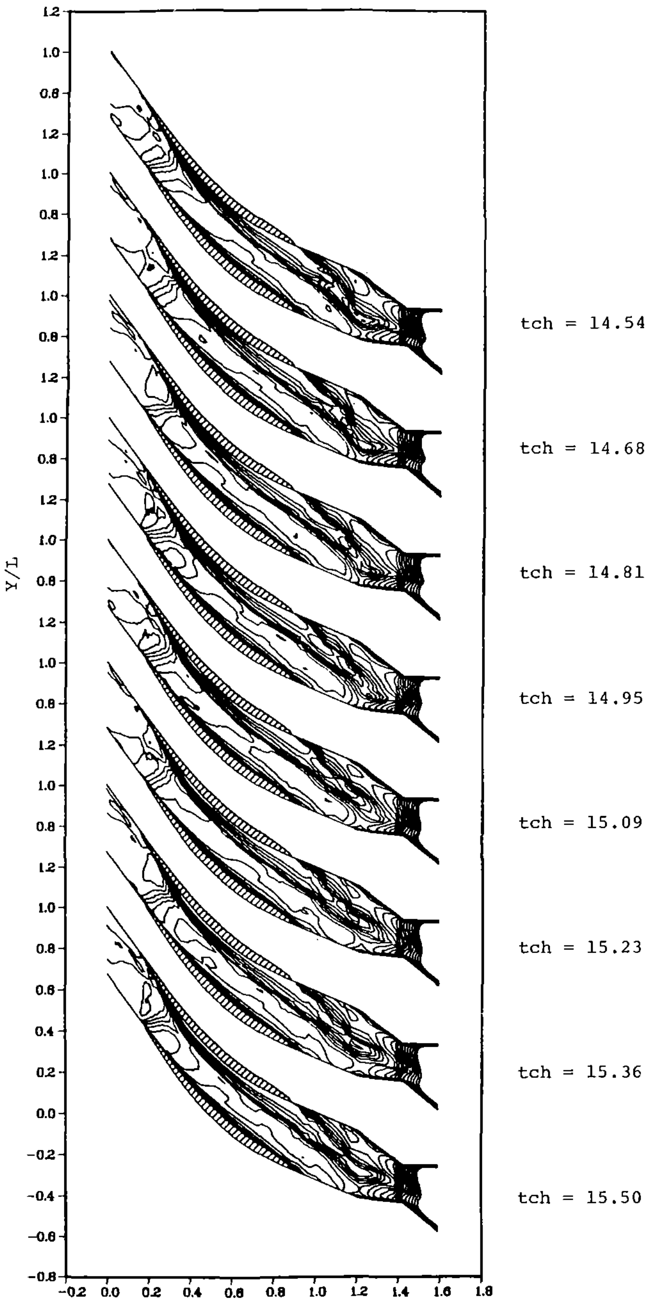

Fig. 8 Mach contours for turbulent computation

With the implementation of the "second throat" the outflow boundary conditions are simply

$$\frac{dU}{dx}=0$$

where U is given in equation (2).

While this approach is still not a true simulation of the downstream boundary, i.e., stator blade row, it provides a more accurate representation of the physical situation than imposing a constant variable, such as static pressure at the outflow boundary.

Lateral Boundaries. Periodic boundary conditions are imposed upstream and downstream of the leading and trailing edges of the outermost blades. At the blade surfaces no slip, no through flow, and a specified wall temperature are imposed. These conditions along with the inflow and outflow boundary conditions are shown in Fig. 4.

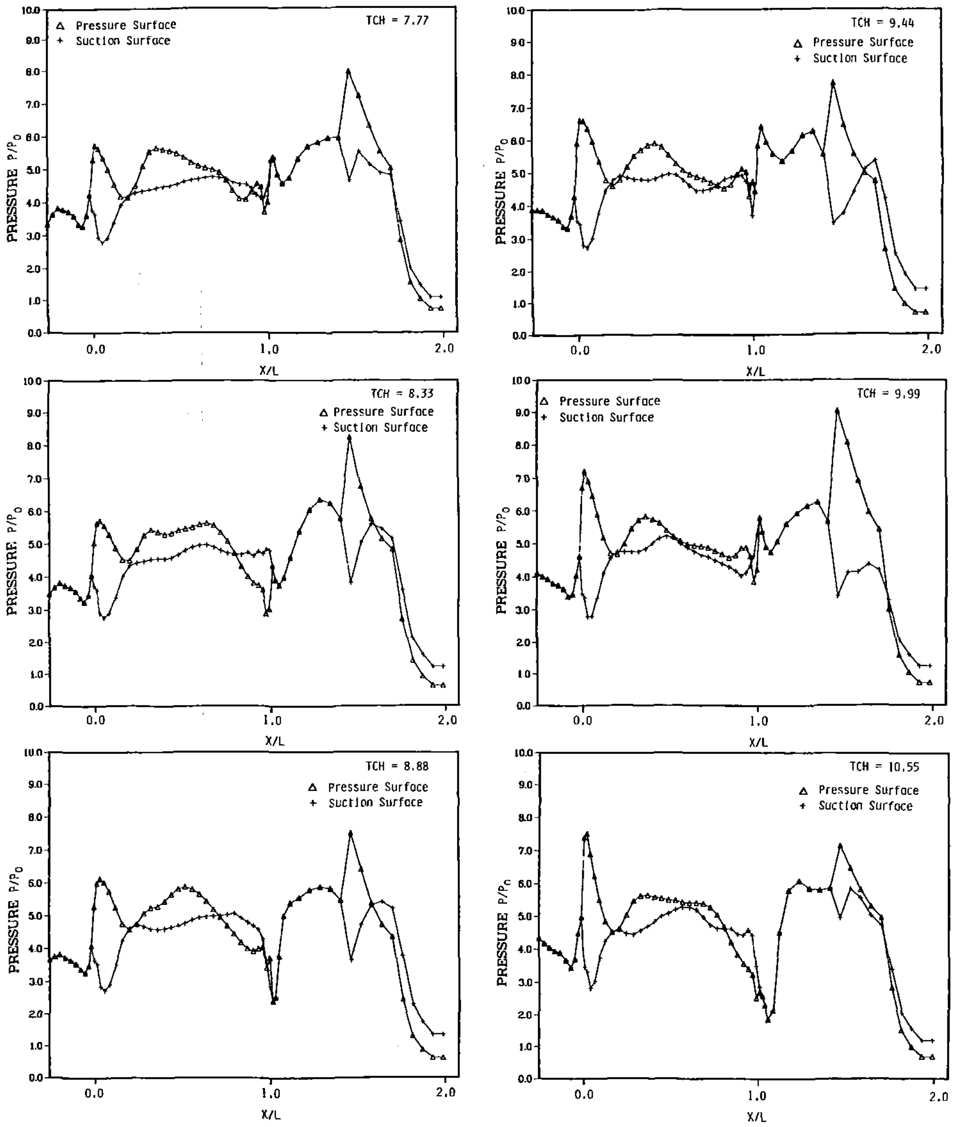

Fig. 9 Blade surface pressure variation with time: laminar case

Results

In this investigation the computations are carried out initially for flow through two adjacent blades in a transonic compressor rotor having a relative inflow Mach number of 1.33 and a relative inflow angle of 61 deg from the axial direction. This particular rotor has a subsonic axial velocity component with a Mach number of 0.66.

The primary goals of the work described in this paper are to determine the influence of a turbulence model on the unsteady flow through the compressor rotor. Initially unsteady laminar computations were performed for flow through a single blade passage with attention focused on the large region of separated flow on the suction surface of the blade [7]. The presence of separated flow in such regions has been noted by other researchers in previous efforts [4, 5]. However, these investigations treated only steady flows. The extent of the separation for the laminar computation from [7] is shown in velocity vectors in Fig. 5. A careful examination of this flow separation reveals the formation of a vortex on the suction surface. This vortex is ultimately shed and migrates through the blade wake region in the direction opposite to the rotation of the blades. Figure 6 shows velocity vectors for the unsteady flow using the Baldwin-Lomax turbulence model incorporated into the computation. These velocity vectors show that the incorporation of the turbulence model diminishes the extent of the flow separation significantly. In fact, the region which was separated in the laminar computation has become primarily a region of very low-speed flow with only a small separation occurring very near the trailing edge of the blade on the suction surface. Although much smaller than in the laminar case, a vortex is shed from the trailing edge and migrates through the wake region in much the same fashion as for the laminar computation.

The Mach contours also display a number of the unsteady flow features. From the results of [7], the Mach number contours show the oscillatory behavior of the oblique shock wave at the blade leading edge (Fig. 7). It is also noted from this figure that the shock wave impinges on the suction surface boundary layer in the region where the onset of separation seems to occur. The oscillatory growth and decay of the separation near the blade trailing edge are also seen in this figure. Comparison with the velocity vector plots shows this behavior is associated with the formation and shedding of the vortex structure. The Mach number contours for the computations with turbulence included are shown in Fig. 8. The time-dependent behavior shown in this figure indicates that the turbulence model reduces the strength of the leading edge shock

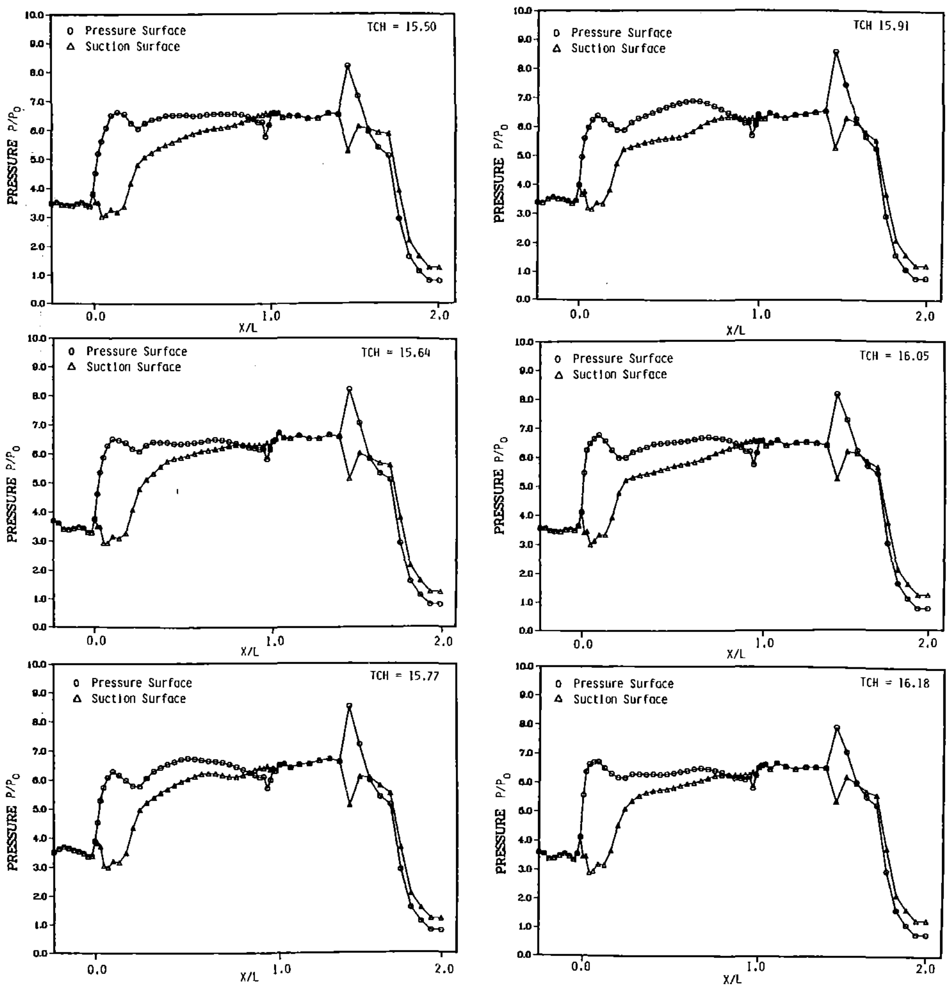

Fig. 10 Blade surface pressure variation with time: turbulent case

and the extent of flow separation. In addition, it can be seen that the oscillatory nature of the flow separation is reduced significantly in amplitude by including the turbulence model. The large fluctuations in the flow for the laminar case are shown in the time-varying blade surface pressure distributions (Fig. 9). Again the large amplitude in pressure fluctuation at the blade trailing edge is associated with the vortex shedding phenomena. This figure also reveals a large spike in the static pressure on both the pressure and suction surfaces at the blade leading edge. This indicates that a detached bow shock is present and that the pressure tends toward the stagnation value on the pressure surface. The flow then rapidly expands around the leading edge on both surfaces and the pressure recovers toward the value which would be produced by a weak attached shock on the pressure surface. This phenomenon is smeared over a much larger region than would be expected in an actual physical flow due to the relatively coarse grid in the vicinity of the blade leading edge. This oblique shock wave then impinges on the suction surface of the adjacent blade causing boundary layer separation in a classical shock wave-boundary layer interaction. The wave is then reflected back toward the pressure surface causing a subsequent rise in the surface pressure. The drop in static pressure on the suction surface shows the presence of the expansion just inside the blade passage. Again comparing with the surface static pressure distribution for the turbulent calculation it is observed that the magnitudes of the fluctuations are reduced significantly (Fig. 10). In particular, the large fluctuation at the trailing edge for the laminar case is almost completely eliminated. Referring to the velocity vectors (Fig. 6), note that in the turbulent case the vortex strength at the trailing edge has been reduced to nearly zero in the turbulent computations. It is also seen that the sharp spike near the leading edge of the pressure surface has been eliminated, supporting the previous observation that the shock strength had been reduced in the turbulent calculations.

Similar observations can be made by comparing the mass flow rates for the laminar and turbulent calculations as in Fig. 11. Here we see that the frequency of the oscillation in the mass flow is the same for both the laminar and turbulent results. However, the amplitude of the oscillation is again reduced in the turbulent flow computation. Another significant distinction between the two mass flow rates is the secondary oscillation present in the laminar case. This oscillation occurs at a frequency much lower than blade passage frequency and can be associated with the vortex shedding phenomena. The physical interpretation of these observations is that the vortex forms and grows in the streamwise direction, resulting in growth of the flow separation which serves as a blockage in the blade passage. This blockage then reduces the mass flow rate in an oscillatory fashion corresponding to the vortex shedding frequency. This phenomenon is completely eliminated in the turbulent flow results. In addition, the oscillation amplitude in the mass flow due to the blade passing frequency has been reduced significantly. Also in Fig. 11, the time-averaged nonsteady mass flow rates are compared with the mass flow computed for a uniform inflow corresponding to the circumferentially mass-averaged rotor inlet conditions. In both cases, the time-averaged nonsteady flow rate is seen to be higher than the rate corresponding to a thermodynamically

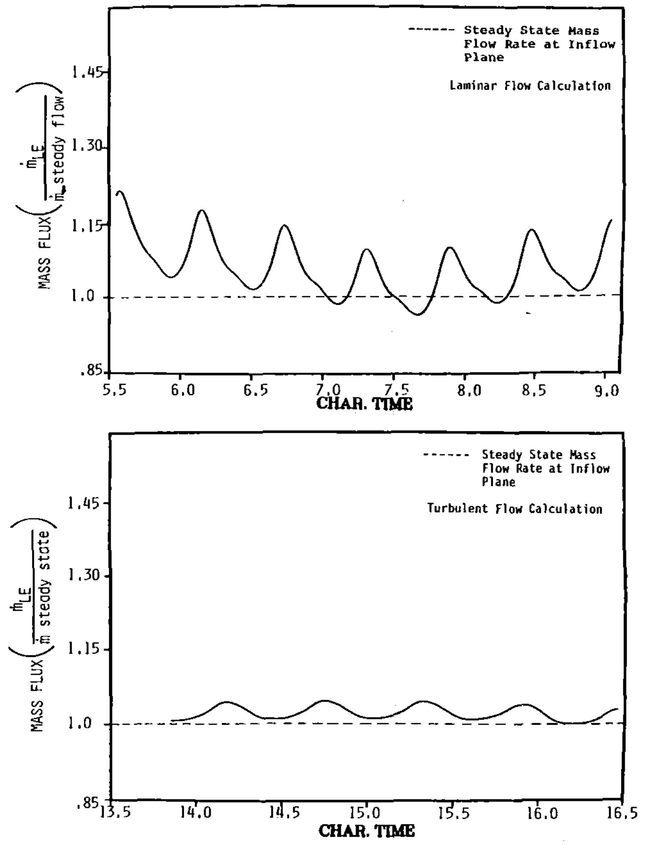

Fig. 11 Mass flow comparison at blade leading edge

equivalent steady flow, although the difference is smaller when turbulence is included.

Examination of the stagnation pressure contours for both the laminar (Fig. 12) and turbulent (Fig. 13) computations is revealing. For the laminar case the periodic behavior is observed to repeat at the blade leading edge at approximately 0.55 characteristic time while the behavior at the trailing edge is not repeatable due to the oscillatory behavior of the flow separation. In the case of the turbulent flow the periodic behavior at the leading edge also repeats at about 0.55 characteristic time. However, it is noted for this case that this periodicity is essentially preserved throughout the blade passage. This is attributed to the fact that the turbulence model suppresses the oscillatory behavior of the flow separation region. It is noted that the time variation of stagnation pressure can be regarded as entropy waves migrating through the blade passage. Viewing the stagnation pressure in this fashion gives a good view of the time history of the wakes from the upstream components.

With the progress of the current analysis it is deemed appropriate to expand the computational domain to more accurately simulate the periodic behavior of the incoming upstream wakes owing to the difference between the number of rotor blades and upstream stator blades. Since insufficient computer storage is available to model the ratio of stator to rotor blades exactly (i.e., 54:72) the real configuration is approximated by computing the flow through three blade passages (four blades) assuming three stator blades upstream for every four rotor blades. Computations are currently under way to simulate flow through four adjacent blades.

Conclusion

Procedures for treating boundary conditions for a supersonic flow entering a two-dimensional compressor rotor blade row and a subsonic flow exiting that blade row have been developed. The upstream boundary conditions are formulated using characteristic variables and an experimentally measured stagnation pressure profile to simulate the pressure and velocity defects from the wake of upstream stators and inlet guide vanes. This formulation also produces the proper entropy variation at the inflow boundary. The downstream boundary conditions are developed by incorporating a "second throat" (A_2^*) downstream of the blade trailing edge and imposing supersonic outflow boundary conditions at the exit of the throat. The area of the "second throat" can be adjusted to relocate the shock and the pressure rise across the blade passage. The computation also incorporates streamtube contraction through the axial component of the continuity equation to allow for some three-dimensional effects. These boundary conditions are used to obtain solutions to the complete time-dependent compressible Navier-Stokes equations for the transonic compressor rotor.

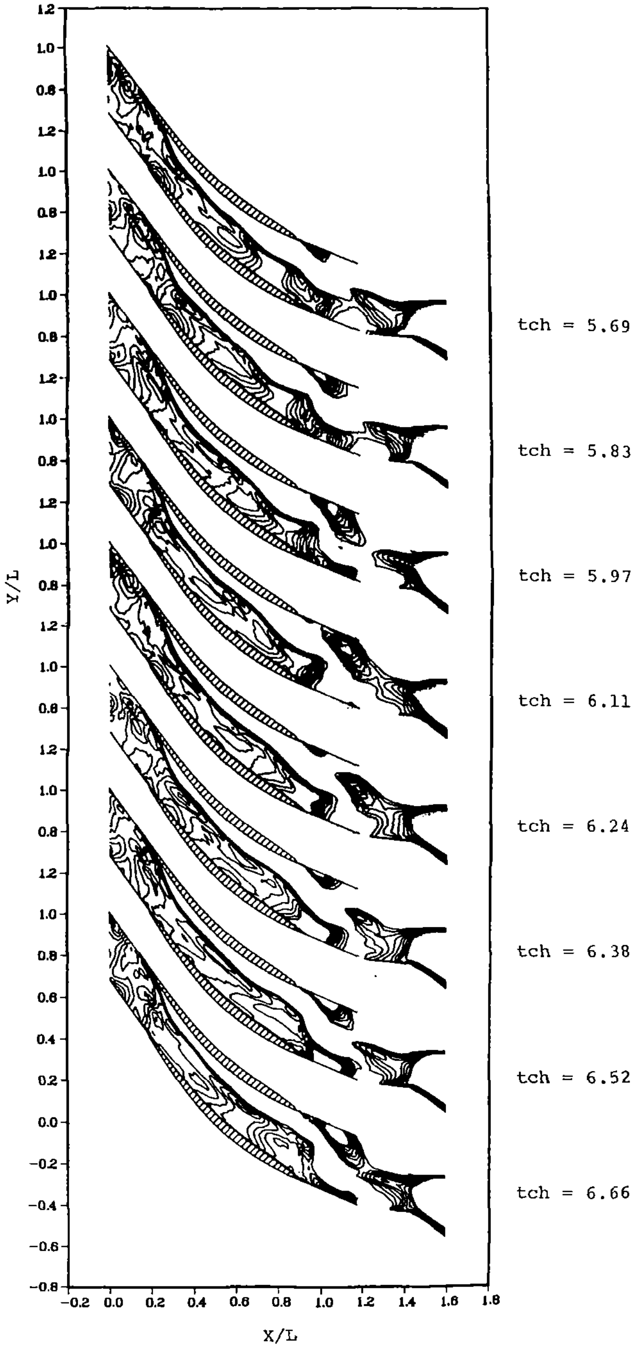

Fig. 12 Stagnation pressure for laminar computation

Both laminar and turbulent cases are computed. Results are

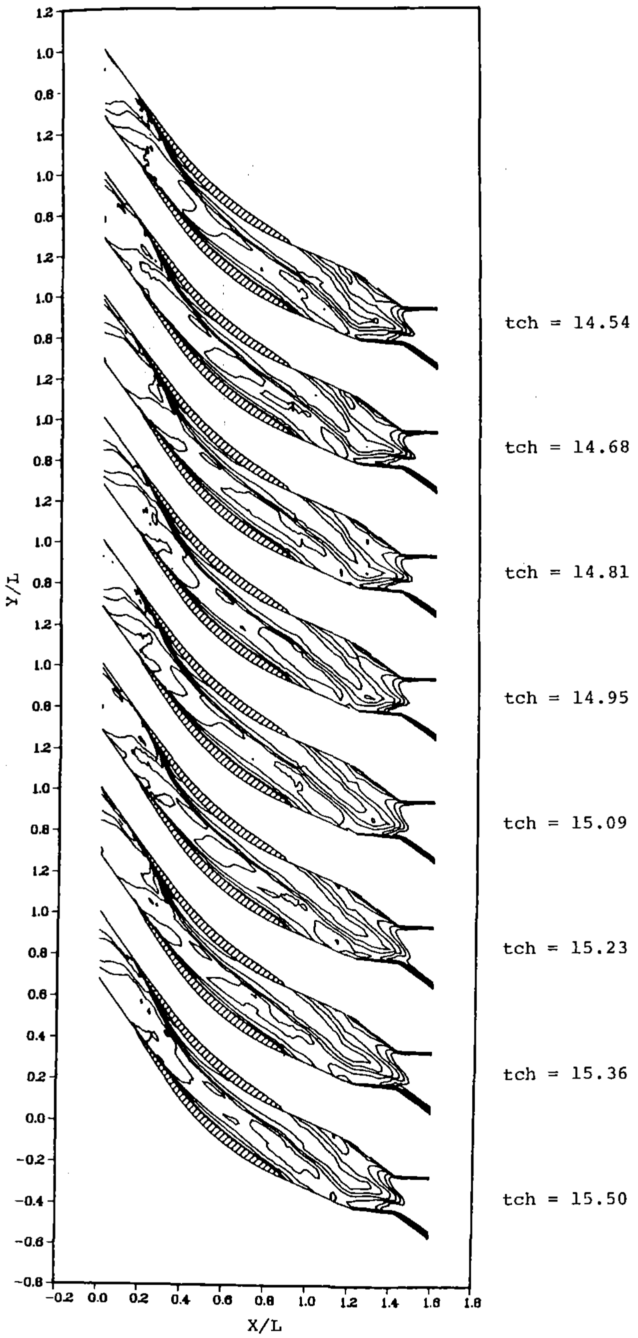

Fig. 13 Stagnation pressure for turbulent computation

presented in the form of velocity vectors, Mach and total pressure contours, blade surface pressure distribution, and mass flow history. The computed results give a good representation of the time-varying flow properties in a compressor rotor and provide a significant advance in solving the time-dependent viscous flowfield in turbomachinery.

Acknowledgments

This work was conducted under Contract No. F33615-83-K-2318 with the Aero Propulsion Laboratory, Wright-Patterson Air Force Base, Ohio. The authors would like to thank the Air Force Technical Monitor, Dr. A. J. Wennerstrom, for providing the rotor design data and background information as well as significant insight into the problem.

References

1 Mitchell, N. A., "A Time Marching Method for Unsteady Two Dimensional Flow in a Blade Passage," CUED/A-TURBO/TR 100, Cambridge University, 1980.

2 Hodson, H. P., "An Inviscid Blade-to-Blade Prediction of a Wake-Generated Unsteady Flow," ASME Paper No. 84-GT-43, June 1984.

3 Denton, J. D., "An Improved Time-Marching Method for Turbomachinery Flow Calculation," ASME JOURNAL OF ENGINEERING FOR POWER, Vol. 105, July 1983.

4 Janssens, P., and Hirsch, C., "A Viscid-Inviscid Interaction Procedure for Two Dimensional Cascades," *Viscous Effects in Turbomachines*, AGARD CP 351, June 1983.

5 Calvert, W. J., "Application of an Inviscid-Viscous Interaction Method to Transonic Compressor Cascades," *Viscous Effects in Turbomachines*, AGARD CP 351, June 1983.

6 Rai, M. M., "Navier-Stokes Simulations of Rotor-Stator Interaction Using Patched and Overlaid Grids," AIAA Paper No. 85-1519, July 1985.

7 Scott, J. N., and Hankey, W. L., "Boundary Conditions for Navier-Stokes Solutions of Unsteady Flow in a Compressor Rotor," *Three-Dimensional Flow Phenomena in Fluid Machinery*, Fluids Engineering Technical Session, Vol. 32, ASME, New York, Nov. 1985.

8 Shang, J. S., "Oscillatory Compressible Flow Around a Cylinder," AIAA Paper No. 82-0098, AIAA 20th Aerospace Sciences Meeting, Orlando, FL, Jan. 11-14, 1982.

9 Shang, J. S., "Numerical Simulation of Wind-Fuselage Aerodynamic Interaction," AIAA Paper No. 83-0225, AIAA 21st Aerospace Sciences Meeting, Reno, NV, Jan. 10-13, 1983.

10 Scott, J. N., and Hankey, W. L., Jr., "Numerical Simulation of Cold Flow in an Axisymmetric Centerbody Combustor," AIAA Paper No. 83-1741, AIAA 16th Fluid and Plasma Dynamics Conference, Danvers, MA, July 12-14, 1983.

11 Baldwin, B. S., and Lomax, H., "Thin Layer Approximation and Algebraic Model for Separated Turbulent Flows," AIAA Paper No. 78-257, Jan. 1978.

12 MacCormack, R. W., "Numerical Solution of the Interaction of a Shock Wave With a Laminar Boundary Layer," *Lecture Notes in Physics*, Vol. 59, Springer-Verlag, 1971.

13 Erdos, J. I., and Alzner, E., "Computation of Unsteady Transonic Flows Through Rotating and Stationary Cascades," NASA CR-2900, 1977.

14 Chima, R. V., "Analysis of Inviscid and Viscous Flows in Cascades With an Explicitly Multiple Grid Algorithm," AIAA Paper No. 83-0257, Jan. 1983.

S. G. Koff

E. M. Greitzer
Gas Turbine Laboratory,
Massachusetts Institute of Technology,
Cambridge, MA 02139

Axisymmetrically Stalled Flow Performance for Multistage Axial Compressors

A study of the stalled flow performance of multistage axial compressors is presented. A proposal is made regarding the form of axisymmetric *pumping performance in stall (which is a requisite of current rotating stall models) over the entire compressor flow range, including reversed flow. It is also shown that the axisymmetric performance can rise above the measured stall point pressure rise, thus indicating greater unstalled pressure rise potential. A simple two-dimensional reversed flow model is presented, and is shown to be in reasonable agreement with available high backflow compressor data. The model predicts that the blade stagger angle greatly influences the reversed flow characteristic. Calculations are also carried out applying this axisymmetric characteristic to the rotating stall model of Moore.*

Introduction

Recovery from a stalled condition is a problem of concern for aircraft gas turbine engines. When these high-performance engines undergo transients due to, for example, throttle motions, maneuvers, or (for an augmented engine) a "hard light" in the afterburner, the compressor can be driven past its stall limit into rotating stall. Recovery from this regime can sometimes be accomplished by either limiting the fuel addition in the combustor (which effectively drops the system throttle line), or by using variable geometry. In some instances, however, these actions may not be enough to promote a return to unstalled operation, so that an engine shutdown is necessary.

Further, it is not always possible in a military engine to provide enough stall margin to avoid any stall. It is therefore important to understand the poststall behavior of the compressor in order to deal more quantitatively with the problem of engine recoverability.

Work in this general area has been carried out by several investigators. References [1, 2] have provided basic descriptions of surge and rotating stall in multistage compressors. Compressor operation in rotating stall has also been modeled in a simple manner using essentially a "parallel compressor" concept [3].

Moore [4, 5] has recently introduced a different approach to rotating stall. He solved for the permissible flow field in the compressor, given the specification of an *axisymmetric* compressor pumping characteristic and upstream and downstream boundary conditions. The axisymmetric characteristic represents the performance of the compressor operating in an axisymmetrically stalled or unstalled flow.

It is important to emphasize that the approach described in [4, 5] (as well as that in [3]) requires the specification of an axisymmetric compressor characteristic. The parallel compressor approach relies on a backflow performance curve to supply information about the stalled flow, while the model developed in [4, 5] uses a continuous axisymmetric characteristic for the entire flow regime, including low forward and reversed flow.

The axisymmetric characteristic is readily measured in either unstalled or reversed flow since axisymmetric flow is the stable mode in these regimes. However, it is not at all well documented at low forward flow conditions because the characteristic is positively sloped, and an axisymmetric flow is inherently unstable. In other words, in low forward flow, a nonaxisymmetric flow pattern (rotating stall) exists during steady-state operation, and the pressure rise in this mode can be very different from this axisymmetric pressure rise.

This paper deals with axisymmetrically stalled performance for multistage compressors, which is not only a key item in any rotating stall model, but it also provides some insight into compressor stall phenomena. The form of the axisymmetric

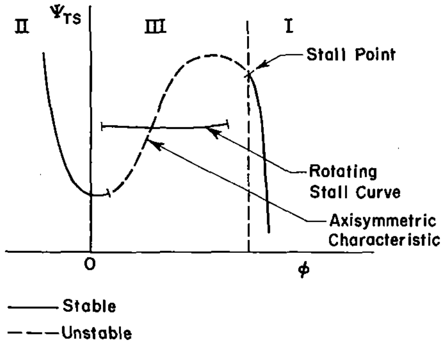

Fig. 1 Complete axisymmetric characteristic partitioned into three regions

Contributed by the Gas Turbine Division and presented at the 29th International Gas Turbine Conference and Exhibit, Amsterdam, The Netherlands, June 4-7, 1984. Manuscript received at ASME Headquarters February 12, 1986.

characteristic in the low forward flow regime is identified from transient compressor data. Possible variations of the axisymmetric curve for different compressor configurations, and their connection with the stall inception point are considered. An approximate technique, including a simple reversed flow model, is also proposed for estimating the axisymmetric characteristic over the entire compressor flow range. Calculations are carried out using the analysis of Moore [4] to show the effects of axisymmetric characteristic shape on performance in rotating stall.

Generalized Shape of the Axisymmetric Characteristic

Proposed Characteristic. As a preface to what follows, the general shape of the proposed axisymmetric performance curve is sketched in Fig. 1. The curve is partitioned into three regions. Region I is the unstalled pumping characteristic with the division drawn between regions I and III at the compressor stall point, i.e., the point at which the axisymmetric flow becomes unstable in the compressor annulus. (Further discussion of the stall point is provided subsequently.) Region II is axisymmetric reversed flow, where the compressor behaves as a throttling device, i.e., there appears to be a monotonic relation between backflow and pressure *drop* (exit to inlet). Region III is designated as low forward flow. The characteristic is shown dashed in this region because axisymmetric flow is unstable for these flow rates, and the stable, steady-state mode is (*nonaxisymmetric*) *rotating stall.*

Unstable Portion of the Axisymmetric Characteristic. To measure the steady-state axisymmetric curve in region III directly, it would be necessary to suppress rotating stall. One technique that has been suggested is using high-loss screens at the inlet and exit of the test compressor to suppress axial velocity nonuniformities, although it is not known how effective this is in the low forward flow regime. Specifically, [3] showed that while an exit screen postponed full-span rotating stall flow, axisymmetry was still not achieved since a part-span stall resulted. Furthermore, at part speed in a multistage compressor, the rear stages can be choked and act like screens for the front stages, which can still operate in *part-span* stall. Thus, the axisymmetric characteristic may not be attainable directly by adding screens to the compressor, so that, in general, other procedures must be used.

One such method is to use *transient* compressor data. In this approach, one "subtracts off" that part of the pressure rise due to flow accelerations (or decelerations) during an axisymmetric compressor *surge cycle.*

Certain conditions must hold in order for this inertial correction procedure to yield the desired quasi-steady axisymmetric characteristic. Three time scales are relevant in this context, namely, the compressor mass flow transient time scale (τ_{tran}), the blade passage performance response time scale (τ_{blade}), and the rotating stall formation time scale (τ_{form}). τ_{tran} is defined as some significant fraction of the time to complete the rapid mass flow acceleration (or deceleration) portion of a surge cycle. τ_{blade} represents the blade passage stalling or unstalling time, and is assumed to be on the order of the time required to shed a vortex through the blade passage,

$$\tau_{blade} \approx \frac{\text{blade chord}}{\text{throughflow velocity}} = \frac{l \cos \gamma}{|\phi_{avg}| U} \tag{1}$$

where ϕ_{avg} = average value for ϕ encountered by the blade passage when transitioning between unstalled and stalled flow. τ_{form} is difficult to quantify since little is known about the dynamics of stall cell formation, although an attempt has been made to calculate its magnitude from an approximate theory governing poststall compressor transients [6]. Nevertheless, based on the (sparse) available data [7], the rotating stall formation time scale has been found, *very roughly*, to be about 2 rotor revolutions,[1]

---

[1] Physical arguments suggest that τ_{form} should scale with ϕ_{avg} as τ_{blade} does. This dependence, however, is not included in τ_{form} since the original data in [7] only established a trend in rotor speed.

Nomenclature

A_c = compressor cross-sectional area
C_x = axial flow velocity
D = mean compressor diameter
L_C = effective compressor length
l = blade chord
N = number of compressor stages
p = static pressure
p_T = total pressure
Δp_{TS} = exit static to inlet total pressure rise for forward flow; and exit total to inlet static pressure rise for reversed flow
Δp_{TT} = exit total to inlet total pressure rise
t = time *or* blade pitch (as in solidity, l/t)
U = mean rotor speed
w = relative flow velocity
x = axial coordinate in compressor
β = flow angle relative to a blade row
β_{LE} = camber line angle at blade leading edge
β_{TE} = camber line angle at blade trailing edge
β_{LE_p} = pressure side metal angle of blade leading edge
γ = blade stagger angle referred to the axial direction
θ = circumferential coordinate in compressor annulus
θ_c = blade camber angle
μ = wake parameter shown in Fig. 7
ν = jet velocity ratio = w_1/w_2
ρ = density
τ_{blade} = blade passage response time scale, defined in equation (1)
τ_{form} = rotating stall formation time scale, defined in equation (2)
τ_{tran} = compressor mass flow transient time scale
ϕ = axial velocity coefficient = C_x/U
ϕ^* = ϕ at the design conditions
ϕ_{avg} = average value for ϕ encountered by a blade passage in the transition region between unstalled and stalled flow
ψ_{TS} or ψ = nondimensionalized exit static to inlet total pressure rise = $[p_{exit} - (p_T)_{inlet}]/\rho U^2$

Subscripts

1 = blade row inlet conditions
2 = jet/wake conditions
3 = blade row exit conditions
i = compressor inlet
e = compressor exit
SP = conditions at the steady-state stall inception point
v or valley = axisymmetric valley coordinate

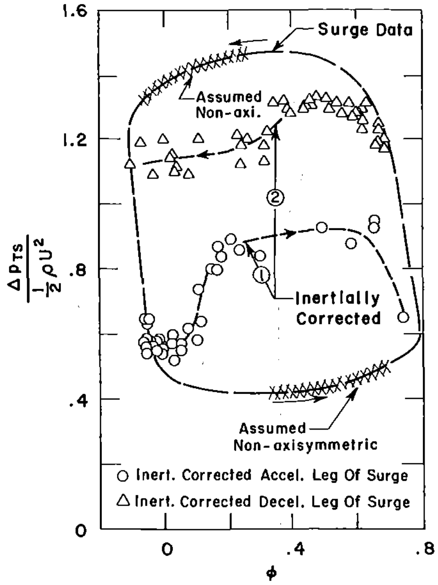

Fig. 2 Inertially corrected surge data from compressor in [1] (U = 92.9 m/s)

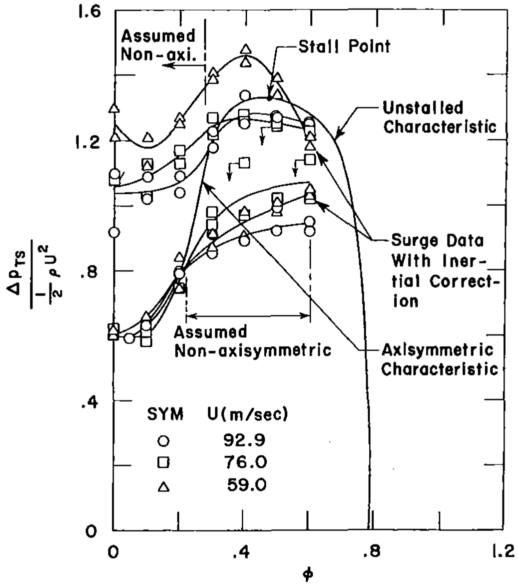

Fig. 3 Quasi-steady axisymmetric characteristic obtained by connecting the axisymmetric regions of inertially corrected surge data

$$\tau_{\text{form}} \approx \frac{2\pi D}{U}. \tag{2}$$

Two conditions must be satisfied to extract axisymmetric performance information from inertially corrected surge data. First, the blade passages must have sufficient time to respond to the rapidly changing flow experienced in the transient portions of the surge cycle. In other words, the compressor transient time scale must be much larger than the blade passage performance response time scale, or $\tau_{\text{tran}} \gg \tau_{\text{blade}}$.

The second condition is the necessity for axisymmetric flow over a significant portion of the highly transient regions of the surge. As the compressor mass flow decreases into the low forward flow region, a stall cell starts to form (since rotating stall is the stable, steady-state mode for the low flow rates). However, if the mass flow change through the compressor is more rapid than the time for rotating stall formation, axisymmetric flow would be maintained for part of the transient. Thus, to have axisymmetric flow over a significant part of the transient regime, $\tau_{\text{tran}} < \tau_{\text{form}}$. To obtain an axisymmetric characteristic by inertially correcting compressor surge data, τ_{tran} must therefore be bracketed as

$$\tau_{\text{blade}} \ll \tau_{\text{tran}} < \tau_{\text{form}}.$$

With the proviso that this does occur, the unstable axisymmetric characteristic can be found by subtracting an inertial correction term, due to the fluid acceleration in the compressor, from the instantaneous overall (plenum minus atmospheric) pressure rise measured in a surge cycle. In doing this, one can model the compressor as operating in a duct of effective length L_c and area A_c, as defined in [1]. The effective length includes the nonaxial flow in the blade passages (i.e., the effect of stagger angle) so that L_c can be greater than the actual (axial) compressor length. If the flow is incompressible and axisymmetric, the duct flow can be modeled as one dimensional, and mass conservation implies that the product of axial velocity and area is solely a function of time, i.e., $C_x(x, t) \bullet A_c(x) = Q(t)$. A momentum balance for the flow in the duct results in an expression for the quasi-steady axisymmetric performance in the case of constant annulus area,

$$(\psi_{TS})_{\substack{\text{quasi-steady,}\\ \text{axisymmetric}}} = (\psi_{TS})_{\text{surge data}} + \frac{L_c}{U} \bullet \frac{d\phi}{dt}. \tag{3}$$

$(\psi_{TS})_{\text{surge data}}$ represents the (nondimensional) transient pressure rise across the compressor measured in a surge cycle, and $(\psi_{TS})_{\text{quasi-steady, axisymmetric}}$ is the inertially corrected pressure rise, i.e., the quasi-steady compressor performance.

This procedure is applied to the surge data described in [1]. Surge cycles at three different mean rotor speeds are examined. The time scales for this compressor are consistent with the necessary bracketing condition on the transient time scale previously discussed.

Even though $\tau_{\text{tran}} < \tau_{\text{form}}$, it is still necessary to examine the time-resolved data to determine whether the surge data in [1] include axisymmetric flow, because of the uncertainty of τ_{form}. The data show (not fully developed) rotating stall toward the end of the highly transient regions, although they are not sufficient to resolve the details of the flow. Consequently, axisymmetric flow *cannot* be assumed for the *whole* transient.

Figure 2 shows a sample of the surge data with the inertially corrected characteristics determined by equation (3). Quasi-steady curves ① and ② are found from correcting the accelerating and decelerating portions of the surge cycle, respectively. The term with $d\phi/dt$ in equation (3) is calculated simply from the surge data using centered differences. Although this is a fairly crude representation, the values for $d\phi/dt$ computed for different cycles are quite close and the approach is adequate for present purposes. Note that since nonaxisymmetric flow (rotating stall) was present toward the end of the rapid mass flow excursions, the inertially corrected curves *in these regions* may not represent the axisymmetric characteristic, as indicated in the figure.

Three sets of inertially corrected characteristics from surge cycles at different rotor speeds are plotted along with the unstalled compressor performance in Fig. 3. Two unique sets of quasi-steady curves seem to result from the three distinct surge cycles. The corrected characteristic on the decelerating portion in the lowest rotor speed case deviates slightly from the other corrected curves for this portion. This may be attributed to the large decelerations in the surge cycle for this case (and consequently large data corrections).

It remains to specify a procedure which yields an axisymmetric compressor characteristic from the information in Fig. 3. In doing this, we draw on the analogy between axisymmetric compressor behavior and diffuser performance. Using a diffuser correlation, Koch [8] presented strong evidence that stall in multistage compressors is generally triggered by boundary layer growth at the compressor endwalls (wall stall),

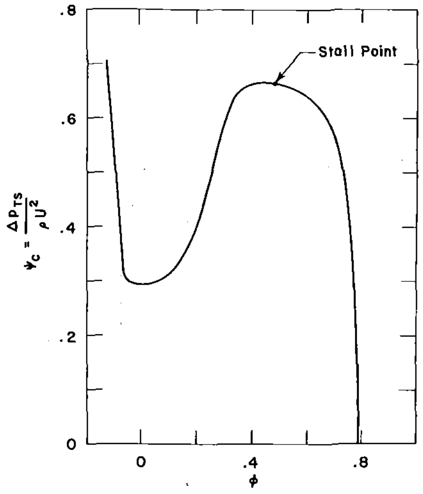

Fig. 4 Proposed axisymmetric characteristic for the compressor in [1]

rather than by a (two-dimensional type of) blade stall. This wall stall, in fact, tends to suppress blade stall by creating more favorable incidence and higher flow velocities on the blades. Thus, the diffuser analogy may well apply not only to stall inception, but also throughout a large portion of the low forward flow region.

This is of importance since as a diffuser begins to stall, it does not exhibit any sudden drop in pressure rise. In fact, the pressure recovery coefficient continues to increase when transitory stall is encountered, and then decreases smoothly to a low value. Also, diffuser characteristics in transitory stall are single-valued, i.e., free of hysteresis. Similarly, if one could suppress the rotating stall mode in a compressor and maintain axisymmetric flow, the compressor might also exhibit a smoothly varying characteristic, free of hysteresis, with no sudden decrease in pressure rise.

If no hysteresis occurs in the axisymmetric characteristic, the inertially corrected curves for both the accelerating and decelerating regions of a completely axisymmetric surge cycle should collapse into a single quasi-steady, axisymmetric characteristic (if $\tau_{\text{tran}} \gg \tau_{\text{blade}}$). For a surge cycle which is not totally axisymmetric, as in the above-mentioned surge data, all that can be done at present is to construct the axisymmetric curve by connecting the *valid* portions of the inertially corrected characteristics. The corrected curves for the decelerating portion of the surge cycles should (and do) coincide fairly closely with the unstalled performance for $\phi \geq \phi_{SP}$ ($\phi_{SP} = 0.48$), as evidenced in Fig. 3. Furthermore, since these quasi-steady curves do *not* exhibit any sudden dropoff in pressure rise at the steady-state stall point, the axisymmetric pumping characteristic is then constructed by (smoothly) continuing the unstalled curve past the stall point. The corrected curves from the decelerating leg, however, begin to drop off at a pressure rise around $\phi \sim 0.4$, and the unstable axisymmetric performance is drawn accordingly in Fig. 3 with no hysteresis. Again, the corrected points from the assumed nonaxisymmetric portion of the surge cycle do not contribute to the proposed axisymmetric characteristic. The complete axisymmetric characteristic for the compressor is then given in Fig. 4 where, as stated in lieu of evidence to the contrary, the assumption of a single-valued axisymmetric curve is employed.

We define the axisymmetric "peak" point as the maximum pressure rise on the axisymmetric curve in forward flow for a ψ_{TS} versus ϕ plot. This point nearly coincides with the stall point for the data shown in Fig. 4. The axisymmetric "valley" point is defined as the relative minimum point of the axisymmetric characteristic. This point occurs at essentially zero flow in Fig. 4.

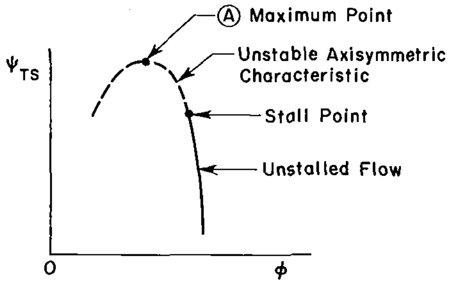

Fig. 5 Rotating stall onset point in relation to axisymmetric peak point

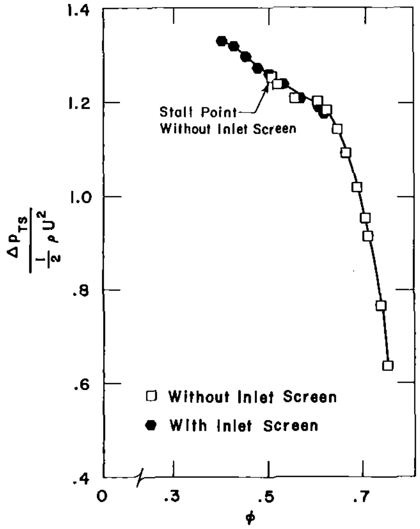

Fig. 6 Effect of inlet screen on unstalled performance from compressor in [1]

Generalized Properties of the Axisymmetric Performance. Due to the scarcity of transient data, the calculation procedure for the unstable axisymmetric characteristic posed in the last section has not been implemented for other compressors. However, many features of the proposed axisymmetric curve can be generalized for various compressor builds. These are:

1 No sudden drop in pressure rise at the compressor stall point
2 No hysteresis in the characteristic
3 The characteristic is relatively "smooth" (in some sense)
4 A steeply positively sloped portion exists between the axisymmetric peak and valley

Note that property (4) encourages an unstable compression *system* [7], as well as an unstable axisymmetric flow for a stable system. This is consistent with the experience of post-stall compressor tests, where rotating stall is always observed as the steady-state low flow mode (region III of Fig. 1), except near shutoff. (Axisymmetric flow can become stable near zero flow when the characteristic flattens or is negatively sloped.)

Observations Concerning the Axisymmetric Peak Point. It is important to distinguish between compression system instability and compressor instability. Compression system instability results in a transient of the *area-averaged* mass flow through the compressor. Compressor instability occurs when the flow through the compressor changes to a different mode of operation, i.e., from axisymmetric flow to rotating stall flow; this could occur at constant area-averaged mass flow. Thus, solving for the flow in the compressor can be thought of as an "inner" stability problem within the overall stability problem.

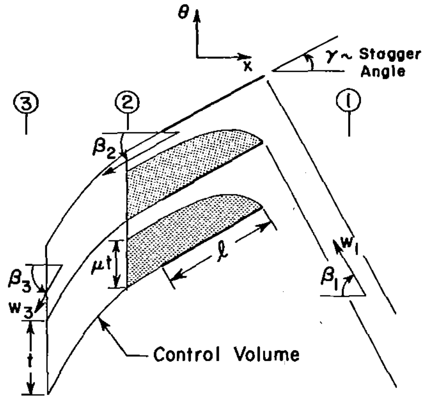

Fig. 7 Cornell's stalled cascade model in the case of backflow

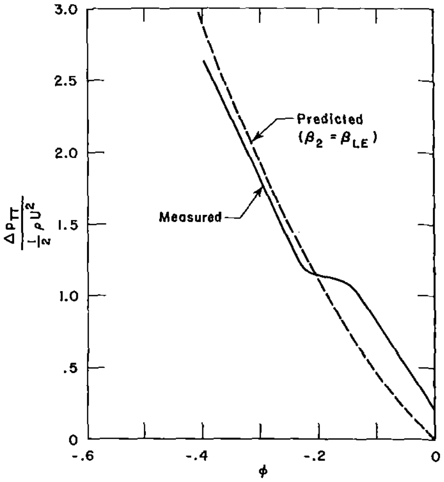

Fig. 8 Predicted and measured reversed flow characteristics for the Turner and Sparkes compressor

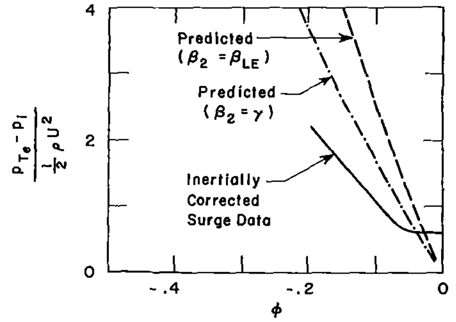

Fig. 9 Predicted backflow curves and inertially corrected surge data for the compressor in [1]

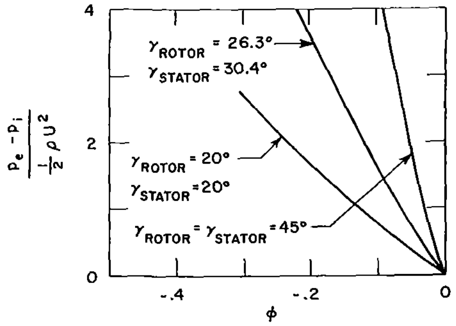

Fig. 10 Effect of blade stagger angle on predicted backflow curves

Many compressors appear to have stall points on the strongly negatively sloped portions of their characteristics. Properties (1) and (3) would imply that their axisymmetric curves will rise in performance above the *observed* stall point. In other words, the peak of the characteristic can occur at a greater pressure rise than the compressor stall point, as sketched in Fig. 5. In this case, a compressor instability first exists at the stall inception point, and if axisymmetric flow could be sustained in the compressor past its stall point, the compression system would not become unstable until point A is reached in Fig. 5.

The notion that the maximum axisymmetric performance can be at a higher pressure rise than the compressor stall point is also supported by data. A full annulus screen was placed at the inlet to the three-stage compressor described in [1]. The resulting pressure rise curve did not show the sharp drop measured without the screen; presumably this was due to the suppression of rotating stall. Figure 6 illustrates that the compressor performance with the screen increased beyond its previous stall point in a smooth, continuous fashion, showing that the stall point can occur before the maximum point of the axisymmetric curve. This variation in the stall point from suppressing nonaxisymmetric flow has also been seen as the result of *downstream* components [9].

The negatively sloped portion of the axisymmetric performance above the stall point pressure rise may be viewed as unstalled pressure rise potential for the compressor, which is not utilized because the axisymmetric flow mode is terminated. One possible mechanism for this is the unsteadiness present in the compressor near the stall inception point (analogously, the unsteadiness experienced in an equivalent diffuser in transitory stall), which induces an instability in the axisymmetric flow field. In order to obtain the potential performance gain, it would be necessary to damp this unsteadiness.

Predicting Axisymmetric Compressor Performance

Axisymmetric Reversed Flow. A simple model is developed which describes compressor performance in reversed flow operation. Applications for this are not only in predicting compressor backflow performance, but also in predicting the pressure forces on the blades during stall [10] to estimate blade forcing functions in either surge or rotating stall. This second application, however, is beyond the scope of this paper.

The backflow model originates from the observations of Day (for a three-stage, high ϕ^* configuration), namely, that a rotating stall cell with a large degree of reversed flow is two dimensional in nature with negligible radial velocities [11]. Figure 7 shows a stage compressor row subjected to planar backflow. Due to the very high incidence (~90 deg), the flow is assumed to be separated and is analyzed using an incompressible, free streamline approach [12]. The blade row is modeled as a two-dimensional cascade of infinitely thin flat plates. The flow separates from the blade trailing edge, resulting in high velocity jets, and wakes of zero velocity at station ② (see Fig. 7). The jets and wakes then mix from ② to ③.

The flow between stations ① and ② is found from a hodograph solution of the problem [12], which leads to two simultaneous equations for the jet velocity ratio, $\nu = w_1/w_2$, and the jet angle, β_2. For solidities of about 1.0 or greater, i.e., for $l/t \geq \sim 1.0$, one can say, approximately, that the jet angle is the stagger angle of the cascade ($\beta_2 = \gamma$) [12]. However, the theory neglects blade camber and a more realistic condition on the jet angle might be that it coincides with the pressure surface metal angle of the blade leading edge β_{LE_p}. For thin blade profiles, the camber line angle at the leading edge could be used as the jet leaving angle. In applica-

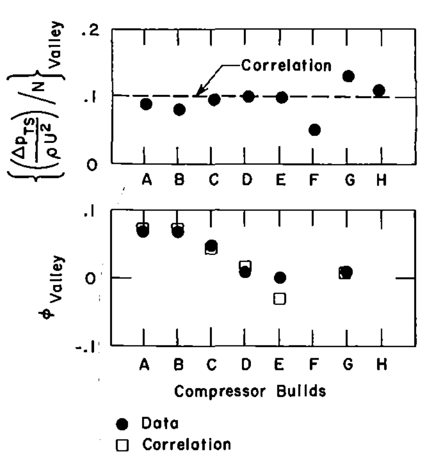

Fig. 11 Correlation for the axisymmetric valley point (compressor builds listed in the Appendix)

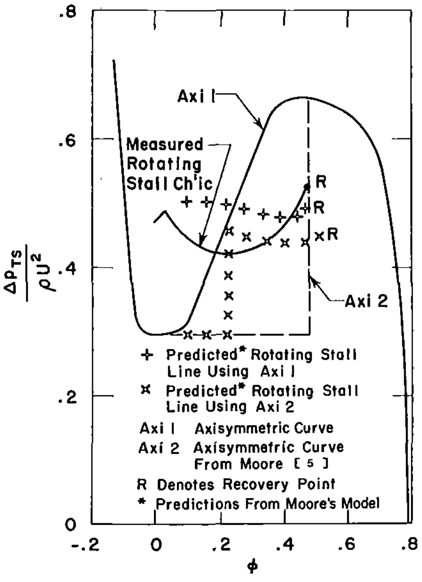

Fig. 12 Predicted and measured rotating stall characteristics

tion to multirow machines, the total pressure losses in the last stator, or outlet guide vane, are neglected. (This should be a good assumption since the entering backflow is taken as axial so that, in most cases, the incidence angle on the stator vane which accelerates the flow is small.) The subsequent blade rows then experience the separated flow previously described. Details of the derivation and calculation procedure are given in [13].

This analysis has been applied to a single stage tested by Turner and Sparkes [14], and the three-stage compressor reported in [1]. Both have constant annulus area. Turner and Sparkes generated the reversed flow curve by blowing flow backward through their compressor, which consisted of an inlet guide vane, a rotor, and a stator vane. In the prediction, the flow through the stator vane is assumed to leave the cascade at the camber line angle of the stator leading edge. Separated flow occurs in the rotor row and the inlet guide vane, and since $l/t > 1.0$, the high solidity approximation is utilized. The blade metal angle on the pressure surface of the leading edge, β_{LE_p}, was not given in [14] so that the camber line angle of the blade leading edge is used instead as the jet angle. The predicted characteristic is shown with the measured backflow curve in Fig. 8. These results compare favorably, especially for larger backflows. However, at shutoff, a pressure rise is measured, while the two-dimensional prediction method does not yield any pressure rise. It is suspected that radial effects produce this axisymmetric pressure rise at zero flow; these are not included in the two-dimensional theory.

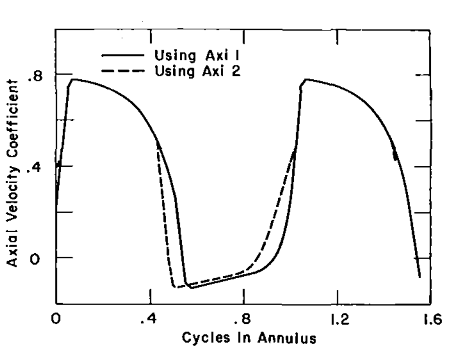

Fig. 13 Comparison of the predicted axial velocity profiles using Axi 1 and Axi 2 characteristics

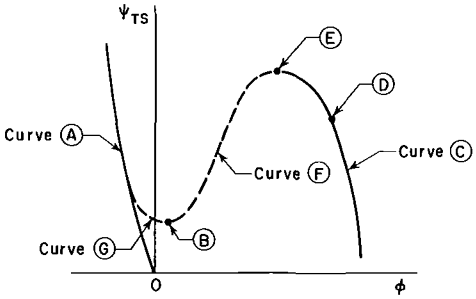

Fig. 14 Prediction process for a complete axisymmetric characteristic

The reversed flow characteristic was also obtained for a three-stage compressor [1] using surge cycle data. As described above, a one-dimensional correction is applied to the surge data in reversed flow but, since the accelerations are small, the corrections over most of this regime are considerably less than those used previously. The prediction is carried out with the high solidity ($l/t \geq 1.0$) approximation.

Two predicted characteristics, for β_2 set equal to either γ or β_{LE}, are compared to the corrected backflow curve in Fig. 9. The prediction only qualitatively follows the corrected characteristic. Similar overestimates in the predicted backflow pressure drop resulted for Gamache's three-stage compressor rig [15]. Possible reasons for the quantitative differences encountered in multistage predictions can be offered. First, radial pumping may occur in the rotors, which would act to reduce the pressure drop of the predicted backflow characteristic. Second, the theory assumes that the jets and wakes completely mix in the axial blade row gaps, whereas this condition is most likely not attained in actual compressors (especially multistage machines) operating with reversed flow. In any event, backflow prediction methods cannot be expected to match data as closely as unstalled predictions, because of the highly complex nature of the flow. As in the unstalled regime, however, experimental data can be used, if available, to improve the prediction of multistage machines under backflow.

The influence of blade stagger angle on backflow performance can also be examined. Figure 10 shows the predicted characteristics for blade stagger angles from 20.0 to 45.0 deg (referred to the axial direction). The middle case is based on the stagger angles in [1]. It is evident that higher stagger angles provide a greater resistance to reversed flow. This observation seems reasonable; however, experimental verification is still necessary to substantiate this claim.

Axisymmetric Peak and Valley Points. It was demonstrated that the axisymmetric peak may not coincide with the compressor stall inception point. One possible method to estimate the axisymmetric peak involves extending an unstalled flow prediction procedure past the anticipated stall point [16].

The backflow model presented in the last section appears to be most useful in "high" reversed flow cases. Additional information is required near shutoff to predict a backflow characteristic. At present, however, there are no models near shutoff which give even qualitative results. Consequently, a correlation involving the axisymmetric valley point is introduced, although data on this quantity are sparse.

The correlation is based on data from [11, 1]. The valley coordinates (ϕ_v, ψ_v) are correlated by the design flow coefficient, ϕ^*, and by the number of stages, N. We would also expect hub/tip radius ratio to be important, since the axisymmetric pressure rise near shutoff presumably results from strong radial recirculation of the flow. However, there are not enough data to examine this effect. The pressure level per stage of the valley point, $\{\psi_{TS}/N\}_v$, appears to be fairly constant for each compressor configuration, while the flow coefficient of the minimum point, ϕ_v, depends on both ϕ^* and N. The axisymmetric valley point is correlated as follows:

$$\phi_v = (-0.25\phi^* + 0.095)(N-1) + 0.075 \tag{4}$$

$$\psi_v = 0.10N. \tag{5}$$

Equation (4), obtained through trial and error, fits the available data fairly well. Equation (5) is just the data average. Figure 11 compares the correlation with the measured axisymmetric valley points for various compressor builds listed in the Appendix.

The position of the valley point is not given in the data for compressors F and H. However, since their measured axisymmetric curves near shutoff are fairly flat, ψ_v for F and H is accurate. Although the data set in the Appendix is represented fairly well by the proposed correlation, equations (4) and (5) can only be regarded as a rough estimate of the axisymmetric valley point since no information concerning the flow field is included.

Positively Sloped Portion of the Characteristic. The unstable portion of the axisymmetric characteristic can consist of a peak and valley, discussed above in the context of a prediction method, and a part with a steep positive slope. As with the entire unstable axisymmetric curve, the positively sloped part is not readily measured. From this point of view, an important question is: How well does one have to measure this portion, i.e., what is its impact on (1) rotating stall performance and (2) more rapid compressor transients such as surge cycles?

To answer the first question, we note that data from Day [11] suggest abrupt transition regions between the unstalled and stalled flow zones in a compressor annulus which contains full-span rotating stall. This implies that the blade passages experience the regime of large positive slope for only short durations in (steady-state) rotating stall. Therefore, one might suspect that the precise shape of the *positively sloped part* of the axisymmetric characteristic is in fact relatively unimportant in steady-state rotating stall.

Calculations using the model developed by Moore support this reasoning. The equations given in [5] have been solved numerically for the compressor in [1] using two axisymmetric curves which have very different behavior in the low forward flow regime. Figure 12 presents the predicted and measured rotating stall characteristics for this compressor rig, with two different axisymmetric curves shown as well. Both axisymmetric characteristics have the same measured unstalled performance, the same (inertially corrected) backflow curve from the surge data presented previously, and similar axisymmetric peak and valley points. However, the two possess quite different portions in the low forward flow region. The curve labeled "Axi 1" in Fig. 12 closely resembles the proposed axisymmetric characteristic for Greitzer's machine (Fig. 4). "Axi 2" represents an axisymmetric curve similar to that used by Moore [5], with a sharp drop in pressure rise at the stall point and a flat region through shutoff.

The predicted *rotating stall* characteristics using Axi 1 and Axi 2 are shown in Fig. 12. The curves are fairly similar for high flow coefficients in rotating stall, but deviate at lower flows. The Axi 2 prediction includes a flow mode change at $\phi = 0.22$, in which an axisymmetric stall is predicted for $\phi \leq 0.22$, whereas Axi 1 predicts rotating stall for low ϕ. The data show that rotating stall is experienced to shutoff. The authors have not seen any data which support a flow mode change from full-span stall to axisymmetric stall at a flow coefficient greater than 0.1, and thus the Axi 2 prediction seems unrealistic for low ϕ. At recovery, however, both predictions are consistent with the data.

The results from the Axi 1/Axi 2 study are consistent with the notion that the positively sloped portion of the axisymmetric curve is unimportant in predicting *steady-state* rotating stall performance. When rotating stall is present for both predictions ($\phi > 0.22$), the performance, as well as the axial velocity profiles (compared in Fig. 13 for an averaged flow of $\phi = 0.30$), are quite similar even though the assumed unstable axisymmetric curves are very different. Small changes in the positively sloped axisymmetric characteristic between the peak and valley therefore appear to have little effect on the predicted steady-state rotating stall characteristic.

This does *not* mean, however, that the positively sloped region of the axisymmetric characteristic is of little general interest. In fact, this part of the axisymmetric curve may well be quite important in predicting surge *transients*. These can include axisymmetric flow and/or *non-steady-state* rotating stall flow (as in stall cell collapse/growth transients). The instantaneous pumping characteristic during these transients is a key item, but since there is little known concerning the details of the transient flow field, one cannot make a definite statement about the effect of the positively sloped axisymmetric characteristic on this quantity.

Predicting a Complete Axisymmetric Characteristic. A prediction technique for the axisymmetric performance over the entire compressor flow map is outlined as follows:

1 The two-dimensional backflow performance calculation results in curve A in Fig. 14.

2 Equations (4) and (5) give the coordinates of the axisymmetric valley point, shown as point B in Fig. 14.

3 An unstalled prediction method provides curve C along with the anticipated stall point (point D) and the axisymmetric peak point (point E).

4 The large positively sloped portion (curve F) can be faired in between the peak and the valley since it seems to be of less importance than the other regions for predicting fully developed rotating stall.

5 The backflow characteristic is completed by fairing in a curve G which connects the axisymmetric valley with the large reversed flow asymptote (curve A), The axisymmetric curve is then defined over the entire flow range by curve C, curve F, curve G, and curve A of Fig. 14.

Summary and Conclusions

1 The axisymmetrically stalled flow performance of multistage axial compressors has been examined. This axisymmetric characteristic is essential for all current compressor rotating stall prediction methods.

2 The (previously undetermined) axisymmetric compressor characteristic in the low forward flow regime can be obtained by inertially correcting transient compressor data. However, this calculation is only possible if the time scale of the mass flow transient lies between the blade passage response time scale and the rotating stall formation time scale.

3 A proposal is made for generalizing the shape of the complete axisymmetric characteristic, over the entire compressor flow range, for different compressor configurations.

4 The axisymmetric characteristic may rise in pressure performance above the compressor stall inception point, indicating greater unstalled pressure rise capability.

5 Predictions from a two-dimensional, axisymmetric backflow model agree well with measurements from a single-stage compressor, but are less accurate in the case of a three-stage machine. This backflow model also predicts that the reversed flow performance curve is sensitive to the blade stagger angle.

6 The unstalled and reversed flow characteristics along with the axisymmetric peak and valley seem to be of greater importance in predicting (steady-state) rotating stall performance than the steeply, positively sloped portion of the axisymmetric curve.

Acknowledgments

The authors would like to thank Pratt and Whitney Aircraft, Government Products Division, for support of this project. They are also grateful for the comments and insight from Professor E. E. Covert of MIT, and Mr. R. E. Davis, Mr. J. T. Lewis, and Mr. R. C. Parsley of Pratt and Whitney Aircraft. In addition, discussions with Captain R. N. Gamache, Dr. C. S. Tan, and Mr. P. L. Lavrich are appreciated. Thanks are also extended to Mrs. C. Callahan for her skilled work in constructing the figures.

References

1 Greitzer, E. M., "Surge and Rotating Stall in Axial Flow Compressors. Part II: Experimental Results and Comparisons With Theory," ASME Journal of Engineering for Power, Vol. 98, Apr. 1976, pp. 199–217.

2 Day, I. J., and Cumpsty, N. A., "The Measurement and Interpretation of Flow Within Rotating Stall Cells in Axial Compressors," *Journal of Mechanical Engineering Sciences*, Vol. 20, 1978, pp. 101–114.

3 Day, I. J., Greitzer, E. M., and Cumpsty, N. A., "Prediction of Compressor Performance in Rotating Stall," ASME Journal of Engineering for Power, Vol. 100, Jan. 1978, pp. 1–14.

4 Moore, F. K., "A Theory of Rotating Stall of Multistage Axial Compressors. Part I: Small Disturbances," ASME Journal of Engineering for Gas Turbines and Power, Vol. 106, Apr. 1984, pp. 313–320.

5 Moore, F. K., "A Theory of Rotating Stall of Multistage Axial Compressors. Part III: Limit Cycles," ASME Journal of Engineering for Gas Turbines and Power, Vol. 106, Apr. 1984, pp. 327–334.

6 Greitzer, E. M., and Moore, F. K., "A Theory of Post-Stall Transients in Axial Compression Systems: Part II – Application," ASME Paper No. 85-GT-172.

7 Greitzer, E. M., "Surge and Rotating Stall in Axial Flow Compressors. Part I: Theoretical Compression System Model," ASME Journal of Engineering for Power, Vol. 98, Apr. 1976, pp. 190–198.

8 Koch, C. C., "Stalling Pressure Rise Capability of Axial Flow Compressor Stages," ASME Journal of Engineering for Power, Vol. 103, Oct. 1981, pp. 645–656.

9 Greitzer, E. M., Mazzawy, R. S., and Fulkerson, D. A., "Flow Field Coupling Between Compression System Components in Asymmetric Flow," ASME Journal of Engineering for Power, Vol. 100, Jan. 1978, pp. 66–72.

10 Koff, B. L., private communication.

11 Day, I. J., "Axial Compressor Stall," Ph.D. Thesis, Cambridge University Engineering Department, 1976.

12 Cornell, W. G., "The Stall Performance of Cascades," *Proc. 2nd Nat. Conf. Appl. Mech.* (Michigan), ASME, New York, 1954.

13 Koff, S. G., "Stalled Flow Characteristics for Axial Compressors," S. M. Thesis, Massachusetts Institute of Technology, Mechanical Engineering Department, May 1983.

14 Turner, R. C., and Sparkes, D. W., "Complete Characteristics for a Single-Stage Axial Flow Fan," Thermodynamics and Fluid Mechanics Convention, Paper 29, Apr. 1964.

15 Gamache, R. N., private communication.

16 Davis, R. E. private communication.

APPENDIX

Compressor builds used in the axisymmetric valley point correlation in Fig. 11

Compressor	N	ϕ^*	(ϕ_v, ψ_v)
A (Day)	1	0.35	0.07, 0.09
B (Day)	1	0.55	0.07, 0.08
C (Day)	2	0.55	0.05, 0.19
D (Day)	3	0.55	0.01, 0.31
E (Greitzer)	3	0.65	0.0, 0.295
F (Day)	1	0.71	–, 0.05
G (Day)	2	0.71	0.01, 0.25
H (Day)	3	0.71	–, 0.34

D. L. Tweedt

T. H. Okiishi

Department of Mechanical Engineering,
Engineering Research Institute,
Iowa State University,
Ames, IA 50011

M. D. Hathaway

U.S. Army Research and
Technology Laboratories,
Cleveland, OH 44135

Stator Endwall Leading-Edge Sweep and Hub Shroud Influence on Compressor Performance

The use of stator endwall leading-edge sweep to improve axial-flow compressor stator row performance was examined experimentally. The aerodynamics of three stator hub (inner diameter) conditions, namely, a running clearance, a stationary clearance, and a shroud, were also investigated. Leading-edge sweep in the endwall regions of a stator blade can be beneficial in terms of loss reduction on the casing (outer diameter) end of a stator blade. It can also help at the hub end of a stator blade when either a stationary hub clearance or a hub shroud is used. A leading-edge sweep is detrimental (local loss increase) on the hub end of a stator blade when a running hub clearance is used. A running clearance is aerodynamically preferable to a stationary clearance.

Introduction

Further reduction of the fluid flow viscous losses occurring in production axial-flow turbomachines continues to challenge designers. Even small gains in aerodynamic efficiency are vigorously sought by manufacturers. Better management of the complicated viscous flows in endwall regions of the blade rows of a turbomachine is one example of a specific performance improvement goal.

This paper deals with low-speed compressor research initiated to provide a clearer understanding of the potential for better management of the endwall flows in an axial-flow compressor. The use of stator leading-edge sweep to improve stator row performance was examined. The aerodynamic benefits of stator hub shrouding were also investigated.

The same rotor rows were used for all tests. Two kinds of stator blades were used. A baseline stator, conventional in geometry, provided baseline data against which to compare data for other stator geometries. A modified stator featuring forward symmetric sweep of the leading edge from midspan to the inner and outer annulus walls was also utilized. The primary objective of symmetric forward sweeping of the stator leading edge was to draw higher-momentum fluid into the suction-side endwall corner flows and force the lower-momentum corner fluid toward midspan. Earlier experience [1, 2] suggested that this kind of geometry modification could be beneficial in terms of reducing the amount of low-momentum fluid in the endwall, suction-side corner.

Stator hub shrouding is commonly used in production compressors. Three different stator hub configurations were examined for merit: a running hub clearance, a stationary hub clearance, and a shrouded hub.

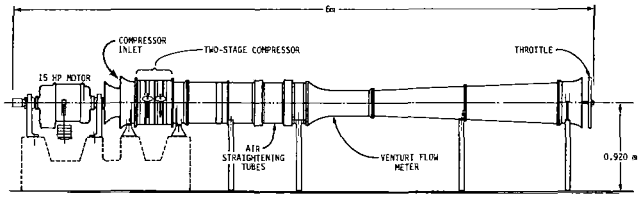

Fig. 1 Schematic of research compressor

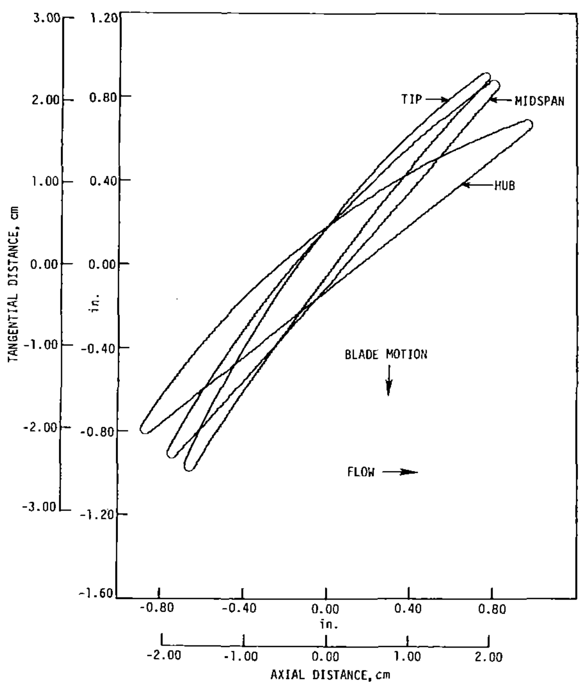

Fig. 2 Representative compressor rotor blade sections (same for baseline and swept stator builds)

Contributed by the Gas Turbine Division of The American Society of Mechanical Engineers and presented at the 31st International Gas Turbine Conference and Exhibit, Düsseldorf, Federal Republic of Germany, June 8-12, 1986. Manuscript received at ASME Headquarters February 11, 1986. Paper No. 86-GT-197.

Table 1 Summary of compressor design data

Number of stages	two
Rotor speed	2400 rpm
Flow rate	5.25 lb_m/s (2.38 kg/s)
Pressure ratio	1.0125
Number of blades per row	
Rotor	21
Stator	30
Blade material	fiberglass with steel trunnion and spine
Blade aerodynamic chord	2.39 in. (6.07 cm) constant for rotor and baseline stator 2.39 in. to 3.03 in. (6.07 to 7.70 cm) for swept stator
Blade aspect ratio	1.0 constant for rotor and baseline stator 1.0 to 0.79 for swept stator
Blade section profile	double circular arc
Blade stacking axis location	radial line through center of gravity of blade sections for rotor and baseline stator blades radial line through blade section trailing edge circle centers for swept stator blade
Leading and trailing edge radius to to aerodynamic chord ratio	0.01 constant
Maximum thickness to aerodynamic chord ratio	0.10 to 0.06 linear variation from blade root to other end of blade span
Annulus flow path	
Hub radius	5.60 in. (14.22 cm) constant
Tip radius	8.00 in. (20.32 cm) constant
Reynolds number based on aerodynamic chord and entering velocity at midspan	
Rotor	2.0×10^5
Stator	1.3×10^5
Flow coefficient	0.587

Axial-Flow Research Compressor

A sketch of the two-stage, axial-flow research compressor rig used for all of the tests is presented in Fig. 1. More details about the system may be found in [3, 4].

Each compressor stage was designed to be representative of typical modern compressor practice in terms of high stage reaction, axially discharging stators, and the absence of inlet guide vanes. A uniform spanwise distribution of total pressure was prescribed for the rotor exit. Double circular arc blade

Nomenclature

aspect ratio = ratio of blade span length to blade aerodynamic chord length
blade angle = angle between tangent to blade section camber line and axial direction, deg
blade setting angle = angle between blade aerodynamic chord and axial direction, deg
c = blade aerodynamic chord length, distance between blade leading and trailing edge circle centers, m
deviation angle = angle between circumferentially averaged exit flow relative to blade and tangent to blade camber line at trailing edge circle center, deg
diffusion factor = $1-\frac{V'_{\text{out}}}{V'_{\text{in}}}+\frac{r_{\text{in}}V'_{\theta,\text{in}}-r_{\text{out}}V'_{\theta,\text{out}}}{(r_{\text{in}}+r_{\text{out}})\sigma V'_{\text{in}}}$
head rise coefficient = ratio of head rise from inlet measurement station to exit measurement station across a blade row to rotor tip speed squared
loss coefficient = ratio of total head loss relative to and across a blade element from inlet measurement station to exit measurement station to dynamic head relative to blade at inlet measurement station
N = compressor drive shaft speed, rpm
overall efficiency = ratio of ψ_{overall} to $\psi_{\text{mechanical}}$
P = pressure side of blade
Q_v = venturi volumetric flow rate, m^3/s
r = radius from compressor axis, m
S = suction side of blade
T = compressor drive shaft torque, Nm
total head = ratio of total pressure to air density, Nm/kg
U = rotor blade speed, m/s
V = fluid velocity, m/s
ρ = air density, kg/m^3
σ = solidity, ratio of blade aerodynamic chord length to blade-to-blade distance between two adjacent blades
ϕ = flow coefficient, ratio of cross-sectional area average axial velocity to rotor tip velocity
$\psi_{\text{mechanical}} = \frac{\pi TN}{30\rho Q_v U_t^2}$
ψ_{overall} = ratio of cross-sectional area average total head at the second stage stator exit measurement station to rotor blade tip speed squared

Subscripts

h = hub (inner diameter) value
in = value at blade-row inlet measurement station
out = value at blade-row exit measurement station
t = tip (outer diameter) value
θ = tangential component

Superscripts

$'$ = relative to blade value

Table 2 Blade design details

		Solidity	Inlet Blade Angle, Degrees	Exit Blade Angle, Degrees	Blade Setting Angle, Degrees	Design Value of Diffusion Factor
Baseline rotor blade	90% span from hub	1.03	58.6	47.4	53.0	0.28
	midspan	1.18	54.3	41.6	47.9	0.29
	10% span from hub	1.37	49.8	32.1	41.0	0.32
Baseline stator blade	90% span from hub	1.47	21.6	-5.0	8.3	0.19
	midspan	1.68	21.6	-4.6	8.5	0.19
	10% span from hub	1.96	24.4	-4.8	9.8	0.20
Swept stator blade	90% span from hub	1.74	20.2	-4.2	7.9	0.18
	midspan	1.67	21.0	-4.5	8.3	0.19
	10% span from hub	2.33	22.8	-4.1	9.4	0.19

Table 3 Comparison of stator blade geometries

Similarities between Baseline and Swept Stator Blades

- Number of blades per row
- Blade surface finish
- Midspan chord length
- Spanwise distribution of maximum thickness to chord ratios

Differences Between Baseline and Swept Stator Blades

Baseline	Swept
Stacking point at center of gravity	Stacking point at trailing edge circle center
No leading-edge sweep	Symmetrical leading-edge forward sweep
Constant spanwise distribution of chord length	Varying spanwise distribution of chord length

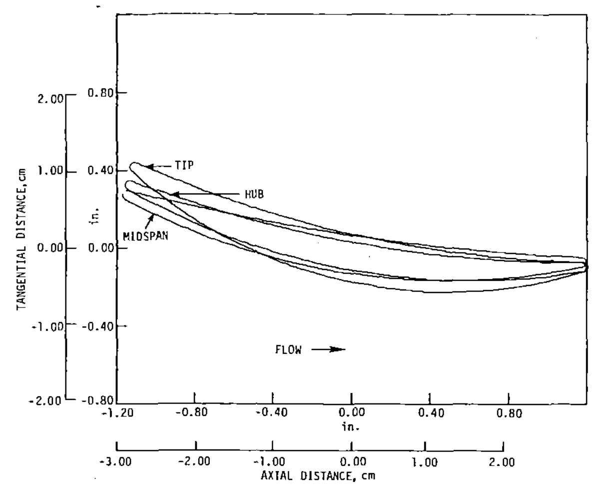

Fig. 3 Representative baseline stator blade sections

sections were considered appropriate for the low-speed testing involved. Design data are summarized in Tables 1 and 2.

The swept stator blades involved symmetric forward sweeping of each stator blade leading edge from midspan to the inner and outer endwalls as specified by the equation

$$\frac{c}{c_t}=1-0.8721\left(\frac{r_t-r}{r_t-r_h}\right)+0.8721\left(\frac{r_t-r}{r_t-r_h}\right)^2$$

Swept and baseline stator blades are compared in Table 3. Representative rotor and stator blade sections are sketched in Figs. 2, 3, and 4.

Stator hub clearances (running and stationary) were set at 0.034 in. (0.864 mm; 1.4 percent span). Other blading details, including fabrication information, may be found in [3, 4].

As illustrated in Fig. 5, the different geometry combinations tested were:

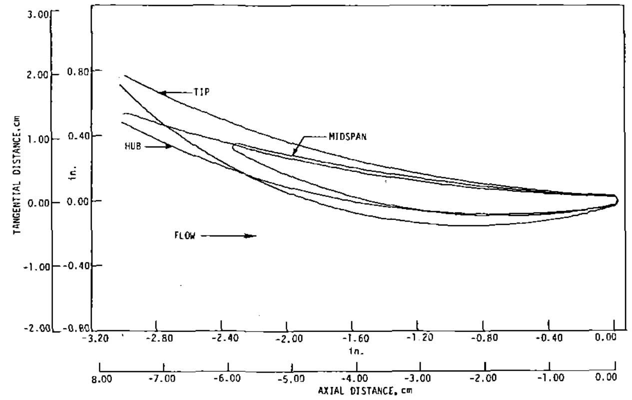

Fig. 4 Representative swept stator blade sections

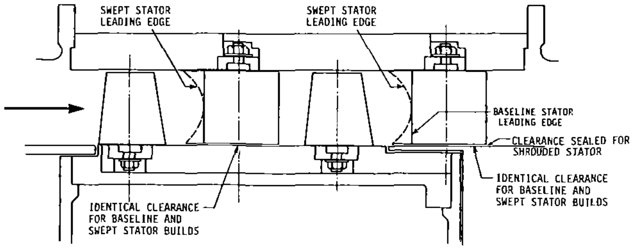

Fig. 5 Meridional plane view of compressor blading

1. baseline or swept stator, running hub clearance (first stage)
2. baseline or swept stator, stationary hub clearance (second stage)
3. baseline or swept stator, shrouded hub (second stage)

The compressor was operated at 2400 rpm for all tests.

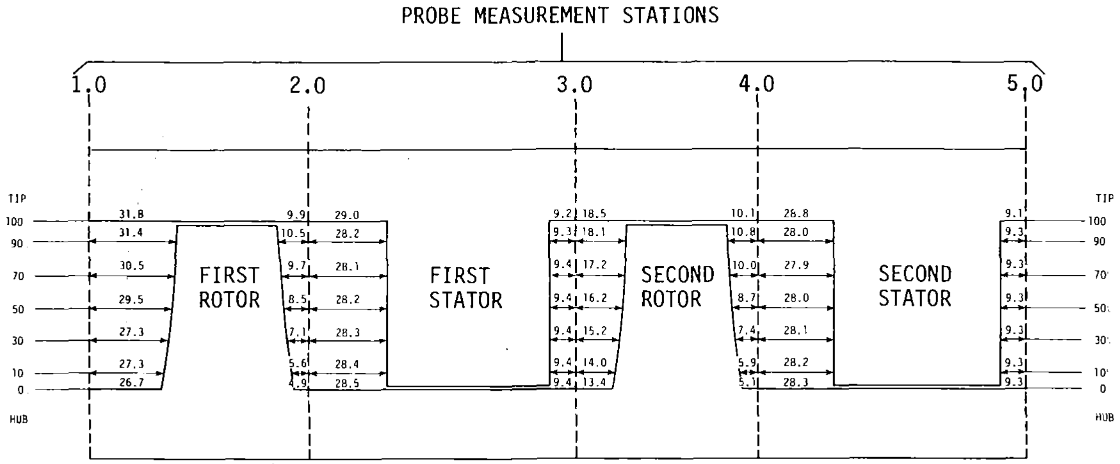

Fig. 6 Schematic showing axial locations of probe measurement stations relative to adjacent blade rows for baseline stator configuration (dimensions in mm)

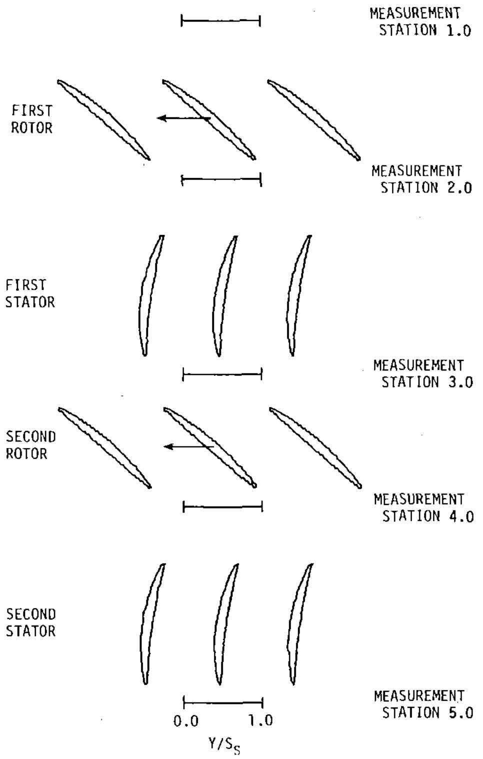

Fig. 7 Blade cascade showing circumferential measurement windows at midspan

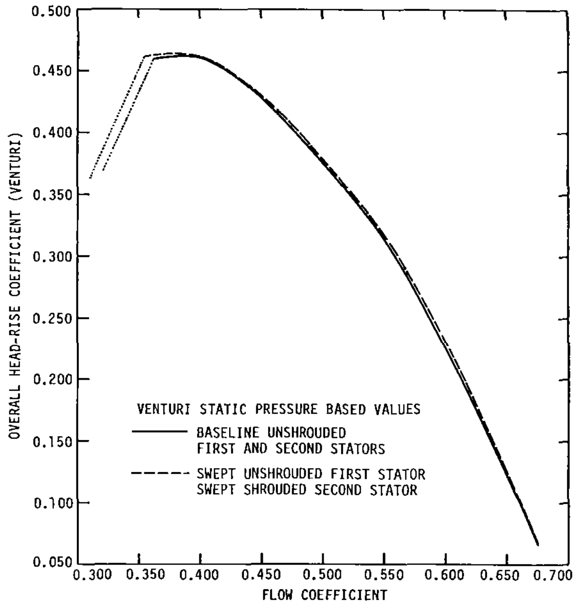

Fig. 8 Overall head rise for two compressor builds

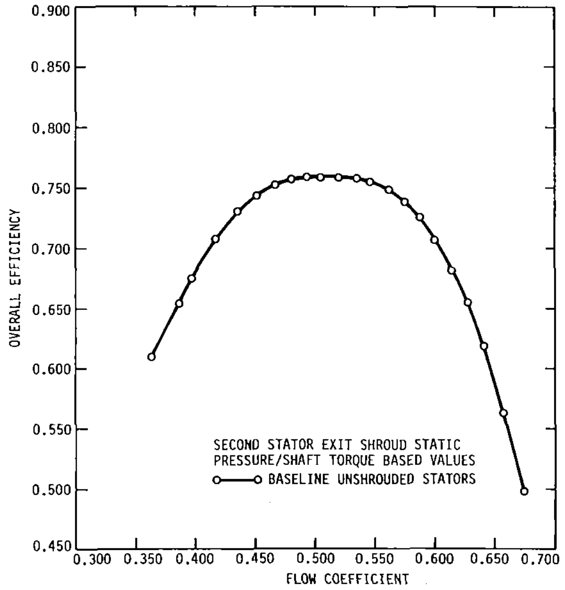

Fig. 9 Overall efficiency for the baseline unshrouded stator build

Table 4 Uncertainty estimates (20:1 odds)

Overall head-rise coefficient	±0.0034
Venturi flow coefficient	±0.0042 at $\phi = 0.4$ ±0.0034 at $\phi = 0.5$ ±0.0028 at $\phi = 0.6$
Overall efficiency	±0.021
Total head	±5.0 N-m/kg
Stator loss coefficient	±0.008
Stator deviation angle	±0.7 degree
Diffusion factor	±0.02

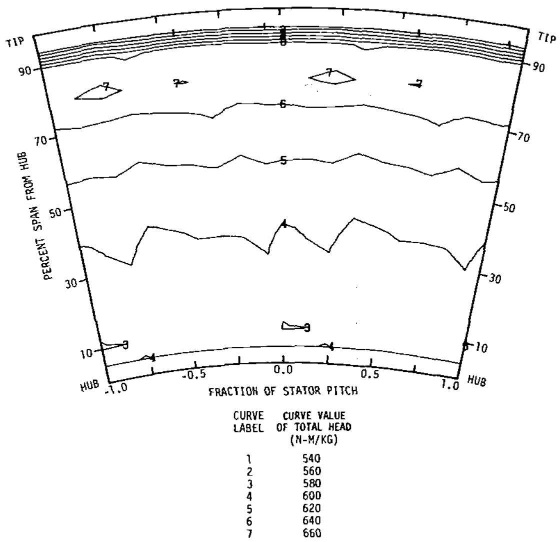

Fig. 10 Representative first-stage rotor exit total head contour map (ϕ = 0.500)

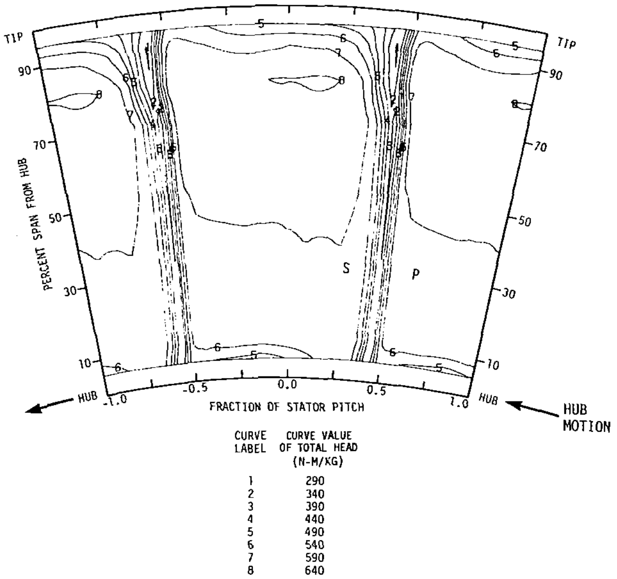

Fig. 11 Baseline unshrouded (running clearance) stator exit total head contour map (ϕ = 0.500)

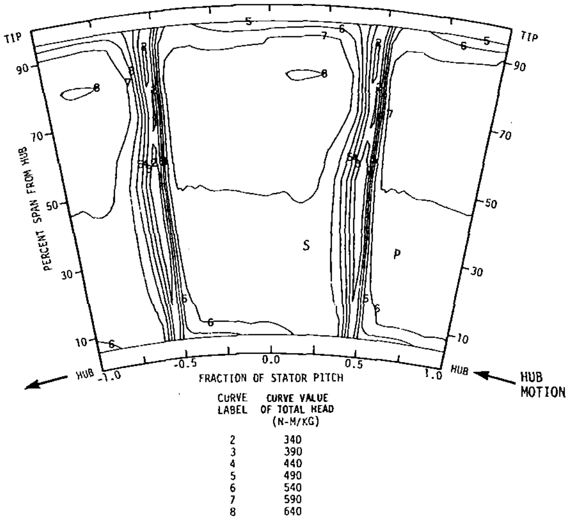

Fig. 12 *Swept unshrouded (running clearance) stator exit total head contour map (ϕ = 0.500)*

Table 5 Representative blade-element diffusion factor values based on experimental data

	90% From Hub	Midspan	10% From Hub
Rotor	0.37	0.36	0.40
Baseline stator with running clearance	0.33	0.28	0.31
Baseline stator with stationary clearance	0.32	0.28	0.36
Shrouded baseline stator	0.32	0.28	0.34
Swept stator with running clearance	0.28	0.29	0.31
Swept stator with stationary clearance	0.27	0.30	0.32
Shrouded swept stator	0.26	0.30	0.32

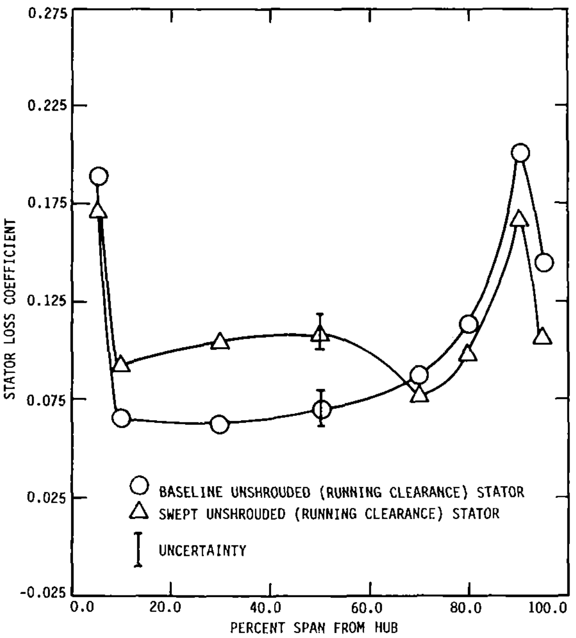

Fig. 13 Constant span total head loss values for baseline and swept unshrouded (running clearance) stators (ϕ = 0.500)

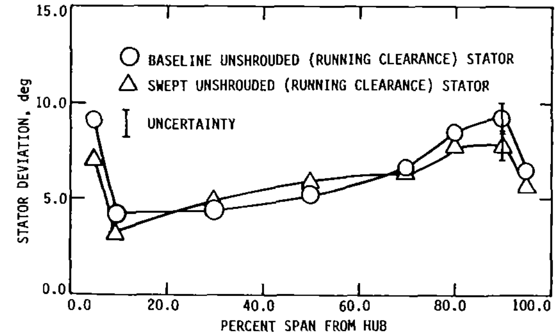

Fig. 14 **Deviation angles for baseline and swept unshrouded (running clearance) stators (ϕ = 0.500)**

Overall (atmosphere to venturi meter) head rise performance data were recorded for a range of flow rates. Detailed data were taken at a flow coefficient ϕ of 0.500 only.

Data Acquisition

All measurements were made with conventional slow-

Table 6 Comparison of passage-average stator loss coefficients for the first-stage stator builds

Build	Stator Loss Coefficient
Baseline unshrouded (running clearance) stator	0.090
Swept unshrouded (running clearance) stator	0.103

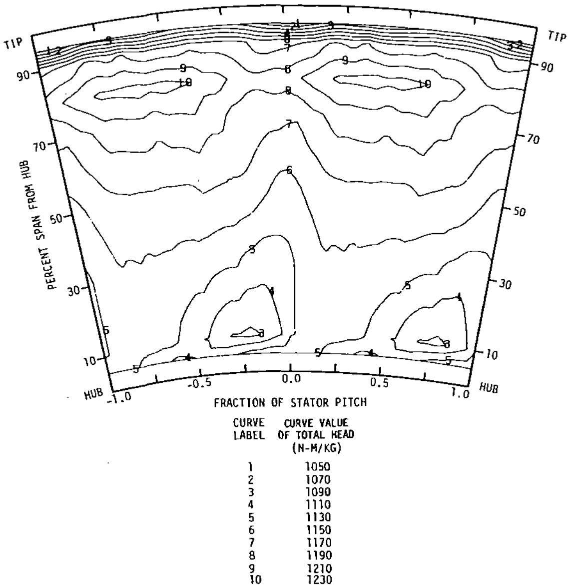

Fig. 15 Representative second-stage rotor exit total head contour map (ϕ = 0.500)

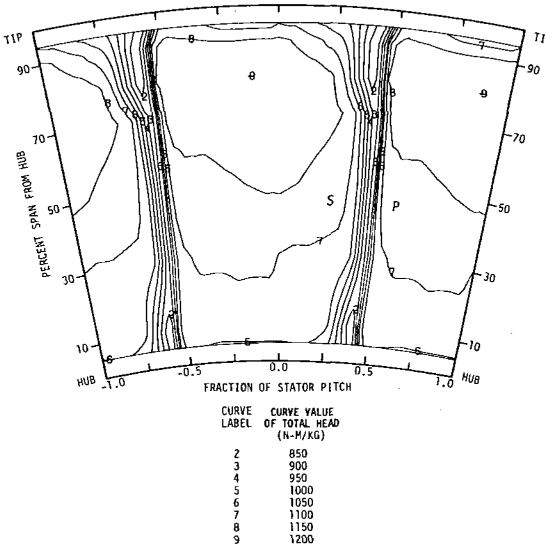

(b) BASELINE SHROUDED STATOR

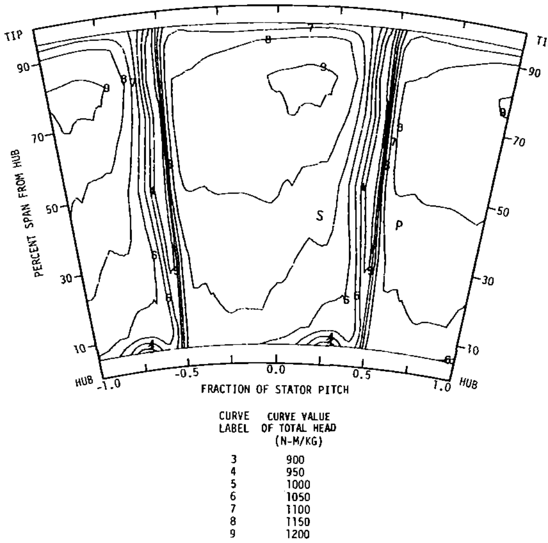

(c) SWEPT UNSHROUDED (STATIONARY CLEARANCE) STATOR

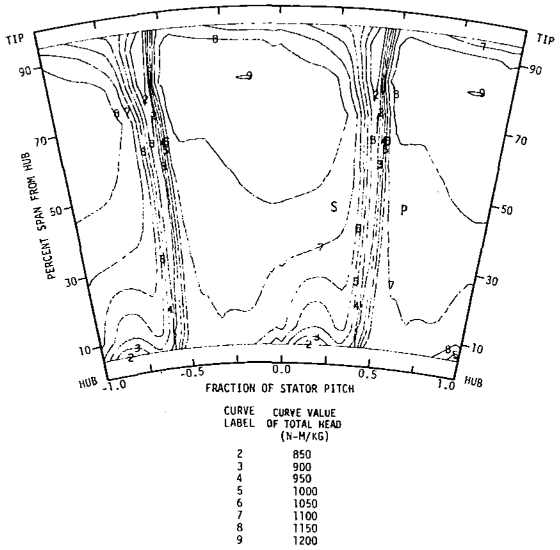

(a) BASELINE UNSHROUDED (STATIONARY CLEARANCE) STATOR

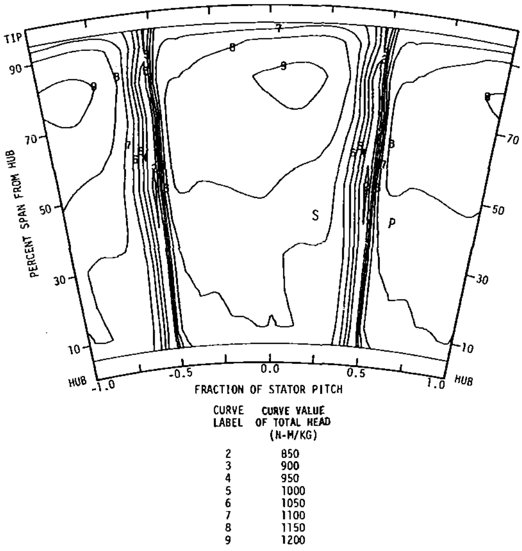

(d) SWEPT SHROUDED STATOR

Fig. 16 Second-stage stator exit total head contour maps for each build (ϕ = 0.500)

response instruments and a computer-controlled data acquisition system as explained in [3, 4]. Total pressures were measured with a Kiel probe. Static pressures were obtained through casing taps. Absolute flow angles were acquired with a "cobra" yaw probe. Axial locations of the measurement stations used are indicated in Fig. 6, and the circumferential location and extent of the midspan measurement windows at each axial station are conveyed in Fig. 7.

Experimental Results

As explained in [4], an uncertainty analysis of the experimental data was accomplished using the procedures of [5, 6]. Uncertainty estimates for data presented in this paper are summarized in Table 4.

Overall (atmosphere to venturi meter) head rise performance curves for two distinct compressor builds are shown in Fig. 8. The head rise and flow coefficient data used to construct these curves were obtained at the venturi flow meter where reliable casing tap data could be quickly acquired over a large range of flow rates for the two builds indicated. The difference in head rise between the two curves, while small, is considered significant in that it was repeatedly obtained. As also indicated in Fig. 8, the stall limit for the swept unshrouded first stator, swept shrouded second stator compressor build was at a lower flow than for the baseline unshrouded first and second stators configuration. Actually, the stall limit improvement shown was also obtained by a baseline unshrouded first stator, baseline shrouded second stator build and a swept unshrouded first and second stators version. The probable reason for the stall limit improvement will be discussed later when detailed second stage data are presented and discussed.

Overall efficiency data for the baseline unshrouded first and second stators build are provided in Fig. 9. These results were obtained with shaft torque and second stage stator row exit casing tap pressure measurements. Note that the operating flow coefficient selected for all of the detailed data runs, namely, $\phi = 0.500$, is well within the peak efficiency range for this configuration.

Measured total head data obtained at station 2.0 (between the first stage rotor and stator) for all baseline and swept stator builds were very similar [4]. For this reason, the results for the baseline unshrouded stators build only are shown in Fig. 10 to represent all station 2.0 data sets. The potential flow field influence of the first stage stator row was not discernible at station 2.0 even when the swept leading edges were used. Representative rotor blade element diffusion factors calculated from blade row solidity values and circumferentially averaged velocity data are summarized in Table 5 and indicate that the rotor was moderately loaded. In Fig. 10 and other similar figures that follow, data were acquired over one stator pitch only and were repeated periodically over a second pitch distance to enhance visualization of the flow patterns involved.

Measured total head data acquired at station 3.0 (between the first-stage stator and the second-stage rotor) for the baseline and swept unshrouded stators are presented in Figs. 11 and 12. The stator pressure and suction surface sides are designated with *P* and *S*. Between stations 2.0 and 3.0, total head losses occurred along all pathlines, even those associated with the core flow. In [7] the authors suggest that this core flow loss probably occurred mainly in the axial gap between rotor trailing and stator leading edges and is attributable to rotor wake mix out. It appears as if the mix-out loss rate is uniform across the core span; the trend in the spanwise distribution of the core flow total head remained unchanged between the measurement stations.

Near the casing (stator outer diameter), a substantially smaller region of lower total head fluid is associated with the suction side corner of the swept stator row than with that same corner of the baseline stator. The swept leading edge appears to have succeeded in drawing higher-momentum fluid into the suction corner and suppressing viscous flow region thickening there. For the pressure side corner, there is a little larger region of lower total head fluid for the swept stator row than for the baseline stator row. These trends are consistent with those observed by Senoo et al. [1] in their plane cascade tests. The swept leading edges alter the static pressure field in the endwall corner region of flow to such an extent that the above described behavior results. On a circumferential-average basis, there is less total head loss in the casing endwall region (70 to 95 percent span from hub) of the swept stator row than for the baseline stator row (see Fig. 13). The deviation angle results in Fig. 14 indicate that sweeping the leading edge also leads to generally better flow turning in the casing endwall region. The blade-element diffusion factors calculated from circumferentially averaged flow field measurements (Table 5) suggest that the swept stator blade was less loaded near the casing than was the baseline blade.

Near the moving hub (right to left motion as indicated by arrows on Figs. 11 and 12), where a 1.4 percent span clearance existed, the total head contours of Figs. 11 and 12 suggest the presence of a low-momentum region of flow from the pressure corner only. This region is an accumulation of lower-momentum fluid scraped off from the rotating hub and is larger for the swept stator blade than for the baseline stator blade. More fluid is scraped off the hub by the longer chord swept stator blade section near the hub. The suction side contours reflect the drawing away of low-momentum fluid from the suction corner by the moving hub surface. On a circumferential-average basis, there is less total head loss at 5 percent span from the hub for the swept stator row than for the baseline stator row; the swept leading edge resulted in a small benefit there. However, at 10 percent span from the hub, the opposite is true and the swept leading edge resulted in a detriment. The deviation angles are slightly smaller in this region of flow for the swept stator than for the baseline stator. The swept and baseline stator blades were about equally loaded near the running hub (Table 5).

From 10 percent to just short of 70 percent span from the hub, the total head loss of the baseline stator blade was appreciably less than that for the swept stator blade (see Fig. 13). The contour plots (Figs. 11 and 12) indicate a smaller portion of lower-momentum fluid on the suction surface of the baseline stator blade in the 10 to 70 percent span region than for the swept stator. The swept leading edge resulted in more lower-momentum, casing suction corner fluid being forced to the midspan region of the blade. The baseline and modified stator wake contours are similar on the pressure side. The deviation angles for the two kinds of blades are similar in the midspan region although slightly better for the baseline stators. The swept and baseline stator blades were equally loaded at midspan (Table 5).

On a passage-average basis, the loss values in Table 6 reveal that sweeping an unshrouded (running clearance) stator blade does not result in less loss for the entire blade. The baseline configuration is superior in the lower two thirds of the span in terms of loss. Sweeping does result in improved turning in the endwall regions and less loading in the vicinity of the casing, however.

Measured total head data obtained at station 4.0 (between the second stage rotor and stator) were very similar for the baseline and modified stator builds [4] and are represented by the contours of Fig. 15. Between measurement stations 3.0 and 4.0, the range of total head values over the passage is reduced substantially. At station 3.0, the range is 350 Nm/kg; at station 4.0, the range is 160 to 180 Nm/kg. There is ample evidence of stator wake chopping and dispersion as described by Smith [8]. A casing wall "boundary layer" is apparent.

Measured total head data acquired at station 5.0

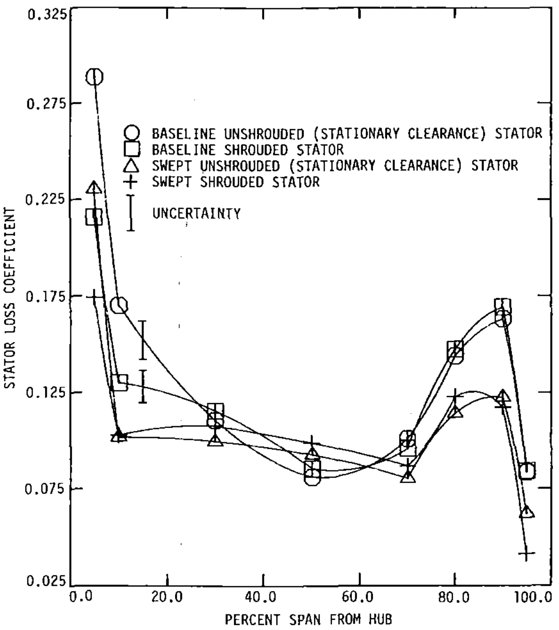

Fig. 17 Constant span total head loss values for baseline and swept unshrouded (stationary clearance) and shrouded stators (ϕ = 0.500)

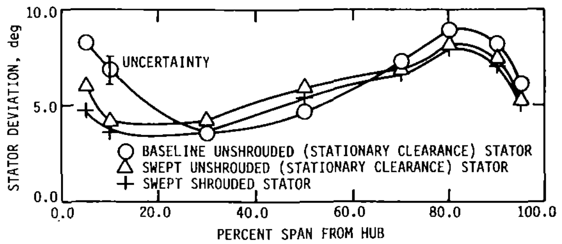

Fig. 18 Deviation angles for baseline and swept unshrouded (stationary clearance) and shrouded stators (ϕ = 0.500)

(downstream of the second-stage stator) for the baseline and swept stator builds are displayed in Fig. 16. Geometric details associated with each of the builds are easily seen in Fig. 5.

As in the first stage, total head losses occur along all pathlines between stations 4.0 and 5.0, even within the core flow.

The total head patterns in the casing and outer half of the annulus regions are similar for the two baseline stator builds and for the two swept stator builds. They differ, however, between baseline and swept stator blades. Hub shrouding did not significantly influence the flow in the outer half of the flow passage. The swept leading edge resulted in a substantial reduction of low-momentum fluid buildup in the suction-side casing (outer diameter) corner and a sizable increase of low-momentum fluid in the pressure side casing corner. On a circumferential-average basis (see Fig. 17), there is much less total head loss in the casing endwall region (70 to 95 percent span from hub) with the swept stator builds in comparison to the baseline ones. The leading-edge sweep also resulted in lower deviation angles in the casing endwall region (see Fig. 18). The second-stage swept stator blade was loaded less than the baseline blade in the casing region as in the first stage (Table 5).

In the stationary hub region of flow, all of the builds behaved differently. The total head contour data of Figs. 16(*a*) and 16(*b*) indicate that hub clearance leakage flow can result in a large accumulation of low-momentum fluid in the suction hub corner. This phenomenon has been observed by others (see, for example, [9]). The extent of this "leakage vortex" is substantially suppressed by the swept leading edge. The circumferential-average loss data of Fig. 17 demonstrate the corresponding large reductions in loss in the hub region (5 to 30 percent span) possible with sweep. Shrouding appears to be beneficial in terms of reduced hub losses for baseline and swept stators but more extensively so for the baseline configuration (Fig. 17). Sweeping a shrouded stator leads to better corner flow management. Data from Fig. 18 suggest that sweeping and shrouding improve blade turning performance in the hub endwall region. The improvement in stall margin noted earlier in this paper could be related to the extent of the second-stage stator hub leakage vortex. Sweeping and/or shrouding suppressed the formation of this vortex. Shrouding did not affect stator blade-element loading near the hub; sweep resulted in only a small reduction in hub loading (Table 5).

Table 7 Comparison of passage-average stator loss coefficients for the second-stage stator builds

Build	Stator Loss Coefficient
Baseline unshrouded (stationary clearance) stator	0.116
Baseline shrouded stator	0.113
Swept unshrouded (stationary clearance) stator	0.095
Swept shrouded stator	0.100

Near midspan, the swept stator blades suffered larger losses (see Fig. 17) and more deviation in flow turning (see Fig. 18) than the baseline stator blades, suggesting that low-momentum fluid from the endwall regions of the swept stators was moved toward midspan. Loading at midspan was similar (within uncertainty limits) for all second-stage stator configurations (Table 5).

Passage-average stator loss coefficients for the different second-stage stator builds are listed in Table 7. The improvements possible with stator leading-edge sweep are significant.

A comparison of the passage-average data of Tables 6 and 7 suggests that the baseline unshrouded (running clearance stator performed best of all those tested in terms of minimum loss. Inspection of more detailed results (see Figs. 11, 12, and 13) could lead to a proposal that in a running clearance situation, sweeping the stator leading edge near the casing only would be beneficial. Comparison of the loss data of Figs. 13 and 17 points out that the running hub clearance resulted in a significant reduction of loss over most of the lower half of the baseline stator span.

Conclusions

Leading-edge sweep in the endwall regions of a compressor stator blade can be beneficial on the casing (outer diameter) end of a stator blade. It can also help at the hub end of a stator blade when either a stationary hub clearance or a hub shroud is used. Sweep can be detrimental on the hub end of a stator blade when a running hub clearance is used.

If structural considerations allow a stator hub clearance, a running clearance is aerodynamically preferable to a stationary one.

Acknowledgments

We are grateful to George Serovy and Art Wennerstrom for suggesting that a study of stator leading-edge sweep as a possible means of improving axial-flow compressor endwall flows might be useful. George Serovy and Elmer Hansen were principals in the blade design process of this project. We appreciate their expertise. The Air Force Office of Scientific Research (Dr. James D. Wilson, Program Manager) is acknowledged for its financial support. The Iowa State University Engineering Research Institute Office of Research Services staff was very helpful in the preparation of this paper. We thank them for their competent assistance.

References

1 Senoo, Y., Taylor, E. S., Batra, S. K., and Hinck, E., "Control of Wall Boundary Layer in an Axial Compressor," Massachusetts Institute of Technology Gas Turbine Laboratory Report Number 59, Cambridge, MA, June 1960.

2 Wennerstrom, A. J., Law, C. H., Buzzell, W. A., and Derose, R. D., "Investigation of a 1500 ft/sec, Transonic, High-Through-Flow, Single Stage Axial Flow Compressor With Low Hub/Tip Ratio," AFAPL-TR-76-92, Air Force Aero Propulsion Laboratory, Wright-Patterson AFB, OH, Oct. 1976.

3 Hathaway, M. D., and Okiishi, T. H., "Aerodynamic Design and Performance of a Two-Stage, Axial-Flow Compressor (Baseline)," TCRL-24, Iowa State University Turbomachinery Components Research Laboratory, Ames, IA, Dec. 1983.

4 Tweedt, D. L., and Okiishi, T. H., "Stator Blade Row Geometry Modification Influence on Two-Stage, Axial-Flow Compressor Aerodynamic Performance," TCRL-25, Iowa State University Turbomachinery Components Research Laboratory, Ames, IA, Dec. 1983.

5 Kline, S. J., and McClintock, F. A., "Describing Uncertainties in Single Sample Experiments," *Mechanical Engineering*, Vol. 75, 1953, pp. 3-8.

6 Moffat, R. J., "Contributions to the Theory of Single-Sample Uncertainty Analysis," ASME *Journal of Fluids Engineering*, Vol. 104, 1982, pp. 250-260.

7 Hansen, J. L., and Okiishi, T. H., "Axial-Flow Compressor Rotor-Stator Interaction," TCRL-31, Iowa State University Turbomachinery Components Research Laboratory, Ames, IA, Dec. 1985.

8 Smith, L. H., Jr., "Wake Dispersion in Turbomachines," ASME *Journal of Basic Engineering*, Vol. 88D, 1966, pp. 686-690.

9 Leboeuf, F., Bario, F., Boris, G., and Papailiou, K. D., "Experimental Study and Theoretical Prediction of Secondary Flows in a Transonic Axial Flow Compressor," ASME Paper No. 82-GT-14, 1982.

Y. Kashiwabara

Y. Matsuura

Y. Katoh

N. Hagiwara

T. Hattori

Mechanical Engineering
Research Laboratory,
Hitachi, Ltd.,
Hitachi, Ibaraki, Japan

K. Tokunaga

Hitachi Works,
Hitachi, Ltd.,
Hitachi, Ibaraki, Japan

Development of a High-Pressure-Ratio Axial Flow Compressor for a Medium-Size Gas Turbine

In this paper, the development of a model 17-stage axial compressor (pressure ratio 14.7) for a medium-size gas turbine is described. The aerodynamic and mechanical design features of the compressor are presented. In advance of the full 17-stage test, the first three and nine stages were tested. Measured results confirm the design performance in the first stages of the 17-stage compressor. The details of the construction of the facilities, instrumentation and data acquisition system for the full 17-stage test are described. Test results for the 17-stage compressor are presented. The measured results are in good agreement with the predicted values.

Introduction

For industrial gas turbines, higher thermal efficiency has become increasingly important, resulting in a trend toward steadily increasing turbine inlet temperature and cycle pressure ratio. Thus, along with the development of high-temperature turbines and combustors, the development of high-pressure-ratio compressors with high efficiency has become important.

Higher thermal efficiency is achieved in a simple-cycle plant through a higher cycle pressure ratio. For a combined cycle plant, however, highest thermal efficiency is achieved by finding the optimum cycle pressure ratio corresponding to gas temperature. In our company the development of an axial flow compressor applicable to both simple and combined cycle plants, and with a pressure ratio of around 15, was planned. This pressure ratio was greater than that of the existing heavy-duty gas turbines. The overall cost of the compressor was to be reduced by decreasing the number of stages. To do this while maintaining the existing compressor efficiency, a highly loaded aerodynamic blading design was decided on.

A compressor size for medium-size gas turbines was chosen, as this size gas turbine is in demand in various markets of gas turbines and because, with slight modifications, the compressor can be used for large-size gas turbines which are also in demand. The particular compressor presented in this paper is a model compressor, and can be widely applied to various-sized gas turbines using the same fundamental technology.

In this paper, the development of the abovementioned compressor is described. The aerodynamic and mechanical design features of the model compressor are given and details of the facilities for testing the compressor, instrumentation, and data acquisition system are presented. Test results presented agree well with the design values.

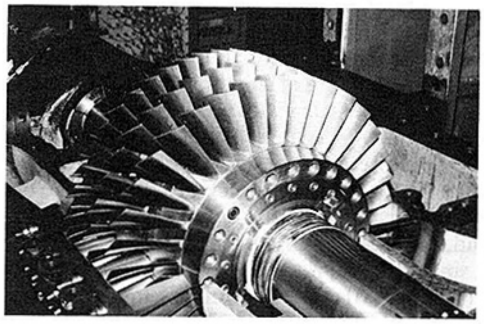

Fig. 1 Three-stage rotor

Compressor Design

Aerodynamic Design. To begin with, the first highly loaded three stages of the 17-stage compressor were designed and tested to confirm the validity of the highly loaded design. Figure 1 shows the three-stage rotor with the upper half of the outer casing open. The design pressure ratio is 2.2 for the three stages with the inlet guide vane (IGV). To achieve such a relatively high pressure ratio, the relative inlet Mach numbers of rotor blades become so high that the NACA-65 profiles used in subsonic blade rows are not appropriate for the rotor blading. To avoid large shock losses caused by higher Mach numbers, the DCA (double circular arc) profiles were used for the first and second-stage rotor blades of the compressor. For the rest of the blading, the NACA-65 profiles were used. The tip speed of the first rotor blade was 354 m/s and the tip

---

Contributed by the Gas Turbine Division of THE AMERICAN SOCIETY OF MECHANICAL ENGINEERS and presented at the 31st International Gas Turbine Conference and Exhibit, Düsseldorf, Federal Republic of Germany, June 8–12, 1986. Manuscript received at ASME Headquarters January 17, 1986. Paper No. 86-GT-85.

Table 1 Main specifications of compressor

SPECIFICATIONS of COMPRESSOR	
PRESSURE RATIO	14.7
MASS FLOW	36.3 kg/s
ROTATIONAL SPEED	10,800rpm
NUMBER OF STAGES	17
POWER	14,000kW

Table 2 Main stage parameters

ROTOR BLADE SPECIFICATIONS			
		1st STAGE	17th STAGE
AEROFOIL of BLADES		DOUBLE CIRCULAR ARC	NACA 65
HUB/TIP RATIO		0.621	0.860
ASPECT RATIO		1.77	1.49
SOLIDITY	TIP	0.88	0.89
	HUB	1.41	1.03
BLADE HEIGHT (mm)		118	37.5
TIP DIAMETER (mm)		625.8	535.9

relative Mach number was 1.03. The outer casing of the flow path has a constant diameter and the hub/tip ratio of the first stage is 0.621.

After several vortex designs were examined, the design of stator blades with constant efflux angles was chosen, because of the small twist in these stator blades.

Various methods of calculating the three-dimensional flow in axial turbomachines have been presented over the past many years. One of the authors [1] has presented a parameter theory for the calculation of the compressible flow in axial turbomachines with arbitrary flow path shapes. This theory is conceptually simple, because the axial velocity profiles are assumed to be expressed by a single parameter. Therefore, this theory is useful for gaining a quick insight into the design and off-design performance of the compressor. However, on the other hand, the accuracy of the theory would deteriorate in the case of a small hub/tip ratio, especially in the vicinity of outer and inner casing. After the preliminary investigations of flow by this theory, the aerodynamic detailed design of blading was finally performed by the streamline analysis method of repeating the streamline approximation based on the radial equilibrium equation for the compressible axisymmetric flow through blade rows [2]. The velocity triangles were decided for each blade row taking into account the shape of the meridional streamline through flow path.

The characteristics of the three-stage compressor were calculated, and compared with the measured results shown later in Fig. 13, *confirming the validity of the design method for highly loaded design stages.* The surge point at each rotational speed was predicted by the theory of [3]. The agreement with the measured surge point was good (see Fig. 13).

Based on the above test results for the three-stage compressor, aerodynamic design of the complete compressor started. Following various investigations a pressure ratio of 14.7 and a stage number of 17 with IGV and EGV (exit guide vane) were finally decided on. The selection of 17 stages was made as a result of the studies considering both the compressor efficiency and cost. Although the aim of the present compressor is application to medium-size gas turbines, detailed tests were performed on the model compressor to develop a machine for application to various-sized gas turbines. Manufacturing an excessively large machine, which requires large facilities, was deemed undesirable. Furthermore, the compressor was expected to function as the air source in testing gas turbine combustors. Considering the requirements of the compressor, the air flow rate of 36.3 kg/s (under ISO conditions) was selected. The main compressor specifications are shown in Table 1.

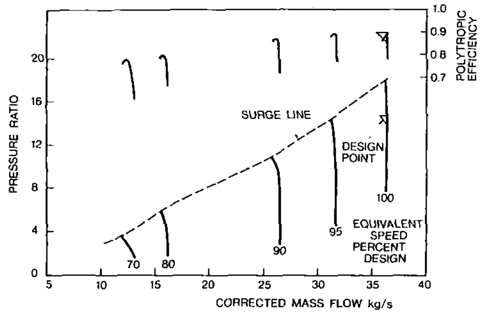

Fig. 2 Predicted characteristic of 17-stage compressor

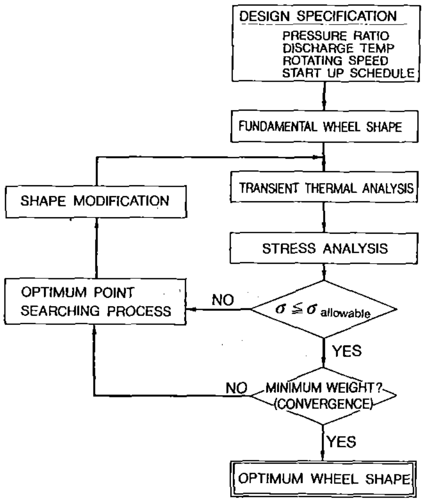

Fig. 3 Wheel shape optimization system flow diagram

The vortex distribution from the first to third stage is the same as that of the three-stage compressor, i.e., constant efflux angle at stator blade outlet. For the 6th to 17th stages, the free-vortex design was adopted, and for the 4th and 5th stages the half-vortex design was selected. Using the streamline analysis method and calculating the development of the end-wall boundary layer, the velocity triangles at each stage were decided in the same way as in the three-stage compressor. The blade parameters of the first and 17th stages are shown in Table 2.

The high pressure ratio of the present compressor requires variable geometry stators and a bleed system in order to ensure an adequate surge margin during startup. For this reason, the first and second-stage stator were made with variable geometry in addition to a variable IGV, and a bleed port was provided for the tenth stage. The schedule of the variable geometry was decided according to the results of the characteristic calculation.

Figure 2 shows the result of the characteristic prediction of the 17-stage compressor. The prediction of the surge line was made by the theory in [3] as in the three-stage compressor. The results of Fig. 2 indicate that the design mass flow and the design pressure ratio are achieved with acceptable efficiency.

Mechanical Design. In the following, among the features of mechanical design of the compressor, the design system of the wheels, blade dovetails, and blade vibration are presented.

Wheel Design. The test compressor has a wheel-stacking construction. Axial flow compressor wheels receive both cen-

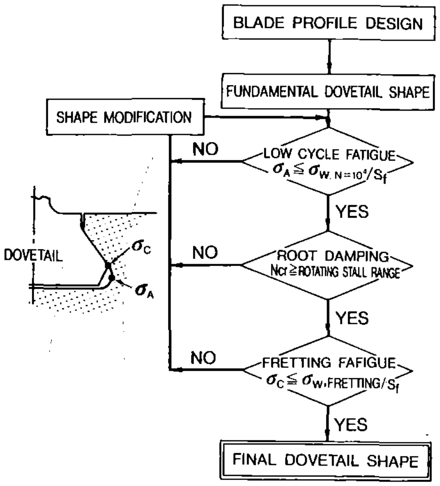

Fig. 4 Dovetail design process flow diagram

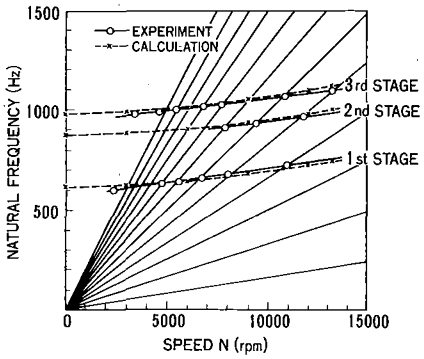

Fig. 5 Natural frequency of rotor blade

trifugal and thermal loads. These loads are increased in accordance with the trend of increase of rotor speed, pressure ratio, and discharge temperature of the compressor. On the other hand, the rotor weight of the compressor has to be kept light under the restriction of bearing loads and rotor dynamics. One of the authors has developed the optimum wheel design system [4] which uses the sequential linear programming method. By this system the minimum weight wheel shape could be obtained keeping both transient thermal stresses and centrifugal stresses less than the allowable stress limit. The flow diagram of this system is shown in Fig. 3. After the aerodynamic design specifications were decided, the fundamental wheel shape can be roughly obtained. Then, the transient thermal analysis and stress analysis were performed. Stress analysis was carried out by using Donath's method. In this method the wheels are divided into many rings and the stress distributions can be calculated by satisfying displacements and stress conditions through whole rings. The optimum wheel shape can be obtained by searching for the minimum weight shape which satisfies the whole-wheel stresses under the allowable stress limit. The details of this design system are described in [4].

Blade Dovetail Design. Blade dovetails have very important functions not only as supporting parts for the centrifugal force of blades but also as dampers of blade vibration. Therefore, in the design of blade dovetails of the compressor, the design criteria shown in Fig. 4 were used.

First, the low cycle fatigue strength at the dovetail slot corner is considered. The equation for calculating the local stress at the dovetail slot corner σ_A was given in [5] by one of the authors. Then the blade damping properties are considered as follows. In the rotating stall condition dovetail contact surfaces should slip and the vibration energy of blades will be absorbed by this slippage. To achieve this condition the dovetail must slip under the allowable bending moment M_a at which the bending stresses of the blade profile reach the fatigue limit of the blade material. The critical bending moment M_{cr}, at which the dovetail slips, can be calculated as given in [5]. Critical rotating speed N_{cr} is defined as that speed at which the critical bending moment M_{cr} reaches the allowable bending moment M_a.

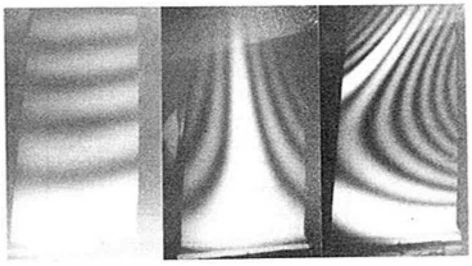

First mode Second mode Third mode

Fig. 6 Blade vibration mode by holography

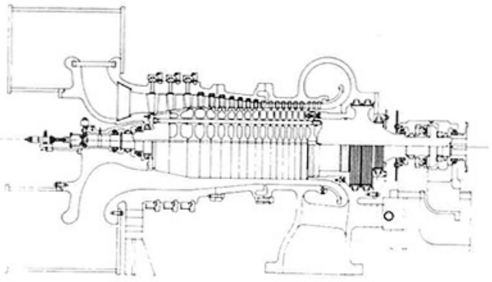

Fig. 7 Cross section of 17-stage compressor

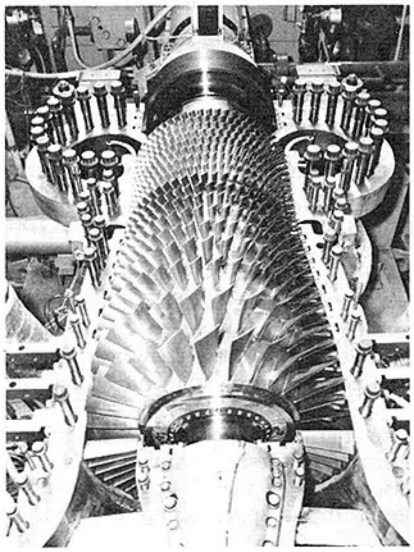

Fig. 8 Seventeen-stage compressor with upper casing removed

Finally, the fretting fatigue strength at the dovetail contact edges is considered. σ_c is the stress at the dovetail contact edges. The stress analysis by Finite Element Method (FEM) and fretting fatigue test of this dovetail region were performed, and detailed information on these criteria may be found in [6].

Design for Blade Vibration. From the viewpoint of blade vibration, there are at least two things that should be considered. The first one is the blade response to engine order excitations. It is necessary to calculate precisely the natural frequencies of each blade and to estimate the vibration response. Figure 5 is the result of an experiment of the previously stated

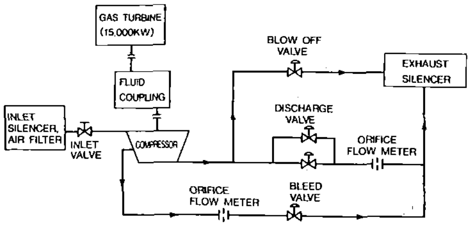

Fig. 9 Test facility arrangement

three-stage model compressor and the calculation by FEM under the boundary condition assuming that each blade is fixed at its roots. The results show that the natural frequencies can be predicted satisfactorily except in the lower speed region which does not cause any severe vibration problems. Concerning the vibration modes, an example of which is shown in Fig. 6 by the holography method, the calculation coincides with the experiment and can indicate where the blade stress is maximum.

The estimation of the blade response is based on the magnification factor method. This method corresponds to the response factor used to calculate an amplitude of vibration stress σ_b from a static stress σ_s

$$\sigma_b = \alpha\sigma_s < \sigma_{\text{all}}$$

$$\sigma_{\text{all}} = \text{allowable stress}$$

where σ_s is the stress of a blade subjected to steady pressure distribution.

The magnification factor α is usually defined as $\alpha = \beta/N$. N is the ratio between the natural frequency and the rotating speed. The coefficient β is obtained from many measurement results, and depends on the boundary conditions of fixed blades.

The second is the blade response to rotating stall phenomena. The rotating stall can occur at a relatively low speed or in the region that the flow decreases and the pressure increases. As the rotating stall shows unqualified different patterns according to the operating condition, several experiments of model compressors have been carried out. The blade response due to rotating stall can be deduced from the results.

According to the abovementioned design systems, the 17-stage compressor was designed and manufactured. Figure 7 shows the cross section of the 17-stage compressor. Figure 8 shows the rotor with the upper casing removed.

Test Facility

The facility for testing the 17-stage compressor was designed to provide the needed aerodynamic and mechanical detailed measurements at the various operating conditions. The arrangement of the facility is shown in Fig. 9. A photograph of the compressor test stand is shown in Fig. 10. The driver of the test compressor is a single-shaft gas turbine with the nominal output of 15 MW. The rotational speed of the output shaft of the gas turbine is constant at 5100 rpm. However, a hydrodynamic power transmission (a variable speed fluid coupling and a step-up gear) was installed between the driver and the test compressor to allow the rotational speed of the compressor to be changed without discontinuity from the design speed to the part speed simply by moving the scoop-tube of the fluid coupling. A butterfly valve was installed in the inlet duct to reduce the inlet total pressure. In the high-speed range, occurrence of a surge would damage the parts of the compressor. The reduction of the inlet pressure is effective in reducing the stresses due to surge. It also reduces the power required to drive the compressor. As the inlet valve introduces a high degree of turbulence while reducing the inlet pressure, it is followed by two perforated plates and a wire mesh to reduce turbulence.

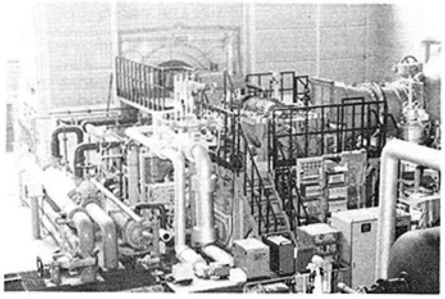

Fig. 10 Compressor test stand

In the discharge ducting, two throttle valves of different sizes are installed. The outlet pressure of the compressor is controlled by these two valves. The larger valve is closed at the smaller mass flow, and only the smaller valve is used to control the outlet pressure. Besides these, a small blow-off valve was installed. It is designed to open rapidly by the action of the compressed air at the surge onset. The bleed flow at the tenth stage can be controlled by a bleed valve. The variable inlet guide vanes and the variable stator blade of the first and second stage can be operated separately with an oil actuator, so that the effect of the variable geometry on the startup operation can be examined.

All of the facilities described above, including the driving gas turbine, are operated through the control panel in the control room.

Instrumentation

The test compressor operating parameters were measured in detail under the various operating conditions. The total pressure distribution in the radial direction at the inlet plane immediately before IGV and at the outlet plane immediately after EGV are measured by use of the kiel-type total pressure rakes respectively located at three different positions on the circumference of the outer casing of the compressor. The wall static pressure was measured at the position between each stage on the outer casing by means of the static pressure orifices, so that the operating conditions of each stage could be examined. The numerous pressure measurement data are connected to the pressure transducer via a scanivalve. According to the pressure range, four different pressure transducers are used to obtain the maximum accuracy.

The total temperature distribution was also measured by total temperature rakes at the inlet and outlet plane. The discharge mass flow and the bleed mass flow at the tenth stage are measured by orifice plates.

In order to measure the internal flow, an attempt to traverse a probe in the radial direction was made. The axial gap between blade rows is small, so the traversing was possible only at limited locations in the compressor. The traversing apparatus attached to the outer casing was prepared, which was remotely controllable at the control room. The probe is driven into the gap between the blade rows by a motor through a flexible shaft.

In a multistage compressor, rotating stall usually occurs in the low-speed region. It is important for designers to get information about this unsteady phenomenon, in order to avoid high vibratory stresses on the blades. The phenomenon of rotating stall has been studied extensively by various investigators. However, so far no theory can predict accurately the number and speed of stall cells for the present compressor; therefore, measurements of rotating stall were performed. The dynamic wall static pressure was measured by means of the miniature strain gage pressure transducer attached to the pressure orifices at the outer casing. Different transducers were used for different pressure ranges. The dynamic wall pressure was measured at the outlet of the rotor blades of the

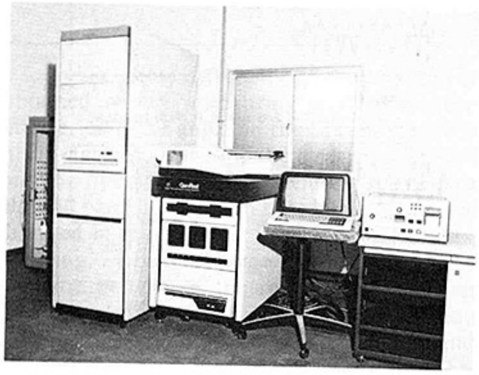

Fig. 11 Computer and peripherals in control room

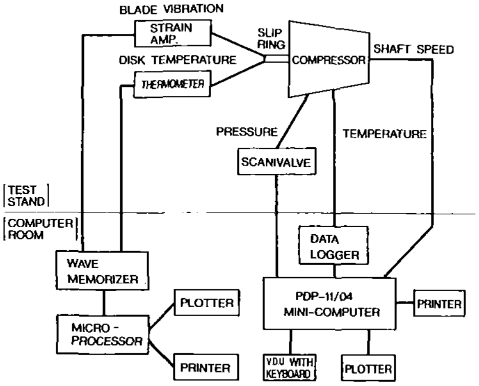

Fig. 12 Data acquisition system

second, eighth, and thirteenth stages. At the second stage two transducers were located at two different positions on the circumference of the casing. At the eighth and thirteenth stages, water-cooled transducers were used. The outputs from the transducers were passed through an amplifier and recorded by a data recorder.

While aerodynamic measurements were taken, the stresses and temperatures of the rotor were also measured. The vibratory stresses of blades were measured by means of strain gauges located at the roots of the blades. The data obtained for rotors were taken out through a slipring (100 ch.).

The usual monitoring of shaft vibration, bearing temperature, etc., was carried out to protect the compressor mechanically.

All the data obtained on the compressor were transmitted to the control room. A mini-computer PDP-11/04 was used to sample and analyze the data. Peripherals such as a line printer, a graph plotter, and a Visual Display Unit (VDU) with keyboard were also available. Characteristics of the compressor can be displayed on these peripherals quickly.

Figure 11 shows the computer and peripherals located in the control room. Figure 12 shows the entire system of data acquisition.

Test Results

As described previously the test of the first three stages was carried out first. The measured characteristics and the achievement of the design goals are shown in Fig. 13. The relatively good agreement between the measured and calculated surge point can also be seen.

Then, prior to the complete 17-stage compressor test, the test of the first nine stages was carried out. The results of the test showed the achievement of the design performance for the 9-stage compressor. Following that, the test of the full 17 stages started. Next, the measured results of both the steady-state performance and the rotating stall of the 17-stage compressor are presented.

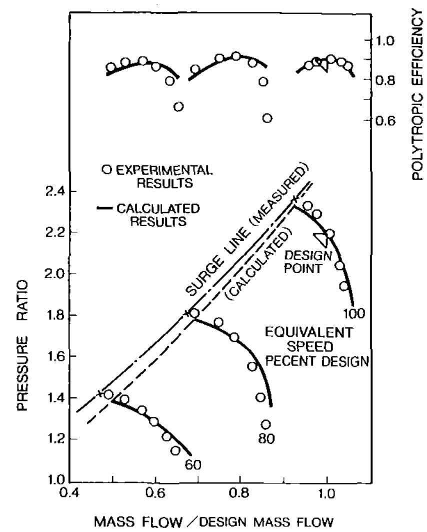

Fig. 13 Three-stage compressor characteristics

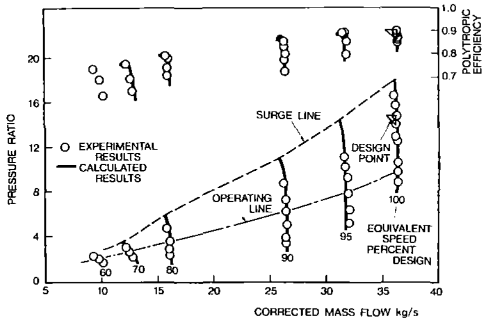

Fig. 14 Measured characteristics of 17-stage compressor

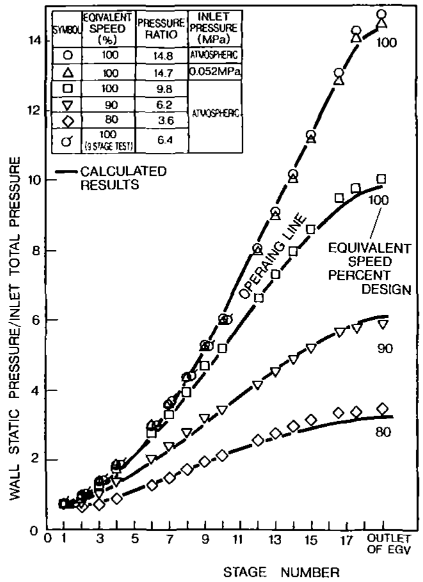

Fig. 15 Wall static pressure variation

The measured overall characteristics of the compressor are shown in Fig. 14, which also shows that the design performance was achieved. Comparison between the measured and predicted results (Fig. 2) shows good agreement. The surge line was predicted by the theory of [3]. As mentioned above, the accuracy of this method seems to be acceptable. Figure 14 shows the compressor has an adequate surge margin, more than 20 percent at each point on the operating line, and also at the design point, which was aimed at the aerodynamic design. Figure 15 shows the wall static pressure rise at each stage.

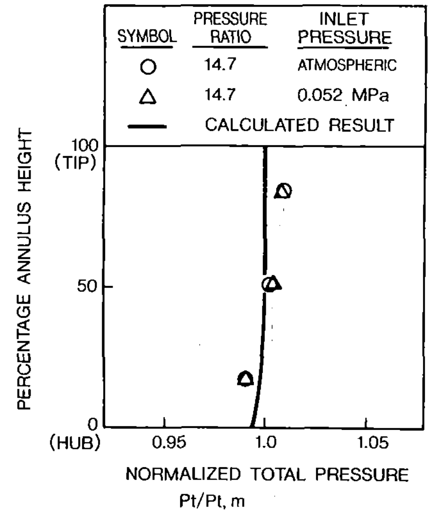

Fig. 16 Radial distribution of total pressure at compressor outlet (design point)

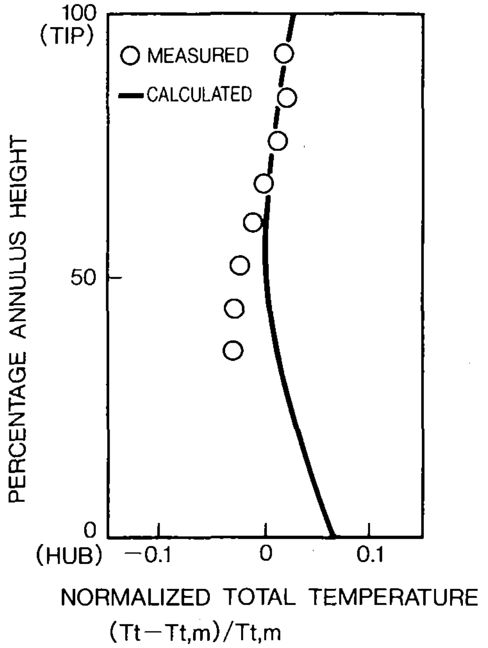

Fig. 17 Radial distribution of total temperature at thirteenth stage (design point)

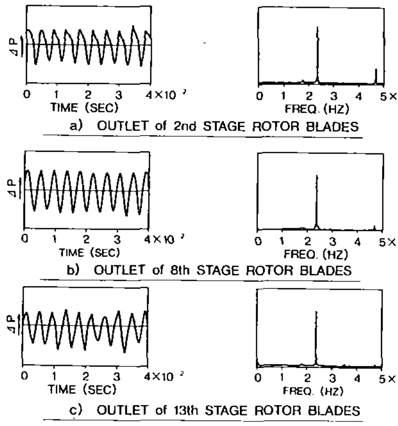

Fig. 18 Instantaneous wall static pressure and spectrum (7000 rpm)

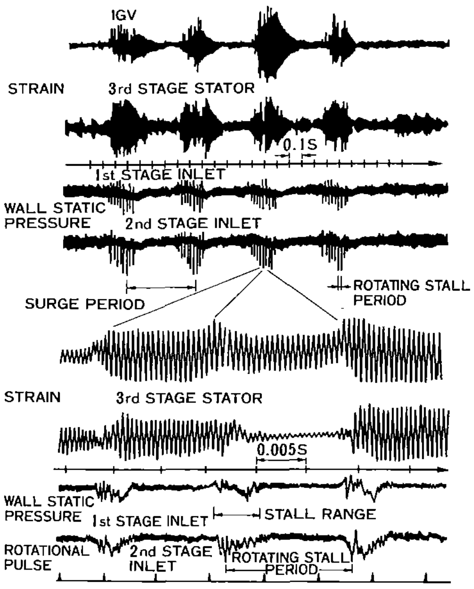

Fig. 19 Blade vibration and wall static pressure variation during rotating stall in three-stage compressor

These data show the pressure rise at the design point and at the point on the operating line of Fig. 14. On the whole, comparison of the measured results with the calculated results given by the solid lines shows good agreement, and it confirms the good aerodynamic matching of each stage. In the same figure, the results of the test of the first nine stages are shown. The agreement with the 17-stage test results was good. In Fig. 15, the results of 17-stage test at a reduced inlet pressure of about 0.5 atmosphere are also shown. At the point on the constant speed line close to the predicted surge line, the test was carried out at the reduced inlet pressure, in order to avoid damage at surge onset. The mean cascade Reynolds number of the compressor is 1.2×10^6, so that, at the reduced inlet pressure of 0.5 atmosphere, the particular change of the pressure rise cannot be recognized.

Next, the results of the measurement of the internal flow are shown. The results of measuring the total pressure and total temperature at the inlet plane before IGV confirmed their uniform distribution at the inlet of the compressor in both the radial and circumferential directions. Figure 16 shows the radial distribution of the total pressure at the outlet plane after EGV at the design point. The total pressure is normalized by the calculated value at 50 percent height $P_{t,m}$. Also the results of the reduced inlet pressure test are shown. The difference between the measured and calculated total pressure was less than 1 percent of the mean value. Figure 17 shows the radial distribution of total temperature at the outlet of the rotor blade of the thirteenth stage which was measured by means of the traversing apparatus as stated already. The axial distance between the blade rows was very small. A cylindrical total temperature probe of 4 mm diameter was used. However, because of the danger of contact with the rotor blades, the measurement near the hub was omitted. The total temperature is shown by normalizing with its value at 50 percent height. Both the measured and calculated results show the increase of total temperature at the outer casing. The agreement between calculation and measurement is relatively good.

As shown above, the results of the measurement of the steady-state performance of the 17-stage compressor confirmed the validity of the design method described herein.

As mentioned previously, it is important to have accurate knowledge of rotating stall occurrence in the present compressor. The dynamic wall static pressure was measured by means of pressure transducers attached to the static pressure orifices on the outer casing. The number of the stall cell K and the propagation frequency of the stall cell f_s are obtained as follows

$$K = \Delta\varphi / \Delta\theta \quad (1)$$

$$f_s = f_R / K \quad (2)$$

where $\Delta\varphi$ is the phase difference of the two stall cell frequencies obtained at two measuring stations on the same circumference, $\Delta\theta$ is the angle on the circumference between two measuring stations, and f_R is the frequency of stall cell.

Along the operating line of the compressor plotted in Fig. 14, below 50 percent of design speed the distinct stall cells were not observed in the dynamic pressure signals obtained at the outer casing. Above 50 percent of design speed, the characteristic pattern of the rotating stall cell appeared. In Fig. 18 examples of the instantaneous wall static pressure variations at the outlet of the second, eighth, and thirteenth stage rotor blades are given. From the spectra calculated from the pressure variations and using equations (1) and (2), the number of stall cells was four and the speed of the cell was 50 percent of the rotor speed. The phase difference $\Delta\varphi$ was obtained from two signals measured at two positions on the annulus outlet of the second-stage rotor blades. Above 74 percent of the design speed the stall cell disappeared. During rotating stall the number of cells was unchanged and also the speed ratio of the cell to the rotor speed was nearly constant—50 percent. Reference [7] showed analytically that for multistage compressors the speed of cell approached 50 percent of the rotor speed. The results of Fig. 18 supported this conclusion experimentally. From Fig. 18, it can be supposed the stall cells penetrate the front and middle stages. The cross correlations of the signals at each measuring position showed the cells extended almost axially through the stages.

The measurements of the vibratory stresses of blades were also carried out during the rotating stall. They were less than 50 $\mathrm{N/mm^2}$.

The measurement of rotating stall cells was also performed during the previously described three-stage compressor test. Figure 19 shows the results measured at the operating point which is beyond the limit of surge occurrence at the design speed [8]. It indicates that rotating stall and surge happened simultaneously in this case. This composite variation might be a transient phenomenon to surge range, but more detailed studies will be needed. When a stall cell passes a blade, it causes the blade to vibrate as an impulsive force. The blade vibration, once excited by an impulsive stall cell, decreases gradually as a free vibration until the next stall cell comes to the blade. The amplitude of the blade vibration can decrease or increase according to the relation of the phases and the frequencies between the blade and the rotating stall.

Conclusion

The development of a 17-stage axial flow compressor with a pressure ratio of 14.7 and a mass flow of 36.3 kg/s was presented. The main features of the aerodynamic and mechanical design of the compressor were described.

The test facility, instrumentation, and data acquisition system were presented.

The test results of the first three stages and nine stages and of the complete 17-stage compressor showed the achievement of the design performance. Along with the results of the steady-state performance the results of measuring rotating stall were given.

Acknowledgment

The authors would like to acknowledge the contributions of all personnel at Mechanical Engineering Research Laboratory and Hitachi Works, Hitachi, Ltd. involved in the development of the compressor, construction of the test facility, and in the test of the compressor.

References

1 Kashiwabara, Y., "A Two-Parameter Theory of Axisymmetric Compressible Flow in Axial Turbomachines," *Bull. JSME*, Vol. 11, No. 43, 1968, p. 134.

2 Novak, R. A., "Streamline Curvature Computing Procedures for Fluid-Flow Problems," ASME JOURNAL OF ENGINEERING FOR POWER, Vol. 89, 1967, p. 478.

3 Ohyama, K., "Investigation on Compressor Surge," *Trans. Jpn. Soc. Mech. Eng.*, Vol. 44, No. 387B, 1978, p. 3810.

4 Hattori, T., Ohnishi, H., and Taneda, M., "Optimum Design Technique of Rotating Wheels," ASME Paper No. 86-GT-255, 1986.

5 Hattori, T., Okamoto, H., and Mori, Y., "Deformation and Slipping Behavior of Blade Dovetail," *Journal of Gas Turbine Soc. of Japan*, Vol. 10, No. 40, 1983, p. 33.

6 Hattori, T., Sakata, S., and Ohnishi, H., "Slipping Behavior and Fretting Fatigue in the Disc/Blade Dovetail Region," *Proc. of Tokyo Int. Gas Turbine Cong.*, 83-Tokyo-IGTC-122, 1984, p. 945.

7 Takata, H., "Rotating Stall in a Multistage Axial Compressor," *Trans. Jpn. Soc. Mech. Eng.*, Vol. 26, No. 1711, 1960, p. 1598.

8 Hagiwara, N., Yoneyama, M., Ishii, H., Matsuura, Y., and Kashiwabara, Y., "Blade Vibration During Rotating Stall in Axial Flow Compressor," *Turbomachinery*, Vol. 13, No. 4, 1985, p. 193.

The "Axi-Fuge"—A Novel Compressor

J. O. Wiggins
Chief, Research Aerodynamicist,
Solar Turbines Incorporated,
San Diego, CA 92138

Modifying a simple-cycle gas turbine to include heat exchangers can improve its thermal efficiency significantly (as much as 20 percent). Advanced regenerative and intercooled regenerative gas turbines for marine application have recently been the subject of numerous studies, most of which have shown that lower fuel consumption can be achieved by adding heat exchangers to existing simple-cycle gas turbines. Additional improvements in thermal efficiency are available by increasing the efficiency of the turbomachinery itself, particularly that of the gas turbine's air compressor. Studies by Caterpillar Tractor Company and Solar Turbines Incorporated on a recuperated, variable-geometry gas turbine indicate an additional 8 to 10 percent improvement in thermal efficiency is possible when an improved higher efficiency compressor is included in the gas turbine modification. During these studies a novel compressor, the Axi-Fuge, was devised. This paper discusses the Axi-Fuge concept, its origin, design criteria and approach, and some test results.

Introduction

In gas turbines there are two types of air compressor configurations: the axial type which has a small frontal area and small pressure rise across the stage, and the centrifugal type which has a large frontal area, relatively high pressure ratio across the stage, and small axial length. In addition, an axial compressor with multiple stages is generally more efficient than a centrifugal compressor in which compression takes place in only one stage. In the past these two types of compressor have been used separately in gas turbines. To combine some of the advantages of each type, the compression process in some more recent gas turbines is achieved first by axial stages followed by a centrifugal stage. In this way, the advantages of moderate axial length and small frontal area are retained since the centrifugal compressor operates with relatively high-density gases and small volume flow, which requires only a small centrifugal compressor. The axial-centrifugal compressor combination has proved itself to be a rugged, low-weight, small-size component.

However, with recent emphasis on increasing efficiency, the higher efficiency of axial stages is preferred over that of centrifugal impellers. This suggests the need for a design that features blade rows which resemble axial compressor stages but are located in a radial flow path.

A novel compressor, the Axi-Fuge, has been developed that has an efficiency potential of 88 percent, compared to conventional compressors at 80 to 83 percent. The Axi-Fuge compressor has a typical centrifugal compressor annulus but with individual stages of rotor and stator blades similar to an axial compressor. The Axi-Fuge greatly increases the efficiency of a centrifugal compressor while preserving the compactness and structural simplicity of prior single-stage centrifugal compressors. Efficiencies may in fact exceed those realized in axial compressors of similar pressure ratio and flow capacity because centrifugal effects aid the compression process.

Compressors

Background. To understand current and advanced technology, a review of the background art is helpful.

Compressors with rotating vanes or blades may be divided into two categories on the basis of the configuration of their airflow passage. Centrifugal or radial flow compressors, which constitute the first category, have a flow passage that increases in diameter in the direction of the airflow. Axial flow compressors form the second category and have a flow passage of constant or almost constant diameter.

Centrifugal compressors are basically simpler, more compact, and less costly than the axial type. A single compressor stage consists of a set or blade row of revolving compressor blades followed by at least one set or blade row of diffuser blades which may be stationary or counterrotating. A sizable proportion of the energy imparted to incoming air by the revolving compressor blades initially is tangential energy of motion of the airflow. To complete the compression process the airflow must then pass through the diffuser blades which are oriented at a different angle than the compressor blades in order to convert tangential velocity energy into static pressure head.

The degree of compression accomplished in a rotary compressor is expressed by the pressure ratio which is the ratio of pressure at the outlet to that in the inlet. A high pressure ratio across a single compressor stage requires a high loading on the compressor blades, the blade loading being quantitatively expressed by the diffusion factor. In a centrifugal compressor such as the Axi-Fuge compressor, diffusion factor (DF) [1] is defined by the expression

---

Contributed by the Gas Turbine Division of The American Society of Mechanical Engineers and presented at the 31st International Gas Turbine Conference and Exhibit, Düsseldorf, Federal Republic of Germany, June 8–12, 1986. Manuscript received at ASME Headquarters January 14, 1986. Paper No. 86-GT-224.

$$\mathrm{DF} = \left(1 - \frac{W_2}{W_1}\right) + \frac{r_2 W\theta_2 - r_1 W\theta_1}{(r_1 + r_2)\sigma W_1}$$

where

W = flow velocity relative to blade row
W_1 = inlet flow velocity relative to blade row
W_2 = outlet flow velocity relative to blade row
$W\theta$ = tangential flow velocity relative to blade row
σ = blade row solidity (proportion of open flow space to total cross-sectional area of flow path in blade region)
r_1 = mean radius of blade row inlet
r_2 = mean radius of blade row outlet

The de Haller number [2], which is a measure of the degree of diffusion occurring at a blade row as is understood in the art, is equal to

$$\frac{W_2}{W_1}$$

and occurs as a component term in the above stage diffusion factor equation.

Where sizable pressure ratios are to be achieved with a single stage, the diffusion factor must necessarily be high. Isentropic efficiency, which is an inverse function of the diffusion factor, is therefore necessarily low.

In the case of axial flow compressors, it has been recognized that high efficiency may be realized by providing a series of compression-diffusion stages along a flow path of constant or near-constant diameter with the blade sets at each stage being configured to establish a diffusion factor below a critical limit and a de Haller number above a critical limit. The overall pressure ratio of a multistaged axial compressor of this kind is the product of the lower pressure ratios of the individual stages of the series. As each stage has a low pressure ratio, each operates at high efficiency and the efficiency of the axial compressor as a whole is also high.

Prior centrifugal compressors are either single stage or have multiple stages that collectively do not provide a desirable high efficiency. In other instances, a series of essentially separate single-stage centrifugal compressors have been connected together in tandem through bulky and complex high loss air ducting for channeling the outlet flow from one stage radially inward to the smaller diameter inlet of the subsequent stage.

Development of the Axi-Fuge Concept. The concept was developed from consideration of the factors limiting the performance of a specific engine, but can be applied readily to other engines as well as to gas compressors. The baseline engine generates 3500 hp and has a two-stage compressor capable of 6.5:1 pressure ratio with an efficiency of about 80 percent. The other engine components (gas producer turbine, power turbine, and recuperator) are capable of operating with efficiencies at or near 90 percent. No major improvements in fuel consumption are likely to be gained from the turbines or the heat exchanger. However, a significant reduction in fuel consumption is possible if compressor efficiency could be improved to the level of the other engine components.

Work on the unique Axi-Fuge compressor began in the mid-1970s. The concept was first explored using a mean streamline analysis procedure and axial compressor cascade data. This phase of the study concentrated on the aerodynamic aspects of the design with little or no emphasis on the physical and mechanical design constraints. This analysis determined that an 88 percent isentropic efficiency could be achieved in five stages for a 6.5-to-1 pressure ratio. A six-stage configuration also was evaluated. The six-stage configuration achieved the desired performance while being somewhat more conservative than the five-stage design from both aerodynamic and mechanical design considerations. Conventional diffusion factor criteria for axial compressor were used to judge stage loadings. The six-stage configuration maximum rotor and stator diffusion factors were 0.45 and 0.51, respectively, which are well below the conventional practice maximum of 0.6. Rotor inlet Mach numbers were also well within acceptable limits.

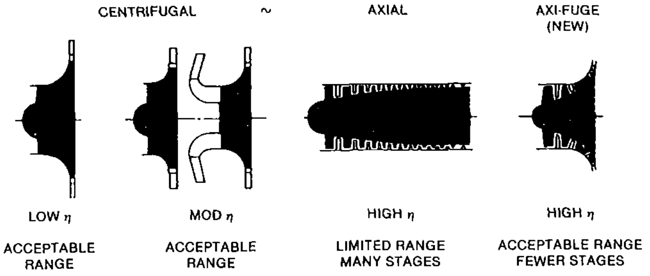

Fig. 1 Compressor comparison for 6.5 pressure ratio

These encouraging results suggested a more rigorous multistreamline quasi-three-dimensional analysis of the concept. In order to do the quasi-three-dimensional analysis, software based on existing axial compressor analysis had to be devised to account for the transition from axial to radial flow. The software conversion effort took about one year, during which time the manufacturing and mechanical feasibilities of the idea were studied.

By mid-1978 the feasibility of the concept was verified, mechanical limits were determined, and material and manufacturing processes were defined. At this point the final aerodynamic and mechanical design was initiated. After several iterations a six-stage configuration emerged in 1979 designed to match the design point conditions of the baseline 3500 HP engine compressor. The actual compressor configuration consisted of six stages and had a target efficiency of 88 percent at 6.5-to-1 pressure ratio. This configuration verified all the claims set forth in the initial concept by use of the most sophisticated and rigorous aerodynamic (quasi-three-dimensional) and mechanical (finite element) analyses available.

The hardware was procured in the late 1979–1980 time period for the compressor in an existing rig size and was equipped with adjustable stator vanes for test stand tuning purposes. The rig mass flow at design point is 15.4 lbm/s. Testing for this configuration was carried out in several steps beginning late 1980. Detailed analyses were performed after each step to determine stator modifications for the succeeding step. The latest tests were completed in 1983.

In summary, the novel (Axi-Fuge) compressor has an efficiency potential of 88 percent. The Axi-Fuge compressor has a typical centrifugal compressor annulus but individual stages of rotor and stator blades similar to those of an axial compressor. The Axi-Fuge greatly increases the efficiency of a centrifugal compressor while preserving the compactness and structural simplicity of prior single-stage centrifugal compressors (see Fig. 1). Efficiencies may in fact exceed those realized in axial compressors of similar pressure ratio and flow capacity since centrifugal effects aid the compression process.

Comparison of Axi-Fuge With Centrifugal Compressor. Advantages of the Axi-Fuge compressor over conventional centrifugal compressors are best described by the reduction in diffuser vane inlet Mach number. Centrifugal compressors have high tangential air velocity, hence a high diffuser-vane-inlet Mach number ($V_{\text{inlet}}/V_{\text{sound}}$). The Axi-Fuge concept limits the diffuser-vane-inlet Mach number, which results in lower losses and higher efficiency. The table below compares a single-stage centrifugal compressor with the Axi-Fuge.

	Centrifugal	Axi-Fuge
Diameter, in.	38.1	27.2
Length, in.	8.4	12.5
Diffuser vane Mach number	1.0	0.68
P/P (pressure ratio)	6.5	6.5
Efficiency, percent	76	88

Comparison of Axi-Fuge With Axial Compressor. Advantages of the Axi-Fuge over axial compressors are best described by the reduction in the number of stages and axial length as shown in the table below.

	NASA eight stage axial compressor*	Axi-Fuge
Diameter, in.	20.4	27.2
Length, in.	46.7	12.5
Number of stages	8	6
P/P (pressure ratio)	6.5	6.5
Efficiency, percent	85	88

---

*Scaled to Axi-Fuge rig size (15.4 lbm/s from data provided in [3]).

Development of Plan for Axi-Fuge Compressor. A plan was prepared to achieve the 88 percent efficiency goal indicated by the analyses. Three configurations were planned to be fabricated and tested. A goal of 80 percent efficiency at a pressure ratio of 6.0 was set for the first configuration but was exceeded in both pressure ratio (6.5) and efficiency (84 percent).

The plan for realizing the efficiency potential of this compressor identified the need for three configurations with the three sets of stator angles. The goal for each configuration is shown below:

	Objective	
	P/P	(percent)
Configuration I (original design)	6.0	80
Configuration II (first modified blades and/or annulus)	6.5	84
Configuration III (second modified blade and/or annulus)	6.5	88

The compressor rig was highly instrumented to provide diagnostic information as well as reliable, well-defined overall performance. Wall static pressures were measured before and after each blade row, and total pressures and total temperatures were measured at three radial locations behind several rotors. Full radial traverses of total pressure, total temperature, and angle were obtained behind several rotors. Wake traverses at hub, mean, and tip at the outlet guide vane exit also were obtained.

All pressure ratios are discharge static to inlet total. Efficiencies are also total to static.

Initial Axi-Fuge compressor tests with design stator angles yielded a pressure ratio of 5.5 and efficiency of 82.7 percent.

The Axi-Fuge compressor was retested with the third-stage stators reset to alleviate a fourth-stage rotor stall condition. A pressure ratio of 6.6 was achieved at an efficiency of 83 percent.

A set of stator angles was defined to relieve a choked condition on rotor six and to increase the loading on stator six. An efficiency in excess of 84 percent and a pressure ratio of 6.5 was demonstrated during this test, meeting the program goal of 6.5 pressure ratio and Configuration II efficiency goal of 84 percent.

As of this writing, this set of hardware had over 160 running hours, most of which were at or near 100 percent speed.

The table below shows that Axi-Fuge Configuration 1 compressor measured performance already has met the second configuration's goal.

	Goal		Measured	
	P/P	percent	*P/P*	percent
Configuration 1	6.0	80	6.5	84
Configuration 2	6.5	84		
Configuration 3	6.5	88		

Axi-Fuge Compressor Effect on Baseline Engine Design Goal. Preliminary examination of engine concepts shows significant gains in specific fuel consumption may be available when a highly efficient compressor like the Axi-Fuge is used. A comparison of the baseline engine performance goal with the existing two-stage compressor and with the Axi-Fuge compressor is as follows:

	Goal (with two-stage compressor)	Goal (with Axi-Fuge compressor)
Compressor efficiency (percent)	81	88
Percent horsepower (maximum) increase		10
Percent specific fuel consumption (improvement)		9

Concluding Remarks

The results of designing and testing the Axi-Fuge machine have verified the achievability of the claims set forth by this type of compressor configuration. A summary of the Axi-Fuge compressor pros and cons is given in Table 1. Slight modifications to the existing hardware are expected to produce the design goal total-to-static efficiency of 88 percent with a minimum amount of development. Furthermore, it is envisioned that efficiencies (total to static) in excess of 90 percent could be achieved with advanced concepts such as controlled diffusion and/or multicircular arc blading.

Table 1 Axi-Fuge compressor pros and cons

	Pros	Cons
1 Performance		
(A) Rotors	• Lower loading (diffusion factor) for same work input versus axial machine • Higher efficiency for same number of stages as an axial machine or same efficiency with fewer stages	
(B) Stators	• Lower Mach number levels and diffusion requirements than centrifugal machines of equivalent ratio, hence higher efficiency	
2 Packaging	• Shorter length than axial or conventional multistage centrifugal	Larger diameter than axial
	• Smaller diameter than single or conventional multistage centrifugal	Longer than single-stage conventional
3 Family Concept	• Readily adaptable to major power changes by adding or subtracting stages • Readily adaptable to minor power adjustments by stator stagger changes	
4 Cost	• Probably lower cost than axial. Probably equal or lower cost than conventional multistage centrifugal	More expensive than a single-stage conventional centrifugal

Acknowledgments

The author wishes to express appreciation to Solar Turbines Incorporated and Caterpillar Tractor Company for aid and support in preparing and releasing the paper. Also appreciation is expressed to all members of Caterpillar's Power Plant Research group where the design and testing were performed, and in particular to Messrs. Cletus Kinsey and J. P. Grandfield.

References

1 Lieblein, S., Schwenk, F. C., and Broderick, R. G., "Diffusion Factor for Estimating Losses and Limit Loadings in Axial-Flow-Compressor Blade Elements," RME-53D01, National Advisory Committee for Aeronautics, June 8, 1953.

2 de Haller, P., "Das Verhalten von Tragflugelgittem in Axialverdichtern und im Windkanal," *Brenst. Warmekr.*, Vol. 5, 1953, p. 333.

3 Voit, C. H., "Investigation of a High Pressure Ratio Eight-Stage Axial-Flow Research Compressor With Two Transonic Inlet Stages. I – Aerodynamic Design," NASA RME53124, 1953.

4 Wiggins, J. O., United States Patent No. 4,428,715, Multistage Centrifugal Compressor, Jan. 31, 1984.

Splitter Blades as an Aeroelastic Detuning Mechanism for Unstalled Supersonic Flutter of Turbomachine Rotors

D. A. Topp[1]

S. Fleeter
Professor of Mechanical Engineering,
Director Thermal Sciences and
Propulsion Center

Purdue University,
West Lafayette, IN 47907

A mathematical model is developed to demonstrate the application of splitter blades as an aeroelastic detuning mechanism for unstalled supersonic flutter of turbomachine rotors. The splitters introduce both aerodynamic and structural detuning, thereby leading to enhanced aeroelastic stability. The aerodynamic detuning is due to the variable circumferentially spaced splitters between each pair of full chord airfoils, with aerodynamic detuning due to alternate circumferential spacing of the full chord airfoils also considered. The structural detuning arises from the lower natural frequencies of the splitters as compared to that of the full chord airfoils. The enhanced torsion mode flutter stability due to the incorporation of splitters into a rotor design is demonstrated by applying this model to two unstable baseline twelve-bladed rotors which are based on Verdon's Cascade A and Cascade B configurations. In each case, the unstable baseline rotor is stabilized by the introduction of appropriate splitters. The critical parameters for this stability enhancement are the chord length and the circumferential and axial locations of the splitters.

Introduction

Unstalled supersonic flutter is a significant problem in the development of high-speed compressor fan stages as it imposes a limit on the high-speed operation of the engine. This flutter is typically eliminated from the operating range of a fan by paying an aerodynamic performance penalty and incorporating part-span shrouds into the blade design.

One approach to removing this flutter region from the operating range without resorting to part-span shrouds is structural detuning, defined as designed blade-to-blade differences in the natural frequencies of a rotor blade row. Mathematical models have been developed which demonstrate that even small amounts of structural detuning can have a beneficial effect on the flutter characteristics of a rotor [1-4]. However, structural detuning is not a universally accepted passive flutter control mechanism because of the associated manufacturing, material, inventory, engine maintenance, control, and cost problems [5].

A second approach to passive unstalled supersonic flutter control is aerodynamic detuning, defined as designed passage-to-passage differences in the unsteady aerodynamic flow field of a blade row. Thus, aerodynamic detuning affects the fundamental driving mechanism for flutter, the unsteady aerodynamics. This results in the blading not responding in a classical traveling wave mode typical of the flutter behavior of a conventional aerodynamically tuned rotor. The enhanced torsion mode unstalled supersonic flutter stability due to one type of aerodynamic detuning, alternate circumferential spacing of adjacent rotor blades, was demonstrated in [6].

In this paper a mathematical model is developed to predict the aeroelastic stability of a rotor with splitters operating in the unstalled supersonic flow regime. The incorporation of splitter blades into the rotor offers the potential of enhanced supersonic flutter stability due to both aerodynamic and structural detuning, while eliminating the difficulties associated with structural detuning. The splitters introduce both aerodynamic and structural detuning into the rotor. The aerodynamic detuning is due to the variable circumferentially spaced splitters between each pair of full chord airfoils, with aerodynamic detuning due to alternate circumferential spacing of the full chord airfoils also considered. The structural detuning arises from the lower natural frequency of the splitters as compared to that of the full chord airfoils.

Unsteady Aerodynamic Model

The unstalled flutter characteristics of conventional aerodynamically tuned and structurally detuned supersonic rotors are determined from models which consider a flat plate airfoil cascade embedded in an inviscid supersonic inlet flow field with a subsonic axial flow component. The cascade is assumed to be executing small perturbation harmonic torsion mode oscillations in a classical traveling mode, i.e., with a

---

[1] Currently employed at Allison Gas Turbine Division, General Motors Corporation.

Contributed by the Gas Turbine Division of THE AMERICAN SOCIETY OF MECHANICAL ENGINEERS and presented at the 31st International Gas Turbine Conference and Exhibit, Düsseldorf, Federal Republic of Germany, June 8-12, 1986. Manuscript received at ASME Headquarters January 20, 1986. Paper No. 86-GT-99.

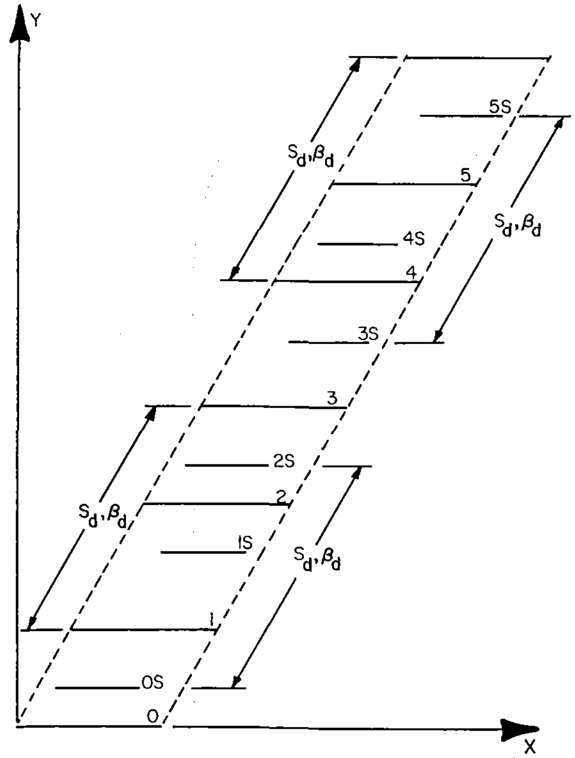

Fig. 1 Finite cascade representation of an alternately spaced rotor incorporating splitters

constant interblade phase angle β between adjacent airfoils. The semi-infinite cascade can be considered as a finite cascade, with the cascade periodicity condition enforced by stacking sufficient numbers of uniformly spaced single airfoils until convergence in the unsteady flow field is achieved.

For the aeroelastically detuned rotor configuration of interest herein, i.e., a rotor incorporating splitters with variable circumferential spacing of both the full chord and splitter blades, an analogous finite cascade unsteady aerodynamic model is developed. In this model, the full chord airfoils need not be uniformly spaced circumferentially, but may consist of a reduced spacing passage and an increased spacing passage, as was considered in [6]. Thus, these detuned full chord airfoils are composed of two separate sets of airfoils. For convenience, these full chord airfoils are termed the set of even-numbered airfoils and the set of odd-numbered airfoils.

Splitters are incorporated into the rotor between each pair of full chord airfoils. Each splitter is associated with the full chord airfoil immediately upstream, with the two sets of splitters termed the set of even-numbered splitters and the set of odd-numbered splitters. The splitters in the odd-numbered set are not restricted to having the same chord length as the splitters in the even set, nor are they restricted to being located in the same relative positions within the full chord airfoil passages. Thus, there are four distinct flow passages, with each passage bounded by one airfoil from two of the four airfoil sets: an even-numbered full chord airfoil, an even-numbered splitter, an odd-numbered full chord airfoil, and an odd-numbered splitter, as depicted in Fig. 1. Consequently, four-passage periodicity is required for this detuned cascade configuration, i.e., the periodic cascade unsteady flow field is achieved by stacking sufficient numbers of four nonuniform flow passages or four airfoils, one from each set.

Each of the four individual sets of airfoils has a constant spacing equal to S_d. Thus, the individual sets of even full chord, even splitter, odd full chord, and odd splitter airfoils can be considered as cascades of uniformly spaced airfoils each with four times the spacing of the associated baseline uniformly spaced cascade

$$S_1 + S_2 + S_3 + S_4 = 4S \tag{1}$$

where S is the spacing of the baseline uniformly spaced cascade and S_1, S_2, S_3, and S_4 denote the spacing between successive sets of airfoils in the detuned cascade. The level of aerodynamic detuning which defines the nonuniform airfoil spacing is specified in equation (2)

$$S_1 + S_2 = (1-\epsilon)2S \tag{2a}$$

$$S_3 + S_4 = (1-\epsilon)2S \tag{2b}$$

where ϵ is the percent nonuniformity of the full chord airfoil spacing.

An interblade phase angle for this aerodynamically detuned cascade configuration can be defined. In particular, each set of airfoils is individually assumed to be executing harmonic torsional oscillations with a constant aerodynamically detuned interblade phase angle β_d between adjacent airfoils of each set (Fig. 1). Thus, this detuned cascade interblade phase angle is four times that for the corresponding baseline uniformly spaced cascade.

Figure 2 depicts the complete model of the alternate nonuniformly spaced rotor with splitters. The splitter geometry is specified by three parameters: Sp_{cord}, the splitter chord length as a percentage of the chord length of a full chord airfoil; P_{start}, the axial distance between the leading edges of the splitters and the full chord airfoils, as a percentage of the chord length of a full chord airfoil; and P_{split}, the splitter circumferential spacing as a percentage of the flow passage between two full chord airfoils. These parameters are defined in equation (3)

$$S_1 = P_{\text{split1}}(1-\epsilon)2S; \qquad S_3 = P_{\text{split2}}(1-\epsilon)2S \tag{3a}$$

$$P_{\text{start1}} + Sp_{\text{cord1}} \leq 1; \qquad P_{\text{start2}} + Sp_{\text{cord2}} \leq 1 \tag{3b}$$

The fluid is assumed to be an inviscid perfect gas with the flow isentropic, adiabatic, and irrotational. The unsteady continuity and Euler equations are linearized by assuming that the unsteady perturbations due to the harmonic airfoil oscillations are small as compared to the uniform throughflow. Thus, the boundary conditions, which require the unsteady flow to be tangent to the blade and the normal velocity to be continuous across the wake, are applied on the mean positions of the oscillating airfoils.

Nomenclature

a = dimensionless perturbation sonic velocity
C = airfoil chord
C_M^n = influence coefficient of airfoil n
I = mass moment of inertia
k = reduced frequency = $\omega C/u_\infty$
K = spring constant
M = dimensionless unsteady aerodynamic moment
M_∞ = cascade inlet Mach number
P_{split} = splitter circumferential spacing
P_{start} = splitter leading location
S = airfoil spacing
Sp_{cord} = splitter chord length
u = dimensionless perturbation chordwise velocity
v = dimensionless perturbation normal velocity
α = amplitude of oscillation
$\hat{\alpha}$ = complex oscillatory amplitude
β = interblade phase angle
ϵ = level of aerodynamic detuning

Subscripts

d = detuned cascade
R = reference airfoil

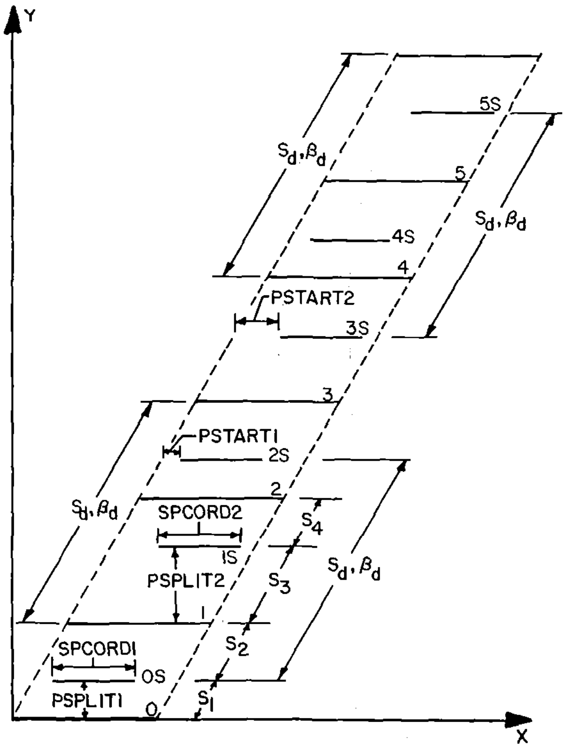

Fig. 2 Finite cascade representation for aerodynamic detuning of a rotor incorporating splitters

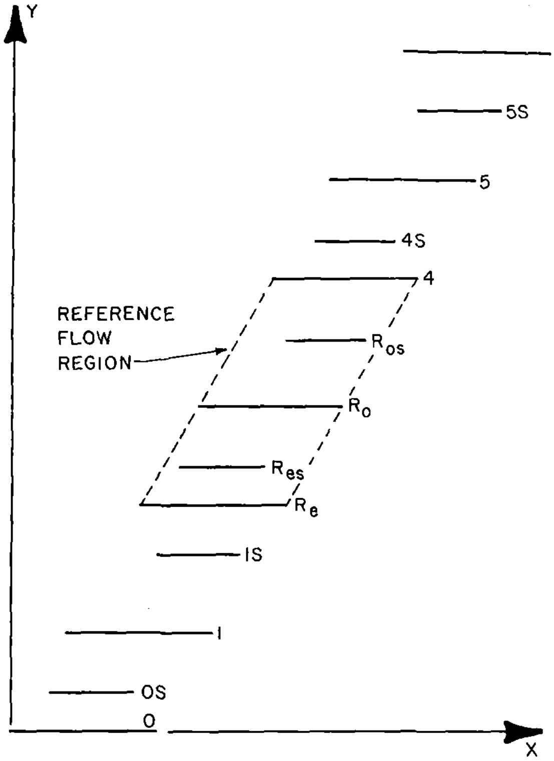

Fig. 3 Reference flow region for aerodynamically detuned rotor with splitters

The formulation of the linearized differential equations describing the unsteady perturbation quantities for the finite aerodynamically detuned cascade is based on the method of characteristic analysis of the finite uniformly spaced airfoil cascade of Brix and Platzer [7]. In particular the dependent variables are the nondimensional chordwise, normal, and sonic perturbation velocities, u, v, and a, respectively.

Assuming harmonic motion at a frequency ω, the nondimensional continuity and momentum equations are specified in equation (4)

$$\frac{\partial u}{\partial x}+\sqrt{M_\infty^2-1}\,\frac{\partial v}{\partial y}+M^2\frac{\partial a}{\partial x}+ikM_\infty^2 a=0 \qquad (4a)$$

$$\frac{\partial u}{\partial x}+\frac{\partial a}{\partial x}+iku=0 \qquad (4b)$$

$$\frac{\partial u}{\partial x}-\sqrt{M_\infty^2-1}\,\frac{\partial v}{\partial x}=0 \qquad (4c)$$

Solutions are obtained by the method of characteristics, which identifies characteristic paths along which the partial differential equations can be rewritten in total differential form. The compatibility equations are specified in equation (5)

$$\left(\frac{du}{dx}\right)_\zeta-\left(\frac{dv}{dx}\right)_\zeta+\frac{ikM_\infty^2}{M_\infty^2-1}(u-a)=0 \qquad (5a)$$

$$\left(\frac{du}{dx}\right)_\eta+\left(\frac{dv}{dx}\right)_\eta+\frac{ikM_\infty^2}{M_\infty^2-1}(u-a)=0 \qquad (5b)$$

$$\left(\frac{du}{dx}\right)_{\text{str}}+\left(\frac{da}{dx}\right)_{\text{str}}+iku=0 \qquad (5c)$$

where the subscripts ζ, η, and str indicate that the relation is valid along the left or right running Mach lines or the streamline direction, respectively.

The flow tangency boundary condition requires that the normal perturbation velocity component v be equal to the normal velocity of the airfoil surfaces. For an airfoil cascade executing harmonic torsional motions about an elastic axis located at x_o as measured from the leading edge, the dimensionless normal perturbation velocity component on the nth airfoil is specified in equation (6)

$$v_n(x, y_s, t)=-\alpha_o\left\{1+(x-x_o)ik\right\}e^{i(kt+n\beta)} \qquad (6)$$

where y_s denotes the mean position of the airfoils, k is the reduced frequency, and α_o denotes the amplitude of oscillation of the oth airfoil.

A finite difference approximation is used to solve the mathematical problem specified by equations (5) and (6) at each point in the flow field. The unknown chordwise, normal, and sonic dimensionless perturbation velocities, u, v, and a, in each of the four periodic flow passages of the semi-infinite cascade are determined by means of the four airfoil passage stacking technique. The dimensionless unsteady perturbation pressure distributions on the surfaces of a reference airfoil from each set in the periodic detuned cascade are defined by these perturbation velocities. The nondimensional unsteady aerodynamic moments acting on a reference airfoil from each set are then calculated by integrating the unsteady surface perturbation pressure difference across the chordline per equation (7)

$$M_{R_i}=\int_0^1 \Delta p(x, y_s, t)\,(x-x_0)dx\; e^{i\omega t} \qquad (7)$$

where R_i is an index equal to R_e, R_{es}, R_o, or R_{os}.

Influence Coefficient Technique

The boundary conditions specified in equation (6) require that the nonuniformly spaced airfoils oscillate with equal amplitudes, a situation not appropriate for the detuned airfoil cascade. This is rectified by calculating the unsteady aerodynamic moments by means of an influence coefficient technique.

For the detuned nonuniformly spaced cascade, a reference flow region consisting of four reference airfoils must be considered (Fig. 3). The reference airfoil for the lower boundary of the reference flow region and for the set of even-numbered airfoils is denoted by R_e. The intermediate reference airfoils, the even-numbered splitter, odd-numbered airfoil, and odd-numbered splitter are denoted by R_{es}, R_o, and R_{os}, respectively. The unsteady aerodynamic moments acting on these four reference airfoils can each be written in terms of influence coefficients, equation (8). The four groups of bracketed terms are associated with the motion of the sets of odd-numbered and even-numbered full chord and splitter airfoils, respectively

$$\begin{aligned} M_{R_i} = &\left\{\hat{\alpha}_1 \left(C_M^1\right)_{R_i} + \hat{\alpha}_3 \left(C_M^3\right)_{R_i} + \ldots + \hat{\alpha}_{R_o} \left(C_M^{R_o}\right)_{R_i} \right. \\ &\left. + \ldots + \hat{\alpha}_N \left(C_M^{N-2}\right)_{R_i} \right\} \\ &+ \left\{\hat{\alpha}_{1s} \left(C_M^{1s}\right)_{R_i} + \hat{\alpha}_{3s} \left(C_M^{3s}\right)_{R_i} + \ldots + \hat{\alpha}_{R_{os}} \left(C_M^{R_{os}}\right)_{R_i} \right. \\ &\left. + \ldots + \hat{\alpha}_{N-1} \left(C_M^{N-1}\right)_{R_i} \right\} \\ &+ \left\{\hat{\alpha}_2 \left(C_M^2\right)_{R_i} + \hat{\alpha}_4 \left(C_M^4\right)_{R_i} + \ldots + \hat{\alpha}_{R_e} \left(C_M^{R_e}\right)_{R_i} \right. \\ &\left. + \ldots + \hat{\alpha}_{N-2} \left(C_M^{N}\right)_{R_i} \right\} \\ &+ \left\{\hat{\alpha}_{2s} \left(C_M^{2s}\right)_{R_i} + \hat{\alpha}_{4s} \left(C_M^{4s}\right)_{R_i} + \ldots + \hat{\alpha}_{R_{es}} \left(C_M^{R_{es}}\right)_{R_i} \right. \\ &\left. + \ldots + \hat{\alpha}_{N-3} \left(C_M^{N-3}\right)_{R_i} \right\} \end{aligned} \tag{8}$$

where R_i is an index equal to R_e, R_{es}, R_o, or R_{os}.

The amplitude of the harmonic oscillations of the set of even-numbered full chord airfoils is denoted by $\hat{\alpha}_{R_e} \exp(in\, \beta_d)$, with β_d defining the constant interblade phase angle between sequentially even-numbered full chord airfoils. The sets of even splitter, odd full chord, and odd splitter airfoils are assumed to oscillate with complex amplitudes $\hat{\alpha}_{R_{es}} \exp(in\, \beta_d)$, $\hat{\alpha}_{R_o} \exp(in\, \beta_d)$, and $\hat{\alpha}_{R_{os}} \exp(in\, \beta_d)$, respectively. The amplitude and phase difference between the motions of the various sets of airfoils are accounted for by considering the amplitudes of oscillation, $\hat{\alpha}_{R_e}$, $\hat{\alpha}_{R_{es}}$, $\hat{\alpha}_{R_o}$, and $\hat{\alpha}_{R_{os}}$, to be complex quantities. Thus, the dimensionless unsteady aerodynamic moments acting on the four reference airfoils can be rewritten in terms of the amplitudes of oscillation of the four reference airfoils

$$\begin{bmatrix} M_{R_e} \\ M_{R_{es}} \\ M_{R_o} \\ M_{R_{os}} \end{bmatrix} = \begin{bmatrix} \left(CM^2\right)_{R_e} & \left(CM^{2s}\right)_{R_e} & \left(CM^1\right)_{R_e} & \left(CM^{1s}\right)_{R_e} \\ \left(CM^2\right)_{R_{es}} & \left(CM^{2s}\right)_{R_{es}} & \left(CM^1\right)_{R_{es}} & \left(CM^{1s}\right)_{R_{es}} \\ \left(CM^2\right)_{R_o} & \left(CM^{2s}\right)_{R_o} & \left(CM^1\right)_{R_o} & \left(CM^{1s}\right)_{R_o} \\ \left(CM^2\right)_{R_{os}} & \left(CM^{2s}\right)_{R_{os}} & \left(CM^1\right)_{R_{os}} & \left(CM^{1s}\right)_{R_{os}} \end{bmatrix} \begin{bmatrix} \hat{\alpha}_{R_e} \\ \hat{\alpha}_{R_{es}} \\ \hat{\alpha}_{R_o} \\ \hat{\alpha}_{R_{os}} \end{bmatrix} \tag{9}$$

where

$$\begin{aligned} \left(CM^2\right)_{R_i} &= \left(C_M^{R_e}\right)_{R_i} + e^{i\beta_d} \left(C_M^2\right)_{R_i} \\ &\quad + \ldots + e^{i\left(\frac{N-1}{4}\right)\beta_d} \left(C_M^N\right)_{R_i} \end{aligned}$$

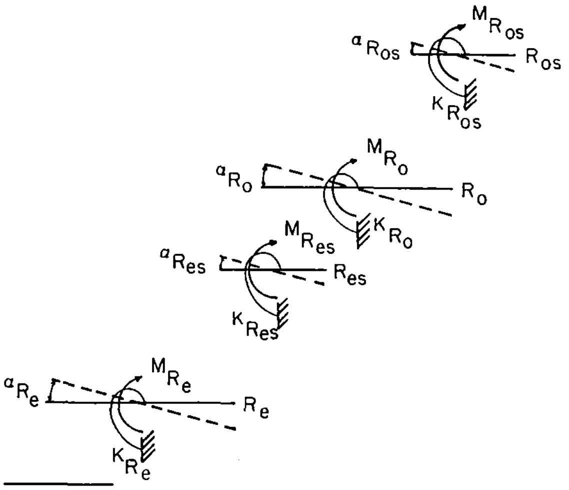

Fig. 4 Single degree of freedom model for aerodynamically detuned cascade

$$\begin{aligned} \left(CM^{2s}\right)_{R_i} &= \left(C_M^{R_{es}}\right)_{R_i} + e^{i\beta_d} \left(C_M^{2s}\right)_{R_i} \\ &\quad + \ldots + e^{i\left(\frac{N-5}{4}\right)\beta_d} \left(C_M^{N-3}\right)_{R_i} \\ \left(CM^1\right)_{R_i} &= \left(C_M^{R_o}\right)_{R_i} + e^{i\beta_d} \left(C_M^3\right)_{R_i} \\ &\quad + \ldots + e^{i\left(\frac{N-5}{4}\right)\beta_d} \left(C_M^{N-2}\right)_{R_i} \\ \left(CM^{1s}\right)_{R_i} &= \left(C_M^{R_{os}}\right)_{R_i} + e^{i\beta_d} \left(C_M^{3s}\right)_{R_i} \\ &\quad + \ldots + e^{i\left(\frac{N-5}{4}\right)\beta_d} \left(C_M^{N-1}\right)_{R_i} \end{aligned}$$

The terms $(CM^1)_{R_i}$ describe the influence that the set of odd-numbered airfoils has on the unsteady aerodynamic moment developed on reference airfoils R_e, R_{es}, R_o, and R_{os}. $(CM^2)_{R_i}$, $(CM^{2s})_{R_i}$, and $(CM^{1s})_{R_i}$ represent the effect on these four reference airfoils of the set of even-numbered airfoils, even-numbered splitters, and odd-numbered splitters, respectively.

Equations of Motion

The equations describing the single degree of freedom torsional motion of the four reference airfoils of the nonuniformly spaced cascade are developed by considering the typical airfoil sections depicted in Fig. 4. Positive torsional displacements are defined as a clockwise motion such that the airfoil is in a leading-edge-up configuration. The elastic restoring forces are modeled by linear torsional springs at the elastic axis location, with the inertial properties of the airfoils represented by their mass moment of inertia about the elastic axis. The following equations of motion are then determined using Lagrange's technique

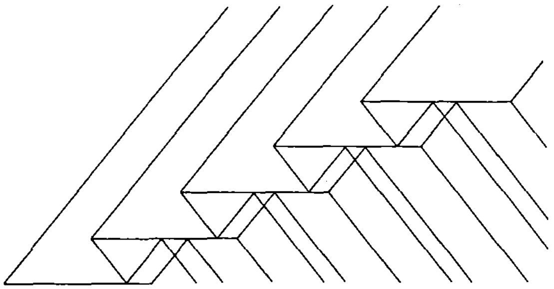

Fig. 5 Verdon's Cascade B flow geometry

$$I_{\alpha_{R_i}}\ddot{\alpha}_{R_i}+(1+2ig_{\alpha_{R_i}})I_{\alpha_{R_i}}\omega^2_{\alpha_{R_i}}\alpha_{R_i}=M_{R_i} \tag{10}$$

where the undamped natural frequencies are

$$\omega^2_{\alpha_{R_i}}=\frac{K_{\alpha_{R_i}}}{I_{\alpha_{R_i}}}$$

R_i denotes R_e, R_{es}, R_o, R_{os}, and $g_{\alpha_{R_i}}$ are the corresponding structural damping coefficients.

The natural frequencies of the splitters are related to the natural frequency of the full chord airfoils. In particular, considering all of the airfoils to be slender beams and assuming that the material density and thickness are constant, the ratio of the splitter to full chord airfoil natural frequencies is presented in equation (11)

$$\frac{\omega_{R_{os}}}{\omega_{R_o}}=\sqrt{\frac{C_{R_{os}}}{C}};\quad \frac{\omega_{R_{es}}}{\omega_{R_e}}=\sqrt{\frac{C_{R_{es}}}{C}} \tag{11}$$

where C_{R_e} and $C_{R_{es}}$ are the splitter chord lengths and C is the chord length of a full chord airfoil.

Considering harmonic motion of the reference airfoils and utilizing the unsteady aerodynamic moments defined in equation (9), the single degree of freedom torsion mode equations of motion can be expressed in matrix form

$$\begin{bmatrix} \mu_e & (CM^{2s})_{R_e} & (CM^1)_{R_e} & (CM^{1s})_{R_e} \\ (CM^2)_{R_{es}} & \mu_{es} & (CM^1)_{R_{es}} & (CM^{1s})_{R_{es}} \\ (CM^2)_{R_o} & (CM^{2s})_{R_o} & \mu_o & (CM^{1s})_{R_o} \\ (CM^2)_{R_{os}} & (CM^{2s})_{R_{os}} & (CM^1)_{R_{os}} & \mu_{os} \end{bmatrix} \begin{bmatrix} \hat{\alpha}_{R_e} \\ \hat{\alpha}_{R_{es}} \\ \hat{\alpha}_{R_o} \\ \hat{\alpha}_{R_{os}} \end{bmatrix} = \begin{bmatrix} 0 \\ 0 \\ 0 \\ 0 \end{bmatrix} \tag{12}$$

where

$$\mu_{e,es}=\mu_{R_{e,es}}r^2_{\alpha R_{e,es}}+(CM^2)_{R_{e,es}} - (1+2ig_{\alpha R_{e,es}})\mu_{R_{e,es}}r^2_{\alpha R_{e,es}}\gamma^2_{\alpha R_{e,es}}\gamma$$

$$\mu_{o,os}=\mu_{R_{o,os}}r^2_{\alpha R_{o,os}}+(CM^1)_{R_{o,os}} - (1+2ig_{\alpha R_{o,os}})\mu_{R_{o,os}}r^2_{\alpha R_{o,os}}\gamma^2_{\alpha R_{o,os}}\gamma$$

$$\mu_{R_i}=\frac{m_{R_e}}{\pi\rho b^2};\qquad r^2_{\alpha R_i}=\frac{I_{\alpha_{R_i}}}{m_{R_e}b^2}$$

$$\gamma^2_{\alpha R_i}=\frac{\omega_{\alpha_{R_i}}}{\omega_o}\qquad \gamma=\frac{\omega_o^2}{\omega^2}$$

ω_o = reference frequency

Equation (12) is an eigenvalue problem. The eigenvalues correspond to the frequency ratio γ associated with the mode shape, $\hat{\alpha}_{R_e}$, $\hat{\alpha}_{R_{es}}$, $\hat{\alpha}_{R_o}$, and $\hat{\alpha}_{R_{os}}$. The absolute amplitudes of vibration can not be determined from the mode shape, which is normalized by a reference amplitude, but, rather, the relative displacements are calculated. The stability of the cascade is obtained by relating the frequency ratio γ to the exponent $(i\omega)$ as indicated

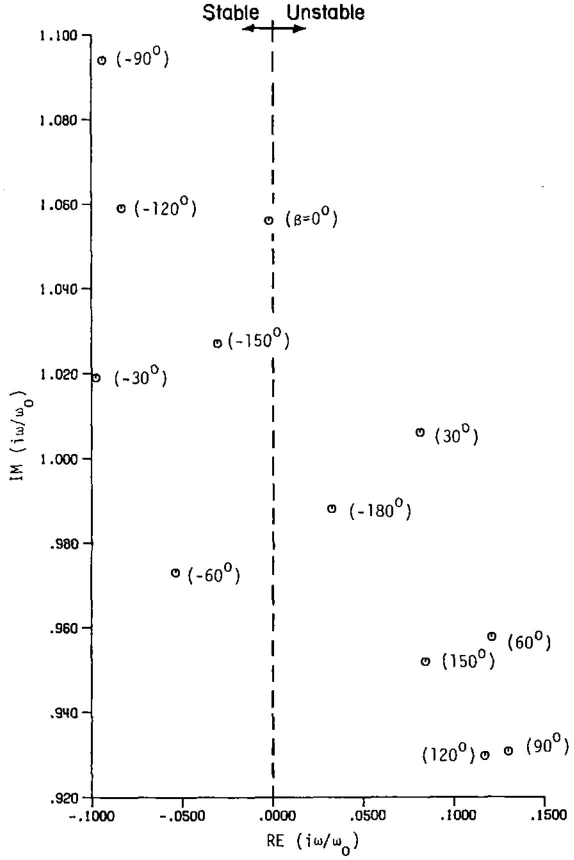

Fig. 6 Stability of baseline Cascade B rotor

$$\frac{i\omega}{\omega_o}=\frac{i}{\sqrt{\gamma}}=\mu\pm i\nu \tag{13}$$

Thus a positive value for μ corresponds to an unstable cascade configuration.

The mathematical model specified by equation (12) represents both an aerodynamically and a structurally detuned airfoil cascade as well as a tuned cascade in which all of the airfoils are structurally identical and uniformly spaced. Aerodynamic detuning is accounted for through the influence coefficients $(CM^2)_{R_i}$, $(CM^{2s})_{R_i}$, $(CM^1)_{R_i}$, and $(CM^{1s})_{R_i}$. Structural detuning is associated with the terms μ_e, μ_{es}, μ_o, and μ_{os}.

Results

To demonstrate the stability enhancement associated with the incorporation of splitters into an unstalled supersonic

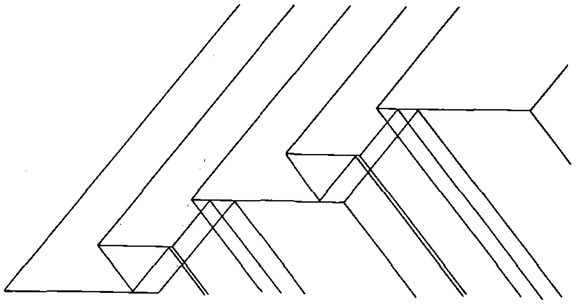

Fig. 7 Cascade B1 flow geometry: $Sp_{\text{cord1}} = Sp_{\text{cord2}} = 50.0$ percent, $P_{\text{start1}} = P_{\text{start2}} = 0.0$ percent, $P_{\text{split1}} = P_{\text{split2}} = 50$ percent

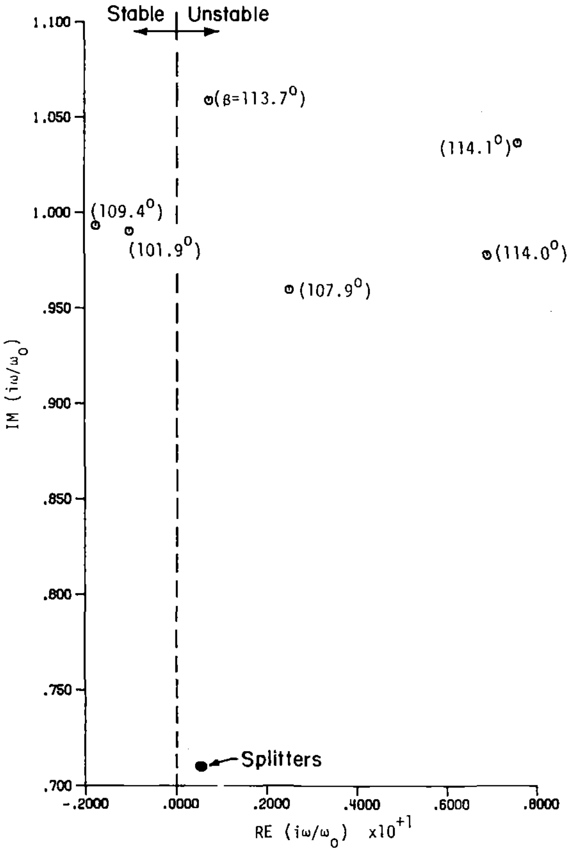

Fig. 8 Stability of Cascade B1 rotor

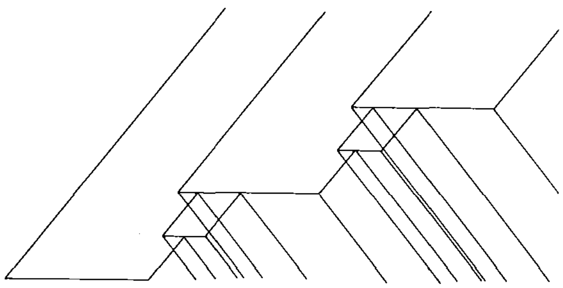

Fig. 9 Cascade B2 flow geometry: $Sp_{\text{cord1}} = Sp_{\text{cord2}} = 30$ percent, $P_{\text{start1}} = P_{\text{start2}} = 50$ percent, $P_{\text{split1}} = P_{\text{split2}} = 50$ percent

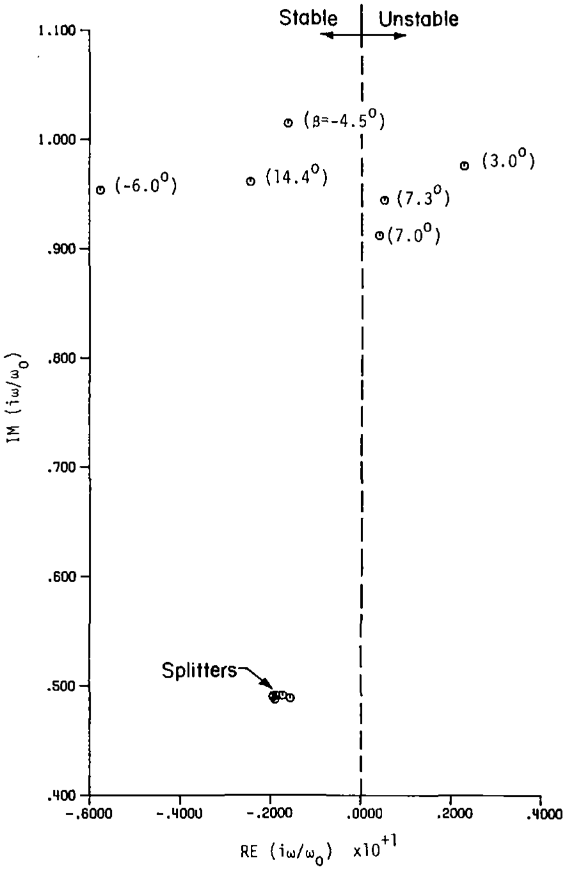

Fig. 10 Stability of Cascade B2 rotor

rotor design, two unstable baseline twelve-bladed rotor configurations which are based on Verdon's Cascade A and Cascade B [8] are considered. These rotors are individually stabilized primarily by an appropriate choice of splitter chord length and location within the full chord airfoil passages and secondarily by the level of nonuniformity of the full chord airfoil circumferential spacing.

Verdon's Cascade B is considered as the first baseline configuration. The inlet Mach number is 1.281, the reduced frequency is 0.5, the stagger angle is 63.4 deg, and the elastic axis is located at midchord. The geometry and stability of this baseline are presented in Figs. 5 and 6, respectively. As seen, it is unstable for forward-traveling waves.

Five aerodynamically detuned variations of this baseline configuration are considered, with the inlet Mach number, reduced frequency, stagger angle, and elastic axis location maintained at the baseline values.

The Cascade B1 aerodynamically detuned geometry is achieved by decreasing the chord length of alternate full chord airfoils by one half. This configuration results in Mach wave–airfoil surface intersections near the trailing edge of the suction surface of the full chord airfoils and near the leading edge of the pressure surface of the full chord airfoils, as depicted in Fig. 7. The root locus of the eigenvalues of this detuned configuration (Fig. 8) shows that Cascade B1 is still unstable, although considerably more stable than the baseline Cascade B. Also, the least stable mode of Cascade B1 corresponds to a forward-traveling wave characterized by an interblade phase angle of 114.1 deg, as compared to an interblade phase angle of 90 deg for the least stable mode of baseline Cascade B. Because the natural frequency of the splitters is substantially lower than that of the full chord airfoils, the eigenvalues ($i\ \omega/\omega_0$) gather into two distinct groups. On the imaginary axis of the root locus plot the eigenvalues associated with the full chord airfoils cluster around unity, while those associated with the splitters are clustered at a lower value.

Figure 9 shows the geometry of aerodynamically detuned Cascade B2. It is similar to Cascade B1 except that the splitters have a chord length of 30 percent of the full chord airfoils, and the leading edge of the splitters is located at the midchord of the full chord airfoils. For this case, the Mach wave intersections on the full chord airfoils occur only on the pressure surface. A comparison of the root locus plots of Cascade B1

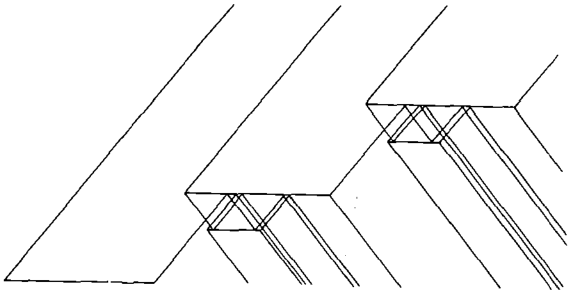

Fig. 11 Cascade B3 flow geometry: $Sp_{\mathrm{cord1}} = Sp_{\mathrm{cord2}}$ = 35 percent, $P_{\mathrm{start1}} = P_{\mathrm{start2}}$ = 65 percent, $P_{\mathrm{split1}} = P_{\mathrm{split2}}$ = 60 percent

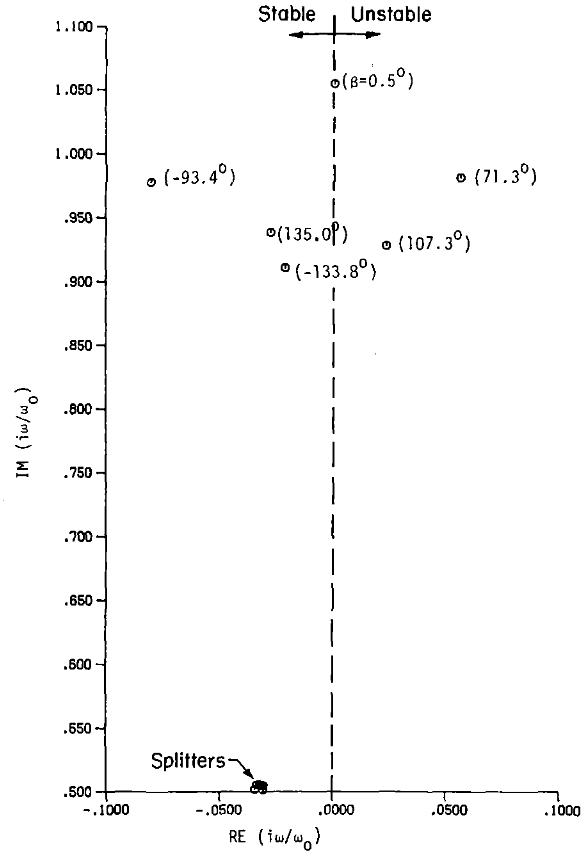

Fig. 12 Stability of Cascade B3 rotor

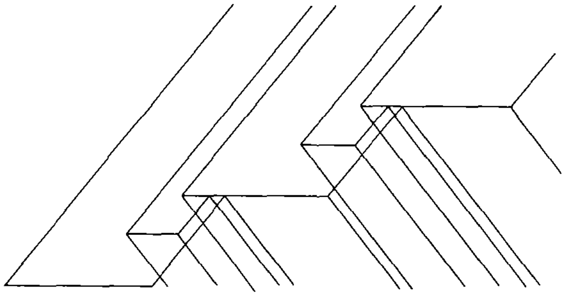

Fig. 13 Cascade B4 flow geometry: $Sp_{\mathrm{cord1}} = Sp_{\mathrm{cord2}}$ = 35 percent, $P_{\mathrm{start1}} = P_{\mathrm{start2}}$ = 15 percent, $P_{\mathrm{split1}} = P_{\mathrm{split2}}$ = 60 percent

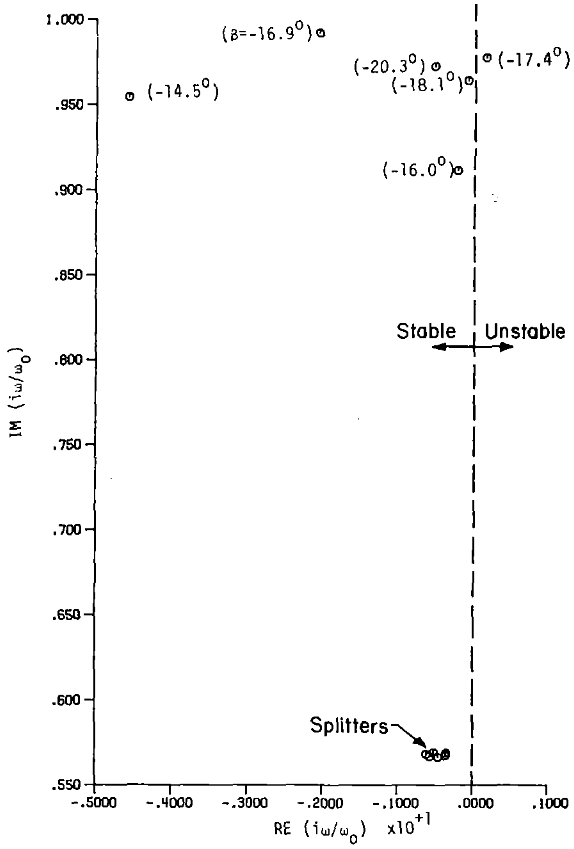

Fig. 14 Stability of Cascade B4 rotor

and Cascade B2 (Figs. 8 and 10) shows that Cascade B2 is substantially more stable than Cascade B1. There are now only three unstable vibrational modes, characterized by interblade phase angles of 3.0, 7.3, and 7.0 deg. The stability gain is attributed to the absence of Mach wave intersections in the trailing edge region of the suction surface of the full chord Cascade B2 airfoils.

Aerodynamically detuned Cascades B3 and B4 demonstrate the effect of Mach wave intersections on the pressure surface of the full chord airfoils. Cascade B3 (Fig. 11) is made up of uniformly spaced full chord airfoils with alternate splitters with chord lengths 35 percent of the full chord airfoils and leading edges located at 65 percent of the full chord airfoil length, spaced 60 percent of the distance between them. As seen, the Mach wave intersections on the full chord airfoils occur only on the pressure surface, both upstream and downstream of midchord. The root locus of the eigenvalues (Fig. 12) indicates an unstable cascade with all unstable modes corresponding to forward-traveling waves, the least stable having an interblade phase angle of 71.3 deg. As seen, Cascade B3 is more stable than either Cascade B1 or the baseline Cascade B. This is because, unlike Cascade B1 and the baseline Cascade B, Cascade B3 has no Mach wave intersections near the trailing edge of the suction surface of the full chord airfoils.

Figure 13 shows the Cascade B4 configuration. As seen, the splitter leading edges have been moved upstream to 15 percent of the full chord length. All Mach wave intersections on the full chord airfoils occur on the leading half of the pressure surface. The root locus of the eigenvalues (Fig. 14) shows greatly enhanced stability over all of the previous cases. Cascade B4 is, in fact, neutrally stable, i.e., there are no unstable interblade phase angles. The stability gain is attributed to moving the Mach wave intersections on the pressure surface of the full chord airfoils forward of the midchord elastic axis.

All of the cases discussed thus far have employed uniformly spaced full chord airfoils and identical alternate splitters. Additional aeroelastic stability can be achieved by considering nonuniformly spaced full chord airfoils and by specifying two different set of splitters. Cascade B5 serves to illustrate these effects.

Figure 15 shows the Cascade B5 configuration. The full chord airfoil spacing has been aerodynamically detuned by 10

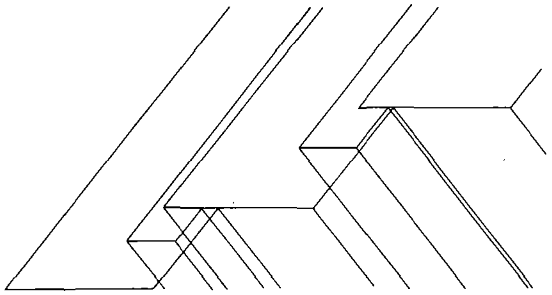

Fig. 15 Cascade B5 flow geometry: Sp_{cord1} = 33 percent, Sp_{cord2} = 38 percent, P_{start1} = 20 percent, P_{start2} = 15 percent, P_{split1} = 60 percent, P_{split2} = 60 percent

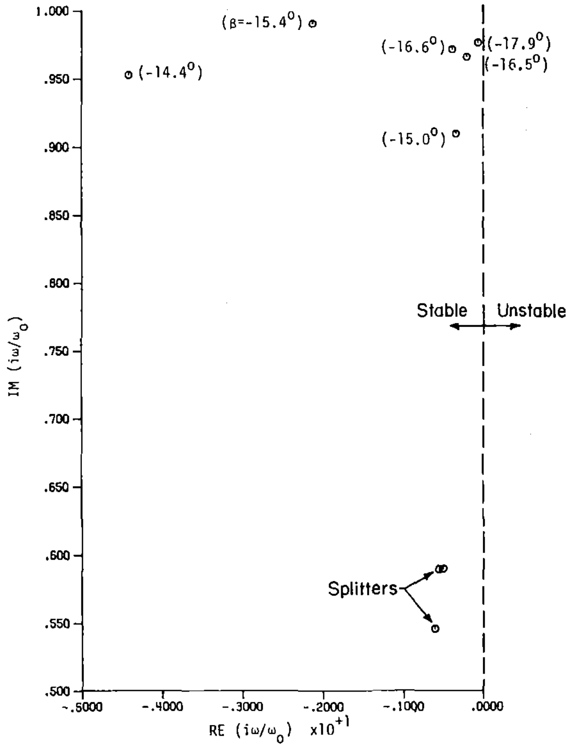

Fig. 16 Stability of Cascade B5 rotor

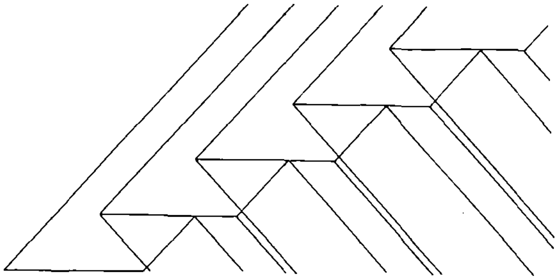

Fig. 17 Verdon's Cascade A flow geometry

percent such that there are reduced and increased spacing full chord airfoil passages. The splitters are similar to those of Cascades B4. The stability of the cascade is specified by the root locus of the eigenvalues (Fig. 16). As seen, Cascade B5 is a stable configuration.

To further demonstrate the enhanced aeroelastic stability associated with this type of aerodynamic detuning, Verdon's Cascade A is also considered as a baseline configuration. Cascade A is characterized by a Mach number of 1.345, a reduced frequency of 0.601, a stagger angle of 59.5 deg, and a midchord elastic axis location. The geometry and root locus

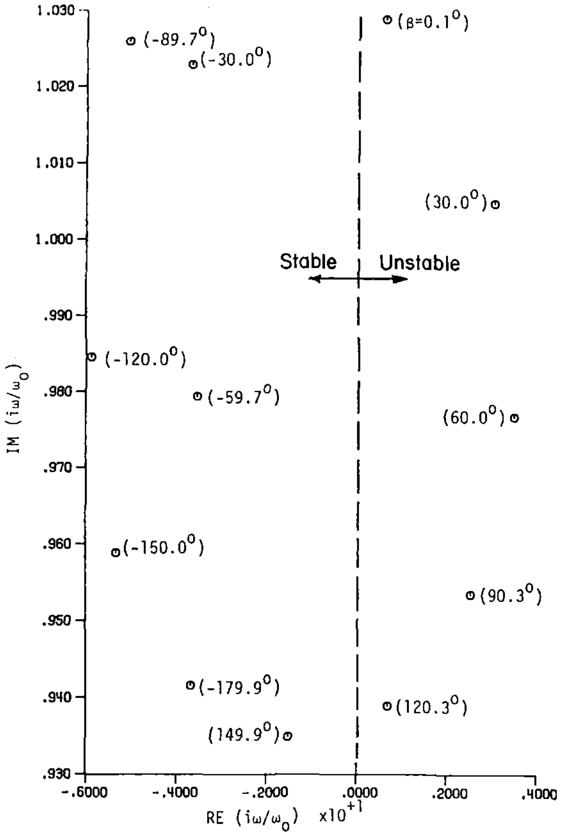

Fig. 18 Stability of baseline Cascade A rotor

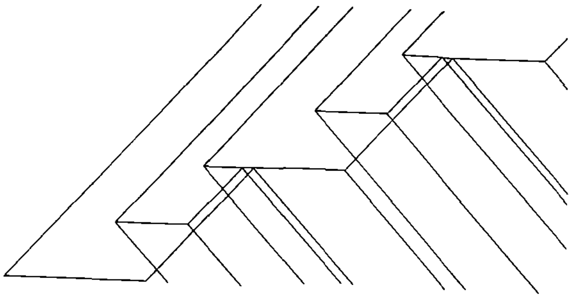

Fig. 19 Cascade A1 flow geometry: Sp_{cord1} = Sp_{cord2} = 50 percent, P_{start1} = P_{start2} = 10 percent, P_{split1} = P_{split2} = 50 percent

plot for this baseline Cascade A are presented in Figs. 17 and 18.

While maintaining the inlet Mach number, reduced frequency, stagger angle, and elastic axis location, two aerodynamically detuned variations of Cascade A are considered.

Cascade A1 (Fig. 19) utilizes uniformly spaced full chord airfoils with identical alternate splitters. The geometry is prescribed in accordance with the observations about Mach wave-airfoil intersections made in the Cascade B investigation: no Mach wave intersections on either the suction side of the full chord airfoils or the trailing half of the pressure side of the full chord airfoils. As seen in Fig. 20, which presents the root locus plot for Cascade A1, this aerodynamically detuned configuration is stable.

A second stable configuration, constructed with uniformly spaced full chord airfoils and two different sets of splitters, is Cascade A2 (Fig. 21). The set of odd Cascade A2 splitters has the same chord length as the splitters in Cascade A1, but is located 5 percent farther downstream. The set of even splitters, having a common leading edge location with the Cascade A1 splitters, is 5 percent longer than its Cascade A1 counterpart. The two different splitter chord lengths cause the eigen-

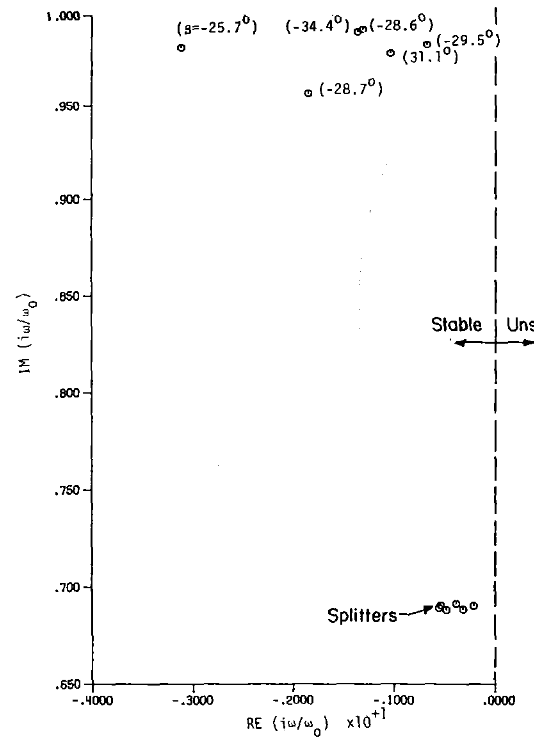

Fig. 20 Stability of Cascade A1 rotor

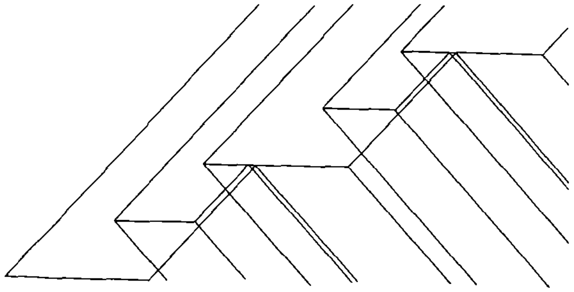

Fig. 21 Cascade A2 flow geometry: Sp_{cord1} = 55 percent, Sp_{cord2} = 50 percent, P_{start1} = 10 percent, P_{start2} = 15 percent, P_{split1} = 50 percent, P_{split2} = 50 percent

values to cluster into three distinct groups, corresponding to the three different airfoil natural frequencies (Fig. 22).

Summary and Conclusions

A mathematical model has been developed and utilized to demonstrate the use of splitter blades as an aeroelastic detuning mechanism for unstalled supersonic flutter of turbomachine rotors. The splitters significantly alter the chordwise distributions of the unsteady pressure and aerodynamic moment distributions on the rotor blading, i.e., the splitters provide a large measure of control of the location of the Mach wave-full chord airfoil and splitter intersections. The level of structural detuning introduced into the system by the splitters is a function of the ratio of the natural frequencies of the splitters to that of the full chord airfoils, specified by the relative chord lengths of the splitter and full chord airfoils. Thus, the splitter chord length and location within the full chord airfoil passages have a significant influence on the stability of the rotor.

The enhanced flutter stability due to the incorporation of the splitters is demonstrated by applying this model to two unstable baseline twelve-bladed rotor configurations. In each case, the unstable baseline rotor is stabilized by the introduction of appropriate splitters. The critical parameters for this

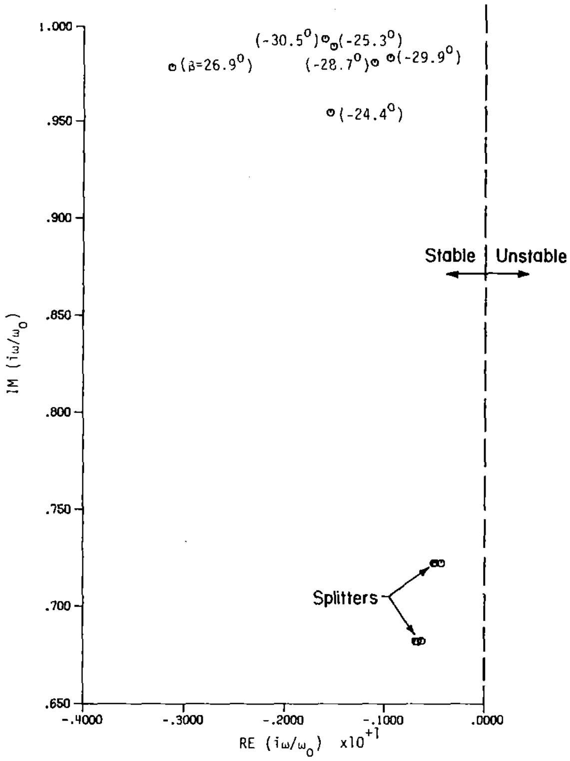

Fig. 22 Stability of Cascade A2 rotor

stability enhancement are the chord length and the circumferential and axial locations of the splitters. The greatest stability gains are realized by designing the splitters such that there are no Mach wave intersections on the suction surface of the full chord airfoils and the pressure surface intersections occur on the leading half of the full chord airfoils. Also, the chord length of the splitters is of particular importance because it contributes to both the aerodynamic and the structural detuning.

Acknowledgments

The NASA Lewis Research Center and, in particular, Dan Hoyniak, Don Boldman, and Cal Ball, are most gratefully acknowledged for their encouragement, discussions, and support.

References

1 Whitehead, D. S., "Effect of Mistuning on the Vibration of Turbomachine Blades Induced by Wakes," *Journal of Mechanical Engineering Science*, Vol. 8, No. 1, Mar. 1966.

2 Kaza, K. R. V., and Kielb, R. E., "Effect of Mistuning on Bending-Torsion Flutter and Response of a Cascade in Incompressible Flow," *AIAA Journal*, Vol. 20, No. 8, Aug 1982.

3 Kielb, R. E., and Kaza, K. R. V., "Aeroelastic Characteristics of Mistuned Blades in Subsonic and Supersonic Flows," ASME *Journal of Vibration, Stress, and Reliability in Design*, Vol. 105, Oct. 1983.

4 Bendiksen, O. O., "Flutter of Mistuned Turbomachinery Rotors," ASME JOURNAL OF ENGINEERING FOR GAS TURBINES AND POWER, Vol. 106, 1984, pp. 25-33.

5 Crawley, E. F., and Hall, K. C., "Optimization and Mechanisms of Mistuning of Cascades," ASME JOURNAL OF ENGINEERING FOR GAS TURBINES AND POWER, Vol. 107, 1985, pp. 418-426.

6 Hoyniak, D., and Fleeter, S., "Aerodynamic Detuning Analysis of an Unstalled Supersonic Turbofan Cascade," ASME JOURNAL OF ENGINEERING FOR GAS TURBINES AND POWER, Vol. 108, 1986, pp. 60-67.

7 Brix, C. W., and Platzer, M. F., "Theoretical Investigation of Supersonic Flow Past Oscillating Cascades With Subsonic Leading Edge Locus," AIAA Paper 74-14, Jan. 1974.

8 Verdon, J. M., "The Unsteady Aerodynamics of a Finite Supersonic Cascade With Subsonic Axial Flow," ASME *Journal of Applied Mechanics*, Vol. 40, Sept. 1973.

The Effect of Circumferential Aerodynamic Detuning on Coupled Bending-Torsion Unstalled Supersonic Flutter

D. Hoyniak
Aerospace Engineer,
NASA Lewis Research Center,
Cleveland, OH 44135

S. Fleeter
Professor,
School of Mechanical Engineering;
Director, Thermal Sciences and
Propulsion Center,
Purdue University,
West Lafayette, IN 47907

A mathematical model is developed to predict the enhanced coupled bending-torsion unstalled supersonic flutter stability due to alternate circumferential spacing aerodynamic detuning of a turbomachine rotor. The translational and torsional unsteady aerodynamic coefficients are developed in terms of influence coefficients, with the coupled bending-torsion stability analysis developed by considering the coupled equations of motion together with the unsteady aerodynamic loading. The effect of this aerodynamic detuning on coupled bending-torsion unstalled supersonic flutter as well as the verification of the modeling are then demonstrated by considering an unstable twelve-bladed rotor, with Verdon's uniformly spaced Cascade B flow geometry as a baseline. It was found that with the elastic axis and center of gravity at or forward of the airfoil midchord, 10 percent aerodynamic detuning results in a lower critical reduced frequency value as compared to the baseline rotor, thereby demonstrating the aerodynamic detuning stability enhancement. However, with the elastic axis and center of gravity at 60 percent of the chord, this type of aerodynamic detuning has a minimal effect on stability. For both uniform and nonuniform circumferentially spaced rotors, a single degree of freedom torsion mode analysis was shown to be appropriate for values of the bending-torsion natural frequency ratio lower than 0.6 and higher than 1.2. However, for values of this natural frequency ratio between 0.6 and 1.2, a coupled flutter stability analysis is required. When the elastic axis and center of gravity are not coincident, the effect of detuning on cascade stability was found to be very sensitive to the location of the center of gravity with respect to the elastic axis. In addition, it was determined that when the center of gravity was forward of an elastic axis located at midchord, a single degree of freedom torsion model did not accurately predict cascade stability.

Introduction

To analyze the aeroelastic stability of gas turbine engine bladed-disk assemblies, a typical airfoil section approach is utilized. Thus, the three-dimensional flow field is approximated by two-dimensional strips along the span of the blade. Also, the rotor is assumed to be tuned, with all of the blades identical and uniformly spaced. Hence, the airfoil structural properties and the unsteady aerodynamic loading at a particular span location are assumed to be identical for each airfoil. However, due to manufacturing tolerances, the individual airfoil natural frequencies are never identical, i.e., the rotors are structurally detuned.

Whitehead [1] developed an analysis which demonstrated the effects of this natural frequency structural detuning on the flutter characteristics of a rotor. Several other investigators have shown that the deliberate introduction of structural detuning into a rotor design can be utilized as a passive means of controlling rotor stability [2-5]. In these analyses, the ratio of the airfoil bending mode frequency to that of the torsion mode was assumed to be small. Thus, the stability analyses were performed on equivalent single degree of freedom models. However, Bendiksen and Friedmann [6] showed that the coupling between the bending and the torsion modes of vibration can have a significant effect on the flutter characteristics of a tuned rotor configuration.

Another approach to passive rotor stability control, termed aerodynamic detuning, has recently been proposed [7]. Aerodynamic detuning is defined as designed passage-to-passage variations in the unsteady aerodynamic flow field of the blade row. The subsequent blade-to-blade differences in the unsteady aerodynamic loading result in the blading not responding in a classical traveling wave mode typical of conventional tuned rotor analyses. In [7], the effect of aerodynamic detuning on unstalled supersonic single degree of freedom torsion mode flutter, with the aerodynamic detuning

---

Contributed by the Gas Turbine Division of THE AMERICAN SOCIETY OF MECHANICAL ENGINEERS and presented at the 31st International Gas Turbine Conference and Exhibit, Düsseldorf, Federal Republic of Germany, June 8-12, 1986. Manuscript received at ASME Headquarters January 20, 1986. Paper No. 86-GT-100.

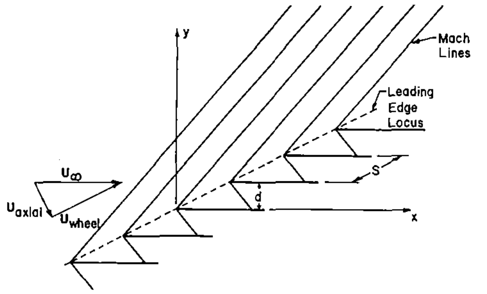

Fig. 1 Uniformly spaced tuned cascade in a supersonic inlet flow field with a subsonic leading edge locus

accomplished by alternating the circumferential spacing of adjacent rotor blades, was considered.

In this paper, this alternate circumferential spacing aerodynamic detuning torsional model is extended to analyze the unsteady translational unsteady aerodynamics to account for the coupling between the bending and torsion motions of the airfoils. The unsteady aerodynamic loading resulting from both the torsional and the translational motions of the airfoils is developed in terms of aerodynamic influence coefficients. A coupled bending-torsion unstalled supersonic flutter analysis appropriate for both conventional tuned and aerodynamically detuned rotors is then developed by considering the coupled equations of motion together with the unsteady aerodynamic loading. The enhanced coupled bending-torsion unstalled supersonic flutter stability due to alternate circumferential aerodynamic detuning is then demonstrated by applying this analysis to an unstable twelve-bladed rotor, with Verdon's Cascade B flow geometry [8] as a baseline uniformly spaced geometry.

Unsteady Aerodynamic Model

The unsteady aerodynamic models utilized in flutter analyses of fan and compressor blading consider a two-dimensional cascade with uniformly spaced airfoils to represent a typical rotor blade section. The motion-dependent unsteady aerodynamic loading is determined by harmonically oscillating the airfoils in a classical traveling wave mode, i.e., each airfoil has the same amplitude and the interblade phase angle between adjacent airfoils is constant.

For unstalled supersonic flutter, a flat plate airfoil cascade embedded in a supersonic inlet flow field with a subsonic leading edge locus is considered (Fig. 1). The fluid is assumed to be an inviscid perfect gas with the flow isentropic, adiabatic, and irrotational. The unsteady continuity and Euler equations are linearized by assuming that the unsteady perturbations are small as compared to the uniform through flow. The boundary conditions, applied on the mean positions of the oscillating airfoils, require the flow to be tangent to the airfoil surfaces.

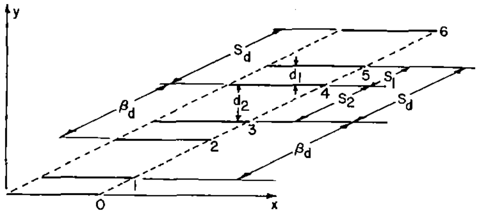

Fig. 2 Finite cascade representation for alternate nonuniform circumferentially spaced cascade

Several investigators have utilized various techniques to predict the unsteady aerodynamics associated with the torsional and translational motions of the airfoil cascade depicted in Fig. 1. Of particular interest are the analyses of Verdon [9], Brix and Platzer [10], and Caruthers [11]. These utilize a finite cascade representation of the semi-infinite cascade, with the cascade periodicity condition enforced by stacking sufficient numbers of uniformly spaced single airfoils until convergence in the unsteady flow field is achieved. An analogous finite cascade model is utilized for the alternate circumferentially spaced aerodynamically detuned cascade (Fig. 2). As shown, for this detuned cascade configuration, there are two sets of airfoils, for convenience termed the set of even-numbered airfoils and the set of odd-numbered airfoils. Thus, convergence in the detuned unsteady flow field is achieved by stacking sufficient numbers of airfoils two at a time.

The formulation of the linearized differential equations describing the unsteady perturbation quantities for a finite aerodynamically detuned cascade is based on the method of characteristic analysis developed by Brix and Platzer for the finite uniformly spaced cascade [10]. The independent variables are the dimensionless chordwise and normal coordinates, x and y. The dependent variables are the chordwise, normal, and sonic perturbation velocities, u, v, and c, respectively. Assuming harmonic motion, the linearized differential equations describing the unsteady perturbation flow field are specified in equation (1)

Nomenclature

a = dimensionless elastic axis offset
b = blade semichord
c = perturbation in speed of sound
$\mathbf{h}$ = complex bending displacement
h = amplitude of bending displacement
k = reduced frequency = ω/U_∞
l = dimensionless unsteady aerodynamic lift coefficient
m = dimensionless unsteady aerodynamic moment coefficient
r_α = dimensionless radius of gyration
u = perturbation chordwise velocity
v = perturbation normal velocity
x = dimensionless chordwise coordinate = X/C
x_α = dimensionless CG-EA offset
y = dimensionless normal coordinate = Y/C
C = airfoil chord
I = mass moment of inertia
K = linear spring constant
L = unsteady aerodynamic lifting force per unit span
M = unsteady aerodynamic moment per unit span
M_∞ = cascade inlet Mach number
S = airfoil spacing
S_α = static mass moment per unit span about elastic axis
S_d = nonuniform airfoil spacing
U_∞ = cascade inlet velocity
$\boldsymbol{\alpha}$ = complex torsional displacement
α = amplitude of torsional displacement
β = interblade phase angle
γ = complex eigenvalue
γ_α = ratio of natural frequency in torsion to the reference frequency
γ_h = ratio of natural frequency in bending to the reference frequency
μ = mass ratio
ζ = damping ratio
ω_α = natural frequency in torsion
ω_h = natural frequency in bending
ω = oscillatory frequency
$[\ ]$ = matrix

Subscripts

d = detuned cascade
h = refers to bending displacement
R_e = reference for the set of even-numbered airfoils
R_o = reference for the set of odd-numbered airfoils
α = refers to torsional displacement

$$\frac{\partial u}{\partial x}+\sqrt{M_\infty^2-1}\,\frac{\partial v}{\partial y}+M^2\,\frac{\partial c}{\partial x}+ikM_\infty^2 c=0 \qquad (1a)$$

$$\frac{\partial u}{\partial x}+\frac{\partial c}{\partial x}+iku=0 \qquad (1b)$$

$$\frac{\partial u}{\partial x}-\sqrt{M_\infty^2-1}\,\frac{\partial v}{\partial x}=0 \qquad (1c)$$

The flow tangency boundary condition requires that the normal perturbation velocity component v be equal to the normal velocity of the oscillating airfoils, and is applied at the mean airfoil positions. For the aerodynamically tuned airfoil cascade executing both harmonic translational (bending) and torsional motions, the dimensionless normal perturbation velocity component on the nth airfoil is specified in equation (2)

$$v_n(x, y_s, t)=\{h_o[ik]-\alpha_o[1+(x-x_o)ik]\}e^{i(kt+n\beta)} \qquad (2)$$

where h_o and α_o denote the nondimensional translational and torsional amplitudes of a reference airfoil; β is the interblade phase angle; and x_o, y_s, and k are the elastic axis location as measured from the airfoil leading edge, the mean position of the airfoil, and the reduced frequency, respectively.

The unsteady perturbation pressure distributions on the two reference airfoils, one for the set of even-numbered airfoils and the other for the set of odd-numbered airfoils, R_e and R_o, are determined from the perturbation velocities by the unsteady Bernoulli equation. The unsteady aerodynamic lift and moment on these reference airfoils are then calculated by integrating the unsteady perturbation pressure differences across their chord lines

$$L_{R_e,R_o} = \int_0^1 \Delta p(x, y_s, t)dx \qquad (3a)$$

$$M_{R_e,R_o} = \int_0^1 (x-x_o)\Delta p(x, y_s, t)dx \qquad (3b)$$

The double subscript is a shorthand equation notation, with the subscript R_e denoting the equation for the reference airfoil of the set of even-numbered airfoils, and R_o the equation for the reference airfoil of the set of odd-numbered airfoils.

When the boundary conditions specified in equation (2) are applied to an aerodynamically detuned cascade, the alternate circumferentially spaced airfoils are required to oscillate with an equal amplitude and a constant interblade phase angle, a situation not appropriate for the detuned cascade. In addition, the application of this analysis is unduly costly because the complete periodic perturbation flow field must be recalculated, not only for every new cascade geometry and flow condition, but also for each interblade phase angle for a particular cascade geometry and flow field.

These restrictions can be eliminated by using the aerodynamic influence coefficient technique introduced in [7]. A complete derivation of the influence coefficients required to describe the unsteady aerodynamic moments resulting from harmonic torsional motion of the airfoils in an alternate circumferentially spaced detuned cascade is presented in this reference. The required unsteady aerodynamic translational lift coefficients are obtained in an analogous manner, with this derivation not repeated herein.

The unsteady aerodynamic lift and moment on the two reference airfoils of an alternate circumferentially spaced detuned cascade undergoing both harmonic torsional and translational motions are defined in terms of influence coefficients in equation (4)

$$L_{R_e,R_o}=-\Pi\rho b^3\omega^2\Big\{\Big(\frac{h_{R_e}}{b}\Big)[l_h^e]_{R_e,R_o}+\Big(\frac{h_{R_o}}{b}\Big)[l_h^o]_{R_e,R_o} + \alpha_{R_e}[l_\alpha^e]_{R_e,R_o}+\alpha_{R_o}[l_\alpha^o]_{R_e,R_o}\Big\}e^{i\omega t} \qquad (4a)$$

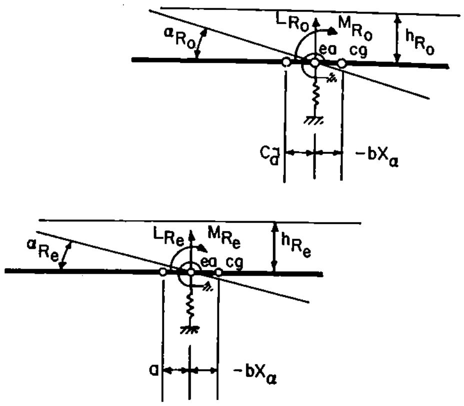

Fig. 3 Coupled bending-torsion model of typical blade sections in a circumferentially detuned cascade

$$M_{R_e,R_o}=\Pi\rho b^4\omega^2\Big\{\Big(\frac{h_{R_e}}{b}\Big)[m_h^e]_{R_e,R_o}+\Big(\frac{h_{R_o}}{b}\Big)[m_h^o]_{R_e,R_o} + \alpha_{R_e}[m_\alpha^e]_{R_e,R_o}+\alpha_{R_o}[m_\alpha^o]_{R_e,R_o}\Big\}e^{i\omega t} \qquad (4b)$$

The superscripts e and o refer to the sets of even-numbered and odd-numbered airfoils, respectively. The negative sign in equation (4a) indicates that for a positive downward translational displacement, the lift is negative, and thus acts in an upward direction.

The term $[l_h^e]_{R_e,R_o}$ is the nondimensional unsteady lift per unit translational displacement on the reference airfoil R_e or R_o due to unit amplitude translational displacements of all of the even-numbered airfoils with the odd-numbered airfoils fixed. $[l_h^o]_{R_e,R_o}$ is the corresponding lift on the reference airfoils due to unit amplitude translational displacements of all of the odd-numbered airfoils with the even-numbered airfoils fixed. Similarly, $[l_\alpha^e]_{R_e,R_o}$ is the unsteady lift per unit torsional displacement developed on the two reference airfoils due to unit amplitude torsional motions of the set of odd-numbered airfoils while the set of even-numbered airfoils is fixed. The unsteady aerodynamic moments on the reference airfoils, $[m_h^e]_{R_e,R_o}$, $[m_h^o]_{R_e,R_o}$, $[m_\alpha^e]_{R_e,R_o}$, $[m_\alpha^o]_{R_e,R_o}$, are defined in an analogous manner.

The relation between the unsteady aerodynamic lift and moment coefficients specified in equation (4) and those utilized by Kaza and Kielb [2] for a uniformly spaced cascade, l_{hh}, $l_{h\alpha}$, $l_{\alpha h}$, and $l_{\alpha\alpha}$, are readily obtained

$$l_{hh} = [l_h^e]_{R_e}+\Big(\frac{h_{R_o}}{h_{R_e}}\Big)[l_h^o]_{R_e} \qquad (5a)$$

$$l_{h\alpha} = [l_\alpha^e]_{R_e}+\Big(\frac{h_{R_o}}{h_{R_e}}\Big)[l_\alpha^o]_{R_e} \qquad (5b)$$

$$l_{\alpha h} = [m_h^e]_{R_e}+\Big(\frac{\alpha_{R_o}}{\alpha_{R_e}}\Big)[m_h^o]_{R_e} \qquad (5c)$$

$$l_{\alpha\alpha} = [m_\alpha^e]_{R_e}+\Big(\frac{\alpha_{R_o}}{\alpha_{R_e}}\Big)[m_\alpha^o]_{R_e} \qquad (5d)$$

Similar expressions can also be obtained in terms of the reference airfoil for the set of odd-numbered airfoils R_o.

Equations of Motion

The equations of motion for both conventional uniform and alternate circumferentially spaced aerodynamically detuned cascade configurations are developed by considering the

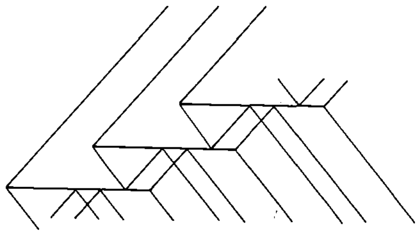

Fig. 4 Baseline Cascade B uniformly spaced flow geometry

typical airfoil sections depicted schematically in Fig. 3. Translational displacements of the reference airfoils h_{R_e} and h_{R_o} are defined as positive in the downward direction. Torsional motions of the reference airfoils α_{R_e} and α_{R_o} are defined as positive with the leading edge up. The unsteady aerodynamic lift and moment were defined in equation (4) such that a positive lift is upward and a positive moment is leading edge up.

The inertia and stiffness properties of the airfoil section are modeled by the mass moment of inertia about the elastic axis and by linear springs attached at the elastic axis. Applying Lagrange's technique, the following differential equations of motion for the two reference airfoils of the detuned cascade are obtained

$$\begin{aligned} & m_{R_e,R_o}\ddot{\mathbf{h}}_{R_e,R_o} + S_{\alpha_{R_e,R_o}}\ddot{\alpha}_{R_e,R_o} \\ & \qquad + (1+2i\zeta_{h_{R_e,R_o}})m_{R_e,R_o}\omega^2_{h_{R_e,R_o}}\mathbf{h}_{R_e,R_o} = -L_{R_e,R_o} \\ & S_{\alpha_{R_e,R_o}}\ddot{\mathbf{h}}_{R_e,R_o} + I_{\alpha_{R_e,R_o}}\ddot{\alpha}_{R_e,R_o} \\ & \qquad + (1+2i\zeta_{\alpha_{R_e,R_o}})I_{\alpha_{R_e,R_o}}\omega^2_{\alpha_{R_e,R_o}}\alpha_{R_e,R_o} = M_{R_e,R_o} \end{aligned} \tag{6}$$

where the damping ratios for both translation and torsional motions are denoted by $\zeta_{h_{R_e,R_o}}$ and $\zeta_{\alpha_{R_e,R_o}}$, and the undamped natural frequencies are

$$\omega_{h_{R_e,R_o}} = \sqrt{K_{h_{R_e,R_o}}/m_{R_e,R_o}} \text{ and } \omega_{\alpha_{R_e,R_o}} = \sqrt{K_{\alpha_{R_e,R_o}}/I_{\alpha R_e,R_o}}.$$

For harmonic motions of the airfoils, the differential equations of motion, equation (6), can be written as an eigenvalue problem from which the stability of the conventional and the aerodynamically detuned cascade configurations can be determined. This eigenvalue problem is specified in matrix form in equation (7)

$$\begin{bmatrix} \mu_{h1} & [l_h^o]_{R_e} & \mu_{h3} & [l_\alpha^o]_{R_e} \\ [l_h^e]_{R_o} & \mu_{h2} & [l_\alpha^e]_{R_o} & \mu_{h4} \\ \mu_{\alpha 1} & [m_h^o]_{R_e} & \mu_{\alpha 2} & [m_\alpha^o]_{R_e} \\ [m_h^e]_{R_o} & \mu_{\alpha 3} & [m_\alpha^e]_{R_o} & \mu_{\alpha 4} \end{bmatrix} \begin{Bmatrix} \dfrac{h_{R_e}}{b} \\ \dfrac{h_{R_o}}{b} \\ \alpha_{R_e} \\ \alpha_{R_o} \end{Bmatrix} = \begin{Bmatrix} 0 \end{Bmatrix} \tag{7}$$

where

$$\begin{aligned} \mu_{h1} &= \mu_{R_e} + [l_h^e]_{R_e} - (1+2i\zeta_{h_{R_e}})\mu_{R_e}\gamma^2_{h_{R_e}}\gamma \\ \mu_{h2} &= \mu_{R_o} + [l_h^o]_{R_e} - (1+2i\zeta_{h_{R_o}})\mu_{R_o}\gamma^2_{h_{R_o}}\gamma \\ \mu_{h3} &= \mu_{R_e}x_{\alpha_{R_e}} + [l_\alpha^e]_{R_e} \\ \mu_{h4} &= \mu_{R_o}x_{\alpha_{R_o}} + [l_\alpha^o]_{R_o} \\ \mu_{\alpha 2} &= \mu_{R_e}r^2_{\alpha_{R_e}} + [m_\alpha^e]_{R_e} - (1+2i\zeta_{\alpha_{R_e}})\mu_{R_e}r^2_{\alpha_{R_e}}\gamma^2_{\alpha_{R_e}}\gamma \\ \mu_{\alpha 4} &= \mu_{R_o}r^2_{\alpha_{R_o}} + [m_\alpha^o]_{R_o} - (1+2i\zeta_{\alpha_{R_o}})\mu_{R_o}r^2_{\alpha_{R_o}}\gamma^2_{\alpha_{R_o}}\gamma \\ \mu_{\alpha 1} &= \mu_{R_e}x_{\alpha_{R_e}} + [m_h^e]_{R_e} \\ \mu_{\alpha 3} &= \mu_{R_o}x_{\alpha_{R_o}} + [m_h^o]_{R_o} \end{aligned}$$

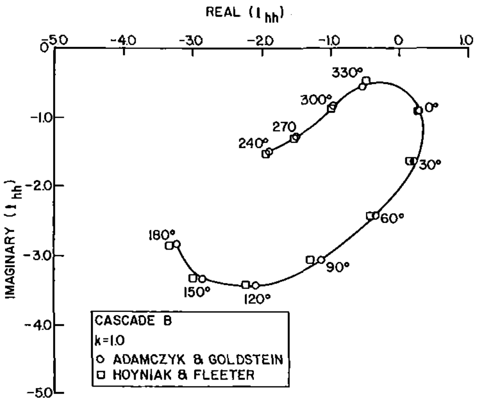

Fig. 5 Unsteady lift coefficient l_{hh} for Cascade B

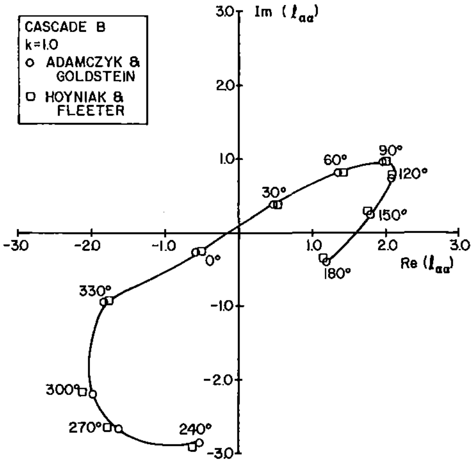

Fig. 6 Unsteady moment coefficient $l_{\alpha\alpha}$ for Cascade B

$$\begin{aligned} \mu_{R_e,R_o} &= \frac{m_{R_e,R_o}}{\Pi\rho b^2}\,;\ r^2_{\alpha_{R_e,R_o}} = \frac{I_{\alpha_{R_e,R_o}}}{m_{R_e,R_o}b^2} \\ \gamma_{h_{R_e,R_o}} &= \frac{\omega_{h_{R_e,R_o}}}{\omega_o}\,;\ \gamma_{\alpha_{R_e,R_o}} = \frac{\omega_{\alpha_{R_e,R_o}}}{\omega_o} \\ x_{\alpha_{R_e,R_o}} &= \frac{S_{\alpha_{R_e,R_o}}}{m_{R_e,R_o}b}\,;\ \omega_o = \text{reference frequency} \\ \gamma &= \left(\frac{\omega_o}{\omega}\right)^2 \end{aligned}$$

The stability of the cascade configuration is obtained by solving equation (7) and then relating the complex eigenvalue γ to the complex frequency ratio (ω_o/ω), with the result given in equation (8)

$$\frac{\omega}{\omega_o} = \frac{1}{\sqrt{\gamma}} \tag{8}$$

The eigenvalues obtained from equation (7) are complex. Therefore, the stability of the system is determined by the sign of the real part of (ω/ω_o) in equation (8). When the real part of (ω/ω_o) is negative, the amplitude of the harmonic motion of the airfoil will decay, indicating a stable cascade configuration. A positive sign for the real part of (ω/ω_o) indicates that the airfoil motion will increase in amplitude and that the cascade is unstable. A value of zero indicates that the cascade is neutrally stable. The imaginary part of (ω/ω_o) specifies the ratio of the flutter frequency ω to the reference frequency ω_o.

Results

To demonstrate the stability enhancement due to alternate

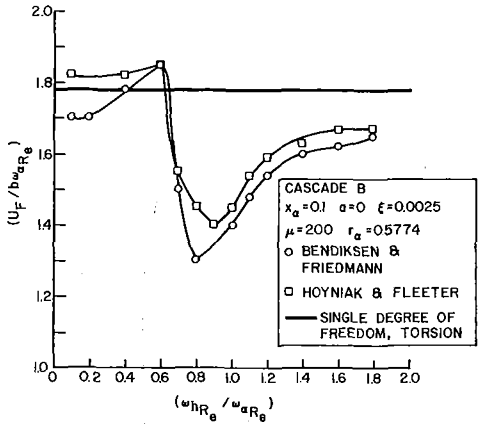

Fig. 7 Verification of the coupled bending-torsion eigenvalue model

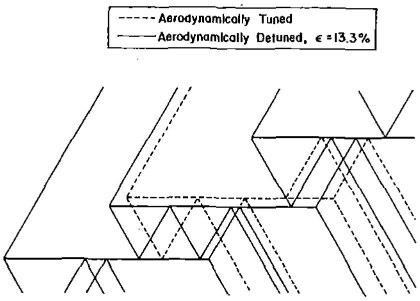

Fig. 8 The flow geometries of the baseline and circumferentially detuned cascades

circumferential blade spacing aerodynamic detuning on unstalled supersonic coupled bending-torsion flutter, an unstable baseline uniformly spaced twelve-bladed rotor based on Verdon's Cascade B is considered. This baseline rotor is also utilized to verify the validity and the formulation of this mathematical model. The baseline uniform circumferentially spaced Cascade B flow geometry is schematically depicted in Fig. 4, and is characterized by a stagger angle of 63.4 deg, a solidity of 1.497, and an inlet Mach number of 1.281.

The validity of both the aerodynamic influence coefficient formulation and the translational and torsional unsteady aerodynamic finite cascade model are verified by correlating predictions for the translational and torsional unsteady aerodynamic coefficient, l_{hh} and $l_{\alpha\alpha}$, from the model developed herein with corresponding predictions from the infinite cascade analysis of Adamczyk and Goldstein [12] for a uniformly spaced baseline Cascade B flow geometry at a unity reduced frequency. As seen in Figs. 5 and 6, there is good agreement for both coefficients between the two techniques.

The formulation of the coupled bending-torsion eigenvalue problem is verified by correlating the coupled stability predictions from the model developed by Bendiksen and Friedmann for a uniformly spaced cascade [6] with corresponding predictions from the model developed herein. For this verification, the baseline Cascade B rotor is considered with a midchord elastic axis location, a center of gravity specified by $x_\alpha = 0.1$, and a damping ratio of $\zeta = 0.0025$. Figure 7 presents the results of this correlation in the format of the critical reduced frequency versus the bending-torsion natural frequency ratio. The good correlation between these two models is apparent.

With the validity and formulation of this mathematical model verified, attention is now turned to utilizing this model to consider the stability enhancement due to alternate circumferential blade spacing aerodynamic detuning on unstalled supersonic coupled bending-torsion flutter. This is accomplished by utilizing an unstable baseline uniformly spaced twelve-bladed rotor based on Verdon's Cascade B flow geometry as well as an alternate circumferentially spaced rotor with 10 percent aerodynamic detuning. The flow geometries for these uniformly spaced and nonuniformly spaced cases are schematically depicted in Fig. 8.

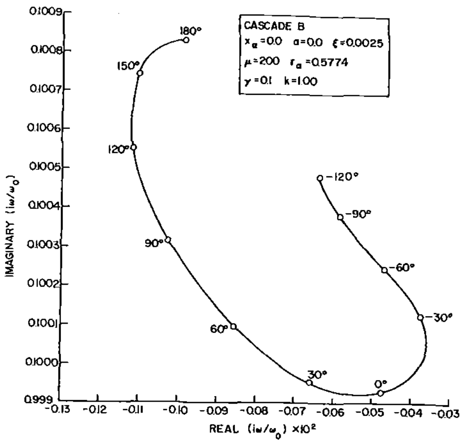

Fig. 9 Bending mode root locus plot for a twelve-bladed rotor

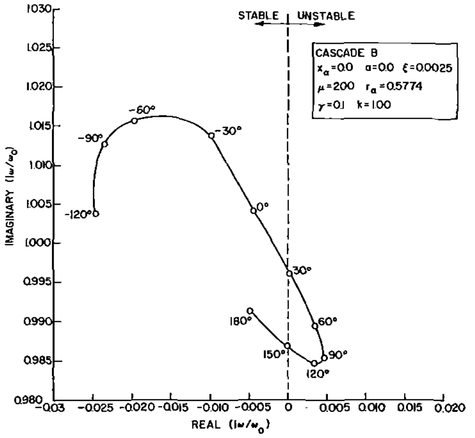

Fig. 10 Torsion mode root locus plot for a twelve-bladed rotor

The stability of a given rotor design is predicted by the eigenvalue problem specified in equation (7). Typical bending and torsion mode root locus plots are presented in Figs. 9 and 10, respectively, for the baseline Cascade B twelve-bladed rotor at a reduced frequency of 1.0. These were determined from equation (7) by considering a value of 0.1 for the bending-torsion natural frequency ratio. Figure 9 shows that the bending modes are all stable. However, as seen in Fig. 10, the torsion modes are unstable for forward-traveling waves characterized by interblade phase angles between 30 and 150 deg.

The coupled bending-torsion stability results for both the baseline uniformly spaced and the 10 percent alternate circumferential aerodynamically detuned rotors are presented in Fig. 11 in the format of the critical reduced frequency as a function of the bending-torsion natural frequency ratio. For both cascades, the elastic axis and the center of gravity are coincident at the blade midchord. Also indicated are the single degree of freedom torsion mode results for both cascades. It should be noted that with the elastic axis and the center of gravity coincident, the equations of motion are coupled only through the unsteady aerodynamic loading terms.

As seen in Fig. 11, the aerodynamically detuned rotor has a lower critical reduced frequency value than does the baseline tuned rotor, thereby demonstrating the stability enhancement due to aerodynamic detuning. Also, both the tuned and the detuned cascades behave like their single degree of freedom

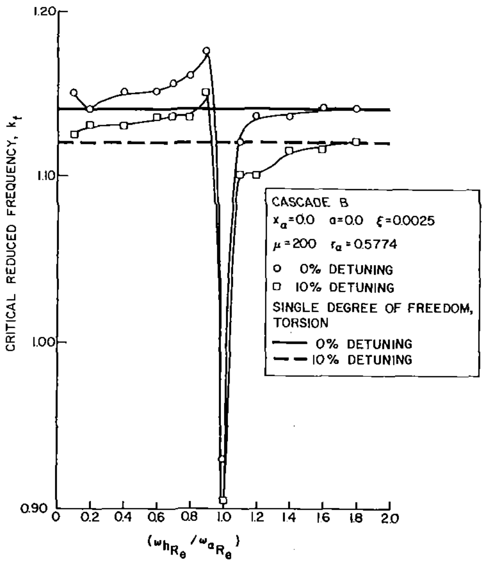

Fig. 11 The effect of aerodynamic detuning on the critical reduced frequency with a midchord elastic axis and center of gravity

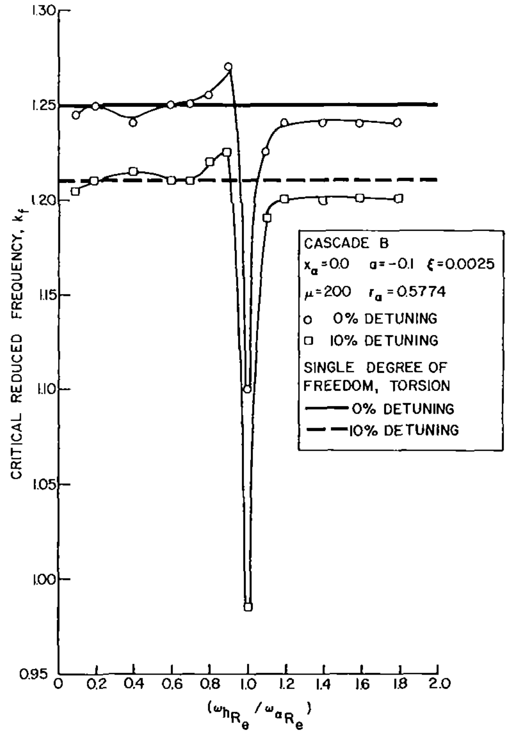

Fig. 12 The effect of aerodynamic detuning on the critical reduced frequency with the elastic axis and center of gravity located at 40 percent of the chord

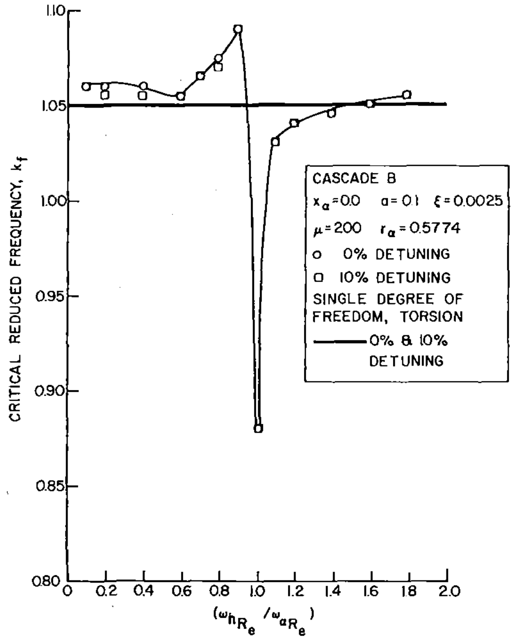

Fig. 13 The effect of aerodynamic detuning on the critical reduced frequency with the elastic axis and center of gravity located at 60 percent of the chord

torsion mode counterparts for values of the bending-torsion natural frequency ratio lower than 0.6 and greater than 1.2. This indicates that the bending mode is not coupling with the torsion mode at the higher natural frequency ratios for these cascade configurations. However for values of this ratio greater than 0.6 and less than 1.2, coupling effects are significant. It is interesting to note that the difference between the tuned and detuned results for the coupled bending-torsion model is approximately the same as found for the single degree of freedom results. Thus, the effect of aerodynamic detuning appears to be independent of the bending-torsion frequency ratio.

For coupled bending-torsion stability, the locations of the elastic axis and the center of gravity are significant. Figures 12 and 13 show the effect of moving the elastic axis and the center of gravity forward and aft of midchord, respectively, on the stability of both the baseline and 10 percent circumferential aerodynamically detuned rotors.

With the elastic axis and the center of gravity located at 40 percent of the chord ($a=-0.1$), Fig. 12 shows the stability enhancement due to aerodynamic detuning, with the alternate circumferentially spaced rotor more stable than the uniformly spaced baseline rotor. Also, for values of the bending-torsion natural frequency ratio lower than 0.6 and higher than 1.2, the stability of both the baseline and the detuned rotors are predicted by the single degree of freedom torsion mode results. Again, this indicates that the bending mode is not coupling with the torsion mode at the higher natural frequency ratios. However, coupling between the bending and the torsion modes for both the baseline and the detuned rotors is seen to be significant for values of the natural frequency ratio between 0.6 and 1.2.

With the elastic axis and the center of gravity shifted aft to 60 percent of the chord ($a=0.1$), Fig. 13 shows that circumferential aerodynamic detuning has minimal effect on the critical reduced frequency value. Also, a single degree of freedom torsion mode stability analysis is again seen to be appropriate for values of the bending-torsion natural frequency ratio lower than 0.6 and higher than 1.2. For values of this ratio between 0.6 and 1.2, a coupled stability analysis is required.

The effect of circumferential aerodynamic detuning on cascade stability when the center of gravity is located aft of the elastic axis ($x_\alpha=0.1$) is shown in Fig. 14. This figure indicates that for values of the frequency ratio greater than 1.0, the circumferential aerodynamic detuning has a very beneficial effect on cascade stability. However, for frequency ratios less than 1.0, the detuning has little effect on the critical reduced frequency. The flutter modes associated with each of the values of reduced frequency of Fig. 14 are listed in Table 1. For values of the bending-torsion frequency ratio less than 0.40 and greater than 1.60, the coupling between the bending and torsion modes is small and the flutter behavior of both the tuned and detuned cascades can be predicted reasonably well by the single degree of freedom torsion model. It should be noted that these conclusions are only valid for the case of a single degree of freedom model with the elastic axis and center of gravity coincident at midchord.

Table 1 Flutter modes for the cases where the elastic axis is at midchord and $x_\alpha = \pm 0.1$

$X_\alpha = 0.1$ $a = 0.0$ $\xi = 0.0025$
$\mu = 200$ $r_\alpha = 0.5774$

$\varepsilon = 0\%$			$\varepsilon = 10\%$		
ω_h/ω_α	k_F	MODE	ω_h/ω_α	k_α	MODE
0.1	1.100	Torsion	0.1	1.100	Torsion
0.2			0.2		
0.4	1.100	Torsion	0.4	1.085	Torsion
0.6	1.085	Torsion	0.6	1.080	Torsion
0.7	1.060	Torsion	0.7		
0.8	1.080	Bending	0.8	1.080	Bending
0.9	1.230	Bending	0.9	1.230	Bending
1.0	1.280	Torsion	1.0	1.255	Torsion
1.1	1.235	Torsion	1.1		
1.2	1.210	Torsion	1.2	1.175	Torsion
1.4	1.190	Torsion	1.4	1.145	Torsion
[illegible]	1.175	Torsion	1.6	1.150	Torsion
[illegible]	1.170	Torsion	1.8	1.135	Torsion

$X_\alpha = -0.1$ $a = 0.0$ $\xi = 0.0025$
$\mu = 200$ $r_\alpha = 0.5774$

$\varepsilon = 0\%$			$\varepsilon = 10\%$		
ω_h/ω_α	k_F	MODE	ω_h/ω_α	k_F	MODE
0.1	1.200	Torsion	0.1	1.175	Torsion
0.2			0.2		
0.4	1.210	Torsion	0.4	1.175	Torsion
0.6	1.225	Torsion	0.6	1.200	Torsion
0.7			0.7		
0.8	1.270	Torsion	0.8	1.230	Torsion
0.9	1.285	Torsion	0.9	1.230	Torsion
1.0	1.300	Torsion	1.0	1.285	Torsion
1.1	1.260	Torsion	1.1	1.245	Torsion
1.2	1.200	Bending	1.2	1.195	Bending
1.4	1.120	Bending	1.4	1.112	Bending
1.6	1.100	Torsion	1.6	1.090	Torsion
1.8	1.110	Torsion	1.8	1.10	Torsion

When the center of gravity is located forward of the elastic axis ($x_\alpha = -0.1$), the behavior of the critical reduced frequency as a function of the bending-torsion frequency ratio is presented in Fig. 15. In this case, the circumferential aerodynamic detuning has a beneficial effect on cascade stability for values of the frequency ratio lower than 1.0, but very little effect when the frequency ratio is above 1.0. Table 1 gives the flutter modes associated with the values of the reduced frequency shown in Fig. 15. With this value of x_α, the coupling between the bending and torsion modes is such that even for low values of the bending-torsion frequency ratio, a single degree of freedom torsion model with the center of gravity and elastic axis coincident at midchord should not be utilized to predict the flutter behavior.

Summary and Conclusions

A model to demonstrate the enhanced coupled bending-torsion unstalled supersonic flutter due to alternate circumferential blade spacing aerodynamic detuning has been developed. This is a finite cascade model, with periodicity achieved by stacking two airfoils at a time. Also, the translational and torsional unsteady aerodynamic lift and moment coefficients were developed in terms of aerodynamic influence coefficients in a manner that enables both a conventional uniform circumferentially spaced rotor as well as an alternate circumferentially spaced aerodynamically detuned rotor to be analyzed. The coupled bending-torsion stability analysis was then developed by considering the coupled equations of motion together with the unsteady aerodynamic loading.

The effect of alternate circumferential spacing aerodynamic detuning on coupled bending-torsion unstalled supersonic flutter as well as the verification of the modeling and formulation were demonstrated by applying this analysis to an unstable twelve-bladed rotor, with Verdon's Cascade B flow geometry as a baseline uniformly spaced geometry.

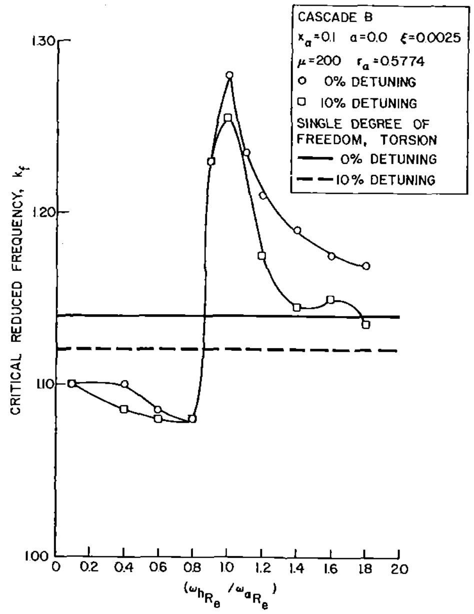

Fig. 14 The effect of aerodynamic detuning on the critical reduced frequency with the elastic axis at midchord and $x_\alpha = 0.1$

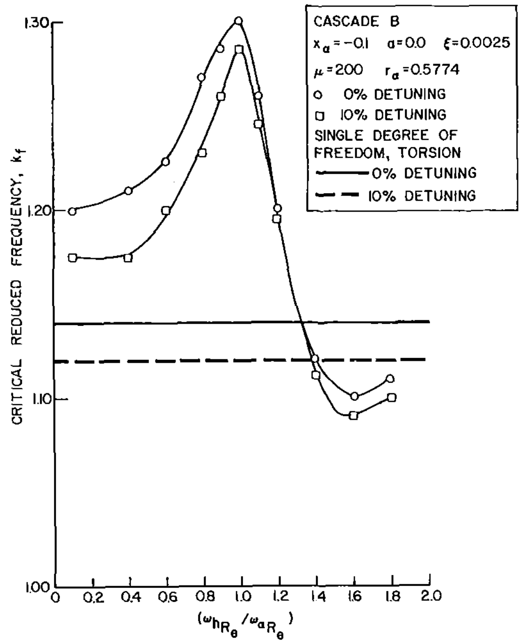

Fig. 15 The effect of aerodynamic detuning on the critical reduced frequency with the elastic axis at midchord and $x_\alpha = -0.1$

With the elastic axis and the center of gravity at or forward of midchord, it was shown that 10 percent alternate circumferential spacing aerodynamic detuning results in a lower critical reduced frequency value than does the baseline tuned rotor over the complete range of bending-torsion natural frequency ratios, thereby demonstrating the stability enhancement due to aerodynamic detuning. However, with the elastic axis and the center of gravity at the 60 percent chord location, the circumferential aerodynamic detuning had a minimal effect on the critical reduced frequency. Also, it was shown that for both the uniform and nonuniform circumferentially spaced rotors, a single degree of freedom flutter torsion mode analysis was appropriate for values of the bending-torsion natural frequency ratio lower than 0.6 and higher than 1.2, indicating that the bending mode does not couple with the torsion mode at the higher values of the bending-torsion natural frequency ratio. However, for values of this natural frequency ratio between 0.6 and 1.2, a coupled flutter stability analysis is required.

When the elastic axis and center of gravity are not coincident, the effect of circumferential aerodynamic detuning on cascade stability was found to be highly dependent on the position of the center of gravity with respect to the elastic axis. When the center of gravity is forward of an elastic axis located at midchord, the introduction of aerodynamic detuning had a beneficial effect for bending-torsion frequency ratios below 1.0. However, detuning had very little effect when the frequency ratio was above 1.0. Moving the center of gravity aft of a midchord elastic axis had the opposite effect. In this case aerodynamic detuning was shown to have beneficial effect when the frequency ratio was greater than 1.0, and very little effect for frequency ratios lower than 1.0. In addition, when the center of gravity was forward of the elastic axis, the coupling between the bending and torsion modes was such that a single degree of freedom torsion analysis with the center of gravity and elastic axis coincident at midchord did not yield an accurate stability prediction. This condition was found to be true even for low values of the bending-torsion frequency ratio.

Acknowledgments

The NASA Lewis Research Center and, in particular, Cal Ball, Don Boldman, and Larry Bober, are most gratefully acknowledged for their encouragement, discussions, and support.

References

1 Whitehead, D. S., "Torsional Flutter of Unstalled Cascade Blades at Zero Deflection," *Aeronautical Research Council R&M 3429*, 1965.

2 Kaza, K. R. V., and Kielb, R. E., "Flutter and Response of a Mistuned Cascade in Incompressible Flow," *AIAA Journal*, Vol. 20, No. 8, Aug. 1982, pp. 1120–1127.

3 Kielb, R. E., and Kaza, K. R. V., "Aeroelastic Characteristics of Mistuned Blades in Subsonic and Supersonic Flows," ASME *Journal of Vibration, Stress, and Reliability in Design*, Vol. 105, Oct. 1983, pp. 425–433.

4 Bendiksen, O. O., "Flutter of Mistuned Turbomachinery Rotors," ASME JOURNAL OF ENGINEERING FOR GAS TURBINES AND POWER, Vol. 106, 1984, pp. 25–33.

5 Crawley, E. F., and Hall, K. C., "Optimization and Mechanisms of Mistuning in Cascades," ASME JOURNAL OF ENGINEERING FOR GAS TURBINES AND POWER, Vol. 107, 1985, pp. 418–426.

6 Bendiksen, O. O., and Friedmann, P. P., "The Effect of Bending-Torsion Coupling on Fan and Compressor Blade Flutter," ASME JOURNAL OF ENGINEERING FOR POWER, Vol. 104, 1982, pp. 617–623.

7 Hoyniak, D., and Fleeter, S., "Aerodynamic Detuning of an Unstalled Supersonic Turbofan Cascade," ASME JOURNAL OF ENGINEERING FOR GAS TURBINES AND POWER, Vol. 108, 1986, pp. 60–67.

8 Verdon, J. M., and McCune, J. E., "Unsteady Supersonic Cascade in Subsonic Axial Flow," *AIAA Journal*, Vol. 13, No. 2, Feb. 1975, pp. 193–201.

9 Verdon, J. M., "The Unsteady Aerodynamics of a Finite Supersonic Cascade With Subsonic Axial Flow," ASME *Journal of Applied Mechanics*, Vol. 40, No. 3, Sept. 1973.

10 Brix, C. W., and Platzer, M. F., "Theoretical Investigation of Supersonic Flow Past Oscillating Cascades With Subsonic Leading Edge Locus," AIAA Paper No. 74-15, Jan. 1974.

11 Caruthers, J. E., and Riffel, R. E., "Aerodynamic Analysis of a Supersonic Cascade Vibrating in a Complex Mode," *Journal of Sound and Vibration*, Vol. 71, 1980.

12 Adamczyk, J. J., and Goldstein, M. E., "Unsteady Flow in a Supersonic Cascade With Subsonic Leading Edge Locus," *AIAA Journal*, Vol. 16, No. 12, Dec. 1978, pp. 1248–1254.

N. C. Baines
Dept. of Mechanical Engineering,
Imperial College,
London, United Kingdom

M. L. G. Oldfield
Dept. of Engineering Science,
Oxford University,
Oxford, United Kingdom

J. P. Simons

J. M. Wright

Rolls-Royce Ltd.,
Filton, Bristol, United Kindgom

The Aerodynamic Development of a Highly Loaded Nozzle Guide Vane

A series of high-pressure turbine nozzle guide vanes has been designed for progressively increasing blade loading and reduction in blade solidity without additional loss penalty. Early members of the series achieved this by changes to the suction surface contour, but for the latest design the pressure surface contour was extensively modified to reduce the velocities on this surface substantially. Cascade testing revealed that this vane had a higher loss than its predecessor, and this appears to be largely due to a long region of boundary layer growth on the suction surface and possibly also an unsteady separation. These tests demonstrated the value of a flattened pitot tube held against the blade surface in determining the boundary layer state. By using a pitot probe of only modest frequency response (of order 100 Hz) it was possible to observe significant qualitative differences in the raw signals from laminar, transitional and turbulent boundary layers, which have previously been observed only with much higher frequency instruments. The test results include a comparison of boundary layer measurements on the same cascade test section in two different high-speed wind tunnels. This comparison suggests that freestream turbulence can have a large effect on boundary layer development and growth.

Introduction

The quest for increasing work output per stage and aerodynamic efficiency remains central to the development of turbine stages in gas turbine engines, and over the years great advances have been made by improved design methods together with rigorous prototype testing and evaluation. In this process cascade testing has an important role to play in validating flowfield and boundary layer prediction methods, and in the early stages of assessing a blade design prior to more extensive and more expensive rotating rig and engine testing. A variety of flow prediction techniques are now available to the designer, which in many cases are capable of calculating a two-dimensional flow such as in a plane cascade with very satisfactory accuracy. However, there remain phenomena, such as boundary layer transition, flow separation, and shock-boundary layer interactions, which are much more difficult to predict, and which may have a large influence on the blade performance. In these circumstances cascade testing is an important tool in understanding the fluid dynamic processes occurring, particularly in transonic flows.

The investigation presented here concerns a Rolls-Royce Ltd. program, the objective of which is progressively to increase the pitch/chord ratio of a high-pressure nozzle guide vane stage in order to reduce the engine weight and cost without sacrificing efficiency. This program now extends to four vanes. The first of these, designated T2, was just supercritical, but subsequent designs (T4, T8, and T12) have substantial regions of supersonic flow on the suction surface and exhibit many of the phenomena mentioned above. All of these vanes have been designed at Rolls-Royce Bristol, and T2, T4, and T8 were tested in the high-speed cascade tunnel at DFVLR Braunschweig [1]. The results of these tests were discussed in [2], and this paper reviews the performance of these designs as an introduction to the latest member of the series, T12.

Following the closure of the Braunschweig tunnel, the T8 cascade was retested in the Oxford University Blowdown Tunnel [3] to give a new baseline against which to judge T12. This was done to avoid any problems of tunnel-to-tunnel variations in the data which recent research has shown can exist [4, 5]. A plane cascade of T12 vanes was then tested, with measurement of blade surface pressure distributions, profile loss by means of wake traverses, and Schlieren photography. The previous investigations [2] had demonstrated the value of boundary layer measurements with a flattened pitot probe held against the blade surface as a means of detecting transition, and this was done on the suction surfaces of both T8 and T12.

Nozzle Guide Vane Profile Development

The design parameters for the sequence of nozzle guide vanes are:

inlet angle, $\alpha_1 = 0$ deg
exit angle, $\alpha_2 = 65.2$ deg
exit Mach number (isentropic), $M_{2,is} = 0.955$
exit Reynolds number (based on true chord, isentropic exit conditions), $Re_2 = 5 \times 10^5$

The choice of a constant Reynolds number is arguable. The

Contributed by the Gas Turbine Division of THE AMERICAN SOCIETY OF MECHANICAL ENGINEERS and presented at the 31st International Gas Turbine Conference and Exhibit, Düsseldorf, Federal Republic of Germany, June 8–12, 1986. Manuscript received at ASME Headquarters February 14, 1986. Paper No. 86-GT-229.

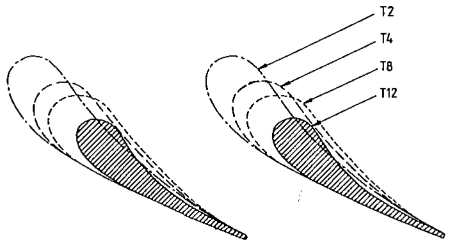

Fig. 1 Comparison of blade profiles, scaled to the same pitch

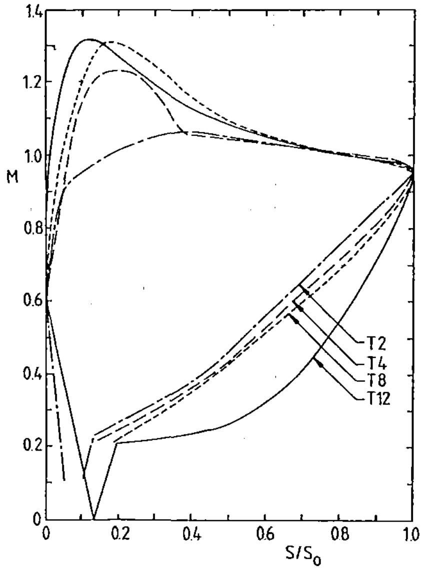

Fig. 2 Mach number distributions used for PVD design method

progressively increasing pitch/chord ratio of this series of vanes implies for a given engine installation different chord lengths, and therefore different design Reynolds numbers, unless the engine is rematched. From the point of view of cascade testing, however, the results from different vanes are more easily compared if the operating points are identical.

As designed, all vanes are suitable for cooling, with a common trailing edge geometry (*te/o*) = 0.05 suitable for ejection at that point, although all of the cascade tests have been performed on solid profiles with no attempt to simulate cooling air flows. The four profiles, scaled to the same pitch, are shown in Fig. 1. The profile coordinates of the first three vanes are given in [2], and those of T12 are listed as an appendix to this paper.

The datum profile, T2, was designed in 1969 using a prescribed velocity distribution (PVD) method based on that of Stanitz [6]. The peak suction surface Mach number was just slightly greater than unity. Subsequently an attempt was made to design a new profile, T4, with higher velocities on the suction surface in order to increase the blade lift and the pitch/chord ratio. The PVD method is inviscid and not fully compressible, and is not reliable on the suction surface downstream of the throat, particularly in the case of a supercritical profile where a supersonic flow diffuses to a subsonic flow, usually with the accompaniment of shock waves. This process requires very careful control if excessive losses are to be avoided. There was insufficient confidence that this could be achieved using the PVD method, and consequently it was decided to confine velocity increases to a region upstream of the throat, in the belief that design optimization should proceed within the limitations of the available design tools. The Mach number distributions prescribed for T2 and T4 are shown in Fig. 2, and it can be seen that a rapid diffusion was necessary to achieve this. The cascade results [2] showed no strong shock in this region but a controlled diffusion. At the design point the loss coefficients of T2 and T4 were almost identical, suggesting that the shorter chord of T4 reduced the suction surface boundary layer thickness and counteracted the effects of increased diffusion.

Following the tests on T4, a time-marching program developed from Denton [7] became available, and it was then possible to predict the flow through a given cascade geometry with much greater confidence, with a fully compressible analysis and the ability to handle shock waves. Accordingly, a new profile, T8, was designed by iteration between PVD and time-marching analysis. The prescribed velocity distribution which was used to start the iteration is shown for comparison in Fig. 2. Velocity levels were raised mainly around the throat region, while the diffusion rate was no greater than that of T4. The pitch/chord ratio of T8 was now 25 percent greater than that of T2. Tests showed [2] that the actual diffusion rate was in fact lower than that predicted, and was accompanied by an extended region of transition. The boundary layer on T8 was laminar over a much greater portion of the suction surface than on T4, and this contributed to a lower loss coefficient.

In designing T12, it was thought that there was not much scope for further developing the suction surface because this would involve higher rates of diffusion, which would be liable to suffer from separation in a shock-boundary layer interaction, with consequent reduction in efficiency. The aim was therefore to produce a profile having a similar suction surface distribution to T8, the increase in lift coming from reduced velocities on the pressure surface (Fig. 2). It can be observed in Fig. 1 that the pitch/chord ratio of T12 was now sufficiently large that the vanes no longer overlap in the axial direction. The design of T12 was done using a later standard of time-marching program incorporating some of the improvements described in [8], and Fig. 2 shows the results from this program.

An indicator which is often used to compare the aerodynamic duty of a cascade is the Zweifel coefficient

$$\psi_z = \frac{h}{cax}\,\rho\,\frac{\Delta V_w V_a}{P_{01}-P_2}$$

The disadvantage of using this as a comparator is that the exit conditions will be affected by the total pressure loss assumed to occur within the cascade. In the absence of a uniform standard of loss prediction methods, it is safer to assume an

Nomenclature

a_0 = speed of sound, m/s
c = true chord, m
cax = axial chord, m
$F(M)$ = multiplying factor
f_n = resonant frequency, Hz
h = pitch, m
L = length, m
M = Mach number
P = pressure, Pa
q = dynamic pressure, Pa
Re = Reynolds number
S = surface length, m
V = velocity, m/s
α = angle, deg
β_s = stagger angle, deg
γ = specific heat ratio
Δ = finite difference
ρ = density, kg/m^3
ψ_z = Zweifel coefficient

Subscripts

a = axial
is = isentropic
p = probe
w = whirl
0 = stagnation, freestream
1 = inlet
2 = exit

Table 1 Comparison of blade profile data

Profile	h/cax	h/c	$\psi_{z,is}$	β_s
T2	0.956	0.670	0.583	45.8
T4	1.190	0.775	0.725	45.8
T8	1.373	0.842	0.837	44.85
T12	1.625	0.946	0.991	49.95

isentropic flow when making comparisons between different blade profiles. It can be shown that the "lossless" Zweifel coefficient is then equal to the incompressible lift coefficient multiplied by a factor $F(M)$ for the special case of $\alpha_1 = 0$

$$\psi_{z,is} = \frac{h}{cax} \cos^2 \alpha_2 \tan \alpha_2 F(M)$$

where

$$F(M) = \frac{\gamma M_{2,is}^2}{\left[1 + \frac{\gamma - 1}{2} M_{2,is}^2\right]^{\gamma/(\gamma-1)} - 1}$$

The vanes are compared and $\psi_{z,is}$ for each is listed in Table 1. On this assessment T12 may be seen to be 18 percent more highly loaded than T8, which is itself 44 percent more highly loaded than the datum profile T2.

Cascade Test Details

The Oxford University Blowdown Tunnel [3] is a short-duration tunnel which features an exhaust which can be pumped down to 0.15 bar by means of two stages of air-driven ejectors, thus allowing an independent and continuous variation of exit Mach and Reynolds numbers over wide ranges. The run time is typically 5 s, and high-frequency response instrumentation and transient testing techniques described in [9] are employed for data acquisition. Upstream of the cascade a bar grid is fitted in order to produce a freestream turbulence intensity of 4 percent.

A large test section may be fitted, and in order to keep as many components as possible common to T8 and T12, the span and pitch of T8 and T12 were kept constant at 300 mm and 67.2 mm, respectively. The aspect ratio (span/chord) therefore varied from 3.75 for T8 to 4.24 for T12. Both cascades contained seven blades, and in each case two of the central blades were instrumented with a total of approximately 50 static pressure tappings. For measurements of loss, the wakes of the central blades were traversed with a trident probe described in [10] in order to measure local values of total and static pressure and flow angle. These local quantities are averaged using the conservation laws applied to a control volume in the analysis by Amecke [11]. Windows were fitted to T12 to allow Schlieren photography, but unfortunately this was not possible for T8.

Cascade Performance

Comparison of T8 and T12. The measured blade surface Mach number distributions of T8 and T12 at the design point are shown in Fig. 3, and from this it would appear that the aims of a similar suction surface velocity distribution and significantly reduced velocities on the pressure surface have been largely achieved. The peak suction surface Mach numbers are practically identical, and the fact that the peak appears to occur earlier on T12 is a consequence of the leading edge geometry and the coordinate system. The subsequent diffusion is, if anything, slightly more uniform on T12 than on T8. The Schlieren photograph of T12 (Fig. 4) at this condition shows that the supersonic patch is free from strong shocks, and exhibits only a weak normal shock toward the trailing edge. A comparable photograph of T8 in [2] shows a similar result, but with several weak passage shocks spread over a slightly larger area of the blade. In both cases the shock waves are sufficiently weak (the local Mach number is only just above unity) that the blade surface pressure distributions are little influenced.

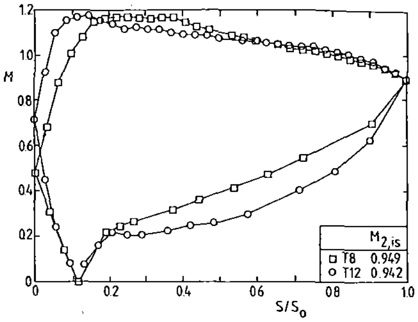

Fig. 3 Measured blade surface Mach number distributions for T8 and T12 at $M_2 = 0.955$ and $Re_2 = 5 \times 10^5$

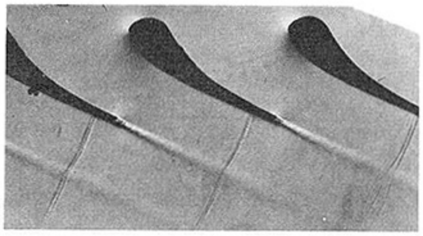

Fig. 4 Schlieren photograph of T12 at $M_2 = 0.955$ and $Re_2 = 5 \times 10^5$

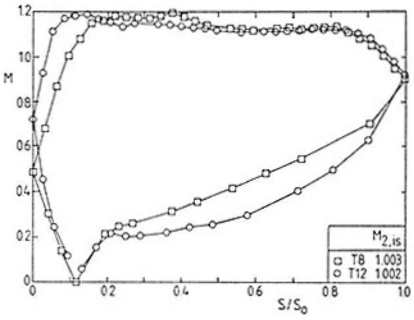

Fig. 5 Measured blade surface Mach number distributions for T8 and T12 at $M_2 = 0.955$ and $Re_2 = 5 \times 10^5$

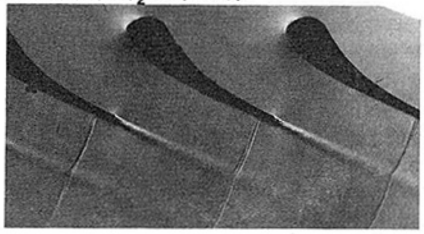

Fig. 6 Schlieren photograph of T12 at $M_2 = 1.0$ and $Re_2 = 5 \times 10^5$

At a slightly higher exit Mach number (Fig. 5) the suction surface region of T12 after the peak becomes one of slight diffusion which ceases at about the geometric throat at $S/S_0 = 0.25$ and is followed by a long region of almost constant pressure before a rapid diffusion near the trailing edge. This last process is accompanied by a series of weak shock waves and a very rapid thickening of the suction surface boundary layer is visible in the Schlieren photograph (Fig. 6). At sub-

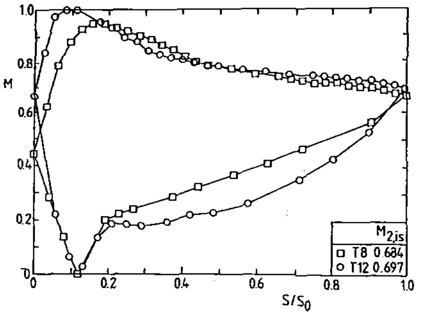

Fig. 7 Measured blade surface Mach number distributions for T8 and T12 at $M_2 = 0.7$ and $Re_2 = 5 \times 10^5$

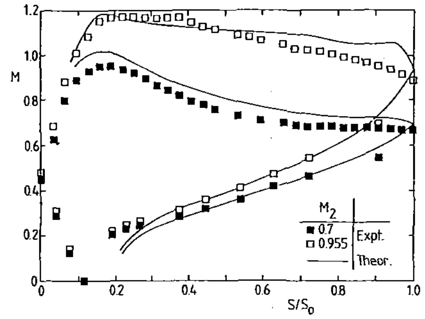

Fig. 8(a) Profile T8: comparison of measured and predicted blade surface Mach number distributions

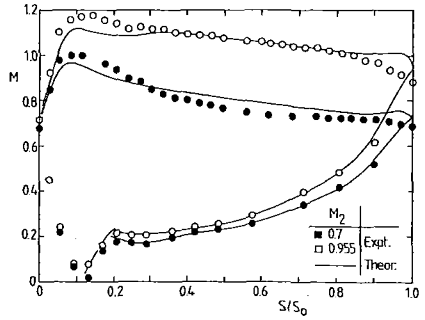

Fig. 8(b) Profile T12: comparison of measured and predicted blade surface Mach number distributions

critical Mach numbers such as shown in Fig. 7, T12 appears to diffuse initially rather more rapidly than T8, and although Schlieren photographs at this condition do not show any unusual features, it might be expected that there is a substantial thickening of the boundary layer due to this.

The most striking differences between the measured and prescribed velocity distributions at the design condition (Figs. 2 and 3) are that the actual suction surface peak velocity is lower and the diffusion rate is consequently also lower on both blades. This effect had previously been noted in the tests on T8 at Braunschweig. The time-marching program predictions are, as might be expected, rather better than this, and serve to emphasize the restricted application of the PVD method in designing supercritical aerofoils (Fig. 8). Even with the time-marching method, however, significant discrepancies remain. The prediction for T8 at $M_2 = 0.955$ does not show such a flattened peak and has a less rapid diffusion except very close to the trailing edge. The latter effect is also apparent at $M_2 = 0.7$, which suggests that the model may be in difficulty at the trailing edge. The comparison also provides circumstantial evidence of a separation bubble on the suction surface peak, although this cannot be observed in the Schlieren photographs. The prediction for T12 suffers from the same trailing edge problem, shows a lower peak suction surface Mach number, and at the design point shows some reacceleration after the peak and an initial diffusion. The measured distribution also shows some evidence of reacceleration, although to a much lower degree.

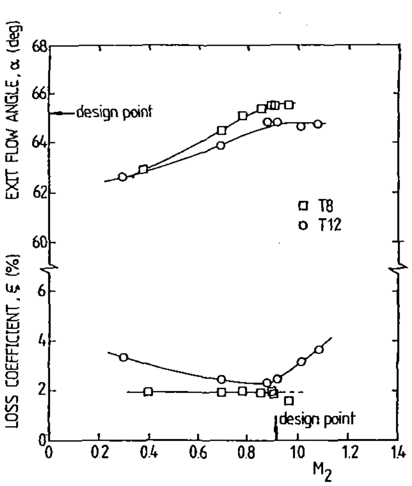

Fig. 9 Loss coefficient and exit flow angle as functions of Mach number

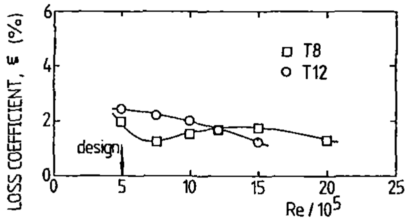

Fig. 10 Loss coefficient as a function of Reynolds number

The loss coefficient characteristics (Fig. 9) show that whereas the loss of T8 remains practically constant with Mach number up to the design condition (and even appears to fall thereafter, although with only one data point this may be misleading), that of T12 is consistently higher and has a distinct minimum near the design Mach number. The increasing loss at lower Mach numbers is consistent with a boundary layer growth caused by the less well-controlled diffusion seen in Fig. 7. It is interesting that this is consistent with the measured velocity distributions, but the predictions (Fig. 8) do not show the same trend.

At Mach numbers higher than design the thickening of the boundary layer after a shock wave near the trailing edge is likely to be responsible. At still higher Mach numbers it has also been observed that at trailing edge shock wave from the adjacent blade impinges on the suction surface and causes a local separation, further increasing the loss coefficient. The exit angle characteristic, also shown in Fig. 9, shows some underturning at low Mach numbers, but practically the design exit flow angle for both blades at the design Mach number.

The variation of loss coefficient with Reynolds number reveals quite different behavior for each blade (Fig. 10). That of T8 has a minimum at about 7×10^5 and an increase at lower Reynolds numbers, and behavior of this type can usually be explained in terms of increasing regions of laminar boundary layer flow at decreasing Reynolds numbers, but that of T12 shows only a steady increase with decreasing Reynolds number.

In order to gain some further understanding, investigations into the suction surface boundary layer transition behavior were undertaken. In making the connections between boundary layer state, loss coefficient, and surface pressure distributions, useful evidence was also available from the comparison

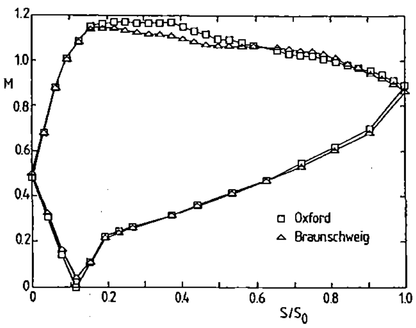

Fig. 11(*a*) Comparison of T8 blade surface Mach number distributions at M_2 = 0.955

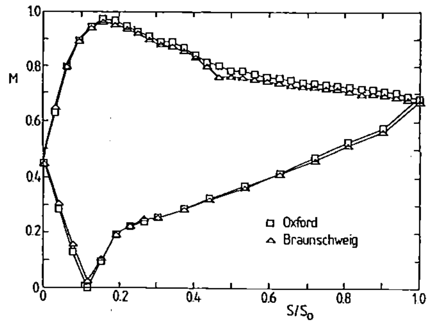

Fig. 11(*b*) Comparison of T8 blade surface Mach number distributions at M_2 = 0.7

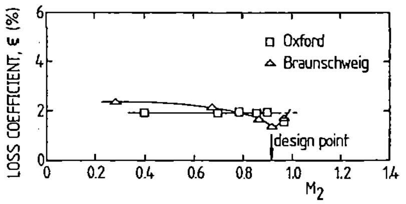

Fig. 12 Comparison of T8 loss coefficients

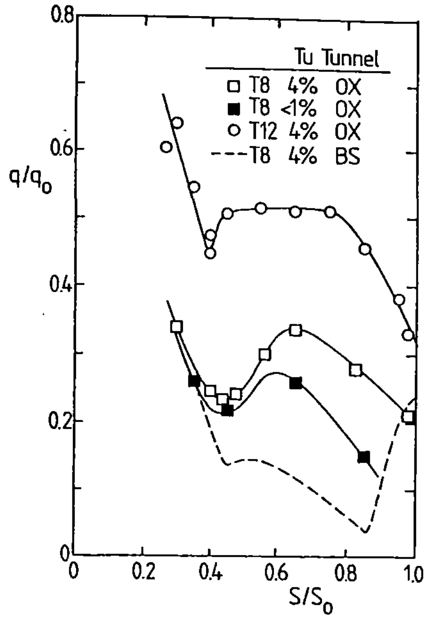

Fig. 13 Suction surface boundary layers at M_2 = 0.955 and Re_2 = 5 × 10^5

of results on the T8 vane measured at Braunschweig and Oxford, so that these are first summarized.

Comparison of T8 at Braunschweig and Oxford. The problems of making this type of tunnel-to-tunnel comparison have been discussed by two of the present authors elsewhere [4, 5], and one of the conclusions of that work was that there is often a problem in measuring comparable downstream conditions (especially static pressure in transonic flow) in order to define the run conditions. In this respect there is some small uncertainty associated with the comparisons presented in Figs. 11 and 12.

At the design point Mach number the most significant effect on the blade surface Mach number distribution is that, relative to tests at Braunschweig, diffusion on the suction surface at Oxford is delayed and is more rapid (Fig. 11(*a*)). In this respect, the Braunschweig results are closer to the time-marching prediction shown in Fig. 8(*a*). The more rapid diffusion, particularly if it is preceded by a separation bubble, will contribute to the greater loss at the design point which was measured at Oxford (Fig. 12). In Fig. 11(*b*) at the lower exit Mach number of 0.7, there is no evidence at Oxford of the laminar separation bubble at a surface distance of about 0.4 which was observed at Braunschweig, and in fact Fig. 12 shows that at Mach numbers much below design a lower loss was measured at Oxford.

Boundary Layer Transition Detection

Technique. The use of a flattened pitot probe in contact with the blade surface as a detector of transition is well known. Provided that the tip of the probe is sufficiently small to be well immersed in the boundary layer, transition is detectable as an increase in velocity. In practice the pitot probe measures total pressure, it is assumed that the static pressure is constant normal to the surface (and interpolated from the measured surface pressure distribution), and the ratio of local to freestream dynamic pressures is calculated and plotted as a function of blade surface coordinates S

$$\left[\frac{q}{q_0}\right]_S = \frac{P_{0p} - P(S)}{P_{01} - P(S)}$$

The height of the pitot probe at its tip normal to the blade surface was 0.3 mm external and 0.2 mm internal, so that total pressure measurements ideally refer to a height of 0.15 mm above the blade surface (although the total pressure gradient through the boundary layer means that the true figure is probably slightly greater than this). This compares with a boundary layer 99 percent thickness calculated to be about 0.4 mm in the likely regions of transition. The pitot probe is immersed sufficiently in the boundary layer to detect a velocity change caused by transition.

The short running time of the Oxford University Blowdown Tunnel makes high-frequency response instrumentation essential, and for the boundary layer probe this means a close-coupled pressure transducer. The requirement of a small probe tip makes it impossible to locate a transducer at that point, and in practice there was approximately 200 mm of pneumatic tube between the probe tip and the transducer diaphragm. As long as the diaphragm stiffness is much greater than that of the air in the tube, the resonant frequency of the assembly is

$$f_n = \frac{a_0}{4L}$$

where L is the tube length and a_0 the speed of sound, so that in this case f_n = 400 Hz. The digitization rate for data acquisition was set at one half of this, and the analogue signal was low-pass filtered at 100 Hz to prevent aliasing. The requirement of a rapid response also precluded the use of a probe significantly smaller than the one used here.

Comparison of Results. For T8 at the design condition the

Table 2 Prediction of boundary layer transition

Profile	M_2	Tu	Transition (S/S_0)		
			Start	90 percent	Finish
T8	0.955	4 percent	0.42	0.82	
T12	0.955	4 percent	0.40		0.94

boundary layer measurements indicate a region of transition beginning at about $S/S_0 = 0.4$, but whereas at Braunschweig this region extends almost to the trailing edge, at Oxford transition appears to be complete by about $S/S_0 = 0.65$ (Fig. 13). Although efforts were made to ensure that the pitot probes used in the two tunnels were the same size, there are probably small dimensional differences which result in the probes being immersed to different depths in the respective boundary layers, which accounts for the differences in absolute magnitudes of q/q_0 seen in Fig. 13. Reducing the level of freestream turbulence from 4 percent to below 1 percent appears to thicken the boundary layer slightly but does not appear to move the region of transition further downstream. This effect may be deceptive, because the pitot probe will not respond to the immediate onset of transition, but requires some degree of transition to have occurred before there is a measurable effect on the velocity profile of the boundary layer. A calculation of the transition region, based on an integral boundary layer analysis with a momentum thickness Reynolds number correlation of the onset of transition, predicts very well the start of transition, and also a lengthy transition region which is in better agreement with the Braunschweig than the Oxford results (Table 2). This method is capable of indicating separation by means of a locally zero or negative value of skin-friction coefficient, but this was not predicted.

It is instructive here to compare the actual time-varying signals recorded on T8 and shown in Fig. 14(*a*) and (*b*). Despite the relatively low frequency of data capture, the natures of the signals recorded at surface distances below 0.4, between 0.4 and 0.6, and above 0.6, are quite distinctly different, and support the hypothesis that these are laminar, transitional, and turbulent regions of the boundary layer. (The recordings closest to the trailing edge are affected by the normal shock in this region of the blade.) These signals are qualitatively in agreement with signals recorded under similar circumstances using hot wire or hot film probes [2, 12, 13] with a frequency response at least an order of magnitude greater. In the transition region the signals are considerably more disturbed than in either the laminar or turbulent regions. The difference between laminar and turbulent regions is magnified by the reduction in freestream turbulence intensity (Fig. 14(*b*)) which suggests that a major component of the low-frequency unsteadiness in the laminar boundary layer is actually convected in from the freestream turbulence.

In the two tunnels the start of transition is observed at almost identical points on the blade, so that the development of the laminar boundary layer up to this point is likely to be very similar. The earlier completion at Oxford allows the turbulent boundary layer more space in which to grow and thicken, and this is also consistent with the higher design point loss coefficient measured there (Fig. 8).

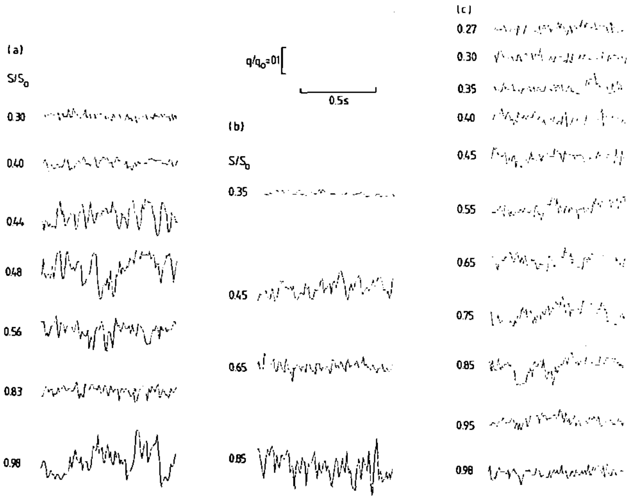

Fig. 14 Time-varying pressure fluctuations measured by flattened pitot in the suction surface boundary layer: (*a*) T8, Tu = 4 percent; (*b*) T8, Tu < 1 percent; (*c*) T12, Tu = 4 percent

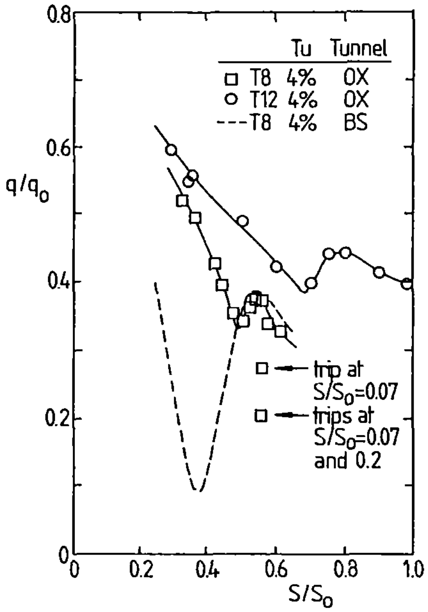

Fig. 15 Suction surface boundary layers at $M_2 = 0.7$ and $Re = 5 \times 10^5$

For T12 the evidence is not as conclusive. Figure 13 shows a small rise in q/q_0 at $S/S_0 = 0.4$ followed by a long flat region, which could indicate either a rapid transition to turbulence or a very long region of transition. The time-varying signals in Fig. 14(*c*) show a steadily increasing level of unsteadiness up to a surface distance of about 0.85, which tends to support the latter hypothesis. Hodson [13] suggests that a region of constant q/q_0 can indicate an unsteady separation, and if this is so it could explain the higher loss of T12. As with T8, the theoretical predictions listed in Table 2 indicate the correct onset of transition followed by a long region before transition is complete. Again no separation is indicated.

Suction surface boundary layer measurements at a lower Mach number of 0.7 are shown in Fig. 15. The results for T8 measured in Braunschweig clearly show the effect of the laminar separation bubble forcing an early transition. The Oxford results indicate that transition does not begin until $S/S_0 = 0.48$ on T8 and 0.65 on T12. Since these results were not as clear as those at the design point (Fig. 13), two tests on T8 were conducted with the boundary layer tripped by means of 0.05 mm diameter wires. Figure 14 shows the thicker boundary layers produced by these early transitions. The explanation for the larger loss of T12 than T8 at this condition appears to be that the thickening of the boundary layer due to more rapid diffusion on T12 after transition more than offsets the effect of a longer region of laminar suction surface boundary layer.

Comparison of Boundary Layer Measurements on T8 at Oxford and Braunschweig. The high-speed cascade tunnels at Oxford and Braunschweig have been extensively compared in [4, 5], but without boundary layer measurements, and Figs. 13 and 15 are of interest from this point alone. Despite using the identical cascade test section and taking care in setting up to duplicate as far as possible the test conditions, the boundary layer development in the two tunnels was quite different. At the design point there is good agreement on the start of transition, but at Oxford transition finishes much earlier than at Braunschweig. One flow parameter which has an important influence on transition, and which may not have been duplicated sufficiently well, is the freestream turbulence. In both tunnels this is generated by a grid upstream of the cascade, but whereas at Oxford this is a bar grid in a constant-area inlet duct, at Braunschweig it was a cross grid upstream of a contraction before the test section. This contraction accelerates the flow and stretches the turbulent eddy length scales. Furthermore, data from heated thin films on T8 in Braunschweig revealed a large component of low-frequency (below 1 kHz) flow disturbance which may have been due to blade vibration. No turbulence spectral data are available from Oxford, so it is not known whether similar disturbances exist in this tunnel. Although this evidence is short of conclusive, it does indicate that the influence that freestream turbulence has on boundary layer transition under these conditions would repay further study.

Conclusions

The primary design objective of this sequence of nozzle guide vanes has been to increase the blade loading and reduce the blade solidity without incurring additional loss. The first three vanes achieved this by progressive modification to the suction surface contour. The most recent vane, T12, achieved the increased loading by modifications to the pressure surface contour to reduce the velocities there, but in doing so suffered from additional loss. The suction surface boundary layer of T12 shows many interesting features including a long region of diffusion growth and also a long region of transition which may also involve an unsteady separation.

These results suggest that the design tools available at the time for this vane were not adequate for truly reliable predictions on a profile as extreme as this, involving a high pitch/chord ratio and a very long region of the suction surface downstream of the throat, and in this case two-dimensional cascade tests played an important role in the design process. It would be interesting to perform boundary layer calculations for the predicted velocity distributions and compare them with results using the measured velocity distributions. This would clarify the usefulness and limits of the prediction methods used in the design process.

This work has confirmed previous testing [2, 12, 13] which demonstrated the value of a flattened pitot probe in determining the state of the suction surface boundary layer. Whereas earlier tests used what were essentially steady-state instruments, the present work has shown that a probe with only a modest frequency response (of order 100 Hz) is capable of producing useful qualitative information to distinguish laminar, transitional, and turbulent regions. In other respects it is, however, limited. For example, it is not good at detecting separation, for which other techniques such as hot wires and hot films are much superior.

The comparison of T8 results between Oxford and Braunschweig adds to similar comparisons of the well-known VKI-1 profile published elsewhere [4, 5], and now includes traverses of the suction surface boundary layer. In general there is good agreement about the point at which transition starts (within the limitations of sensitivity of the pitot probe), but the boundary layer develops quite differently in the two tunnels, and completes much earlier at Oxford than at Braunschweig. It is not possible to account completely for this behavior, although it is likely that the freestream turbulence has an important influence. The nature of this influence, and the mechanisms by which freestream turbulence affects the boundary layers of a high-turning blade in high-speed flow, and ultimately the performance of that blade, appear to be significant gaps in our understanding and worthy of further study.

Acknowledgments

The authors wish to thank Mr. A. T. Holmes of Rolls-Royce Ltd., and Mr. J. L. Allen and Mr. S. C. Harding of Oxford University Engineering Department, for their assistance in this work. The advice and encouragement of Rolls-Royce Ltd. and the Ministry of Defence (Procurement Executive) is gratefully acknowledged.

References

1 Hoheisel, H., and Kiock, R., "Zwanzig Jahre Hochgeschwindigkeits-Gitterwindkanal des Instituts fuer Aerodynamik der DFVLR in Braunschweig," *Zeitschrift fuer Flugwissenschaften und Weltraumforschung*, Vol. 1, 1977, pp. 17–29.

2 Oldfield, M. L. G., Kiock, R., Holmes, A., and Graham, C. G., "Boundary Layer Studies on Highly Loaded Cascades Using Heated Thin Films and a Traversing Probe," ASME JOURNAL OF ENGINEERING FOR POWER, Vol. 103, 1981, pp. 237–246.

3 Baines, N. C., Oldfield, M. L. G., Jones, T. V., Schultz, D. L., King, P. I., and Daniels, L. C., "A Short Duration Blowdown Tunnel for Aerodynamic Studies on Gas Turbine Blading," ASME Paper No. 82-GT-312, 1982.

4 Kiock, R., Lehthaus, F., Baines, N. C., and Sieverding, C. H., "The Transonic Flow Through a Plane Turbine Cascade as Measured in Four European Wind Tunnels," ASME JOURNAL OF ENGINEERING FOR GAS TURBINES AND POWER, Vol. 108, 1986, pp. 277–284.

5 Baines, N. C., et al., "A Comparison of Aerodynamic Measurements of the Transonic Flow Through a Plane Turbine Cascade in Four European Wind Tunnels," 8th Symposium on Measuring Techniques in Transonic and Supersonic Flow in Cascades and Turbomachines, Genoa, Italy, 1985.

6 Stanitz, J. D., "Design of Two-Dimensional Channels With Prescribed Velocity Distributions Along the Channel Walls," NACA Report 1115, 1953.

7 Denton, J., "A Time-Marching Method for Two and Three Dimensional Blade to Blade Flow," Aero. Res. Council Reports and Memoranda No. 3775, 1975.

8 Denton, J., "An Improved Time-Marching Method for Turbomachinery Flow Calculations," ASME JOURNAL OF ENGINEERING FOR POWER, Vol. 105, 1983, pp. 514–524.

9 Schultz, D. L., Jones, T. V., Oldfield, M. L. G., and Baines, N. C., "Transient Techniques for Turbomachinery Research," Progress in Aerospace Sciences, Pergamon Press, 1986 (in press).

10 Baines, N. C., "The Development of a Nozzle for Calibrating Pressure Probes for Measuring Transonic Flows," *Proceedings of the 7th Symposium on Measuring Techniques for Transonic and Supersonic Flow in Cascades and Turbomachines*, K.-D. Broichhausen and H. E. Gallus, eds., RWTH Aachen, West Germany, 1983.

11 Amecke, J., "Anwendung der transsonischen Aehnlichkeitsregel auf die Stroemung durch ebene Schaufelgitter," *VDI Forschungsheft*, 540, 1970, pp. 16–28.

12 Hodson, H. P., "Boundary Layer Transition and Separation Near the Leading Edge of a High-Speed Turbine Blade," ASME JOURNAL OF ENGINEERING FOR GAS TURBINES AND POWER, Vol. 107, 1985, pp. 127–134.

13 Hodson, H. P., "The Detection of Boundary Layer Transition and Separation in High-Speed Turbine Cascades," *Proceedings of the 7th Symposium on Measuring Techniques for Transonic and Supersonic Flow in Cascades and Turbomachines*, K.-D. Broichhausen and H. E. Gallus, eds., RWTH Aachen, West Germany, 1983.

APPENDIX

Profile coordinates of T12

x/cax	y/cax	x/cax	y/cax	x/cax	y/cax	x/cax	y/cax
0.159393	0.003104	0.000114	0.110576	0.995398	0.017399	0.845606	0.033916
0.150070	0.001221	0.002455	0.125237	0.996656	0.016478	0.815179	0.040217
0.140636	0.000008	0.008986	0.141491	0.997750	0.015366	0.784643	0.045981
0.131140	-0.000530	0.018890	0.155920	0.998651	0.014093	0.754008	0.051359
0.121630	-0.000388	0.038861	0.174775	0.999337	0.012692	0.723273	0.056348
0.112154	0.000431	0.068968	0.192538	0.999788	0.011199	0.692466	0.060846
0.102761	0.001924	0.097112	0.202911	0.999994	0.009654	0.662716	0.064651
0.093498	0.004084	0.126380	0.209615	0.999949	0.008095	0.632922	0.068017
0.084412	0.006898	0.166315	0.214072	0.999655	0.006563	0.603029	0.070955
0.075551	0.010354	0.221419	0.214038	0.999118	0.005099	0.573035	0.073327
0.066959	0.014433	0.273939	0.209446	0.998353	0.003740	0.542999	0.074789
0.058680	0.019115	0.341059	0.199307	0.997380	0.002521	0.517698	0.075096
0.050755	0.024375	0.407518	0.186009	0.996224	0.001474	0.492399	0.074589
0.043226	0.030187	0.519788	0.159121	0.994915	0.000751	0.467124	0.073338
0.036131	0.036522	0.564302	0.147377	0.993487	0.000000	0.429753	0.070121
0.029506	0.043346	0.608715	0.135268	0.991977	-0.000389	0.392529	0.065455
0.023385	0.050625	0.690539	0.122848	0.990424	-0.000531	0.361330	0.060523
0.017798	0.058323	0.725891	0.101867	0.988868	-0.000421	0.330294	0.054642
0.012774	0.066400	0.798570	0.080241	0.987395	-0.000078	0.299499	0.047606
0.008340	0.074814	0.871526	0.057818	0.965285	0.004772	0.247967	0.032951
0.005090	0.081558	0.944224	0.034548	0.943289	0.010207	0.202941	0.017860
0.004815	0.094844	0.992523	0.018582	0.921466	0.015790	0.159834	0.003211
0.000000	0.105295	0.994008	0.018107	0.883558	0.025179	0.159393	0.003104

R. G. Williamson
Head, Gas Dynamics Laboratory,
National Research Council of Canada,
Ottawa, Ontario, Canada K1A 0R6

S. H. Moustapha
Staff Aerodynamicist.

J. P. Huot
Senior Aerodynamicist.

Pratt & Whitney Canada Inc.,
Longueuil, Quebec, Canada J4K 4X9

The Effect of a Downstream Rotor on the Measured Performance of a Transonic Turbine Nozzle

Two nozzle designs, involving the same low aspect ratio, high turning angle vanes, and differing in outer wall contour, were tested over a range of exit Mach numbers up to supersonic values. The experiments were conducted on a large-scale, full annular configuration with and without a representative rotor downstream. Nozzle performance was found to be significantly affected by rotor operation, the influence depending on the detailed characteristics of the nozzle flow field, as well as on the design and operation of the rotor itself. It is suggested that performance evaluation of low aspect ratio nozzles of high turning angle may require appropriate testing with a rotor.

Introduction

The work reported here was conducted as part of a test program initiated in the mid-1970s with the objective of examining the aerodynamic performance of a highly loaded turbine stage. The main results of that investigation, pertaining to stage and rotor performance, are summarized in [1], which also includes a description of overall objectives and design philosophy.

The nozzle design was characterized by twisted vanes with large flow turning, low aspect ratio, high exit Mach numbers, and large trailing edge blockages associated with anticipated cooling requirements. The high work rotor involved large flow deflection angles (130 deg at the root) and high inlet relative Mach numbers. A significant feature of the test hardware was its large scale (blade height about 7.5 cm), which permitted flow characteristics to be traversed in detail, not only at rotor exit, but also between the nozzle exit and rotor leading edge.

Initial tests, conducted before the rotor was installed, explored the nozzle performance when operated as an annular cascade [2, 3]. Subsequent work [1] to assess stage and rotor performance involved detailed traverses at nozzle and rotor exits to attempt to isolate the contributions of each component. The opportunity therefore arose to investigate the effect of the operating rotor on the nozzle performance under flow conditions of high exit swirl and transonic Mach numbers.

A recent study of Boletis and Sieverding [4] contained a careful examination of the literature concerning rotor interactions on nozzle performance, and drew attention to the fact that a number of other investigators (e.g., [5–7]) had commented on the need to ensure correct reproduction of the radial pressure gradient at nozzle exit. Boletis and Sieverding also noted that the flows in nozzle wakes, being particularly susceptible to radial pressure gradients, offer the possibility of significant radial loss migration with change in exit conditions. The results of their experiments, as well as those of Sjolander [6], failed to show any significant interaction of the rotor with the performance of nozzles of moderately high

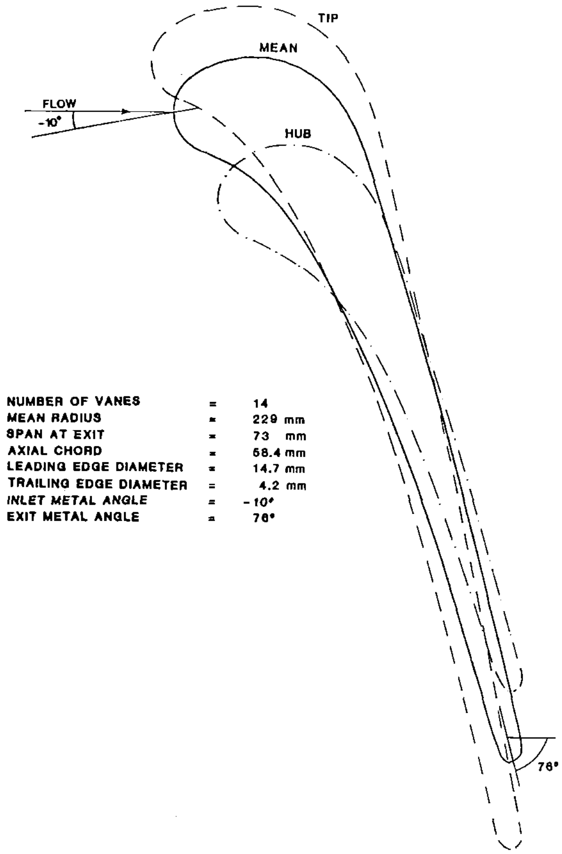

Fig. 1 Vane sections and midspan geometric parameters

Contributed by the Gas Turbine Division of THE AMERICAN SOCIETY OF MECHANICAL ENGINEERS and presented at the 31st International Gas Turbine Conference and Exhibit, Düsseldorf, Federal Republic of Germany, June 8–12, 1986. Manuscript received at ASME Headquarters January 20, 1986. Paper No. 86-GT-103.

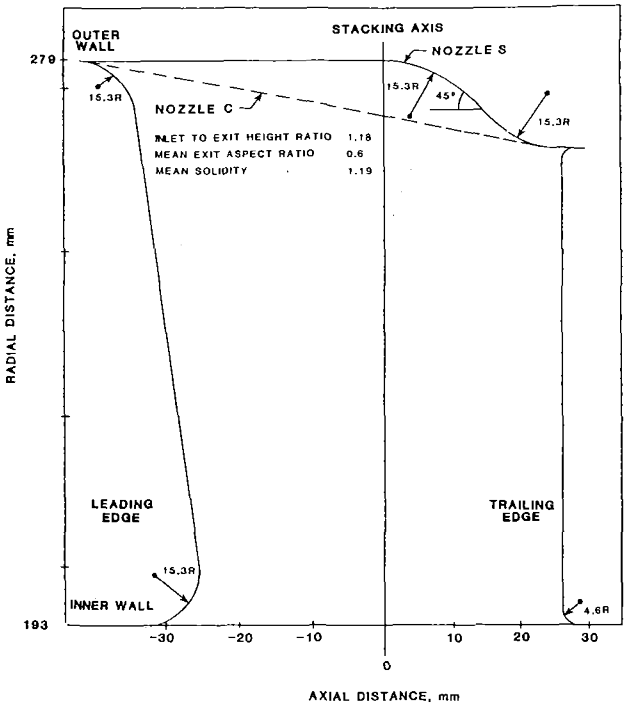

Fig. 2 Stator meridional view

turning angles under conditions of incompressible flow. The present work, involving vanes of high turning angle and tests conducted at exit Mach numbers up to supersonic values, provides a significant extension of previously reported conditions.

Experimental Arrangements

The blading, the turbine test facility, and the instrumentation have been fully detailed in [2, 3], and only the major aspects will be reiterated here.

Details of the vane section employed are presented in Fig. 1. The 14 vanes were stacked such that the trailing edge was straight and radial in meridional and axial views. Design exit Mach number at the mean section was 1.2, corresponding to a value of Pr = 2.3. Vane Reynolds number during the present tests was up to 1.8×10^6 based on mean chord and inlet conditions, and up to 9×10^6 based on exit conditions.

Two nozzle builds of differing meridional outer wall profiling were available, one with a conical outer wall contour from inlet to exit (nozzle *C*), the other with a more rapid "*S*" wall contour starting in the vicinity of the throat. Further information is given in Fig. 2. In order to maintain the same throat area between nozzle builds, it was necessary to restagger the *C* nozzle vanes 0.72 deg open compared to those of the datum *S* version. Most of the tests of this investigation were conducted with the *C* variant; some limited information is available from tests of the *S* nozzle.

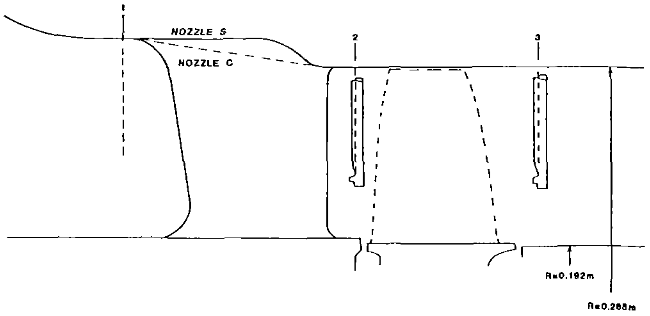

Fig. 3 Turbine stage meridional view

A meridional view of the test facility in the vicinity of the nozzle is shown in Fig. 3. During tests of the nozzle alone, the rotor was replaced by a dummy ring of diameter equal to that of the rotor blade hub platform. It is noted that small steps and gaps were present in the inner wall surface, corresponding to actual design practice associated with rotor clearance and cooling requirements. The magnitude was about 1.3 mm in each case.

Air was drawn through the rig by a large exhauster plant. In tests involving the rotor, the inlet air was prewarmed by mixing with the output of a propane combustor to maintain stage exit temperature near cell ambient conditions. Inlet air temperature could be varied up to the design point value of near 120°C depending upon operating conditions. The prewarming feature was also used to raise the inlet temperature in the tests without the rotor, in order to avoid freezing or condensation problems at nozzle exit.

Instrumentation was designed to explore mean gas angles and pressures under steady-state conditions. Static pressure tappings in the large upstream plenum chamber were used to sense nozzle inlet stagnation pressure. The test facility, designed for investigation of a complete stage, permitted radial and circumferential traversing at nominal nozzle and rotor exit planes (Fig. 3), the actual traverse positions being respectively 8.5 mm and 84.5 mm axially downstream of the nozzle trailing edge (corresponding to 0.14 and 1.43 nozzle axial mean chords). Most traverses were performed using a 4.8-mm-dia wedge probe. (Some limited additional traverse work was carried out using a cobra probe with a thinner, lozenge-shaped stem, which permitted possible probe blockage effects to be investigated.) Approach of the probe to the hub was limited by contact with the wall when the total pressure port was 4.8 mm from the surface. Considerable care was taken to ensure ade-

Nomenclature

Cpo = local nozzle total pressure loss coefficient = $(Pom_1 - Po_2)/(Pom_1 - Psm_2)$
$\overline{Cpo}$ = circumferential mean of Cpo
$\overline{\overline{Cpo}}$ = area-weighted radial mean of $\overline{Cpo}$
$\overline{\overline{Cpo}}_H$ = $\overline{\overline{Cpo}}$ evaluated over hub 50 percent of annulus height
$\overline{\overline{Cpo}}_T$ = $\overline{\overline{Cpo}}$ evaluated over tip 50 percent of annulus height
Cpr = local rotor total pressure drop coefficient = $(Po_2 - Po_3)/(Pom_2 - Psm_2)$
$\overline{Cpr}$ = circumferential mean of Cpr
$\overline{\overline{Cpr}}$ = area-weighted radial mean of $\overline{Cpr}$
Cpr^* = local blockage coefficient, circumferential mean of $(Po_2 - Po_3)/(Po_2 - Ps_2)$
N = rotational speed
Nr = $N/\sqrt{Tom_1}$ relative to design value, percent
$\overline{\overline{Mn}}$ = area-weighted mean Mach number at nozzle exit
Po = local total pressure
Pom = mean total pressure
PR = stage total pressure ratio, Pom_1/Pom_3
Pr = nozzle total to static pressure ratio = Pom_1/Psm_2
Ps = local static pressure
Psm = mean static pressure
Tom = mean total pressure
α = local exit swirl angle (degrees from axial)
$\overline{\alpha}$ = circumferential mean of α
$\overline{\overline{\alpha}}$ = area-weighted radial mean of $\overline{\alpha}$

Subscripts

1 = nozzle inlet plane
2 = nozzle exit plane
3 = rotor exit plane

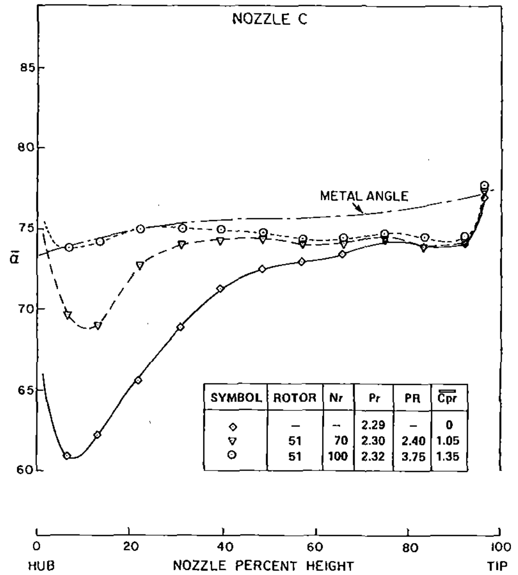

Fig. 4 Effect of rotor operating condition on radial distribution of circumferentially averaged nozzle exit flow angle

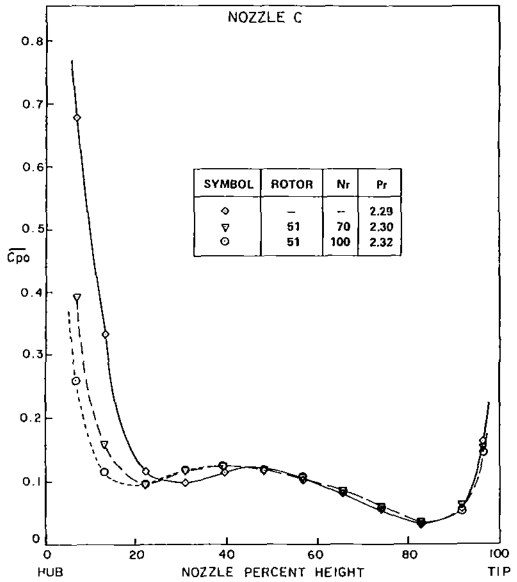

Fig. 5 Effect of rotor operating condition on radial distribution of circumferentially averaged nozzle total pressure loss coefficient

quate sealing of the traverse slots, and checks were made with smoke to ensure no detectable leaks were present.

The probe was operated under computer control, being automatically nulled for flow direction at each preselected point before total pressure data were recorded. For each circumferential position, data were secured at 12 radial immersions of the probe. A total of 11 circumferential increments, equispaced across a nozzle exit, was required to complete the mapping for each test condition.

Nozzle exit wall static pressures were averaged from blade to blade at hub and tip by using circumferential slits which extended over two nozzle exit passages and which connected to relatively large volume subsurface chambers in which the static pressures were measured. A linear variation of static pressure from hub to tip was assumed to permit calculation of local probe Mach numbers for estimation of corrections to measured total pressure under supersonic flow conditions. This was the only requirement for local static pressure estimations, and as the probe Mach number corrections were generally small, it is believed that accuracy was not significantly compromised. It is noted that use of a probe calibration factor to attempt to derive local static pressures in the complex exit flow field (which involved significant total and static pressure gradients in transonic flows) was not judged feasible. For this and other reasons, area weighting of results has been adopted, avoiding the need for locally inferred mass flow weighting which could have introduced significant error. It is further noted that an inaccuracy of 1 deg in measurement of flow swirl angles of around 76 deg incurs an error of 7 percent in mass flow. For a more complete discussion of instrumentation accuracy, the reader is referred to [2].

In the present tests, three rotor variants were available, each employing a different number of rotor blades of the same design. The variants were designated by the number of blades on the disc, i.e., 34, 45, or 51 (details are given in [1]). Within certain operational limitations, it was possible to run the rotor at a variety of rotational speeds and overall stage pressure ratios. Nozzle pressure ratio remained nominally constant near 2.3 above stage pressure ratios of about 2.4 due to choking of the rotor, permitting considerable variation of rotor operating conditions at the nominal nozzle design point.

Results and Discussion

Earlier work [2, 3] had established that, in isolated annular cascade tests, the two nozzle builds had broadly similar performance, with incipient hub flow separation evident at plane 2. For both designs, the hub wall flow reversal developed rapidly in the downstream annulus to become a large region of separation at plane 3. Despite these overall similarities in performance, some distinct differences were evident due to wall contouring. These are further apparent in the current work conducted with an operating rotor. Results pertaining to nozzle *C* are discussed first.

Figures 4 and 5 present data for nozzle *C* derived from traverses at plane 2 for two operating conditions of Rotor 51, together with earlier "no rotor" data, for nominally identical nozzle pressure ratios *Pr* near design conditions. It is immediately apparent that the incipient hub flow separation, associated with the lower swirl angles of Fig. 4 and higher losses of Fig. 5, is substantially reduced by the presence of a rotor. The extent of the improvement appears to be related to the rotor operating conditions. Examination of the nozzle exit hub and tip wall static pressures showed only very minor differences stemming from rotor presence. It is noted that upstream propagation of downstream conditions in supersonic flow can occur due to high swirl angles at nozzle exit. These produced an effective axial component of velocity which was substantially below the sonic level at all test conditions.

Tests were conducted for two other nozzle pressure ratios *Pr* holding rotor rotational speed constant at 70 percent of the design value. (Implicit in the tests was the variation of overall stage pressure ratio.) Results, again presented in the form of radial distributions of angles and mean total pressure loss coefficients, are shown in Figs. 6 and 7, together with equivalent "no rotor" data. Losses and mean flow angles associated with the hub flow separation in the "no rotor" condition were appreciably improved by the presence of the rotor at all nozzle pressure ratios. The extent of the improvement, particularly with respect to flow angle (Figs. 4 and 6), is related to the magnitude of the "no rotor" hub flow separation problem, which increased with nozzle pressure ratio. The presence of a significant rotor interaction effect at a value of *Pr* as low as 1.4 (and subsequently observed in other tests, not shown here, down to the lowest tested value of *Pr* of 1.2) indicates that rotor interaction is not limited to high Mach number nozzle exit flows.

Rotor effects of Figs. 4–7 are further illustrated by the overall area integrated values of mean exit swirl and loss coef-

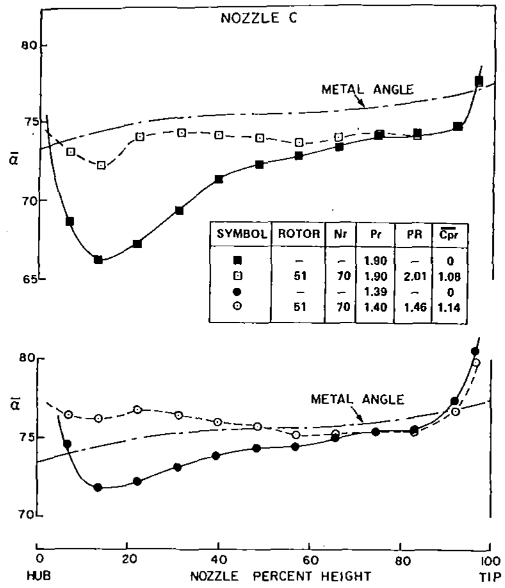

Fig. 6 Effect of rotor operation on radial distribution of circumferentially averaged nozzle exit flow angle

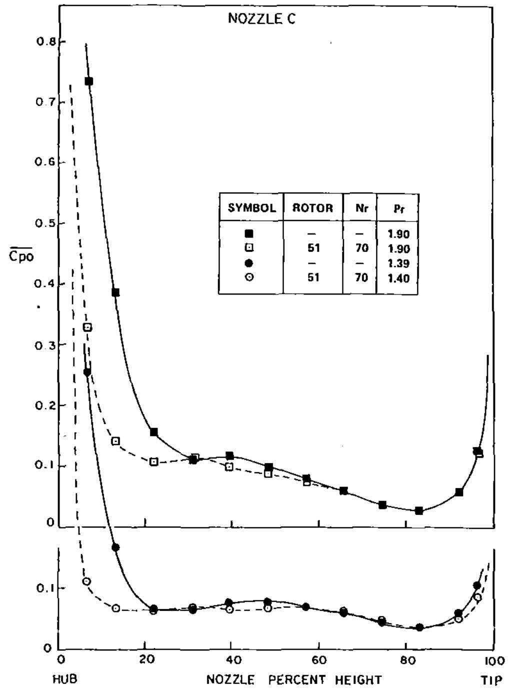

Fig. 7 Effect of rotor operation on radial distribution of circumferentially averaged nozzle total pressure loss coefficient

ficient shown in Fig. 8. The original "no rotor" data are compared with results obtained by operating Rotor 51 at 70 and 100 percent of the design rotational speed, over a range of nozzle pressure ratios. As well as the obvious difference in nozzle performance arising from the presence of the rotor, it is interesting to observe the higher critical Mach number associated with the more uniform nozzle exit conditions in tests with the operating rotor.

Recognizing that total pressure and angularity measurements in the complex transonic flow field at nozzle exit might be suspect, the traversing was repeated with a calibrated cobra probe of reduced stem size (and hence blockage). Although the cobra probe data in transonic Mach number flows were considered less reliable in detail, due to the larger calibration corrections required for that particular

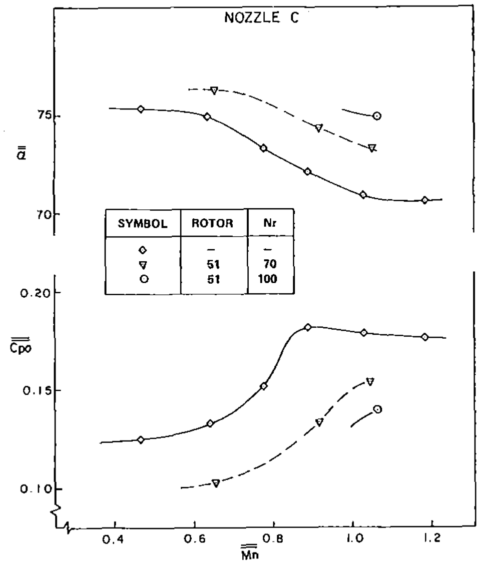

Fig. 8 Effect of stage operating conditions on overall nozzle performance

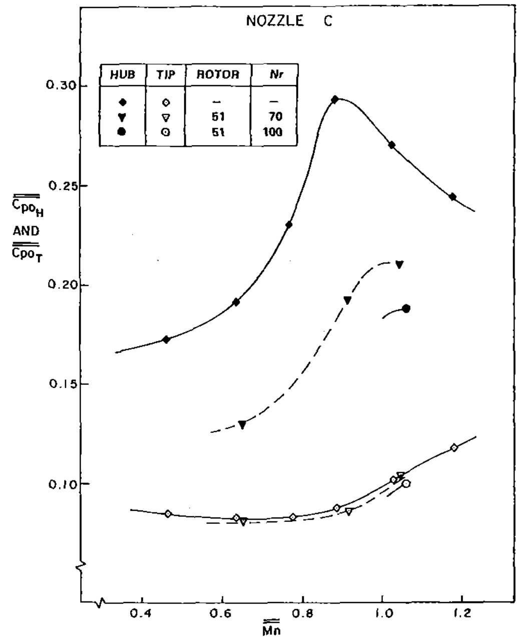

Fig. 9 Effect of stage operating conditions on nozzle hub and tip loss split

probe design, there was generally good agreement between the two sets of data.

An illustration of the effect of the rotor in suppressing hub separation is provided by Fig. 9 in which the data of Fig. 8 have been recast by calculating mean total pressure loss coefficients for the inner and outer halves of the annulus. There is negligible effect of the rotor presence on nozzle tip performance, and all of the observed changes take place at the hub.

Variation of a further rotor parameter, blade number (loading), resulted in a subtle but well-defined modification of the rotor interaction in the hub region, which is best seen in the mean flow angle distributions (Fig. 10). Increasing blade loading apparently reduced the beneficial effect of the rotor in the hub region.

Throughout these tests it was apparent that at least one component of the nozzle exit flow, namely the incipient hub flow separation, was reduced by the presence of an operating rotor. In broad terms, the "blockage" of the rotor would be expected to produce such an effect, and an overall rotor

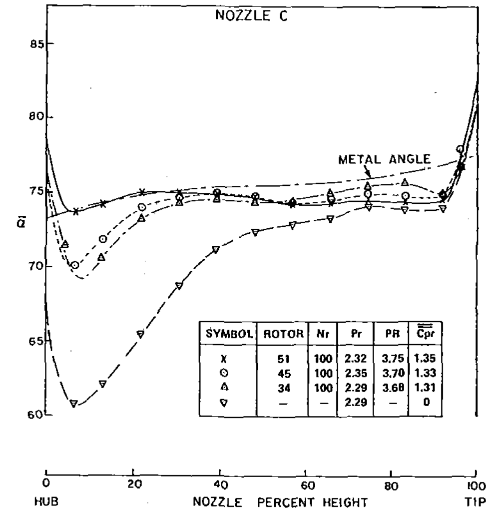

Fig. 10 Effect of rotor blade number on radial distribution of circumferentially averaged nozzle exit flow angle

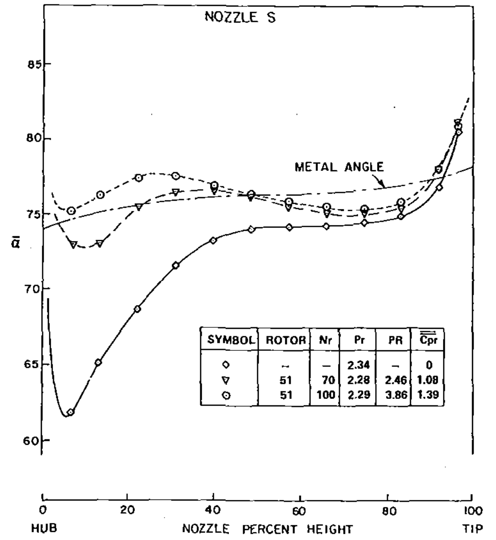

Fig. 11 Effect of rotor operating condition on radial distribution of circumferentially averaged nozzle exit flow angle

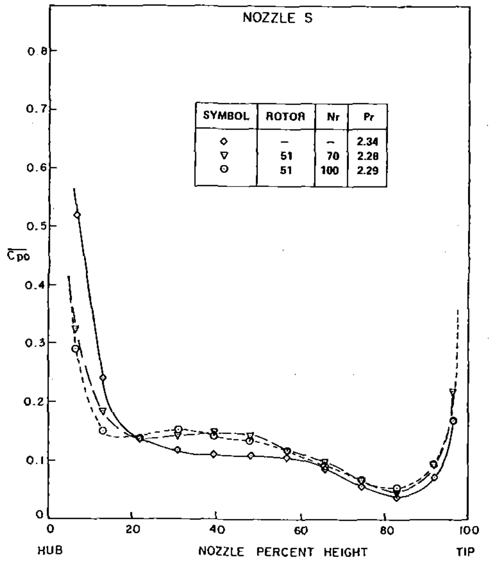

Fig. 12 Effect of rotor operating condition on radial distribution of circumferentially averaged nozzle total pressure loss coefficient

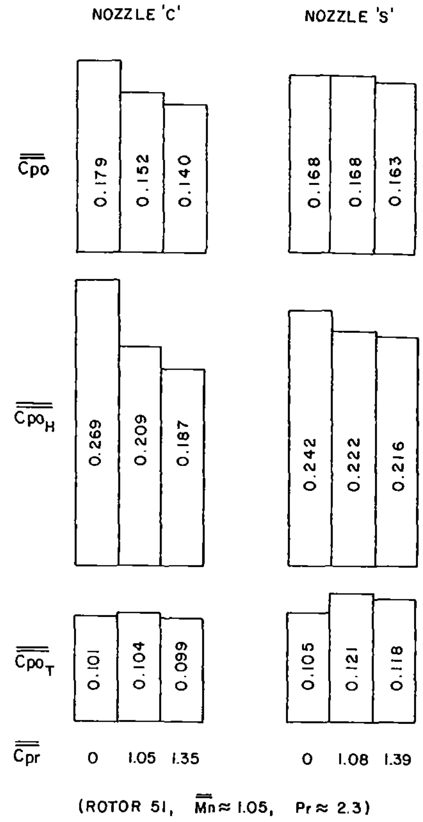

Fig. 13 Comparison of effect of rotor operation on performance of two nozzle variants

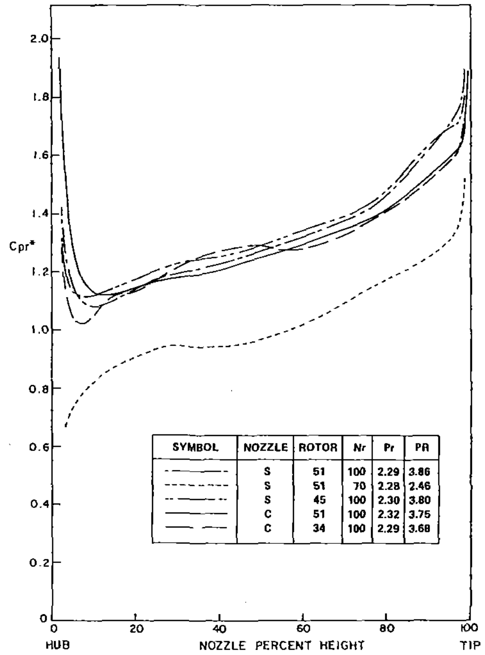

Fig. 14 Radial distribution of local rotor blockage coefficient for various stage builds and operating conditions

pressure drop coefficient $\overline{\overline{Cpr}}$ has been included with the operating point data on the figures to give some indication of the variation of this parameter. Such a general treatment is insufficient to correlate the details of the measured interactions, and it may well be that hub rotation and the "channeling" effect of the rotor leading edges play a part in the redirection of the nozzle exit flow.

Some limited additional data on the effect of a rotor on the performance of a different nozzle (with "*S*" shaped outer wall contour) are also available. Radial distributions of mean exit flow angles and mean total pressure loss coefficients for this nozzle are presented in Figs. 11 and 12, and are seen to show broadly similar trends to the data for nozzle *C* in Figs. 4 and 5. Again, the incipient hub flow separation observed in the isolated nozzle tests is significantly reduced by the rotor presence. Closer examination of the data, however, reveals some significant differences in the details of the rotor interaction.

The bar charts of Fig. 13 compare the $\overline{\overline{Cpo}}$ performance of the two nozzles, including separate evaluation of their hub and tip contributions to total pressure losses, as affected by increasing rotor blockage. It is apparent that, whereas for nozzle *C* the hub total pressure losses are reduced substantially with increasing rotor blockage, the reduction is much less for nozzle *S*. Losses very close to the hub wall are reduced in both cases, the larger separated region in nozzle *C* permitting greater gains from beneficial rotor interaction. In the case of nozzle *S*, the smaller gains are reduced further by the appearance of increased losses in the 20 to 60 percent span region (Fig. 12). This region is also affected in terms of exit angles (Fig. 11), and the results suggest greater three-dimensionality of the *S* nozzle exit flow compared to that of the *C* version (Fig. 4). (The three-dimensionality of the *S* nozzle exit flow is also reflected in the value of the corrected mass flow parameter, which was 4 percent lower than found for the *C* nozzle despite the nominal similarity in geometric throat area.)

Behavior of the tip contributions to nozzle total pressure losses (Fig. 13) also differs between the *S* and *C* builds, some slight increase in loss with increased blockage being apparent for the *S* variant. One of the results of these detailed differences in behavior is that in terms of overall total pressure loss $\overline{\overline{Cpo}}$, the performance of the *S* nozzle is only slightly affected by rotor operation, although overall nozzle exit flow angle $\overline{\overline{\alpha}}$ is substantially increased by the flow angle changes induced by the rotor. It is interesting to note that in terms of $\overline{\overline{Cpo}}$, the relative overall performances of the two nozzles are reversed by rotor operation (Fig. 13).

Two alternative explanations might be suggested to account for the different responses of the *S* and *C* nozzle builds to rotor presence. The distribution of blockage resulting from rotor operation might have been different in the two cases, or the exit flows of the two nozzles might have incorporated features of differing susceptibility to rotor presence.

The first possibility was investigated directly from the results of total pressure traverses at nozzle and rotor exits. Neglecting radial flows, and allowing for the fact that nozzle and rotor traverses were conducted on separate occasions (leading to inherent small errors stemming from matching inaccuracies), the radial distribution of total pressure drop through the rotor was evaluated. The local measured total pressure drops reflect rotor work and losses, and might be expected to vary with rotor operation. In order to obtain a radial distribution of local blockage coefficient Cpr^*, the mean pressure drop at each radius was normalized by the corresponding local mean value of nozzle exit "dynamic" pressure. Results, presented in Fig. 14, show negligible difference in distribution and level of local blockage coefficients for all available nozzle and rotor builds when tested at stage design conditions. This strongly suggests that the differences between the responses of the *S* and *C* nozzles to an operating rotor stem from the flows in the nozzles themselves. It is interesting to note that the characteristic shape of the distribution of local blockage coefficient appears to be maintained for the one off-design condition for which data are available.

The foregoing results suggest that the differences in behavior between the two nozzle variants arise from different susceptibilities of the various loss components to downstream conditions. The higher tip losses of the *S* build, for example, apparently originating with the containment of some of the endwall flow in the tip region, would be expected to be generally less susceptible to downstream effects than the losses associated with hub flow separation. The actual extent of improvement due to the rotor would also depend on the details of the "no rotor" test conditions which might promote or inhibit flow separation. If the combination of exit swirl angle, hub/tip ratio, wake and secondary flow characteristics, and downstream geometry were to promote hub flow separation in a "no rotor" test, then a greater interaction effect due to an operating rotor might well be expected. The differences between the present work and that of [4] may be explainable in these terms.

Conclusion

The results presented here have demonstrated that the overall and relative performances of two nozzle designs can be significantly affected by conditions downstream of the nozzle exit. In general, it appears that low aspect ratio nozzles of high turning angle may be susceptible to hub flow separation, whose propagation can be beneficially influenced by rotor operation. The sensitivity of nozzle performance to rotor presence depends on the characteristics of the nozzle exit flow field and on the rotor design and operation. It is suggested that a realistic assessment of the performance of such nozzles may require appropriate testing with a rotor.

Acknowledgments

The authors are indebted to Mr. U. Okapuu for his valuable input and encouragement in the evaluation of these results, and to Messrs. B. J. Day and D. L. Logan for their assistance in securing the experimental data.

References

1 Moustapha, S. H., Okapuu, U., and Williamson, R. G., "The Influence of Rotor Blade Aerodynamic Loading on the Performance of a Highly Loaded Turbine Stage," ASME Paper No. 86-GT-56.

2 Williamson, R. G., and Moustapha, S. H., "Three-Dimensional Cascade Testing of Turbine Nozzles at High Exit Mach Numbers," in: *Three-Dimensional Flow Phenomena in Fluid Machinery*, ASME FED Vol. 32, Nov. 1985.

3 Moustapha, S. H., and Williamson, R. G., "Investigation of the Effect of Two Endwall Contours on the Performance of an Annular Nozzle Cascade," AIAA Paper No. 85-1218, July 1985.

4 Boletis, E., and Sieverding, C. H., "Experimental Study of the Flow Field Behind an Annular Turbine Nozzle Guide Vane With and Without Downstream Rotor," ASME Paper No. 84-GT-15.

5 Vavra, M. H., *Aero-thermodynamics and Flow in Turbomachines*, R. Krieger Publ. Co., New York, 1974.

6 Sjolander, S. A., "The Endwall Boundary Layer in an Annular Cascade of Turbine Nozzle Guide Vanes," Carleton University, Ottawa, Report TR ME/A 75-4, Dec. 1975.

7 Denton, J. D., "A Review of Current Research Activity on the Aerodynamics of Axial Flow Turbines," VKI LS 1983-06, May 1983.

Inverse Design of Composite Turbine Blade Circular Coolant Flow Passages

T.-L. Chiang
Graduate Assistant.

G. S. Dulikravich[1]
Assistant Professor.

Department of Aerospace Engineering
and Engineering Mechanics,
The University of Texas at Austin,
Austin, TX 78712

An inverse design and optimization method is developed to determine the proper size and location of the circular holes (coolant flow passages) in a composite turbine blade. The temperature distributions specified on the outer blade surface and on the surfaces of the inner holes can be prescribed a priori. In addition, heat flux distribution on the outer blade surface can be prescribed and iteratively enforced using optimization procedures. The prescribed heat flux distribution on the outer surface is iteratively approached by using the Sequential Unconstrained Minimization Technique (SUMT) to adjust the sizes and locations of the initially guessed circular holes. During each optimization iteration, a two-dimensional heat conduction equation is solved using direct Boundary Element Method (BEM) with linear temperature singularity distribution. For manufacturing purposes the additional constraints are enforced assuring the minimal prescribed blade wall thickness and spacing between the walls of two neighboring holes. The method is applicable to both single material (homogeneous) and coated (composite) turbine blades. Three different cases were tested to prove the feasibility and the accuracy of the method.

Introduction

The idea of using an optimization technique coupled with the panel method (a kind of indirect BEM, often used in fluid mechanics to solve Laplace's equation) to develop an inverse design method for multiholed internally cooled turbine blades was originated by Kennon and Dulikravich [1-4]. They used the panel method to solve Laplace's equation for the temperature field in the solid blade material subject to partly Cauchy-type boundary conditions. The computed temperature distibution on the initially guessed inner coolant flow passage walls, and the prescribed coolant temperature on these walls, were then iteratively approached by changing the shapes and sizes of the coolant flow passages until the procedure converged.

The present work represents an improvement over this method which can be summarized as follows:

The temperature and heat flux distributions on the Γ_1 surface (Fig. 1) of the turbine blade are specified a priori in the original method. This is now changed to the temperature distribution and heat flux distribution specified on Γ_1 and the temperature distribution specified on Γ_3 surface, thus changing boundary conditions for Laplace's equation from a partly Cauchy type to a Dirichlet type during each iterative step.

The objective function is changed to the error function defined by the differences between the calculated and specified heat flux distributions on the surface Γ_1 instead of differences in temperatures on the surface Γ_3.

In this paper the direct BEM is used instead of the panel method to solve the two-dimensional Laplace equation for the steady-state temperature field. Also, the elements used now have a linear temperature distribution instead of the constant temperature distribution.

Two constraints that might be required in the practical

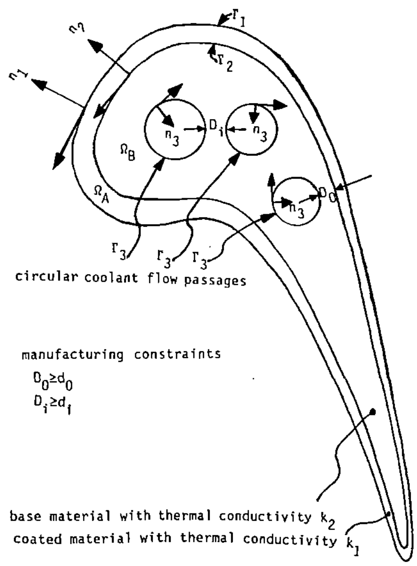

Fig. 1 Geometry and manufacturing constraints

---

[1] Presently Associate Professor, Aerospace Engineering Department, 233 Hammond Boulevard, Pennsylvania State University, University Park, PA 15802.

Contributed by the Gas Turbine Division of The American Society of Mechanical Engineers and presented at the 31st International Gas Turbine Conference and Exhibit, Düsseldorf, Federal Republic of Germany, June 8-12, 1986. Manuscript received at ASME Headquarters February 10, 1986. Paper No. 86-GT-190.

blade manufacturing process are added. They allow a minimum distance d_0 to be maintained between any hole and the Γ_2 surface and a minimum distance d_i to be maintained between the walls of any two neighboring holes (Fig. 1).

The nonhomogeneous blade design is allowed whereby a surface layer of, for example, ceramic material is used to coat the turbine surface Γ_2 (Fig. 1). This results in two coupled Laplace equations that need to be solved simultaneously.

All the inner coolant flow passages are forced to be circular, since the circular shape is more acceptable than the arbitrary shape from the manufacturing point of view.

Analytic Formulation

There are two methods of formulating the boundary-value problems of potential theory. The first method is referred to as an indirect formulation. It represents the potential function u with a single-layer or a double-layer potential generated by continuous source distibution over a surface Γ. This procedure leads to the formulation of integral equations which define the source densities. This method is mainly used in fluid mechanics where it is known as the source panel method.

However, one of the disadvantages of the indirect formulation is that the calculated source strengths usually have no obvious physical relation to the problem [5]. The other disadvantage is that the boundary surface is restricted to be a Liapunov (smooth) surface. These disadvantages can be overcome by using the direct formulation of the BEM [5].

The direct formulation can be deduced [5] from Green's third identity or the weighted residual method, since the latter permits a straightforward extension to solve more complex partial differential equations and can combine the BEM with more classical numerical methods. Therefore the latter method is usually used to formulate integral equations. The weighted residual statement can be written as

$$\int_\Omega (\nabla^2 u)u^* d\Omega = \int_{\Gamma_N} (q-\bar{q})u^* d\Gamma - \int_{\Gamma_E} (u-\bar{u})q^* d\Gamma \tag{1}$$

where u^* is the fundamental solution of the Laplace equation on a domain Ω, that is,

$$\nabla^2 u^* + \Delta_i = 0 \tag{2}$$

where Δ_i is the Dirac delta function. For an isotropic two-dimensional medium

$$u^* = \frac{1}{2\pi} \ln \frac{1}{r} \tag{3}$$

where r is the distance from point i to the point under consideration. Then

$$q = \frac{\partial u}{\partial n} \qquad q^* = \frac{\partial u^*}{\partial n} \tag{4}$$

Usually, $u = \bar{u}$ on Γ_E are called the essential conditions and $\partial u/\partial n = \bar{q}$ on Γ_N are called the natural conditions.

Integrating by parts and substituting equation (2) into the left-hand side of equation (1), the final form of the boundary integral equation is

$$c_i u_i + \int_\Gamma u q^* d\Gamma = \int_\Gamma q u^* d\Gamma \tag{5}$$

This equation provides a functional constraint between u and q over Γ, which ensures their compatibility as boundary data. Here, c_i is the value of the scaled internal angle of the boundary Γ at the point i (Fig. 2*a*), that is

$$c_i = \frac{\theta}{2\pi} \tag{6}$$

Consequently, $c_i = 1/2$ for a point on a smooth boundary where there is a continuous tangent, $c_i = 1$ for a point in the interior Ω, and $c_i = 0$ for a point exterior to Ω.

Numerical Discretization

Equation (5) can be discretized into a series of straight elements on the surface Γ with the variation of u and q assumed to be linear along each element. The points where the unknown derivatives q of the potential are considered are called nodes and are taken to be at the ends of each element (Fig. 2a).

Equation (5) can be written for the n elements as

$$c_i u_i + \sum_{j=1}^{n} \int_{\Gamma_j} u q^* d\Gamma = \sum_{j=1}^{n} \int_{\Gamma_j} q u^* d\Gamma \tag{7}$$

The values of u and q at any point of the element can be defined in terms of their nodal values and the linear interpolation functions ϕ_1 and ϕ_2, that is

$$u(\xi) = [\phi_1 \phi_2] \begin{bmatrix} u_1 \\ u_2 \end{bmatrix} \tag{8}$$

$$q(\xi) = [\phi_1 \phi_2] \begin{bmatrix} q_1 \\ q_2 \end{bmatrix} \tag{9}$$

where ξ is the dimensionless coordinate (Fig. 2*b*), $\xi = 2x/1$, $\phi_1 = (1/2)(1-\xi)$, and $\phi_2 = (1/2)(1+\xi)$. Then

$$\int_{\Gamma_j} u q^* \mathrm{d}\Gamma = [h_{ij}^1, h_{ij}^2] \begin{bmatrix} u_1 \\ u_2 \end{bmatrix} \tag{10}$$

where

$$h_{ij}^1 = \int_{\Gamma_j} \phi_1 q^* d\Gamma \quad h_{ij}^2 = \int_{\Gamma_j} \phi_2 q^* d\Gamma$$

Hence

$$\int_{\Gamma_j} q u^* \mathrm{d}\Gamma = [g_{ij}^1, g_{ij}^2] \begin{bmatrix} q_1 \\ q_2 \end{bmatrix} \tag{11}$$

where

$$g_{ij}^1 = \int_{\Gamma_j} \phi_1 u^* d\Gamma \quad g_{ij}^2 = \int_{\Gamma_j} \phi_2 u^* d\Gamma$$

All coefficients h_{ij}^1, h_{ij}^2, g_{ij}^1, and g_{ij}^2 can be evaluated by using the numerical integration. When $i=j$, g_{ij}^1 and g_{ij}^2 are determined analytically [5].

Substituting these into equation (7), the equation for node i can be obtained as

$$c_i u_i + [\hat{H}_{i1}, \ldots, \hat{H}_{iN}] \begin{bmatrix} u_1 \\ \cdot \\ \cdot \\ \cdot \\ u_N \end{bmatrix} = [G_{i1}, G_{i2}, \ldots, G_{iN}] \begin{bmatrix} q_1 \\ \cdot \\ \cdot \\ \cdot \\ q_N \end{bmatrix} \tag{12}$$

where for all $j \neq 1$

$$\hat{H}_{ij} = h_{i,j-1}^2 + h_{i,j}^1, \; G_{ij} = g_{i,j-1}^2 + g_{i,j}^1 \tag{13}$$

and for $j = 1$

$$\hat{H}_{i,j} = h_{i,1}^1 + h_{i,N}^2, \; G_{ij} = g_{i,1}^1 + g_{i,N}^2 \tag{14}$$

Then

$$c_i u_i + \sum_{j=1}^{N} \hat{H}_{ij} u_j = \sum_{j=1}^{N} G_{ij} q_j \tag{15}$$

or more simply

$$\sum_{j=1}^{N} H_{ij} u_j = \sum_{j=1}^{N} G_{i,j} q_j \tag{16}$$

where

$$\begin{aligned} H_{i,j} &= \hat{H}_{i,j} \text{ for } i \neq j \\ H_{i,j} &= \hat{H}_{i,j} + c_i \text{ for } i = j \end{aligned} \tag{17}$$

Composite Blades

Turbine blades with, say, ceramic coating have two regions of considerably different thermal conductivities. Therefore, two coupled Laplace equations for temperature field need to be solved. The corresponding two matrices can be added together by using the continuity of heat fluxes and equalizing the temperatures themselves at the interface Γ_2 between the coating and the main turbine material.

Assume that there are N_i elements on the surfaces Γ_i where $i = 1, 2, 3$ and that the thermal conductivity in Ω_A is k_1 and in Ω_B is k_2. For domain Ω_A (coating material) the governing equations are then

$$\left(\underbrace{\begin{matrix} H_{1,1} & H_{1,N_1} \\ \cdot & \cdot \\ \cdot & \cdot \\ \cdot & \cdot \\ H_{N_1+N_2,1} & H_{N_1+N_2,N_1} \end{matrix}}_{\substack{\Omega_A \\ H_1}} \;\vdots\; \underbrace{\begin{matrix} H_{1,N_1+1}, & H_{1,N_1+N_2} \\ \cdot & \cdot \\ \cdot & \cdot \\ \cdot & \cdot \\ H_{N_1+N_2,N_1+1} & H_{N_1+N_2,N_1+N_2} \end{matrix}}_{\substack{\Omega_A \\ H_2}}\right) \begin{bmatrix} u_1^{\Gamma_1} \\ \cdot \\ u_{N_1}^{\Gamma_1} \\ u_1^{\Gamma_2} \\ \cdot \\ u_{N_2}^{\Gamma_2} \end{bmatrix} =$$

$$\left(\underbrace{\begin{matrix} G_{1,1} & G_{1,N_1} \\ \cdot & \cdot \\ \cdot & \cdot \\ \cdot & \cdot \\ G_{N_1+N_2,1} & G_{N_1+N_2,N_1} \end{matrix}}_{\substack{\Omega_A \\ G_1}} \;\vdots\; \underbrace{\begin{matrix} G_{1,N_1+1}, & G_{1,N_1+N_2} \\ \cdot & \cdot \\ \cdot & \cdot \\ \cdot & \cdot \\ G_{N_1+N_2,N_1+1} & G_{N_1+N_2,N_1+N_2} \end{matrix}}_{\substack{\Omega_A \\ G_1}}\right) \begin{bmatrix} Q_1^{\Gamma_1}/k_1 \\ \cdot \\ \cdot \\ Q_{N_1}^{\Gamma_1}/k_1 \\ Q_1^{\Gamma_2}/k_1 \\ \cdot \\ \cdot \\ \cdot \\ Q_{N_2}^{\Gamma_2}/k_1 \end{bmatrix} \tag{18}$$

or more simply

$$\begin{bmatrix} \Omega_A & \Omega_A \\ H_1 \;, & H_2 \end{bmatrix} \begin{bmatrix} \Gamma_1 \\ u \\ \Gamma_2 \\ u \end{bmatrix} = \begin{bmatrix} \Omega_A & \Omega_A \\ G_1 \;, & G_2 \end{bmatrix} \begin{bmatrix} \Gamma_1 \\ Q \;/k_1 \\ \Gamma_2 \\ Q \;/k_1 \end{bmatrix} \tag{19}$$

In the same way, for domain Ω_B (main blade material)

$$\begin{bmatrix} \Omega_B & \Omega_B \\ H_1 \;, & H_2 \end{bmatrix} \begin{bmatrix} \Gamma_2 \\ u \\ \Gamma_3 \\ u \end{bmatrix} = \begin{bmatrix} \Omega_B & \Omega_B \\ G_1 \;, & G_2 \end{bmatrix} \begin{bmatrix} \Gamma_2 \\ -Q \;/k_2 \\ \Gamma_3 \\ Q \;/k_2 \end{bmatrix} \tag{20}$$

Combining equation (19) and equation (20) and moving all the unknowns to the right-hand side results in

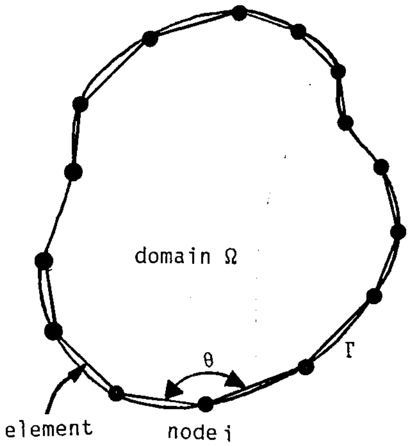

Fig. 2(a) Discretized boundary Γ

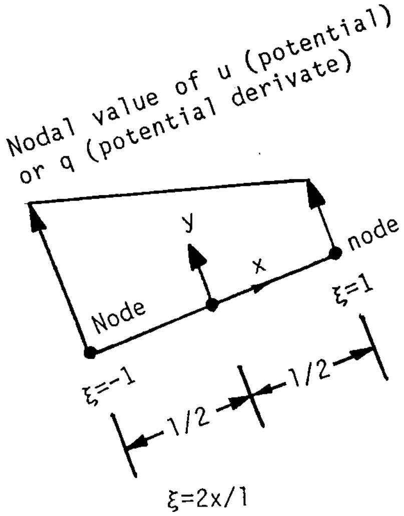

Fig. 2(b) Linear element

$$\begin{bmatrix} \Omega_A & \\ k_1H_1 & 0 \\ & \Omega_B \\ 0 & k_2H_2 \end{bmatrix} \begin{bmatrix} \Gamma_1 \\ u \\ \Gamma_3 \\ u \end{bmatrix} = \begin{bmatrix} \Omega_A & \Omega_A & \Omega_A & \\ G_1 & G_2 & -k_1H_2 & 0 \\ & \Omega_B & \Omega_B & \Omega_B \\ 0 & -G_1 & -k_2H_1 & G_2 \end{bmatrix} \begin{bmatrix} \Gamma_1 \\ Q \\ \Gamma_2 \\ Q \\ \Gamma_2 \\ u \\ \Gamma_3 \\ Q \end{bmatrix} \qquad (21)$$

Notice the directions of the normal defined on different surfaces as shown in Fig. 1. So, for surfaces Γ_1 and Γ_2, the numbering scheme is defined in the counterclockwise direction, while for Γ_3 it is in the clockwise direction.

Problem of Nonuniqueness

For a multiply connected domain, the solution of the integral equation with Dirichlet or mixed-type boundary conditions does not always have a unique solution [6]. That is, for a given curve shape Γ_1 there will always exist a particular curve magnitude, where difficulties will occur in connection with the integral equations of the first kind with logarithmic kernel.

In the present work, this situation is avoided by a simple change of scale—a method adopted by Symm [6], so that the maximum diameter of the domain is not greater than unity. This is sufficient to ensure that there is no possibility of nonuniqueness due to Γ_1 being a Γ contour. Alternatively, a unique solution may also be obtained by adding an appropriate auxiliary condition [7]. Detailed discussions on the nonuniqueness of the solutions of the integral equations can be found in [8, 9].

Optimization Procedures and Concept

The iterative optimization procedure used to modify the sizes and locations of the guessed coolant flow passages can be explained using the following steps:

1 Specify the potential (temperature) distributions u on surfaces Γ_1 and Γ_3.

2 Specify the heat flux distribution $Q^R{}_j$ (for $j=1, \ldots, N_1$) on surface Γ_1, and the thermal conductivities k_1 and k_2.

3 Specify the manufacturing constraints: (*i*) minimum distance d_0 allowed between the holes and surface Γ_2; (*ii*) minimum distance d_i allowed between any two neighboring hole surfaces Γ_3.

4 Specify the number of holes required, and the initial guess of the radii and location of the centers of the holes. Also required is specification of the number of boundary elements to be used on surfaces Γ_1, Γ_2, and each of the holes, Γ_3.

The geometry for each circular hole can be defined by three independent variables: center coordinates x and y, and the radius r. If there are M holes, there will be $3M$ independent variables in the error function.

However, the initially guessed variables should locate the holes entirely in the feasible region of domain Ω_B, that is, the constraints in step 3 must be satisfied (Fig. 1).

5 With the BEM described earlier, solve the Laplace equation for temperature field and calculate the heat flux Q_j^c ($j=1, \ldots, N_1$) on surface Γ_1.

6 Use the Q_j^c to determine the values of the error function and the objective function (OBJ) of the optimization problem.

The nondimensional error function E_0 can be defined as

$$E_0(\mathbf{x}) = E_0(x_i, y_i; r_i) = \frac{\left[\sum_{j=1}^{N_1} (Q_j^c - Q_j^R)^2\right]^{1/2}}{\left[\sum_{j=1}^{N_1} (Q_j^R)^2\right]^{1/2}} \qquad (22)$$

The purpose is to find the optimal value of $\mathbf{x}(x_i, y_i; r_i)$ for $i=1, \ldots, M$ such that E_0 is minimized. A penalty function must be added to E_0 to construct the OBJ function $E^*(\mathbf{x})$ for the two manufacturing constraints, that is,

$$E^*(\mathbf{x}) = E_0(\mathbf{x}) + \text{penalty function} \qquad (23)$$

There are many different forms for the penalty function [10]. The penalty function used here is of the interior method type with the inverse barrier function proposed by Carroll [11]

$$\text{Penalty function} = R \cdot \left[\sum_{j=1}^{N_3} \frac{d_0}{(D_j - d_0)} + \sum_{k=1}^{N_4} \frac{d_i}{(D_k - d_i)} \right] \qquad (24)$$

where $N_4 = M!/2!\,(M-2)!$. Here, D_j is the minimum com-

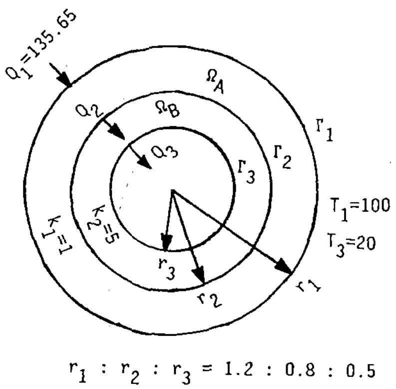

Fig. 3 Geometry and boundary conditions, test case 1

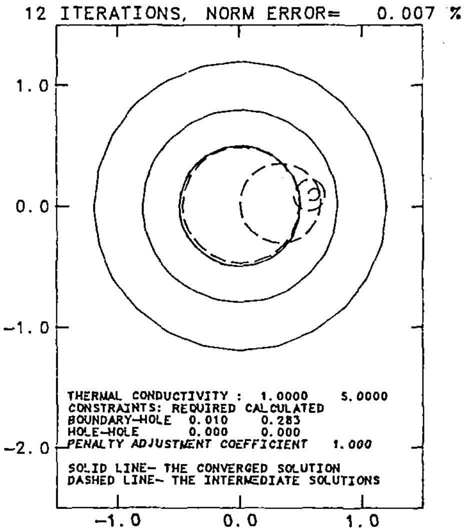

Fig. 4 Iteration sequence, test case 1

puted distance between the element j of Γ_3 and the surface Γ_2 and D_k is the computed distance between any two circular holes

$$D_k=[(x_i-x_{i+1})^2+(y_i-y_{i+1})^2]^{1/2}-(r_i+r_{i+1})$$

for holes i and $i+1$.

R is a positive constant which is chosen to be initially quite large during the first few optimization iterations, and then gradually reduced to near zero. $E^*(\mathbf{x})$ will then approach E_0. This method is called the Sequential Unconstrained Minimization Technique (SUMT).

A relation between the initial penalty function and the error function is defined as the Penalty Adjustment Coefficient (PAC), that is

$$\mathrm{PAC}=\frac{\text{Penalty function}}{E_0}$$

7 Use the steepest-descent optimization technique to find the new values of the independent variables $\mathbf{x}$ until the corresponding $E^*(\mathbf{x})$ is below a satisfactory value, otherwise return to step 5.

Results and Discussion

On the basis of the preceding analysis a computer program [12] was developed and tested using the following three test cases.

The first test case was used to test the reliability of the computer program as an analysis tool. The geometry consists of a coating and a single hole (Fig. 3) with r_3:r_2:r_1 = 0.5:0.8:1.2, $k_1=1$, $k_2=5$, $T_1=100$, $T_3=20$ (uniform distributed). A total of 72 boundary elements were used. The results are listed in Table 1, showing that the largest error between the analytic solution and the BEM solution is about 1.63 percent in Q_1. The accuracy of the BEM can be further improved by either increasing the number of elements or using higher order elements. The inverse optimization solutions were accomplished (Table 1) by specifying the heat flux distribution on Γ_1 and temperature distribution on Γ_1 and Γ_3 surfaces. The heat flux on Γ_1 surface was then calculated by the BEM after each iteration, that is, after each adjustment of the hole shapes and their locations. The initially guessed surface Γ_3 and its iterative evolution sequence are shown in Fig. 4.

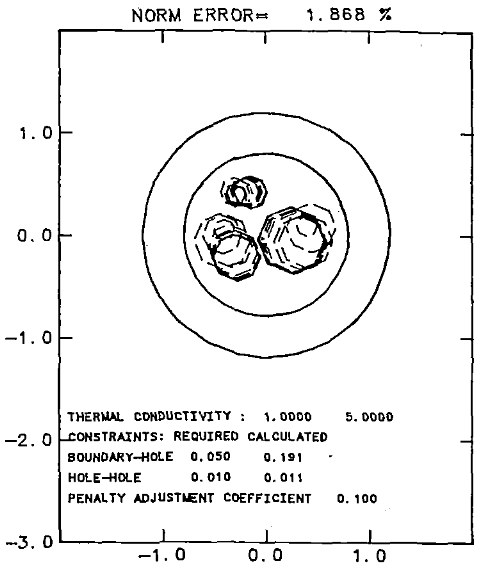

Fig. 5(a) Iteration sequence, test case 2

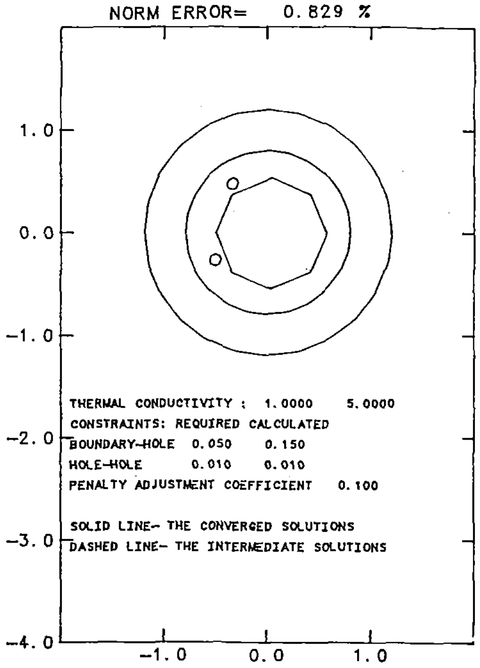

Fig. 5(*b*) Iteration sequence, test case 2

The second test case was used to test the feasibility of the inverse design concept. The same heat flux distribution on the surface Γ_1 was kept as in the first case, but the number of the circular holes was changed to three instead of one (Fig. 5*a*). Temperature distributions on Γ_1 and the holes Γ_3 did not

Table 1 Results for the first test case, using linear BEM; *—values are given at the specified conditions

Surface		Γ_1	Γ_2		Γ_3			
Method / Properties		Q_1	Q_2	T_2	Q_3	hole Center		hole Radius
						x	y	r
Analytic Solution		133.47	-200.21	35.06	-320.34	0.00*	0.00*	0.5*
BEM Approximate Solution		135.65	-200.43	35.21	-324.1	0.00*	0.00*	0.5*
Inverse Optimization Solution	P.A. Coeff							
	0.1	135.65*	-200.52	35.24	-324.74	0.00032	0.0006	0.4998
	1.0	135.65*	-200.44	35.21	-324.64	0.0001	0.0000	0.5001
	5.0	135.65*	-200.34	35.25	-324.90	0.0005	0.0003	0.4994

Table 2 Results for the third test case using a linear element; *—values are given at the specified conditions

		Total Heat Flux on Surface			Hole 1			Hole 2			L2 Norm Error x 100%
					Center		Radius	Center		Radius	
		Γ_1	Γ_2	Γ_3	x_1	y_1	r_1	x_2	y_2	r_2	
Approximate Solution		70554	-70636	-71501	0.3*	1.25*	0.08*	0.5*	1.0*	0.05*	
Inverse Optimization Solution	P.A. Coeff										
	0.1	70570	-70653	-71648	0.2978	1.2511	0.0783	0.5031	1.008	0.053	0.927
	0.5	70214	-70298	-71339	0.2953	1.2530	0.0774	0.4997	1.021	0.055	2.346
	1.0	7.0564	-70647	-71648	0.2976	1.2512	0.0782	0.5031	1.009	0.054	0.991
	1.5	70556	-70639	-71635	0.2977	1.2512	0.0783	0.5031	1.008	0.054	0.95
	5.0	70564	-70647	-71646	0.2977	1.2512	0.0782	0.5031	1.008	0.054	0.972
	8.0	70585	-70669	-71664	0.2977	1.2512	0.0783	0.5031	1.008	0.053	0.921

change, that is, it was still $T_1 = 100$ on Γ_1 and $T_3 = 20$ on Γ_3. Comparison of the calculated heat flux distribution with the specified heat flux is shown in Fig. 6. The corresponding $L2$-norm error was below 2 percent and it is distributed in the form of a sine function (see Fig 6). It can be concluded that the inverse design concept is quite feasible for multihole configurations. Note that when the error was decreased to 0.829 percent (Fig. 5*b*), one of the three holes converged to a large hole located near the center. The other two holes became negligibly small in comparison with the large hole (Fig. 5*b*).

The third test case was used to prove that for an arbitrarily shaped blade, good accuracy can be obtained between the BEM approximate solutions and the inverse optimization solutions.

The contour Γ_1 used in this case was a realistic turbine blade (Fig. 8). The variable temperature distribution specified on the surface Γ_1 can be seen in Fig. 7 and does not represent any actually measured value. The results of the inverse design procedure are listed in Table 2 and the evolutionary history of the holes can be seen in Fig. 8.

No obvious irregularity can be seen from the convergence history of E_0 except when the PAC is chosen to be too big. Then, there will be an upshoot during the first iteration (see Figs. 9 and 10). Note that in Fig. 9 for the PAC equal to 8 and in Fig. 10 for the PAC equal to 0.5, the iterative process converged to local minima.

Also, the third test case, using a PAC of 10, resulted in an infeasible solution, that is, the radius of one of the circular holes became negative. The conclusion is that too big a PAC will create a large $E^*(\mathbf{x})$ value, so the hole radius derived from the quadratic interpolation will fall below a physically meaningful value. The conclusion is that PAC should be of the order one.

The rate of convergence of any optimum search technique is highly dependent on the given function E^*. In certain problems proper scaling can be performed so as to make the contours of constant error as circular as possible. This can significantly accelerate the rate of convergence. Unfortunately, the $E^*(\mathbf{x})$ in this inverse design problem is an implicit function of $\mathbf{x}$ and the scaling technique is hard to apply.

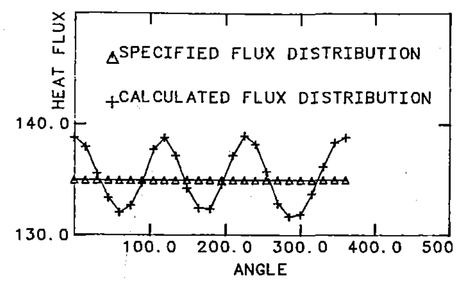

Fig. 6 Calculated and specified heat flux distributions, test case 2

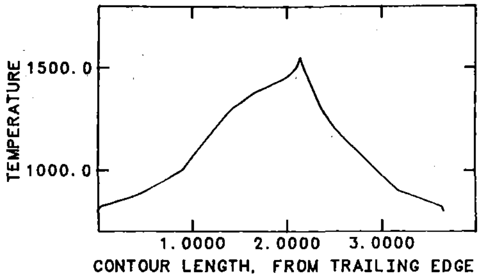

Fig. 7 Temperature distribution prescribed on Γ_1, test case 3

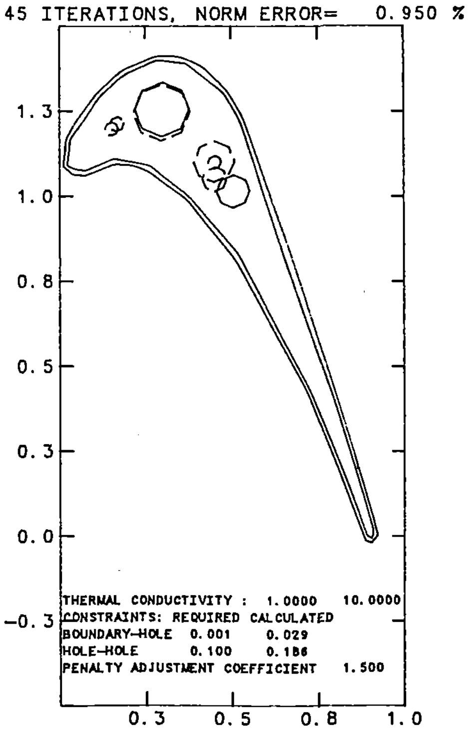

Fig. 8 Iteration sequence, test case 3

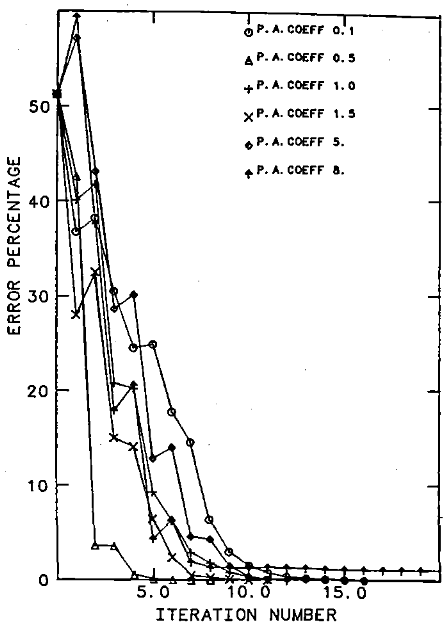

Fig. 9 Convergence history, test case 1

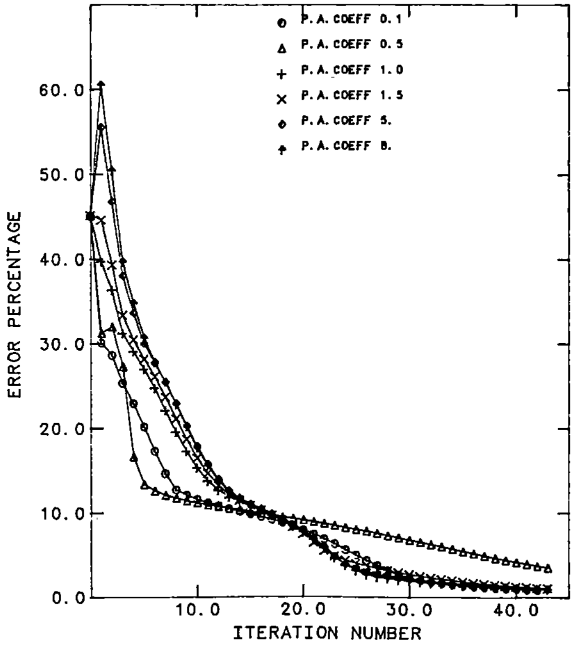

Fig. 10 Convergence history, test case 3

The problem of failing to find the global minimum might be resolved in any optimization technique by recomputing the problem with different initial guesses [13]. The initial variables should be systematically chosen for good distribution over the variable space until a sufficiently low value of E_0 has been located.

Summary

An efficient inverse design procedure for multiple circular holes (coolant flow passages) in nonhomogeneous turbine blades has been developed. The work is accomplished by coupling the direct boundary element method and the sequential unconstrained minimization technique.

The specified heat flux distribution on the outer surface of the blade is iteratively approached while satisfying the prescribed temperature distributions on the outer surface of the blade and on surfaces of the holes by a successive adjustment of the sizes and locations of the holes. Also included are two manufacturing constraints concerning the minimal allowable blade wall thickness and hole spacing.

This procedure can be successfully applied to the inverse design of coated turbine blade multiple coolant flow passage shapes. In earlier works [1-4] it was demonstrated that the coolant flow passage shapes can be changed from circular to other families of noncircular holes by adjusting the relation between the independent variables in the optimization objective function. It can also be revised to be used for the inverse design and analysis of the transient thermal problems or coupled with forced convection boundary conditions on the coolant flow passage walls if the coolant temperature and heat transfer coefficients are provided.

References

1 Kennon, S. R., "Novel Approaches to Grid Generation, Inverse Design, and Acceleration of Iterative Schemes," M.S. Thesis, Dept. of Aerospace Engineering and Engineering Mechanics, University of Texas at Austin, May 1984.

2 Kennon, S. R., and Dulikravich, G. S., "The Inverse Design of Internally Cooled Turbine Blades," ASME JOURNAL OF ENGINEERING FOR GAS TURBINES AND POWER, Vol. 107, 1985, pp. 123-126.

3 Kennon, S. R., and Dulikravich, G. S., "Inverse Design of Multiholed Internally Cooled Turbine Blades," *Proceedings of the International Conference on Inverse Design in Engineering Sciences (ICIDES)*, G. S. Dulikravich, ed., University of Texas at Austin, Oct. 17-18, 1984, pp. 217-240.

4 Kennon, S. R., and Dulikravich, G. S., "Inverse Design of Coolant Flow Passage Shapes With Partially Fixed Internal Geometries," ASME Paper No. 85-GT-118, 1985.

5 Brebbia, C. A., et al., *Boundary Element Techniques*, Springer-Verlag, Berlin-Heidelberg, 1984.

6 Symm, G. T., "The Robin Problem in a Multiply-Connected Domain," in: *Boundary Element Methods in Engineering*, Proceedings of the Fourth International Seminar, Southampton, England, Sept. 1982.

7 Christiansen, S., "Integral Equations Without a Unique Solution Can Be Made Useful for Solving Some Plane Harmonic Problems," *J. Inst. Math. Applics.*, Vol. 16, 1975, pp. 143-159.

8 Jaswon, M. A., "Integral Equation Methods in Potential Theory," *I. Proc. Roy. Soc.* (A), Vol. 275, 1963, pp. 23-32.

9 Hayes, J., and Kellner, R., "The Eigenvalue Problem for a Pair of Coupled Integral Equations Arising in the Numerical Solution of Laplace's Equation," *SIAM J. Appl. Math.*, Vol. 22, 1972, pp. 503-513.

10 Vanderplats, G. N., *Numerical Optimization Techniques for Engineering Design: With Applications*, McGraw-Hill, 1984.

11 Carroll, C. W., "An Operations Research Approach to the Economic Optimization of a Kraft Pulping Process," Ph.D. Thesis, Institute of Paper Chemistry, Appleton, WI, 1959.

12 Chiang, T. L., and Dulikravich, G. S., "CFD8503-FORTRAN Program for Inverse Design of Coolant Flow Passages in Composite Turbine Blades," Computational Fluid Dynamics UTCFD Report 200-85, Dept. of Aerospace Eng. and Eng. Mechanics, University of Texas at Austin, Sept. 1985.

13 Daniels, R. W., *An Introduction to Numerical Methods and Optimization Techniques*, Elsevier North-Holland, New York, 1978.

G. E. Andrews

M. Alikhanizadeh

A. A. Asere

C. I. Hussain

M. S. Khoshkbar Azari

M. C. Mkpadi

Department of Fuel and Energy,
University of Leeds,
Leeds, LS2.9JT, United Kingdom

Small Diameter Film Cooling Holes: Wall Convective Heat Transfer

The wall heat transfer resulting from small diameter holes drilled at 90 deg through gas turbine combustion chamber and turbine blade walls is considered. Available information is briefly reviewed and shown to generally omit the hole approach surface heat transfer and to relate only to the internal hole heat transfer. Experimental techniques are described for the determination of the overall heat transfer in a metal plate with a large number of coolant holes drilled at 90 deg. The results are compared with conventional short-tube internal heat transfer measurements and shown to involve much higher heat transfer rates and this mainly resulted from the additional hole approach flow heat transfer.

Introduction

Cooled turbine blades are essential to the operation of modern gas turbines at high turbine entry temperatures. Although internal convective cooling, such as impingement, multipassages, and pedestal arrays, can accomplish significant cooling, for the highest temperatures film cooling is required. This usually consists of a series of discrete holes in a relatively thin blade wall. The hole length-to-diameter ratio is rarely in excess of five. Gas turbine combustion chambers also often use the same technique of a series of discrete holes to cool local hot spots in the combustor wall. The authors have presented design data for the application of this technique to full coverage flame tube cooling [1, 3]. Wadia and Nealy [4] have recently drawn attention to lack of information on discrete hole film cooling in the blade leading edge region and the importance of internal wall cooling in this application. Lloyd and Brown [5] have shown that there is a lack of information on short hole heat transfer, relevant to turbine blade applications, and this contrasts markedly with the voluminous literature on purely film cooling.

To develop a heat transfer model for turbine blades and combustor wall applications three sets of heat transfer data are required: firstly, the adiabatic film cooling effectiveness; secondly, the convective heat transfer coefficient; and finally, the internal wall heat transfer. The bulk of the literature on discrete hole film cooling has been directed at the first of these and the many variables have recently been correlated by L'Ecuyer and Soechting [6]. Much less information is available on the second effect and it was often assumed that simple flat plate convective heat transfer coefficients would apply. It has been shown by Hey and Lampart [7] that this is not valid for single rows of holes and by the authors [2, 3] for multirows of holes. Internal wall heat transfer is due to the presence of the holes and pipe entry heat transfer correlations have often been used. However, additional heat transfer may occur as the air approaches the hole inlet and the overall heat transfer may be greater than that occurring inside the hole. It is the aim of the present work to review the wall heat transfer information, to describe a technique for determining the overall internal wall heat transfer, and to give some initial results.

Short Hole Heat Transfer

Inlet Flow Separation. The hole geometries considered in the present work are 90 deg holes with sharp-edged inlets. For small holes it is sometimes presumed that the inlet may not be sharp edged and could easily be rounded in the manufacturing process. Holes that have been drilled and spark eroded with a size of approximately 1 mm have been examined under both optical and scanning electron microscopes and the hole edges were found to be square to within 5 percent of the diameter. The hole entry conditions are thus those of simultaneous thermal and aerodynamic development. Pressure loss measurements made on the present full-coverage designs [1] have shown that flow separation must occur at the inlet with subsequent reattachment within the hole. This process has been investigated by Ward-Smith [8] and shown to occur within a length of approximately one hole diameter. Lloyd and Brown [5] have made detailed velocity and turbulence measurements in the entry region of a large diameter pipe (138 mm). They found a region of low velocity and very high turbulence in the wall region for the first pipe diameter. The velocity profile and turbulence profiles changed significantly over the first five diameters and much more slowly for larger

---

Contributed by the Gas Turbine Division of THE AMERICAN SOCIETY OF MECHANICAL ENGINEERS and presented at the 31st International Gas Turbine Conference and Exhibit, Düsseldorf, Federal Republic of Germany, June 8-12, 1986. Manuscript received at ASME Headquarters February 14, 1986. Paper No. 86-GT-225.

L/D. Consequently, holes with $L/D < 5$ may have a greater heat transfer per unit length than longer holes.

Reynolds Number. Andrews and Mkpadi [1], in considering the design principles and pressure loss characteristics of full coverage discrete hole film cooling, have shown, for atmospheric pressure tests and small hole sizes, that the flow in the hole may have Reynolds number well below 2000. Although at practical high-pressure operating conditions the Reynolds number will be increased in direct proportion to the pressure, there are many geometries where $\mathrm{Re} < 10^4$ at pressure. Almost all experimental data apply to atmospheric pressure conditions and the Reynolds numbers are in the transitional regime for practical hole sizes. It is considered that practical small hole sizes should be used as surface roughness effects may be important. For all types of hole manufacture the surface finish relative to the hole size will always result in a very rough pipe condition. Differences in the pressure loss characteristics of holes with different methods of manufacture have been found [1] and an associated difference in the heat transfer characteristics is likely.

Laminar Flow. For laminar flows, most of the investigations have been theoretical and reviewed by Shah and London [9]. This review shows that the predictions of Hornbeck [10] are the best for laminar flow heat transfer. His tabulated predictions have been curved fitted to give

$$\begin{aligned}\mathrm{Nu} = 3.66 \;&-\; 0.126(\mathrm{RePr}\,D/L)^{1/3} + 0.322(\mathrm{RePr}D/L)^{2/3} \\ &-\; 0.0146(\mathrm{RePr}D/L) + 0.00025(\mathrm{RePr}D/L)^{4/3}\end{aligned} \tag{1}$$

One of the few experimental investigations of laminar flow in the inlet region of pipes is that of Barozzi [11]. These data indicate that for $\mathrm{Re} > 150$ flow separation occurs at the sharp-edged hole inlet. Andrews and Mkpadi also reported that inlet flow separation was the only explanation for their pressure loss data for $\mathrm{Re} < 2000$ [1]. Flow separation is not taken into account in any theoretical treatment of laminar flow and hence the predictions of Hornbeck may need some modification. Table 1 compares the data of Hornbeck and Barozzi at an L/D of 1.9 and a Pr of 0.7. This shows that the experimental results are lower than the theoretical at low Re and higher at high Re. However, the differences are not large taking into account the 10 percent data scatter in the experimental results.

The influence of the flow separation at high Re may explain the higher experimental results in this region but the reason for the lower results at low Re is not known.

Turbulent Flow. Most experimental studies of pipe entry region heat transfer have been for turbulent flow and Table 2 summarizes some of the proposed correlations. The correlations used have been chosen to illustrate the range of data available while in no way claiming to be a complete review. Equations (6) and (7) result from a literature review rather than new work. In addition to these correlations Kutateladze [18] and Mills [19] have presented tabulated data for the mean heat transfer in tubes of different lengths. Kutateladze [18] found a dependence on the Reynolds number, but the overall heat transfer was lower than suggested by many of the equations on Table 2. The authors consider that the data of Mills [19] represent the most reliable extensive set of data available and Metzger and Cordoro [20] have obtained experimental results which agree within an error of ±7 percent with those of Mills.

Table 1 Laminar flow entry heat transfer $L/D = 1.9$

Re	Nu [10]	Nu [11]
200	6.3	4.9
300	6.9	5.3
400	8.0	6.5
500	8.7	7.6
1000	11.8	11.9
1500	13.4	17.4
2000	16.5	22.0

The data of Millis are correlated by

$$\mathrm{Nu} = 0.023\mathrm{Re}^{0.8}\mathrm{Pr}^{0.33}R_{\mathrm{Nu}} \tag{12}$$

Tabulated data for R_{Nu} were given by Mills [18] for a range of L/D. For a sharp-edged tube entry these data have been curve fitted by equations (13) for $L/D \leq 2$ and (14) for $L/D > 2$

$$R_{\mathrm{Nu}} = 0.13(L/D)^3 - 0.75(L/D)^2 + 1.04(L/D) + 2.24 \tag{13}$$

$$\begin{aligned}R_{\mathrm{Nu}} = \;&1 - 49.3(D/L)^4 + 58.6(D/L)^3 - 26.5(D/L)^2 \\ &+ 7.48(D/L)\end{aligned} \tag{14}$$

A comparison of the data of Mills with the correlations in Table 2 is made in Table 3 for a particular hole geometry used in the present test series of an L/D of 9.9 and a range of hole Reynolds numbers based on a hole diameter of 0.64 mm and a length of 6.35 mm. The coolant flow per unit surface area G was based on a hole array with a pitch-to-diameter ratio of 10.

Table 3 demonstrates a wide disagreement between the various equations for short hole heat transfer. Part of this may be due to differences in hole inlet conditions but the results of Trushin [16] and Le Grives et al. [17] are clearly much higher than the rest.

Unfortunately, neither paper gives full details of the experimental configuration and the data of Trushin have been correlated in a most unusual way. The correlation in Le Grives is quoted from an internal ONERA report, but the configuration is that of an array of holes drilled in a plate which is the situation for combustor and turbine blade cooling. A second feature of difference in Table 3 is that some correlations have a dependence on Re and this is strongest for the data of Trushin and Le Grives.

Hole Approach Flow Heat Transfer. Examination of the test configuration for investigators of tube entry heat transfer reveals that the approach surface to the hole has always been thermally insulated. Consequently, the correlations only apply to the internal hole heat transfer. However, all configurations of sharp-edged hole inlets and especially the present configuration of holes drilled in a metal plate must have a component of convective heat transfer on the surface normal to the hole inlet. The results of Le Grives et al. [17] include this com-

Nomenclature

A = heat transfer surface area per hole, m^2
A_H = internal hole surface area, m^2
A_p = plate surface area per hole $\sim X^2$, m^2
C_p = specific heat of metal plate, J/kgK
D = hole diameter, m
G = coolant flow per unit surface area, kg/sm^2
h_m = average heat transfer coefficient over the hole length, W/m^{2}K
h_∞ = hole heat transfer coefficient for fully developed tube flow, W/m^{2}K
L = hole length, m
m = mass of the metal wall per hole, kg
n = number of holes per unit surface area, m^{-2}
Nu = Nusselt number based on h_m
Nu_∞ = Nusselt number based on h_∞
Pr = Prandtl number
Re = Reynolds number
R_{Nu} = $\mathrm{Nu}/\mathrm{Nu}_\infty$, equations (12)-(14)
St = Stanton number
T_w = wall temperature, K
T_{wi} = initial wall temperature, K
X = hole pitch, m
τ = time constant, equation (21)

Table 2 Some correlations for pipe entry heat transfer

Author	Reference	Correlation	Equation
Latzko	[12]	$h_m/h_\infty = 1.11 \lvert \mathrm{Re}^{0.2}(D/L)^{0.8} \rvert^{0.275}$	(2)
Latzko	[12]	$h_m/h_\infty = 1+\dfrac{0.144\ \mathrm{Re}^{0.25}}{L/D}$	(3)
McAdams et al.	[13]	$h_m/h_\infty = 1+2.3D/L$	(4)
McAdams	[14]	$h_m/h_\infty = 1+7D/L$	(5)
McAdams	[14]	$h_m/h_\infty = 1+(D/L)^{0.7}$	(6)
Al-Arabi	[15]	$h_m/h_\infty = 1+\dfrac{1.683}{(L/D)^{0.577}}$	(7)
Trushin	[16]	$\mathrm{Nu} = 1.1\ \mathrm{Re}^{0.5} \mathrm{Re} \leq 10^4$ $\mathrm{Nu} = 0.0023\ \mathrm{Re}^{1.17}\ \mathrm{Re} > 10^4$ Nu, Re based on the hole length	(8) (9)
Le Grives et al.	[17]	$\mathrm{St} = \dfrac{0.51\ \mathrm{Re}^{-0.4}}{1+4.3 \times 10^{-2}(L/D)}$	(10)
	or	$\mathrm{Nu} = \dfrac{0.51\ \mathrm{Re}^{0.6}\mathrm{Pr}}{1+4.3 \times 10^{-2}(L/D)}$	(11)

Table 3 Comparison of predictions for h_m/h_∞

G, kg/sm^2		0.84	0.58	0.37	0.27	0.18
Re		4400	3100	1900	1400	900
Equation (2)	[12]	1.11	1.08	1.06	1.04	1.01
Equation (3)	[12]	1.14	1.13	1.11	1.11	1.09
Equation (4)	[13]	1.28	1.28	1.28	1.28	1.28
Equation (5)	[14]	1.84	1.84	1.84	1.84	1.84
Equation (6)	[14]	1.23	1.23	1.23	1.23	1.23
Equation (7)	[15]	1.50	1.50	1.50	1.50	1.50
Equation (8)	[16]	4.55	4.95	5.73	6.28	7.12
Equation (11)	[17]	2.46	2.64	2.91	3.10	3.37
Equation (14)	[19]	1.65	1.65	1.65	1.65	1.65

Table 4 Comparison of Le Grives et al. with equation (19) for $X/D=9.5$, $X=6.11$ mm, $D=0.64$ mm, and $L=6.35$ mm

Re	Nu equation (19)	$\dfrac{\mathrm{Nu}}{\mathrm{Nu}_\infty}$	Le Grives equation (11) Nu	$\dfrac{\mathrm{Nu}}{\mathrm{Nu}_\infty}$	Percent deviation of equation (19) from equation (11)
2000	22.9	2.28	23.9	2.38	−4.4
3000	30.1	2.16	30.5	2.19	−1.2
4000	36.7	2.10	36.2	2.07	+1.3
5000	42.8	2.04	41.4	1.98	+3.4
6000	48.6	2.01	46.2	1.91	+5.2
8000	59.5	1.95	54.9	1.80	+8.4
10000	69.7	1.19	62.8	1.72	+11.0

ponent and it is this that makes their results significantly higher than those of Mills [19].

Sparrow and co-workers [21, 22] have examined the heat transfer of this hole approach flow and the authors were the first to draw attention to the relevance of this work to combustor and blade cooling [1-3]. The two papers by Sparrow refer to a single hole [21] and a multihole [22] system and the two correlations are incompatible with each other. For the present purposes the correlation for multiholes has been used as given in equation (15) which was independent of pitch/diameter ratio

$$\mathrm{Nu} = hl/K = 0.881\ \mathrm{Re}^{0.476}\ \mathrm{Pr}^{1/3} \qquad (15)$$

where Re was based on the hole diameter and Nu on the surface dimension l defined by

$$l = \frac{\text{plate area}}{\text{hole pitch}} = X^2 - \pi D2/4 \qquad (16)$$

For small hole sizes it can be seen from equation (16) that l is approximately the same as the hole pitch X. It may be shown from equations (15) and (16) that the heat removed by the coolant Q is related to the number of holes per unit surface area n and the hole diameter D by

$$Q = \mathrm{const}\frac{\Delta T}{(nD)^{0.476}} \qquad (17)$$

In previous work full coverage discrete hole wall cooling [1-3] the authors have treated the wall heat transfer as the summation of equations (13) or (14) and (15). To compare these results with those of Le Grives, equation (15) has been transformed into the same Nu definition as equation (13) or

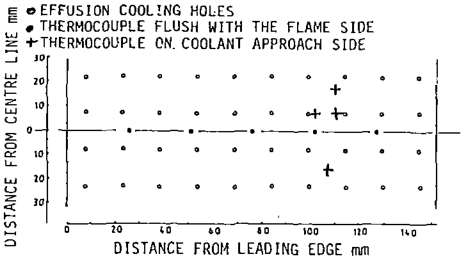

Fig. 1 Thermocouple arrangements

(14). This involves assuming that all the heat transfer occurs in the internal hole wall surface area and equation (18) results

$$\mathrm{Nu}=(0.881\ \mathrm{Re}^{0.476}\ \mathrm{Pr}^{1/3})(X/\pi L) \qquad (18)$$

Equations (18) and (13) or (14) may now be summed as the Nu have the same definition. A comparison has been made with the correlation of Le Grives [16] for a multihole geometry of $X=6.11$, $D=0.64$ mm and $L=6.35$ mm and equation (19) represents the overall result.

$$\mathrm{Nu}=(0.27\ \mathrm{Re}^{0.476}+0.023\ \mathrm{Re}^{0.8}\ R_{\mathrm{Nu}})\mathrm{Pr}^{1/3} \qquad (19)$$

This shows that the two exponents for Re are significantly different and this explains why there should be a Re dependence of the overall short hole heat transfer. Table 4 presents the comparison of equations (19) and (11) using equation (14) for R_{Nu}. This shows that there is a quite good agreement between the two predictions but that there is a difference in their dependence on Re. The authors have shown that for many coolant flow rates the hole approach flow heat transfer is much larger than the internal hole heat transfer [2, 3].

This review has shown that there is a scarcity of heat transfer data for the overall heat transfer in air flow through a multihole plate as used in combustor and turbine blades. The correlation of Sparrow [22] was based on a relatively small number of geometries. The predictions of the film cooling heat transfer coefficient made by the authors [2, 3, 23] are entirely dependent on the accuracy of equations (13), (14), and (15). Consequently, it was decided to develop a technique for the direct determination of the overall wall heat transfer coefficient.

Experimental Techniques

A 152 mm square Nimonic 75 test wall was used with an array of equispaced equal diameter holes. This was bolted to an internally insulated air supply plenum chamber. The test geometries used in the associated program on full coverage discrete hole film cooling [1-3] and impingement cooling [24, 25] were used in the present work. Each test plate was instrumented with at least five type K grounded junction mineral insulated thermocouples vacuum brazed to the exit side of the test plate on the center line of the plate midway between holes. In addition some test plates had thermocouples brazed to the feed side of the test plate. The thermocouple arrangement is shown in Fig. 1.

Three experimental techniques A, B, and C were investigated for the determination of the overall hole heat transfer coefficient. Technique A was a steady-state heat balance similar to that used for impingement heat transfer [24, 25]. The test plate was placed on an insulated electrical heater with holes within the heater for the outflow of air and a subsequent exhaust plenum chamber. Three problems arose with this technique. The first was that the heated surface was bolted to the test plate and heat conduction to the flanges and outer casing of the air supply plenum resulted in an additional heat loss. This was not present in impingement cooling as the impingement gap, maintained with PTFE inserts, was insulated from the plenum chamber. A second problem was that the air passing through the heater holes may remove heat internally from the heater so that all the electrical energy may not be transferred as heat into the test plate. The heater material was made of a good insulator which minimized this effect. The third problem was that for each hole geometry a new heater was required to accommodate the hole configuration. To overcome these problems two transient heat transfer techniques, B and C, were developed.

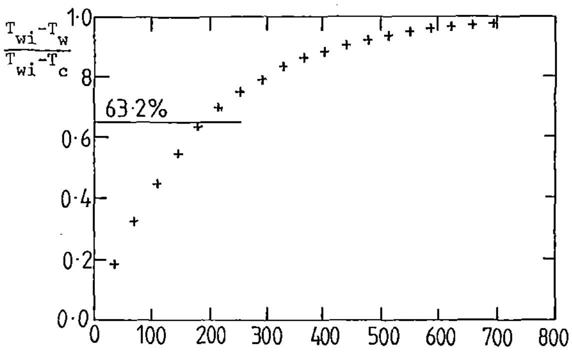

Fig. 2 A typical transient response test record

Technique B used the same heater with holes as in technique A. However, this was only used to heat up the plate to a temperature of approximately 80°C under steady-state coolant flow conditions. Once a stable temperature had been achieved the whole plenum chamber was hoisted well away from the plate heater giving an instantaneous step change in the heat supply. The fall in temperature of the test plate was recorded as a function of time using a fifty-channel multiplexer into a BBC microcomputer. The heat transfer in this situation is governed by the classic first-order differential equation

$$T_w+\tau\frac{dT_w}{dt}=T_{wi} \qquad (20)$$

where τ is the time constant defined by

$$\tau=\frac{mC_p}{h_m A} \qquad (21)$$

The determination of h_m is thus transformed into the measurement of τ. The solution of equation (20) for a step change is given by

$$\frac{T_{wi}-T_w}{T_{wi}-T_c}=1-e^{-t/\tau} \qquad (22)$$

If the initial, T_{wi}, and final plate temperatures ($T_w=T_c$) are reliably known then τ can be determined as the time at which $t=\tau$, when the temperature change is 63.2 percent of the total change. However, there is a certain data scatter in the measured results and some uncertainty in T_{wi} and T_c which makes this technique subject to a significant uncertainty. A smooth experimental curve is required for the measured data points and this requires a knowledge of τ. A typical transient response is shown in Fig. 2. A simpler procedure which enables any data scatter and uncertainty in the initial and final conditions to be taken into account is to use equation (20) directly using successive temperature data points to calculate the local change of temperature with time, as shown in equation (23). Each pair of successive temperatures

$$T_w=T_{wi}-\tau\frac{\Delta T_w}{\Delta t} \qquad (23)$$

was used to calculate $\Delta T_w/\Delta t$ and this was associated with the mean of the two temperatures. This mean temperature T_w was then plotted against $\Delta T_w/\Delta t$ and a least-square fit was made to the data to yield the gradient which was τ. This data analysis was carried out on the microcomputer and interfaced

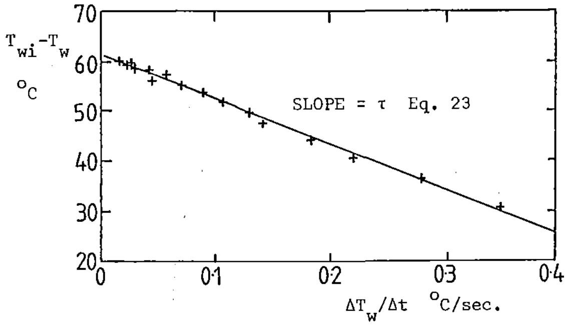

Fig. 3 Transient cooling using technique B

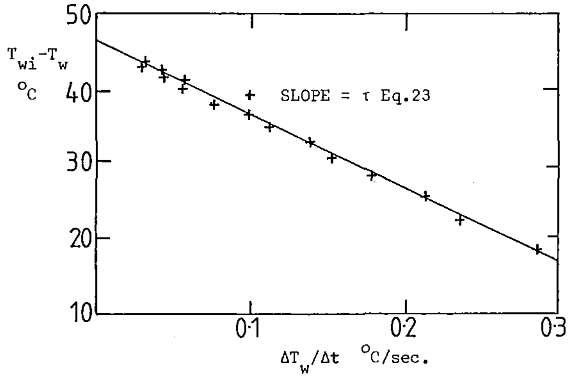

Fig. 4 Transient cooling using technique C

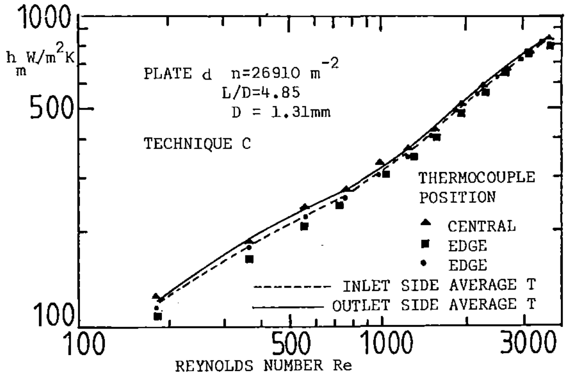

Fig. 5 Influence of thermocouple position on *h*

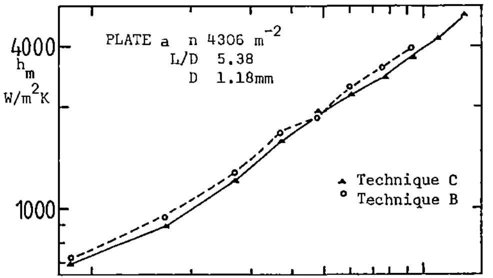

Fig. 6 Influence of the method of electrical heating

Table 5 Test hole geometries

Plate	n, m^{-2}	D, mm	L, mm	L/D	X, mm	X/D	Manufacture technique
a	4306	1.18	6.35	5.38	15.2	12.9	Drilled
b	26910	0.64	6.35	9.92	6.10	9.5	Spark eroded
c	26910	0.90	6.35	7.05	6.10	6.8	Drilled
d	26910	1.31	6.35	4.85	6.10	4.7	Drilled

with a graphics subroutine that plotted the graph and calculated τ and h_c. A typical output graph is shown in Fig. 3.

This measurement technique B overcame the first two disadvantages of the steady-state technique A. However, it still required individual heater geometries for each hole geometry. To overcome this problem the very simple technique C was used which consisted of heating the test plate in the absence of an air flow using a conventional insulated mat heater. Prior to this heating the air flow controls were set to give a desired flow rate so that once the plenum chamber was hoisted one valve was opened and the coolant flow established. This may give some uncertainty in the initial cooling period as there will be a delay time for the establishment of steady flow. However, due to the much longer time constant of the test wall this is unlikely to be a serious problem. Figure 4 shows the transient results using this technique C, for the same condition as in Fig. 3, and there is little difference between the two. Consequently, for most of the present work technique C was used.

All these measurement techniques rely on the plate being uniform in temperature. Comparison of the individual thermocouple temperatures during the transient tests showed that any temperature differences were small. For test geometries with thermocouples on the inlet and exit plate surfaces there was no significant temperature difference as shown in Fig. 5, by the agreement in the values for h_m using different thermocouples. This is in agreement with the findings of the more complex film cooling situation where even at high temperatures the test plate was at a very uniform temperature with maximum temperature differences of less than 3 percent of the mean plate temperature [2]. However, it was found that there were small random differences between thermocouples and a more accurate transient response was obtained if a time constant was found for each individual thermocouple rather than using the mean plate temperature at each time interval. Differences in the time constants and hence h_m produced in this way were small as shown in Fig. 5. For most of the results the thermocouple at the center of the test plate was used. This reduced any possible edge conduction losses which may be responsible for the slightly lower heat transfer coefficients of other thermocouples.

Test Geometries

A large-scale test program is in progress for a range of hole geometries. The initial results are presented here for the four geometries detailed in Table 5. Plate *a* consisted of a 10 × 10 square hole array on the present 152 mm square test size and plates *b*, *c*, and *d* were 25 × 25 hole arrays. Plates *a* and *b* had approximately the same total hole area and hence flow pressure loss characteristics. Plates *c* and *d* had an increased hole size relative to plate *b* and plate *d* had a similar *L/D* to plate *a*.

Experimental Results

At each coolant flow rate a transient test was performed and a range of coolant flow rates per unit surface area G from 0.1 to 1.7 kg/sm² were investigated. Figure 6 shows the heat transfer coefficient for plate *a* as a function of G for the transient cooling techniques B and C. The differences are small and mainly associated with the data scatter in Figs. 3 and 4. All other results used the unperforated blank heater system, technique C, and were based on the center thermocouple transient response.

All the four test geometries in Table 5 are compared in Fig. 7 using the conventional Nu/Pr$^{0.33}$ versus Re correlation procedure. Plates *a* and *d*, which have a similar *L/D*, but different hole diameters and hole pitch have similar results, except for the lowest Re data point for plate *a*. Comparison of plates *b*, *c*, and *d* shows the influence of increasing *L/D* is to

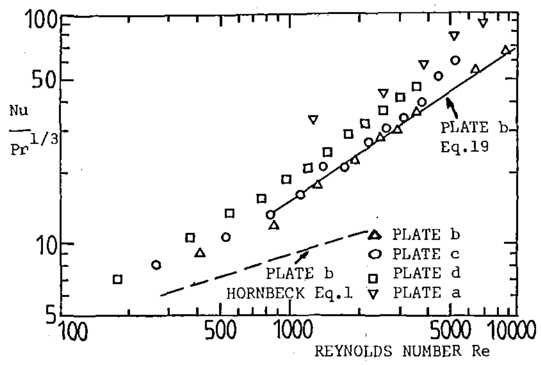

Fig. 7 Heat transfer as a function of the hole Re

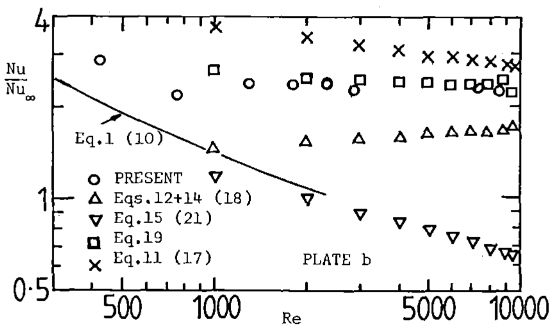

Fig. 9 Overall hole entrance heat transfer enhancement as a function of Re

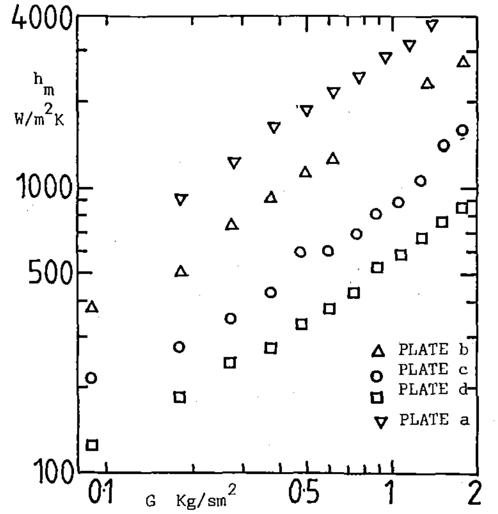

Fig. 8 h_m as a function of G for the four test plates

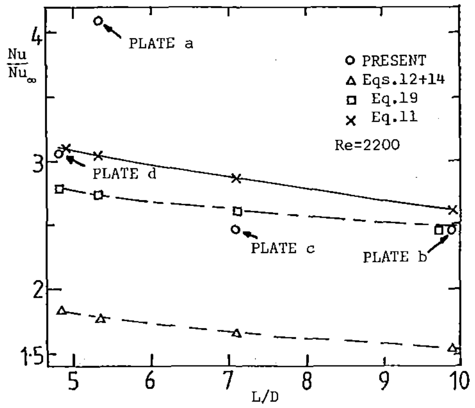

Fig. 10 Overall heat transfer enhancement as a function of *L/D* for Re = 2200

decrease the Nusselt number for a constant Re. However, this paradoxical result may be explained by the implications of the variation of *L/D* by using different hole diameters. As *L/D* was increased, a lower air mass flow was required to achieve a given Re. Figure 8 shows the same data plotted as a heat transfer coefficient h_m as a function of *G*. This shows that more heat transfer occurred as *L/D* was increased for a constant hole pitch. Comparison of plate *a* with *b*, *c*, and *d* shows that the smaller number of holes has increased the heat transfer coefficient at a fixed mass flow rate. One cause of this is the higher hole Re for the larger diameter holes. The influence of the number of holes is the subject of an extensive study by the authors.

Figure 7 also includes a comparison for plate *b* of the present measurements with the prediction of equation (19), evaluated for plate *b* in Table 4. The agreement is quite good and hence the agreement with the Le Grives correlation will also be reasonable, as shown in Table 4. This fair agreement gives strong support to the film convective heat transfer predictions of the authors [2, 3, 6] for discrete hole film cooling. These essentially rely on the accuracy of equation (19) in the heat balance procedure used to calculate the film heat transfer coefficient. Figure 7 also compares the laminar flow prediction of equation (14) for plate *b*. This shows an underprediction indicating that the hole approach heat transfer is still significant even for laminar flow.

Figure 9 compares the ratio of Nu to Nu_∞ as a function of Re for plate *b*. There is a small but significant influence of Re and reasonable agreement with the predictions of equation (19) detailed in Table 4 for plate *b*. The influence of Re is entirely due to the heat transfer on the hole approach surface which has a different dependence on Re than does Nu_∞ for a tube as shown in equation (19). The laminar flow correlation of the predictions of Hornbeck [10], equation (14), underestimates the heat transfer, except at very low Re. For a fixed Re of 2200, Fig. 10 shows the influence of *L/D* on Nu/Nu_∞. The ratios are greater than 2 at all *L/D* and increase as *L/D* is reduced. Comparison with the short hole data of Mills [18] is made in Fig. 10 and this shows that the present results are much higher. The differences emphasize the importance of the hole approach flow heat transfer, which is the dominant process at all *L/D* of relevance to gas turbine film cooling applications.

The magnitude of the differences between the present results and conventional short hole heat transfer correlations have importance in terms of turbine blade and combustion wall heat transfer prediction procedures. For short holes of an *L/D* approximately 4, which is a typical maximum for turbine blades, the present results indicated that the use of conventional tube entrance heat transfer correlations alone may underestimate the overall heat transfer due to the presence of the hole by a factor in excess of 2. The significance of this may be demonstrated by the extensive efforts currently in progress to understand the influence of rotational effects on heat transfer [26, 27]. A decrease in heat transfer of up to 30 percent has been found [26] with a 10 percent reduction as a blade passage average. These changes require the modification of existing computer prediction procedures for blade temperatures [26]. Only in the work of Wadia and Nealy [4] has the significance of the hole approach heat transfer been realized for turbine blades. To predict the influence of the present results for the heat transfer coefficient on the blade overall heat transfer requires h_m to be multiplied by the ratio of the hole to plate surface areas. This results in predicted changes in the overall blade surface heat transfer coefficient in excess of those found for centrifugal effects.

Conclusions

1 Most experimental investigations of short hole heat transfer have ignored the approach surface heat transfer.

2 The correlation of Le Grives et al. [16] gives good agreement with the combined approach surface heat transfer correlation of Sparrow [22] and the internal hole heat transfer data of Mills [19]. At present these correlations are the best data available for gas turbine combustor wall and turbine blade cooling applications.

3 A simple transient cooling method has been developed and shown to give reliable results for the combined hole approach and internal heat transfer.

4 Initial results for three test geometries confirm the importance of the hole approach heat transfer, which is the dominant heat transfer mode for all hole *L/D* of relevance to gas turbine film cooling.

5 The present initial results are in fair agreement with the prediction based on the summation of the hole approach heat transfer correlation of Sparrow [22] and the internal hole heat transfer data of Mills [19].

Acknowledgments

We would like to thank the U.K. Science and Engineering Research Council for a research grant in support of this work (GR/C/59192). We would like to thank Ruston-GEC Gas Turbines for supporting M. C. Mkpadi and A. A. Asere and for manufacturing the test geometries. Technical discussions with M. F. Cannon of Ruston-GEC Gas Turbines have been most useful.

References

1 Andrews, G. E., and Mkpadi, M. C., "Full Coverage Discrete Hole Wall Cooling: Discharge Coefficients," ASME Journal of Engineering for Gas Turbines and Power, Vol. 106, 1984, pp. 183–192.

2 Andrews, G. E., Gupta, M. L., and Mkpadi, M. C., "Full Coverage Discrete Hole Wall Cooling: Cooling Effectiveness," ASME Paper No. 84-GT-212, 1984.

3 Andrews, G. E., Asere, A. A., Gupta, M. L., and Mkpadi, M. C., "Full Coverage Discrete Hole Film Cooling: The Influence of Hole Size," ASME Paper No. 85-GT-47, 1985.

4 Wadia, A. R., and Nealy, D. A., "Development of a Design Model for Airfoil Leading Edge Film Cooling," ASME Paper No. 85-GT-120, 1985.

5 Lloyd, S., and Brown, A., "Fluid Flow and Heat Transfer Characteristics in the Entrance Region of Circular Pipes," ASME Paper No. 85-GT-121, 1985.

6 L'Ecuyer, M. R., and Soechting, F. O., "A Model for Correlating Flat Plate Film Cooling Effectiveness for Rows of Round Holes," AGARD CPP390, 1985, Paper No. 18.

7 Hey, N., Lampard, D., and Saluja, C. L., "Effects of Cooling Films on the Heat Transfer Coefficient on a Flat Plate With Zero Mainstream Pressure Gradient," ASME Journal of Engineering for Gas Turbines and Power, Vol. 107, 1985, pp. 99–104.

8 Ward-Smith, A. J., *Pressure Losses in Ducted Flows*, Butterworths, 1971.

9 Shah, R. K., and London, A. L., *Advances in Heat Transfer. Laminar Flow Forced Convection in Ducts*, Academic Press, 1978.

10 Hornbeck, R. W., "An All Numerical Method of Heat Transfer in the Inlet of a Tube," ASME Paper No. 65-WA/HT-36, 1965.

11 Barozzi, G. S., Dumas, A., and Pompoli, R., "The Influence of an Abrupt Convergence on Heat Transfer in Circular Ducts," *Int. J. Heat and Fluid Flow*, Vol. 3, No. 1, 1982.

12 Latzko, H., and Augew, Z., *Maths U. Mech.*, Vol. 1, 1921, pp. 268–290 (NACA TM 1068, 1944).

13 McAdams, W. H., Kennel, W. E., and Adams, J. N., "Heat Transfer to Superheated Steam at High Pressure," *Trans. ASME*, Vol. 72, 1950, pp. 421–428.

14 McAdams, W. H., *Heat Transmission*, 3rd ed., 1954, p. 225.

15 Al-Arabi, M., "Turbulent Heat Transfer in the Entrance Region of a Tube," *Heat Transfer Engineering*, Vol. 3, 1982, pp. 76–83.

16 Trushin, V. A., "Results of Analysis of Experimental Data From Study of Heat Transfer in Holes Typical for Turbine Blade Perforations by the Local Similarity Method," *Soviet Aeronautics*, Vol. 23, 1980, pp. 120–122.

17 Le Grives, E., Nicolas, J. J., and Genot, J., "Internal Aerodynamics and Heat Transfer Problems Associated to Film Cooling of Gas Turbines," ASME Paper No. 79-GT-57, 1979.

18 Kutateladze, S. S., and Borishauskii, *A Concise Encylopaedia of Heat Transfer* (Russian Trans. by J. B. Arthur), Pergamon Press, p. 109.

19 Mills, A. F., "Experimental Investigation of Turbulent Heat Transfer in Thermal Entrance Region of a Circular Conduit," *J. Mech. Eng. Sci.*, Vol. 4, No. 1, 1962.

20 Metzger, D. E., and Cordoro, J. V., "Heat Transfer in Short Tubes Supplied From a Cross Flowing Stream," ASME Paper No. 79-WA/H-16, 1979.

21 Sparrow, E. M., and Gurdol, U., "Heat Transfer at an Upstream Facing Surface Washed by Fluid on Route to an Aperture in the Surface," *Int. J. Heat and Mass Transfer*, Vol. 24, 1981, pp. 851–857.

22 Sparrow, E. M., and Carranco Ortiz, M., "Heat Transfer Coefficients for the Upsteam Face of a Perforated Plate Positioned Normal to an Oncoming Flow," *Int. J. Heat Mass Trans.*, Vol. 25, 1982, pp. 127–135.

23 Andrews, G. E., Gupta, M. L., and Mkpadi, M. C., "Combined Radiative and Convective Heat Transfer in an Enclosure," 1st U.K. National Heat Transfer Conference, I.Chem.E. Symposium Series No. 86, 1984, pp. 929–988.

24 Andrews, G. E., and Hussain, C. I., "Impingement Cooling of Gas Turbine Components," *High Temperature Technology*, Vol. 2, 1984, pp. 99–106.

25 Andrews, G. E., and Hussain, C. I., "Full Coverage Impingement Heat Transfer: The Influence of Impingement Jet Size," 1st U.K. National Heat Transfer Conference, 1984, I.Chem.E. Symposium Series No. 86, pp. 1115–1124.

26 Clifford, R. J., "Rotating Heat Transfer Investigations on a Multipass Cooling Geometry," AGARD CPP-390, Paper No. 2, Bergen, 1985.

27 Morris, W. D., and Hargraves, S. P., "Local and Mean Heat Transfer on the Leading and Trailing Surfaces of a Square Sectioned Duct Rotating in the Orthogonal Mode," AGARD-CPP-390, Paper No. 3, Bergen, 1985.

M. Menguturk
Associate Professor,
Mechanical Engineering Department.

D. Gunes
Assistant Professor,
Civil Engineering Department.

M. Erten
Graduate Student,
Mechanical Engineering Department.

Bogazici University,
Istanbul, Turkey

E. F. Sverdrup
Advisory Engineer,
Westinghouse Research and Development,
Pittsburgh, PA

Multistage Turbine Erosion

This paper presents a computer package developed to calculate the blade erosion rates in multistage turbines that use particle-laden hot expansion gases. This package is an extension of the single-stage erosion code presented in some of our earlier papers. The present package calculates gas flow and particle trajectories in each stage. The calculated particle outlet conditions of a given stage are processed statistically to generate the particle inlet conditions to the next stage enabling trajectory and erosion calculations to be advanced beyond a single turbine stage. The package allows erosion predictions to be obtained either based on the semi-empirical erosion formula presented earlier or by using an improved model which relies upon direct interpolation of available experimental data. This computer package has been applied to a four-stage electric utility gas turbine. It has been found that, in addition to the first-stage rotor blades, as indicated by our earlier studies, the second-stage rotor and the second and third-stage stator blades may also be exposed to critical erosion damage.

Introduction

The escalating cost of petroleum, together with the uncertainties in its availability, has directed attention to coal as an alternative source of energy for future power plants. In order for coal to find wide use as a petroleum substitute, more efficient and nonpolluting ways of obtaining power from coal must be found than the traditional system of burning pulverized coal in steam turbine plants. In this regard, pressurized fluidized-bed combustion and low-Btu coal gasification processes are under consideration for use in combined-cycle plants where part of the power will be generated by passing the combusted coal gas through a gas turbine.

One of the problems associated with this scheme is that the particulate matter contained in the hot expansion gas is likely to cause turbine blade erosion. Unless the gas is adequately filtered, significant amounts of particles ranging in size from 1 to 10 μm can still pass through and enter the turbine. These particles may erode the blade surfaces and result in an unacceptably short operating life or mechanical failure without any warning.

The trivial solution to this problem is to reduce the particulate content to negligible proportions by extensive cleaning and filtration. However, hot-gas particle filters and separators are very expensive, and therefore, it is desirable to know in advance how much cleaning is required for economic plant operation. It is also desirable to achieve further reduction in filtration costs by taking special design precautions to protect turbines against particle erosion.

The ability to calculate theoretically turbine erosion is vital to the determination of the particle filtration requirements and the development of an erosion resistant turbine design.

In an earlier paper [1] we presented a computer code that calculates the trajectories of particles through a turbine stage and estimates, on the basis of a semi-empirical erosion formula, the resulting erosion damage on blade surfaces. Application of this code to the first stage of a four-stage gas turbine showed that critical wear occurs at the rotor trailing edge, while the rotor leading edge and the stator trailing edge are also subject to high erosion rates. It was estimated that cleaning of the turbine expansion gas to a particulate concentration of 0.005 grams per standard cubic meter with particles larger than 6 μm diameter effectively removed should give satisfactory blade life from an erosion standpoint.

It is not clear whether critical erosion indeed occurs in the first stage of a turbine. It is possible for the following stages to be exposed to higher rates of erosion due to increased deflection of particles from the gas streamlines after repeated impacts with blade surfaces. Therefore, the filtration requirement determined on the basis of first-stage erosion predictions may be unreliable. A more comprehensive analysis that considers all the stages is needed. Extension of the erosion prediction capability to cover the entire machine is required also for development of an erosion-resistant turbine.

This paper presents a computer package for calculation of blade erosion rates in multistage turbines. This package is an extension of the single-stage erosion program presented earlier [1]. The present package calculates gas flow and particle trajectories in a given stage and processes the calculated particle outlet conditions statistically to generate the particle inlet conditions to the next stage thus enabling trajectory and erosion calculations to be advanced to succeeding stages. The semi-empirical erosion formula [1] with constant coefficients is restricted to a short temperature range. To eliminate this deficiency the present package is also equipped with an improved erosion model which relies upon direct interpolation of available experimental data obtained in the temperature range relevant to the multistage turbine operation.

Contributed by the Gas Turbine Division for publication in the JOURNAL OF ENGINEERING FOR GAS TURBINES AND POWER. Manuscript received by the Gas Turbine Division October 18, 1985.

Analysis

The basic approach used in the analysis is to isolate a single blade passage in each row of blades and consider the gas-particle flow over the midstreamsurface of this "characteristic" passage as representative of the total gas-particle flow through the entire row. It is assumed that variations of geometry and flow in the spanwise direction may be neglected.

The program package developed consists of three computer programs: TSONIC, TPART, and TPER that calculate, respectively, the gas flow in the characteristic blade passages, the trajectories of particles, and the blade erosion due to particle impacts with the blade surfaces.

The midstreamsurface gas flow solution of each characteristic passage is obtained from the two-dimensional potential flow program TSONIC developed by Katsanis [2]. In the gas flow calculations row interactions are neglected and the flow entering the characteristic passage is assumed to be steady and uniform. The calculated velocities and densities at the grid points of the finite-difference mesh used are stored for subsequent use in the trajectory calculations.

The TPART program, which is an extended version of the code presented in our earlier paper [1], calculates the trajectories of particles entering the characteristic passages. Trajectories are obtained by solving the following equations which govern the inertial motions of particles against the drag resistance exerted by the gas flow [1]

$$\begin{aligned} \ddot{x} &= G(W_x - \dot{x}) \\ \ddot{\theta} &= \frac{G}{r}\,(W_\theta - r\dot{\theta}) - \frac{2\dot{r}}{r}\,(\dot{\theta}+\omega) \\ \ddot{r} &= G(W_r - \dot{r}) + r(\dot{\theta}+\omega)^2 \end{aligned} \tag{1}$$

where

$$G = \frac{3}{4}\,\frac{\mu C_D \mathrm{Re}}{d_p^2 \rho_p} \tag{2}$$

and

$$\mathrm{Re} = \frac{\rho d_p |\mathbf{V}_g - \mathbf{V}_p|}{\mu} \tag{3}$$

In the above a relative coordinate system is used in which the axial and tangential coordinates x and θ, respectively, are measured from the leading edge of the blade under consideration. The drag coefficient C_D is estimated from Morsi and Alexander's experimental correlations [3].

Equations (1) are integrated numerically for each particle entering a characteristic passage. The coefficients G, W_x, W_θ, and W_r are obtained at each integration step by interpolating the gas flow solution stored. The actual flow of particles of given diameter and density is simulated by trajectories of 100 particles calculated through each characteristic passage. Particles are assumed to be entering the first-stage stator row with uniform tangential distribution and at velocities equal to the inlet gas velocity. Particle inlet conditions for the remaining blade rows are determined based on their calculated conditions of exit from the preceding row together with some statistical considerations to account for relative rotation of successive rows. Addition of the particle exit velocity and the blade relative velocity vectors gives the particle inlet velocity to the next row. However, due to rotation, inlet tangential position is statistically random. Therefore, to each particle leaving a blade row a tangential position is assigned before the next row by using a random number generating routine.

In the earlier version of the TPART program particle equations of motion were integrated by using the Hamming predictor corrector algorithm [4], which is essentially a fourth-order Runge-Kutta scheme. The present version incorporates a new integration method, PES (Piecewise Exact Solution) method, which is about 20 times as fast as Hamming's algorithm in solving equations (1).

In the PES method of integration we seek an exact solution to an approximate form of the governing equation set in small time intervals. In a given time interval equations (1) may be linearized and uncoupled as follows

$$\left.\begin{aligned} \ddot{r} + A_1\dot{r} + B_1 r &= C_1 \\ \ddot{\theta} + A_2\dot{\theta} &= C_2 \\ \ddot{x} + A_1\dot{x} &= C_3 \end{aligned}\right\} t_{n-1} \leq t \leq t_n \tag{4}$$

where the subscripts $(n-1)$ and (n) refer, respectively, to the initial and final points of the nth integration step and

$$\begin{aligned} A_1 &= G_{n-1} \\ A_2 &= \left(G + \frac{2\dot{r}}{r}\right)_{n-1} \\ B_1 &= -(\dot{\theta}_{n-1} + \omega)^2 \\ C_1 &= (GW_r)_{n-1} \\ C_2 &= \left(\frac{G}{r}\,W_\theta\right)_{n-1} - 2\left(\frac{\dot{r}}{r}\right)_{n-1}\omega \\ C_3 &= (GW_x)_{n-1} \end{aligned} \tag{5}$$

The exact solution to equations (4) in the current time interval, i.e., the piecewise exact solution to equations (1), is given by

$$\begin{aligned} r &= K_1 e^{m_1\Delta t} + K_2 e^{m_2\Delta t} + \frac{C_1}{B_1} \\ \theta &= K_3 e^{-A_2\Delta t} + K_4 + \frac{C_2}{A_2}\,\Delta t \\ x &= K_5 e^{-A_1\Delta t} + K_6 + \frac{C_3}{A_1}\,\Delta t \end{aligned} \tag{6}$$

where

$$m_{1,2} = \frac{-A_1 \mp \sqrt{A_1^2 - 4B_1}}{2}$$

Nomenclature

C_D = viscous drag coefficient
d_p = particle diameter, m
e = metal recession rate, m/s
E = total erosion damage, m^3/kg
G = coefficient defined by equation (2)
$K_{1,2}$ = ductile and brittle mode amplitudes of erosion, $(\mathrm{m}^3/\mathrm{kg})/(\mathrm{m/s})^{2.5}$
m = velocity exponent of erosion
r = radial coordinate, m
Re = particle Reynolds number defined by equation (3)
St = Stokes number
$\mathbf{V}_g$ = gas velocity vector, m/s
$\mathbf{V}_p$ = particle velocity vector, m/s
W_x = axial component of relative gas velocity vector, m/s
W_r = radial component of relative gas velocity vector, m/s
W_θ = tangential component of relative gas velocity vector, m/s
x = axial coordinate, m
β = particle impact angle, deg
β_0 = erosion reference angle, deg
θ = tangential coordinate, rad
μ = viscosity, $\mathrm{N\text{-}s/m}^2$
ρ = gas density, $\mathrm{kg/m}^3$
ρ_p = particle density, $\mathrm{kg/m}^3$
ω = rotational speed, rad/s

Table 1 Erosion coefficients estimated for coal ash particles eroding typical blade materials for two different maximum erosion angles [1] ($m = 2.5$)

$\beta_{\max}$, deg	β_0, deg	Erosion coefficients, $m^3/kg/(m/s)^{2.5}$	
		K_1	K_2
20	22.7	6.51×10^{-14}	1.87×10^{-14}
90	90	0	5.60×10^{-14}

$$K_1 = \frac{\dot{r}_{n-1} - r_{n-1} m_2 + \dfrac{C_1}{B_1} m_2}{m_1 - m_2}$$

$$K_2 = \frac{\dot{r}_{n-1} - r_{n-1} m_1 + \dfrac{C_1}{B_1} m_1}{m_2 - m_1}$$

$$K_3 = \frac{C_2}{A_2^2} - \frac{\theta_{n-1}}{A_2} \tag{7}$$

$$K_4 = \theta_{n-1} - \frac{C_2}{A_2^2} + \frac{\dot{\theta}_{n-1}}{A_2}$$

$$K_5 = \frac{C_3}{A_1^2} - \frac{\dot{x}_{n-1}}{A_1}$$

$$K_6 = x_{n-1} - \frac{C_3}{A_1^2} + \frac{\dot{x}_{n-1}}{A_1}$$

$$\Delta t = t - t_{n-1}$$

and $\Delta t_n = t_n - t_{n-1}$ represents the current time interval.

In order to advance integration a step further, the solution at $\Delta t = \Delta t_n$ is used as an initial condition for the next step.

When there is an impact with the blade surface, the velocity, angle, and location of impact are stored for erosion calculations and the trajectory calculation is continued with rebound conditions obtained from the following experimental correlations

$$\frac{V_{n2}}{V_{n1}} = 1.0 - 0.41598\beta_1 - 0.4994\beta_1^2 + 0.292\beta_1^3$$
$$\frac{V_{t2}}{V_{t1}} = 1.0 - 2.12\beta_1 + 3.0775\beta_1^2 - 1.1\beta_1^3 \tag{8}$$

where the subscripts n and t refer to the components of particle velocity normal and tangential to the blade surface, respectively, and the subscripts 1 and 2 to velocities before and after the impact, respectively. These correlations were obtained by Tabakoff and Hamed [5] for erosive quartz and alumina particles impacting stainless steel, titanium, and aluminum alloys at high speeds.

Erosion estimates are obtained by the TPER program, which is equipped with two different routines to process the impact data stored. In the first routine, erosion per particle impact with blade surface is calculated by using the semi-empirical formula presented earlier [1]

$$E = K_1 (V \cos\beta)^m \sin n\beta + K_2 (V \sin\beta)^m \quad \text{for } \beta \le \beta_0$$
$$E = K_1 (V \cos\beta)^m + K_2 (V \sin\beta)^m \quad \text{for } \beta \ge \beta_0 \tag{9}$$

where $n = \pi/2\beta_0$. In this formula the coefficients K_1 and K_2 of ductile and brittle erosion modes, the velocity exponent m, and the reference erosion angle β_0 must be determined experimentally.

In the second routine, erosion is calculated by direct interpolation of the experimental data obtained for the same particles and blade material under the range of conditions typical of the actual operation. This approach requires carefully controlled laboratory tests but is needed for accurate assessment of turbine erosion.

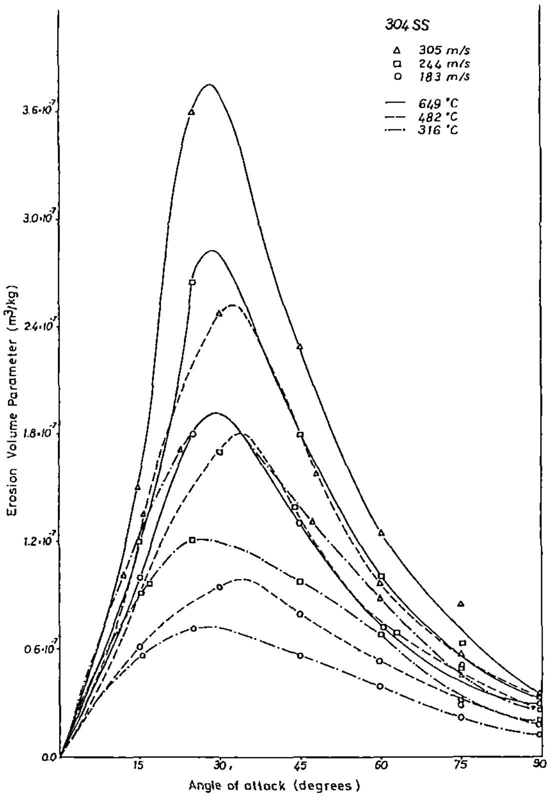

Fig. 1 Erosion volume parameter as a function of angle of attack for blade material 304 stainless steel

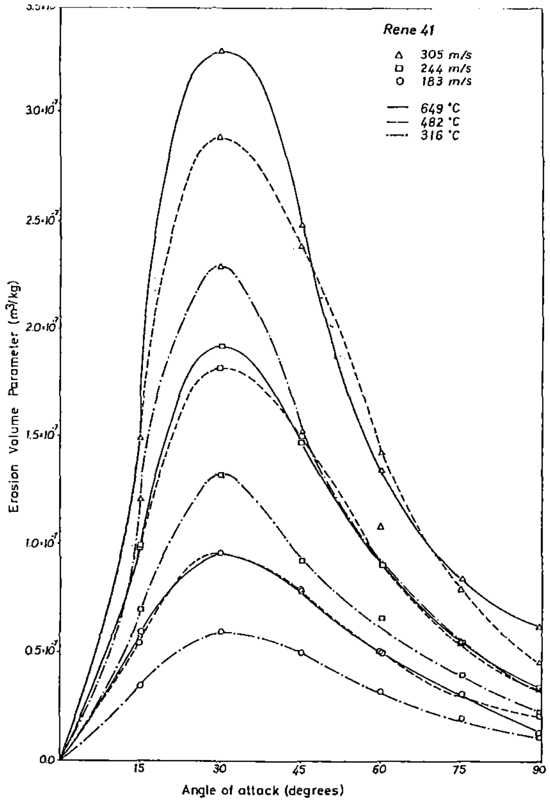

Fig. 2 Erosion volume parameter as a function of angle of attack for blade material Rene 41

Four different blade materials are considered in the application discussed in the next section. The erosion rates of the first two materials, also considered in our original paper [1], were calculated from equations (9). One of these materials is ductile having a maximum erosion angle of 20 deg and the other is brittle with minimum erosion resistance at 90 deg. The experimental data used in these calculations are taken from Finnie et al. [6]. Table 1 gives the model coefficients extrapolated to coal ash erosion from the experimental data for silicon carbide particles eroding a nickel cobalt alloy with 99 percent (Ni + Co). In extending the model to coal ash particles it was assumed that silicon carbide particles are approximately 25 times as erosive as ash particles [1].

The remaining two materials considered are 304 Stainless Steel and Rene 41. Figures 1 and 2 show the experimental coal ash erosion data for these materials at high temperatures [7, 8]. The erosion rates of these materials were directly calculated from these data.

Application

The multistage turbine erosion program package developed in this study was applied to a four-stage electric utility gas turbine rated to drive a 65 MW generator. The first-stage stator and rotor blade erosion rates of the same turbine calculated by the single-stage erosion program were previously reported [1].

Figures 3 and 4 show typical midspan trajectories of 3 μm and 12 μm coal ash particles (density 2.5 g/cc) through the four stages (i.e., eight blade rows) of the turbine. By virtue of their low inertia, the 3 μm particles can follow the gas stream closely, and most of them avoid collision with the blade surfaces. On the other hand, it is noted that the 12 μm particles exhibit considerable deviation from the gas flow and are involved in frequent collisions with the blades, usually on the pressure surfaces except near the leading edge.

Figure 5 shows the stator and rotor blade capture efficiencies[1] for all the stages as a function of particle diameter. In the size range considered, 3–12 μm, the capture efficiencies generally increase with the particle diameter, except in the final row. The capture efficiency of the fourth-stage rotor blades starts to decrease for particles larger than 10 μm which, due to their accumulated deviations in the preceding rows, are directed at decreasing angles of attack to the blade surfaces.

Some general features of the particle motion through the blade passages can be tied in with the following nondimensional parameters: the blade average Stokes number

$$\mathrm{St}_{\mathrm{avg}} = \frac{\rho_p d_p^2 V_{\mathrm{avg}}}{\mu b}$$

where V_{avg} is the average gas velocity in the passage and b the

---

[1] Capture efficiency is defined as the ratio of the number of particles impacting the blade to the total number entering the passage.

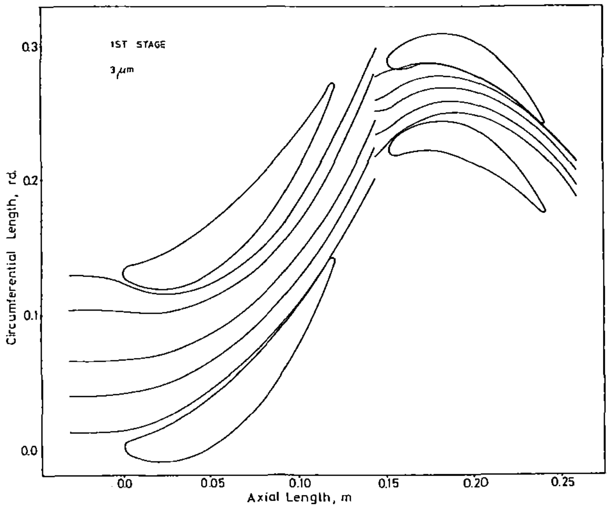

Fig. 3(*a*)

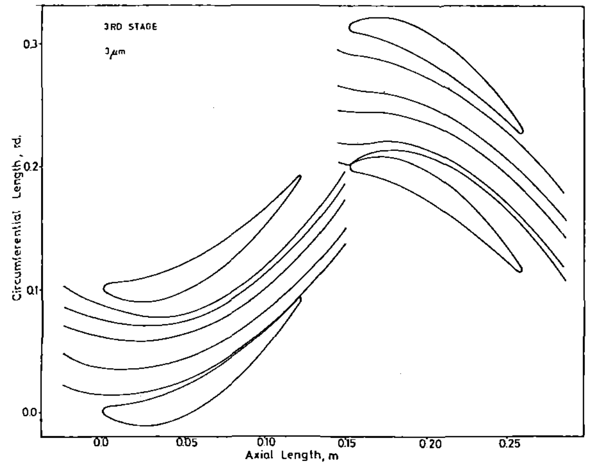

Fig. 3(*c*)

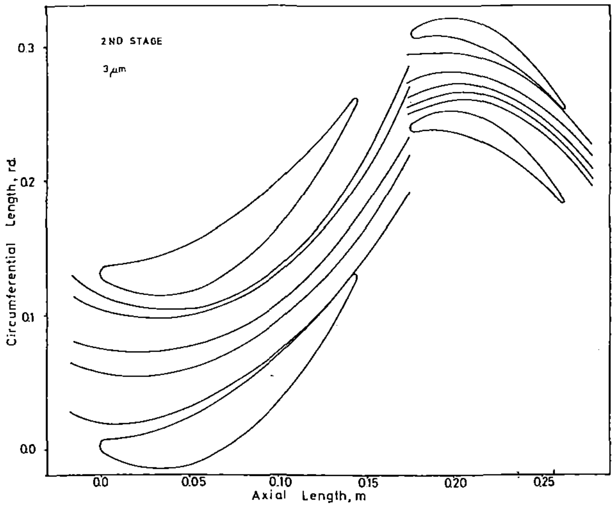

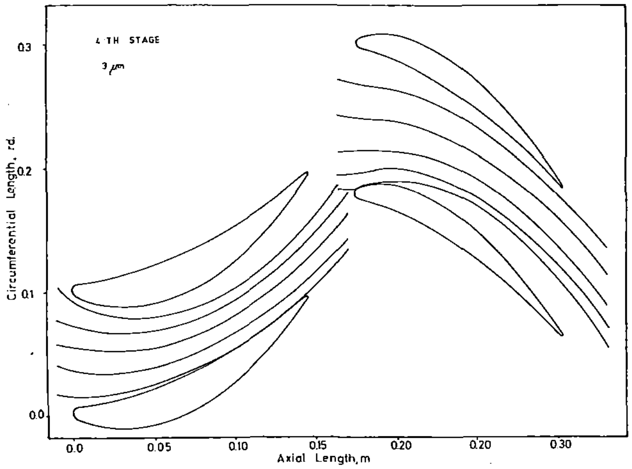

Fig. 3(*b*)

Fig. 3(*d*)

Fig. 3 Trajectories of 3 μm particles: (*a*) stage 1; (*b*) stage 2; (*c*) stage 3; (*d*) stage 4

blade chord; the angle through which the flow is turned α; and the deviation of particles from the gas flow at the passage inlet that may be expressed by the angle $\delta = \beta_p - \beta_g$, where β_p and β_g denote the inlet angles of particles and gas, respectively. In general, capture efficiency in a given blade passage increases with all these parameters (except perhaps the inlet particle deviation δ which might sometimes reduce the capture efficiency as in the fourth-stage rotor discussed above). The fact that the Stokes number is proportional to the square of particle diameter is the explanation for the strong diameter dependence observed in Figs. 3 through 5. The first-stage rotor has the maximum capture efficiency, because the velocities, the turning angle, and the number of blades are relatively large in this row and the blades are relatively small.

The above generalization carries important design implications. An erosion resistant turbine should incorporate the following design features. The annulus area should be large so that the through-flow velocities are low. To decrease stage loadings (turning angles), the number of stages should be increased and work should be uniformly distributed between stages. The blade chords should be large and the number of blades in each row should be minimized.

Before presenting the erosion results it is worthwhile to critically review the basic erosion models used in the calculations. It should be remembered that the erosion responses of two of the materials were calculated from equations (9) with the model coefficients (see Table 1) deduced from a set of constant temperature experimental data for silicon carbide particles eroding nickel-cobalt alloy, based on the rough estimate that silicon carbide particles are 25 times as erosive as coal ash particles eroding "typical" blade materials. Therefore, it is highly questionable whether these models can represent the behavior of some real blade materials to an acceptable accuracy and it is clear that they do not reflect the effect of temperature variations through the turbine. These models had to be used in our original paper [1], because there was a very limited amount of relevant basic erosion data at the time the paper was written. The reason for including these cases in the present study, as well, is to establish a basis of comparison between a ductile material and a brittle material that have similar maximum erosion levels but different angular responses.

Accurate assessment of multistage turbine erosion is dependent on the availability of basic erosion data for the specific blade material used and in the complete operational range of temperatures and velocities. In this respect the interpolative models used to describe the erosion behavior of 304 stainless steel and Rene 41 are more realistic. These models were based on the basic erosion data obtained by Tabakoff et al. [7, 8] in their high-temperature material erosion facility at the University of Cincinnati. Nevertheless, these data (shown in Figs. 1 and 2) cover temperatures up to 649°C (1200°F) and velocities up to 305 m/s (1000 ft/s) which are low in comparison to the maximum temperatures of about 1100°C

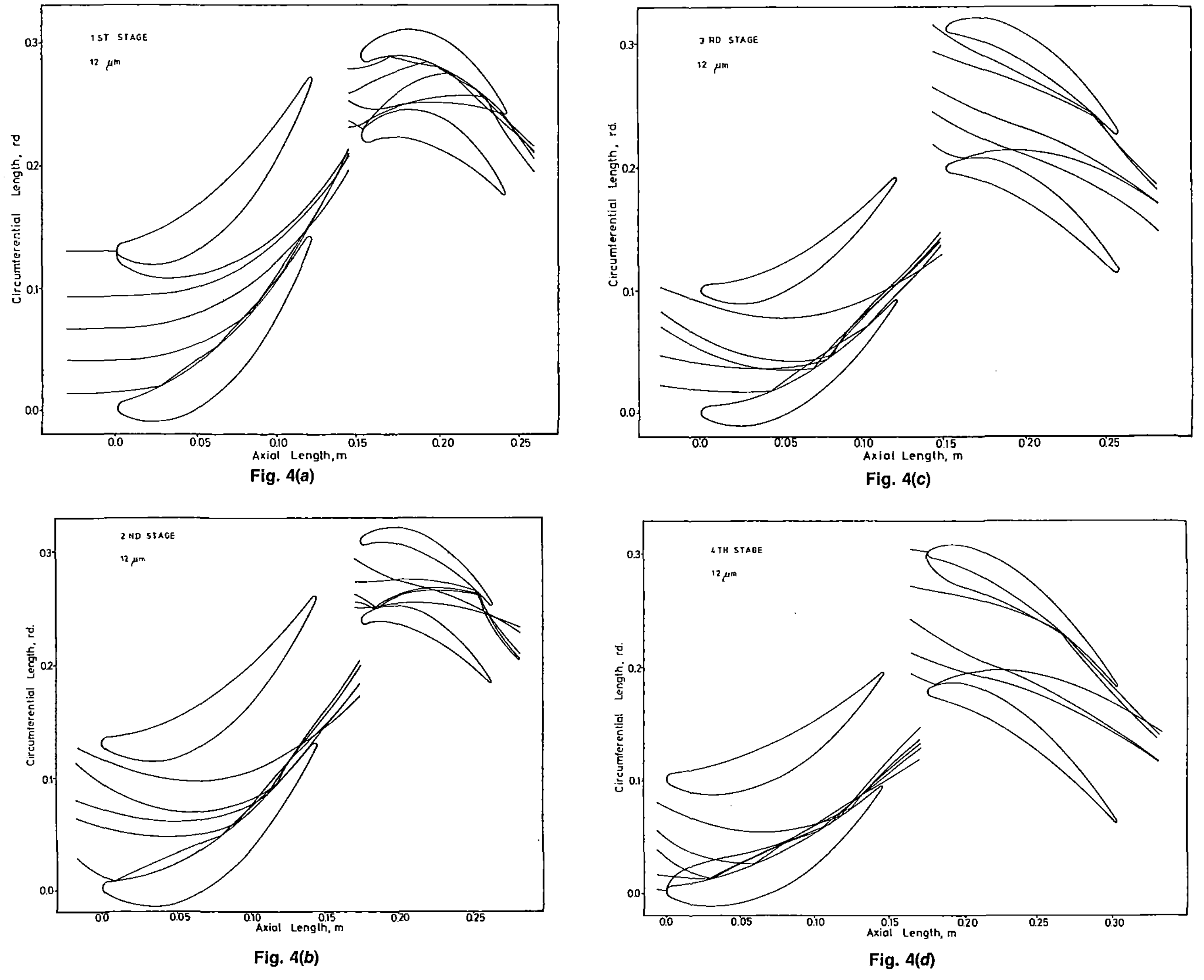

Fig. 4(a)

Fig. 4(c)

Fig. 4(b)

Fig. 4(d)

Fig. 4 Trajectories of 12 μm particles: (a) stage 1; (b) stage 2; (c) stage 3; (d) stage 4

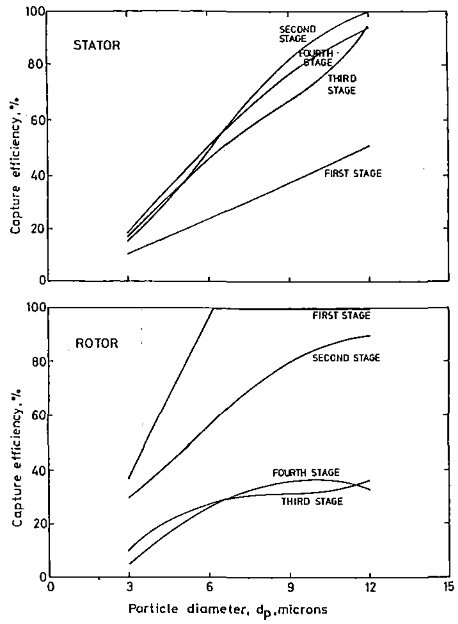

Fig. 5 Capture efficiency as a function of particle size

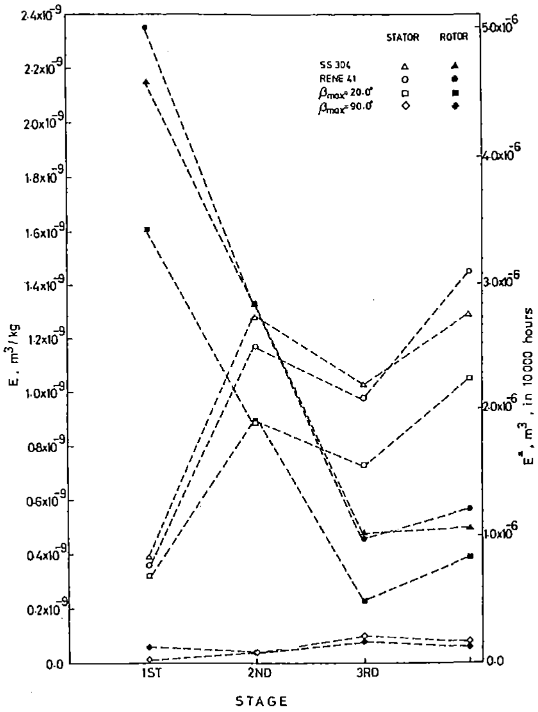

Fig. 6 Total erosion damage by 6 μm particles

(2000°F) and the maximum velocities of about 610 m/s (2000 ft/s) encountered in our turbine. In the present application, erosion rates at velocities above the experimental range were estimated by extrapolation. However, for temperatures above the experimental range the erosion data obtained at the maximum experimental temperature (649°C) was assumed, because it was felt that the erosion response could drastically change near the melting temperatures of the materials (1380°C for 304 stainless steel) and that extrapolation would be misleading. The experimental studies conducted by Tabakoff et al. are greatly appreciated. Such studies should be encouraged so as to extend the data to the range of conditions relevant to modern high-temperature gas turbines.

The total erosion damage per blade caused by 6 μm particles is shown in Fig. 6 as a function of the stage number. The axis on the left gives the total damage per blade in terms of the volume of material (m^3) removed per kilogram of particles entering the turbine. The axis on the right indicates the material volume (m^3) removed from each blade in a given row in 10,000 hr of continuous operation for a reference turbine inlet concentration of 0.00023 gm/m^3 standard (0.0001 grain/ft^3 standard). It is noted that stator and rotor blade total erosion rates exhibit different trends. As we go downstream, the total damage per blade generally increases for the stationary rows but decreases for the rotating rows. It is interesting that damage inflicted on 304 stainless steel and Rene 41 is very similar in both trend and magnitude. Comparison between the "hypothetical" materials with 20 and 90 deg maximum erosion angles shows that ductile materials as blade material are much more susceptible to erosion damage than brittle materials of comparable basic erosion resistance. This is mainly because in the particle diameter range considered most particle–blade impacts occur at small angles to which brittle materials are inherently resistant. It is also interesting to note that the ductile material erosion of 6 μm particles calculated by the semi-empirical erosion model is considerably lower than the 304 stainless steel and Rene 41 erosion calculated by the interpolative model. This is true for all the particle diameters considered (3–12 μm). According to the present results, the filtration requirement previously reported [1] on the basis of the same semi-empirical model appears to have been underestimated.

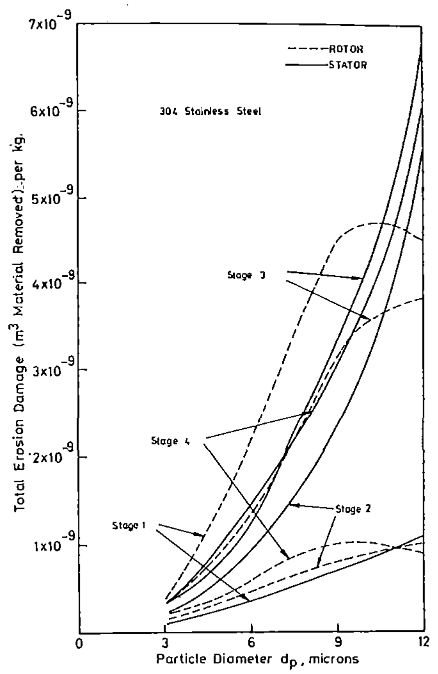

Fig. 7 Total erosion damage as a function of particle size for blade material 304 stainless steel

Figure 7 shows the effect of particle size on the total erosion rates of 304 stainless steel. As expected, damage increases greatly with increasing particle diameter. For long blade life, large particles must be effectively removed from the gas. Another point of interest in these curves is that the total damage on the first-stage stator and the second and fourth-stage rotor blades is considerably lower than in the remaining rows.

Figure 8 shows the predicted material recession rates due to erosion of 304 stainless steel blades as a function of the axial distance measured from the blade leading edge of each row. These results are given for four particle diameters (3, 6, 9, and 12 μm) in millimeters of material recession after 10,000 hours of operation with a reference inlet particle loading of 0.00023 gm/m^3 standard (0.0001 grain/ft^3 standard). It is noted that the recession rate curves are quite sensitive to particle diameter and display considerable trend and magnitude variations between blade rows. These curves are usually characterized by two notable peaks which occur near the leading and trailing edges, the exact locations depending upon the diameter of particles and the blade row under consideration. The trailing edge recession rates are usually larger than the leading edge recession rates for the larger particles (9 μm and 12 μm), but the reverse is usually true for the smaller particles (3 μm and 9 μm).

As an example of the blade erosion pattern of a typical brittle material, Fig. 9 shows the third-stage recession rates calculated for the case with $\beta_{\max} = 90$ deg. Here, the leading edges exposed to particle impacts at relatively large angles erode at much faster rates than the trailing edges.

Figure 10 shows the leading edge and trailing edge recession rates of 304 stainless steel as a function of particle diameter. It appears from these results that the useful life of the machine

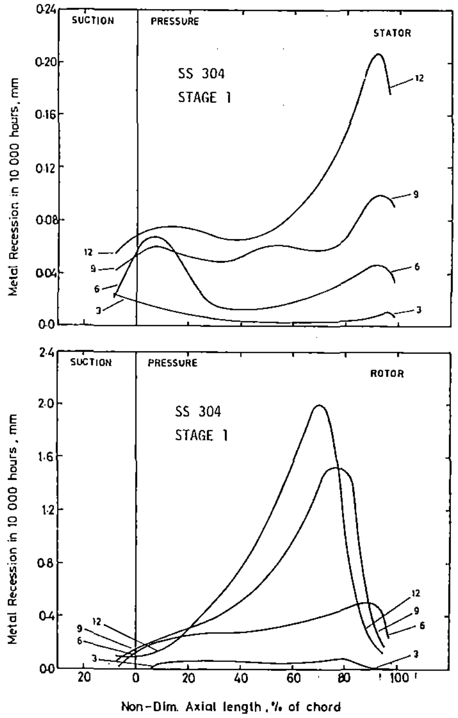

Fig. 8(a)

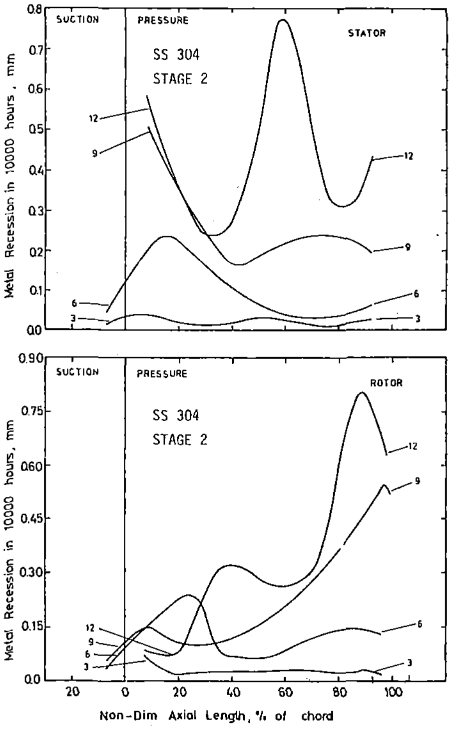

Fig. 8(b)

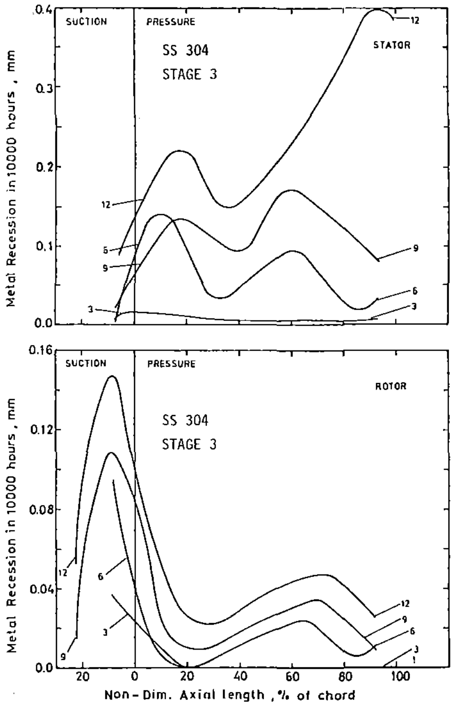

Fig. 8(c)

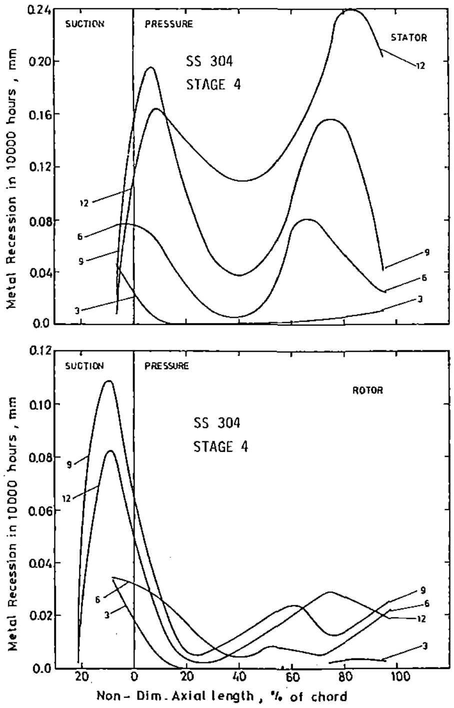

Fig. 8(d)

Fig. 8 Metal recession rates for 304 stainless steel: (a) stage 1; (b) stage 2; (c) stage 3; (d) stage 4

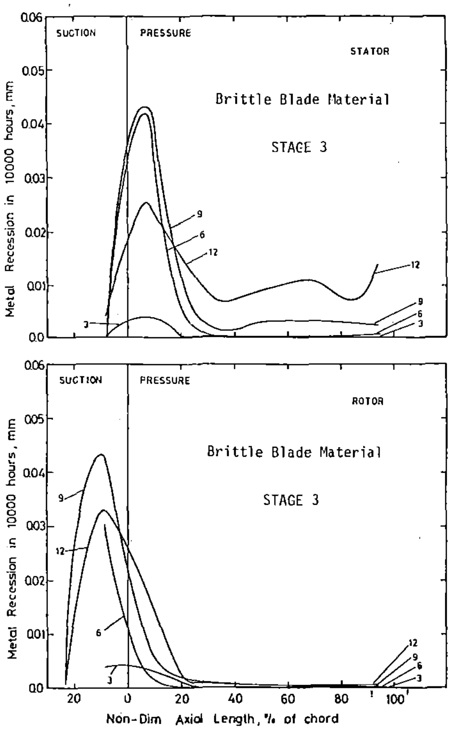

Fig. 9 Third-stage metal recession rates for brittle material, β_{max} = 90 deg

will be dictated by the thinning of the first-stage rotor trailing edge. In addition, the trailing edge regions of the second-stage stator and rotor blades and the third-stage stator blades and the leading edge regions of the second-stage rotor blades are subject to high erosion rates.

Conclusion

A computer program package has been developed to calculate the blade erosion damage in a multistage turbine resulting from the particulate matter contained in the hot expansion gases. The following suggestions have been obtained from the application of this program package to a modern multistage gas turbine:

1 Erosion damage primarily occurs at the leading and trailing edges of blades and is usually confined to the pressure surfaces.

2 Erosion damage has been noted generally to increase with increasing particle diameter and density, flow turning and gas velocity, and with decreasing blade size.

3 The useful life of the machine will be dictated by the thinning of the first stage rotor trailing edge. In addition, the trailing edge regions of the second-stage stator and rotor blades and the third-stage stator blades and the leading edge regions of the second-stage rotor blades are subject to high erosion rates. Erosion of this turbine may be controlled by armoring these high erosion points with field-replaceable erosion shields or by hard facing. Erosion life of a blade may also be increased by increasing the trailing edge thickness.

4 Ductile materials as blade materials are much more susceptible to erosion damage than brittle materials of comparable basic erosion resistance. Use of brittle materials (e.g., ceramic blade) appears to be a promising solution to the blade erosion problem. Erosion of blades made of a brittle material tends to peak around the leading edges. Hard facing or shielding of these areas may prove to be necessary.

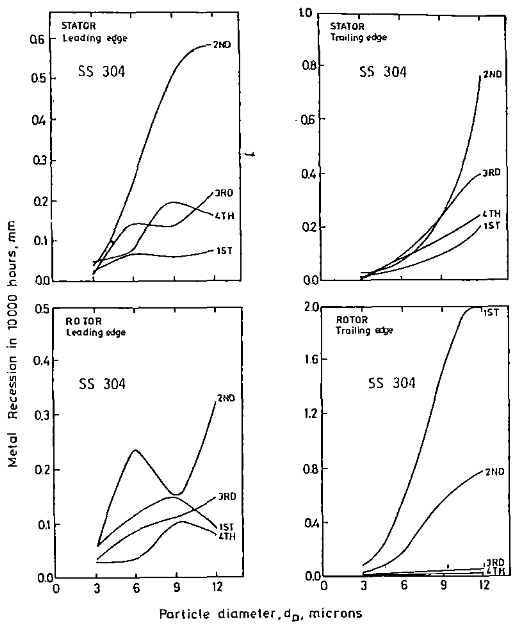

Fig. 10 Maximum metal recession rates as a function of particle size for 304 stainless steel

The models used to simulate the gas particle flow need improvement in the following areas:

1 The present gas flow model is two-dimensional and does not describe the flow in those stages having small hub-to-tip radius ratios accurately. A three-dimensional solution is required.

2 It is known that blade end-wall boundary layers and secondary flows have important effects on the motions of small particles and the resulting erosion damage. For reliable assessment of turbine erosion these effects should be taken into account.

3 Accurate assessment of multistage turbine erosion is dependent on the availability of basic erosion data for specific blade material used and in the complete range of temperatures and velocities typical of modern high-temperature gas turbines. Experimental studies to obtain such data should be encouraged.

References

1 Menguturk, M., and Sverdrup, E. F., "Calculated Tolerance of a Large Electric Utility Turbine to Erosion Damage by Coal Gas Ash Particles," *Erosion Prevention and Useful Applications*, ASTM STP 664, 1979, pp. 193-224.

2 Katsanis, T., "Fortran Program for Calculating Transonic Velocities on a Blade-to-Blade Stream Surface of a Turbomachine," NASA TN-D 5427, 1969.

3 Morsi, S. A., and Alexander, A. J., "Theoretical Low-Speed Particles Collision With Symmetrical and Cambered Aerofoils," ASME Paper No. 72-WA/FE-35.

4 Hamming, R. W., *Numerical Methods for Scientists and Engineers*, McGraw-Hill, New York, 1962.

5 Tabakoff, W., and Hamed, A., "Aerodynamic Effects on Erosion in Turbomachinery," ASME-JSME Joint Gas Turbine Conference, Tokyo, Japan, May 1977, Paper No. 70.

6 Finnie, I., Wolak, J., and Kabil, Y., *Journal of Materials*, Vol. 2, No. 3, Sept. 1967.

7 Tabakoff, W., Ramachandran, J., and Hamed, A., "Temperature Effects on Erosion of Metals Used in Turbomachinery," *Proceedings of the 5th International Conference on Erosion by Solid and Liquid Impact*, Sept. 1979.

8 Tabakoff, W., Hamed, A., and Ramachadran, J., "Study of Metals in High Temperature Coal Gas Streams," ASME JOURNAL OF ENGINEERING FOR POWER, Vol. 102, No. 1, Jan. 1980.

The Dynamics of Suspended Solid Particles in a Two-Stage Gas Turbine

W. Tabakoff
Professor.
Fellow ASME

A. Hamed
Professor.
Mem. ASME

Department of Aerospace Engineering
and Engineering Mechanics,
University of Cincinnati,
Cincinnati, OH 45221

Gas turbine engines operating in dusty environments are exposed to erosion and performance deterioration. In order to provide the basis for calculating the erosion and performance deterioration of turbines using pulverized coal, an investigation is undertaken to determine the three-dimensional particle trajectories in a two-stage turbine. The solution takes into account the influence of variation in the three-dimensional flow field. The change in particle momentum due to their collision with the turbine blades and casings is modeled using empirical equations derived from experimental laser-Doppler velocimetry (LDV) measurements. The results show the three-dimensional trajectory characteristics of the solid particles relative to the turbine blades. The results also show that the particle distributions in the flow field are determined by particle-blade impacts. The results obtained from this study indicate the turbine blade locations which are subjected to more blade impacts and hence more erosion damage.

Introduction

Gas turbine engines often operate in an atmosphere of gas flow laden with solid particles. The particles can be byproducts of advanced fuel combustion or they may be present as a result of operating in a polluted atmosphere. Coal ash particles are also encountered when pulverized coal is used as fuel in industrial applications and power generation. Solid particle separation using cyclones is not effective for particle diameters less than 15 μm. Gas turbine engine performance is known to deteriorate seriously when the hot gases are laden with solid particles. The performance loss can be temporary [1] or permanent [2], depending on the nature of the particles. The temporary performance loss due to nonerosive particles was measured experimentally [1] for an axial flow turbine and was shown to be dependent on the ratio of particle to gas mass flow rates. The experimentally measured pressure distribution over compressor and turbine cascades [3] showed a reduction in the blade loading when the cascades were tested in a tunnel with gas particle flows. If the particles are erosive, impingement of particles on the blade surfaces can cause severe erosion damage, at the blade leading and trailing edges. A permanent loss of performance can result from the change in the airfoil shape, and the increased blade surface roughness [4]. The erosion of turbine blades and other gas turbine components by the suspended fly ash in the hot combustion gases presents a very serious problem to coal-burning turbine designers.

Due to their higher inertia, the particle trajectories in turbomachines generally differ from the flow streamlines, and the particles tend to impact the blade surface and the hub and tip walls. The experimental results for metal erosion by solid particle-laden flows indicate that the erosion rate is affected by the impacting velocity, and impingement angle for a given particle target material combination [4-6], and was found to increase with increased metal and gas temperatures [7, 8]. In addition, the particles migrate in the radial direction under the influence of centrifugal forces as they acquire circumferential velocities either through blade surface impacts or under the influence of the flow field.

The particles' radial and circumferential distribution through multistage turbomachines is hence determined by the blade passage geometry [9-12] and the blade row location [13]. This in turn affects the blade erosion through the particle-blade impact locations as well as their impacting velocities and impingement angle relative to the blade surfaces. The three-dimensional particle trajectory calculations provide detailed information on the magnitude and direction of the particle velocities as well as the particle distribution throughout the machine. The impact velocities and impingement angles relative to the blade, hub, and tip, for a large number of particles, provide the necessary data for calculating the resulting pattern and magnitude of erosion on these surfaces [2].

In the present work, the particle dynamics are studied in a two-stage turbine. The three-dimensional particle trajectories take into account the influence of the three-dimensional variations in the flow field. The change in particle momentum due to their collision with the turbine blades and casings is modeled using empirical equations derived from experimental laser-Doppler velocimetry (LDV) measurements. The results show the three-dimensional trajectory characteristics of the solid particles relative to the turbine blades. They indicate the

---

Contributed by the Gas Turbine Division of THE AMERICAN SOCIETY OF MECHANICAL ENGINEERS and presented at the 31st International Gas Turbine Conference and Exhibit, Düsseldorf, Federal Republic of Germany, June 8-12, 1986. Manuscript received at ASME Headquarters February 14, 1986. Paper No. 86-GT-232.

turbine blade locations which are more subject to particle impacts and hence would suffer the most erosion damage.

Analysis

The equations governing particle motion in the turbomachinery flow field are written in cylindrical polar coordinates relative to a frame of reference fixed with respect to the rotating blade

$$\frac{d^2r_p}{d\tau^2}=F_r+r\left(\frac{d\theta_p}{d\tau}+\omega\right)^2 \quad (1)$$

$$r_p\,\frac{d^2\theta_p}{d\tau^2}=F_\theta-\frac{2dr_p}{d\tau}\left(\frac{d\theta_p}{d\tau}+\omega\right) \quad (2)$$

$$\frac{d^2z_p}{d\tau^2}=F_z \quad (3)$$

where r_p, θ_p, and z_p define the particle location in cylindrical polar coordinates, and ω is the blade angular velocity. The centrifugal acceleration and Coriolis acceleration are represented by the last terms on the right-hand side of equations (1) and (2). The first term on the right-hand side of equations (1)-(3) represents the force of interaction beteen the two phases, per unit mass of particles. This force is dependent on the relative velocity between the particles and the gas flow, as well as the particle size and shape. Under the particulate flow conditions in turbomachines, the effects of the forces due to gravity and to interparticle interactions are negligible compared to those due to the aerodynamic and centrifugal forces. In addition, the force of interaction between the two phases is dominated by the drag due to the difference in velocity between the solid particles and the flow field. The force of interaction per unit mass of solid particles is given by

$$F=\frac{3}{4}\,\frac{\rho}{\rho_p}\,\frac{C_D}{d}\left[\left(V_r-\frac{dr_p}{d\tau}\right)^2+\left(V_\theta-\frac{d\theta_p}{d\tau}\right)^2+\left(V_z-\frac{dz_p}{d\tau}\right)^2\right]^{1/2}(\bar{V}-\bar{V}_p) \quad (4)$$

where V_r, V_θ, and V_z represent the relative gas velocities in the radial, circumferential, and axial directions, respectively, and ρ and ρ_p are the gas and solid particle material densities, d the particle diameter, and C_D the particle drag coefficient. This coefficient is dependent on the Reynolds number, which is based on the relative velocity between the particle and the gas. Empirical relations, as shown in [14], are used to fit the drag curve over a wide range of Reynolds numbers.

Trajectory Calculations. The particle trajectory calculations consist of the numerical integration of the equations (1)-(4) in the flow field, up to the point of blade, hub, or tip impact. The magnitude and direction of particle rebounding velocity after these impacts are dependent on the impacting conditions and the particular particle and surface material combination under consideration.

The particle rebounding conditions are determined from empirical correlations of the restitution parameters. These correlations [13] are based on the experimental data obtained using LDV for particle laden flows over metal samples at various incidence angles and flow velocities in a special tunnel [6, 7]. The ratios were found to be mainly dependent upon the impingement angle [15, 16] for a given particle-material combination.

In the present study the magnitude and direction of the particle rebounding velocity after impact were obtained using the following empirical equations which were obtained from [15] for Kingston fly ash particles impacting on a 410 stainless steel target

$$V_{P_R}/V_{P_I}=1-0.90847\,\beta_I+0.3072\,\beta_I^2+0.05695\,\beta_I^3 \quad (5)$$

and

$$\beta_R/\beta_I=1-0.38746\,\beta_I+0.51442\,\beta_I^2+0.45094\,\beta_I^3 \quad (6)$$

where V_{P_I} and β_I represent the particle impact velocity and impingement angle, while V_{P_R} and β_R are the rebound velocity and rebound angle measured from the impacted surface.

In the case of rotor blade impacts, the velocities and angles of impact and rebound are considered relative to the rotating blade. Furthermore, in order to use the empirical correlations obtained from two-dimensional measurements, in the three-dimensional particle trajectories, a knowledge of the geometry of the solid surface at the impact location is required. Geometric data describing the blade, hub, and tip configuration need to be available during the trajectory calculations for use in the determination of the impact location and the impingement angle relative to the surface.

Effect of Blade Shapes. Accurate representation of the turbine blade geometry in the particle trajectory calculations is crucial as it influences the predicted blade impact locations and particle impact velocity and impingement angle relative to the blades. In addition, the particle trajectory after each blade impact is also affected by these impact conditions through the rebound restitution correlations of equations (5) and (6). Even if the particle distribution is uniform as particles enter the first stator, they are generally redistributed in a nonuniform pattern as they leave the blade row due to blade surface impacts [13]. The turbine blade airfoil shape must therefore be accurately represented in the trajectory analysis as it strongly influences the predicted particle dynamics. In particular, since a large number of particles impact the blunt leading edges of the turbine blades before entering the blade passage, the blade leading edge geometry has an effect on the rest of the trajectory calculations. In addition, the radial variation in the blade shape is also important as it affects the particle rebound characteristics in the three-dimensional trajectories [12], and might influence the particle redistribution in the radial direction. The blade surface coordinates at several sections between the hub and tip are used in the trajectory calculations to describe the blade shapes. Interpolation is used to determine the blade surface coordinates at other locations. The required

Nomenclature

C_D = particle drag coefficient
d = particle diameter
$\bar{F}$ = force of interaction between the gas and the particle
r = radial distance from the turbomachine axis
$\bar{V}$ = gas velocity relative to the blade
$\bar{V}_p$ = particle velocity relative to the blade
z = axial coordinate
β = the angle between the particle trajectory relative to the blade and the blade surface
θ = angular coordinate
ρ = gas density
ω = rotor speed (radians/s)
τ = time

Subscripts

I = refers to particle impact conditions at the surface
p = particle
r = component in radial direction
R = refers to particle rebound conditions after the surface impact
z = component in axial direction
θ = component in circumferential direction

number of sections is dependent on the hub to tip variation in the blade shape.

Effect of the Three-Dimensional Flow Field. The large flow turning angles generally encountered in turbine blading produce large pitchwise as well as radial and axial flow field variations. The flow field affects the particle trajectories, through the aerodynamic forces of interaction consisting mainly of the drag force.

Careful consideration must be given to the flow field description in the particle trajectory calculations [9], to represent the important flow field characteristics. The radial variation in the flow field can be significant under the influence of blade profile radial variation and inner and outer radius contouring. The computer storage required for the three-dimensional flow field data and the computer time for interpolating flow properties at each time step in the numerical integration of the particle equations of motion must also be taken into consideration.

The flow field in a blade passage is synthesized from a number of blade-to-blade stream surface solutions to give the desired accuracy of the three-dimensional flow field representation in the particle trajectory calculations. Each flow field solution on a blade-to-blade stream surface [17] provides accurate description of the pitchwise and streamwise variation in the flow properties. The stream surface shapes and stream filament thickness as determined from a midchannel hub-to-hub stream surface solution [18] model the influence of the hub and tip contours and the hub-to-tip variation in the blade shapes.

All three gas velocity components and gas density are calculated at the same number of blade passage grid points in each blade-to-blade solution, and are used as input to the particle trajectory calculation code. The spanwise, pitchwise and chordwise variations in flow properties are therefore represented in the particle trajectory calculations. In addition the effect of the radial variation in the blade shape and hub and tip contouring is taken into consideration in the particle trajectory calculations. The output of the particle trajectory calculation code consists of three files. The first file provides the input for particle trajectory plots. The second particle trajectory output file contains all particle exit conditions for a given blade row and is used as input to provide the initial conditions for the particle trajectories in the following blade row. These data are first adapted to the new frame of reference, which is fixed in each blade row. The particle axial and radial location is not affected by the relative motion between successive blade rows. The circumferential variation in the particle distribution at the exit of a given blade row is in reality evened out at the inlet to the following blade row due to the relative motion between successive blade rows. This effect is simulated in the computations by redistributing the particles randomly in the circumferential direction, in the new frame of reference which is fixed relative to the subsequent blade row. The third file contains all computed particle impact data, including impact locations, and the impact velocity and impingement angle relative to the solid surfaces, for use in the code for blade surface erosion computations.

Results and Discussion

The results of the three-dimensional particle trajectories are presented through the blade rows of a two-stage turbine [19]. The flow conditions correspond to 7.071 lb/s mass flow rate at 1893 rpm in the presence of 15 μm fly ash particles. The results show the three-dimensional particle trajectories relative to the various blade rows as viewed from the z-θ plane and also their meridional projection in the r-z plane. Additional figures show particle impact locations and particle distributions at each blade row exit.

Figures 1-4 show sample particle trajectories in the different blade rows as viewed from the tip in the z-θ plane. An examination of these figures reveals that all the particles impact the blade pressure surface at least once but not the blade suction surface. Comparing Figs. 1-4, one can see that, while only about one third of the particles impact the blade leading edge of the first nozzle, almost all the particles impact the blade leading edge of subsequent blade rows. This is due to the fact that the direction of the particle motion relative to the blades at inlet is generally very different from the inlet flow angles in all the blade rows, except in the first nozzle. After the blade leading edge impacts, these particles lose most of the their initial axial momentum with some rebounding such that their axial velocities are in the upstream direction. The influence of the flow field on the trajectories of these particles can be observed to be more significant after the blade leading edge impact. The flow field influence is manifested in the particles re-acquiring axial velocities, while their circumferential velocities are reduced under the influence of the aerodynamic forces of interaction. All the particles that initially impact the leading edge, on either pressure or suction side, again impact the blade pressure surface further toward the trailing edge.

Figure 5 shows the projection of the particle trajectories in the meridional (z-r) plane throughout the turbine. The particle impacts with the blade blunt leading edges can be clearly seen in this figure as they are characterized by subsequent upstream particle motion. One can observe in Fig. 5 the strong influence of the impact with the blades on the particle radial motion. The particle blade impacts impart circumferential rebounding particle velocities, causing particle centrifugation away from the hub. This centrifugal effect is found to be significant only after the first rotor blade impact.

The particle-blade impact locations are shown in Figs. 6 and 7 over the blade suction and pressure surfaces, respectively. Comparing the two figures one can see that blade pressure surfaces are subject to many more impacts than the suction surfaces. The very few suction surface impacts are seen to be mostly restricted to the first third of the blade chord (Fig. 6), while the rest of the blade suction surface is not subject to any particle impacts. The impacts are so closely spaced that they appear as a line in Figs. 6 and 7, and represent repeated impacts for a single particle. This condition arises when the particle impingement angle relative to the blade becomes so small that the particle also rebounds with very small relative angle and continues its motion very close to the blade surface, suffering many closely spaced repeated impacts. Figure 7 shows that in the first nozzle, the blade pressure surface impacts increase toward the trailing edge with little radial variation in the impact pattern. The particle-blade impact pattern, however, is seen to change strongly in the radial direction in subsequent blade rows. The absence of particle-blade impacts toward the hub can be seen in Fig. 7 to start in the first rotor. The portion of the blade surface with no particle impacts continues to grow in subsequent blade rows. The trajectories of Fig. 5 show that the particle centrifugation after rotor blade impacts, and the blade flaring at the hub, combine to produce this effect. The same figure shows that the particle impacts are mostly concentrated at the blade leading edge with some particle impacts in the trailing edge regions of the blade pressure surface of the first rotor, and the second stator.

The particle radial and circumferential distribution between the successive blade rows is shown in Fig. 8. This figure shows that the effect of particle centrifugation toward the tip starts in the first rotor and continues until most of the particles are in the tip region at the turbine exit. One can see from Fig. 8 that the particles are generally concentrated in a narrow band of the blade passage pitch only at the first nozzle exit. Figure 1

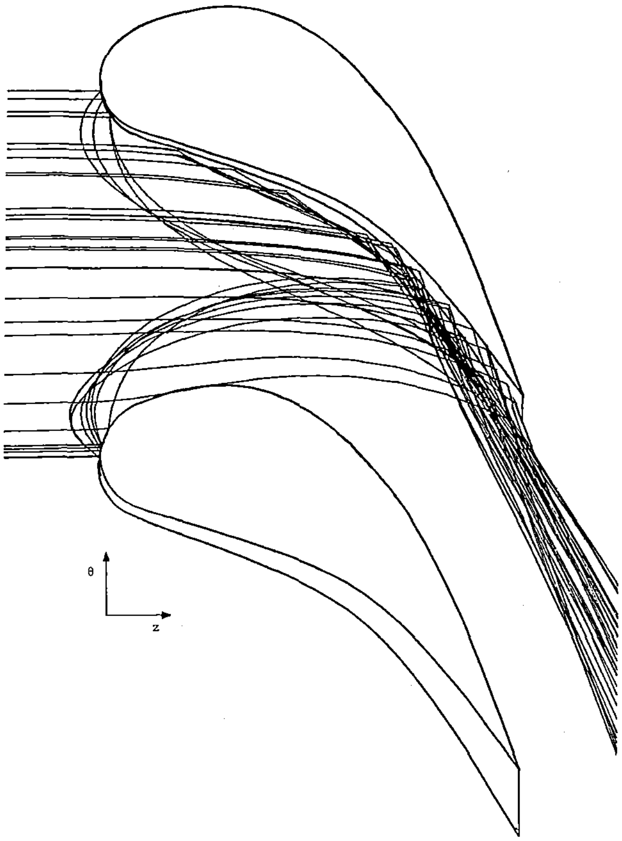

Fig. 1 Projected particle trajectories in the *z*-*θ* plane, first nozzle

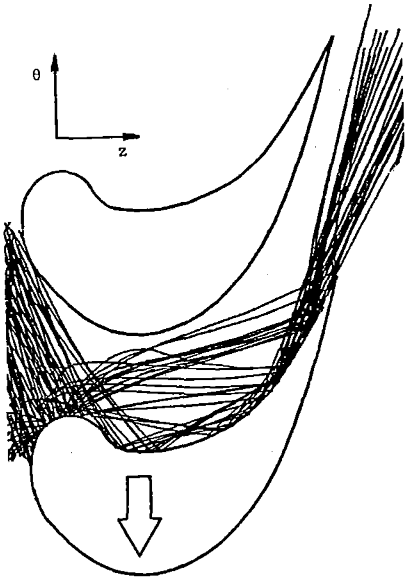

Fig. 2 Projected particle trajectories in the *z*-*θ* plane, first rotor

reveals that this circumferential redistribution of the particles is caused by blade pressure surface impacts. The continued particle centrifugation is reflected in the extent of the region near the hub containing no particles. At the turbine outlet, 90 percent of the particles are seen to be concentrated in the outer 10 percent of the blade span.

Conclusion

An investigation was undertaken to determine the three-dimensional particle trajectories in a two-stage turbine. The

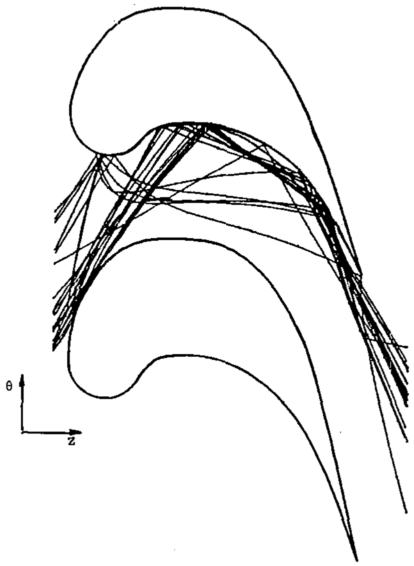

Fig. 3 Projected particle trajectories in the *z*-*θ* plane, second nozzle

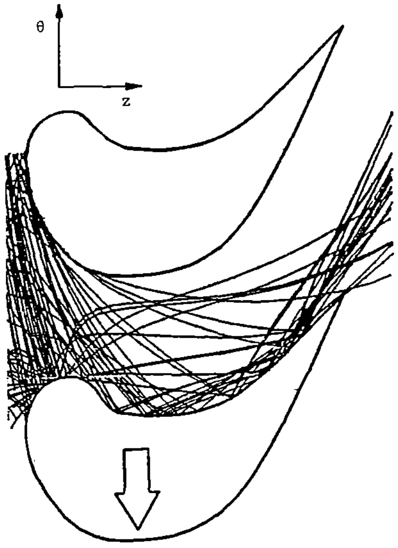

Fig. 4 Projected particle trajectories in the *z*-*θ* plane, second rotor

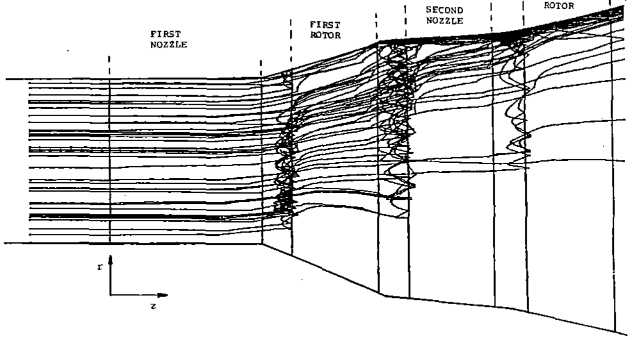

Fig. 5 Projected particle trajectories in the meridional (*z*-*r*) plane through the two-stage turbine

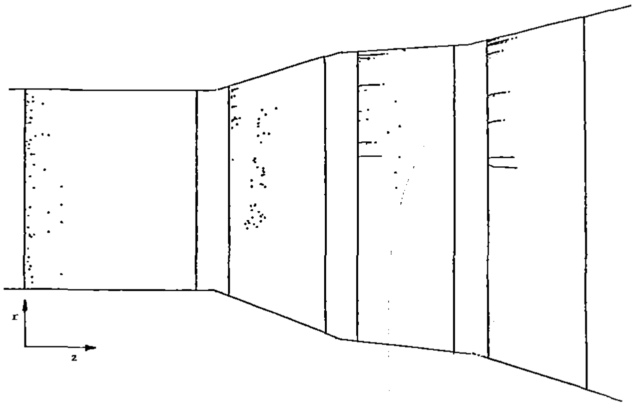

Fig. 6 Locations of particle impacts on the suction side of the blades

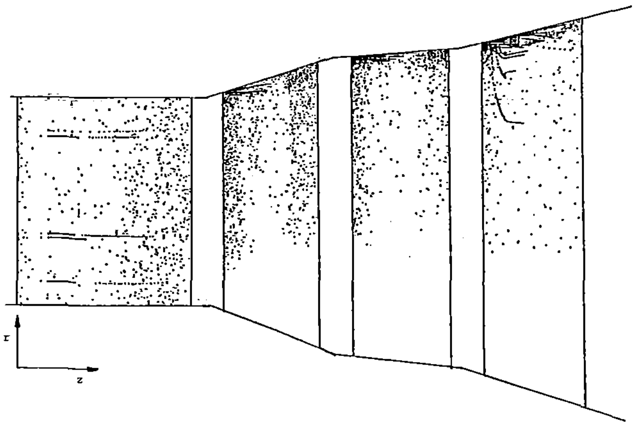

Fig. 7 Locations of particle impacts on the pressure side of the blades

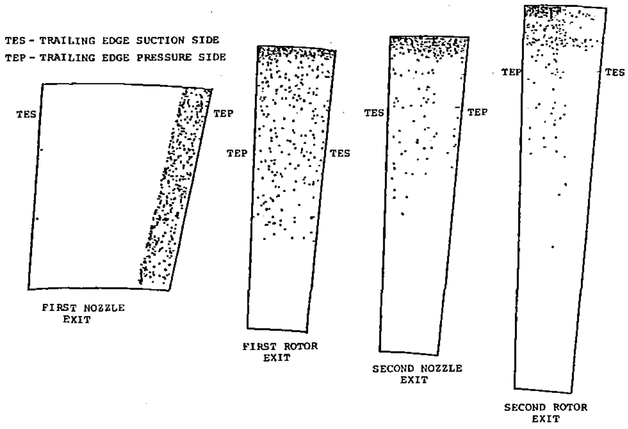

Fig. 8 Particle distribution at the nozzle and rotor blade exits

solution takes into account the influence of the variation in the three-dimensional flow field. The change in particle momentum due to their collision with the turbine blades and casings is modeled using empirical equations derived from experimental LDV measurements. The results show that the three-dimensional trajectory characteristics of the solid particles change with the blade row location. The particle blade impact locations and the particle distribution in the flow field are found to be strongly influenced by the preceding blade row configurations. The results also show that very few particles impact the blade suction surfaces but all the particles impact the blade pressure surface at least once. All the particles are found to impact the leading edge of all blade rows starting with the first rotor. The results indicate that the continuous centrifugation of the particles subjects the outermost radial blade locations to a higher number of particle impacts.

Acknowledgments

This research was sponsored in part by U.S. Department of Energy, and in part by the General Electric Company, Evendale, OH.

References

1 Tabakoff, W., Hosny, W., and Hamed, A., "Effect of Solid Particles on Turbine Performance," ASME Journal of Engineering for Power, Vol. 98, 1976, pp. 47-52.

2 Hamed, A., and Fowler, S., "Erosion Pattern of Twisted Blades by Particle Laden Flows," ASME Journal of Engineering for Power, Vol. 105, 1983, pp. 839-843.

3 Tabakoff, W., and Hussein, M. F., "Effect of Suspended Solid Particles on the Properties in Cascade Flow," *AIAA Journal*, Vol. 9, 1971, pp. 1514-1519.

4 Tabakoff, W., "A Study of the Surface Deterioration due to Erosion," ASME Journal of Engineering for Power, Vol. 105, 1983, pp. 834-839.

5 Grant, G., and Tabakoff, W., "Erosion Prediction in Turbomachinery Resulting From Environmental Solid Particles," *Journal of Aircraft*, Vol. 12, 1975, pp. 471-478.

6 Tabakoff, W., Hamed, A., and Ramachandran, J., "Study of Metals Erosion in High Temperature Coal Gas Streams," ASME Journal of Engineering for Power, Vol. 102, 1980, pp. 148-152.

7 Tabakoff, W., and Hamed, A., "Investigation of Gas Particle Flow in Erosion Wind Tunnel," 7th Annual Conference on Materials for Coal Conversion and Utilization, National Bureau of Standards, Gaithersburg, MD, Nov. 16-18, 1982.

8 Tabakoff, W., Hamed, A., and Balan, C., "Performance Deterioration of an Axial Flow Compressor Stage With Presence of Solid Particles," *Proceedings of the 5th International Symposium on Airbreathing Engines*, 1980.

9 Hamed, A., "Solid Particle Dynamic Behavior Through Twisted Blade Rows," ASME *Journal of Fluids Engineering*, Vol. 106, 1984, pp. 251-256.

10 Beacher, B., Tabakoff, W., and Hamed, A., "Improved Particle Trajectory Calculations Through Turbomachinery Affected by Coal Ash Particles," ASME Journal of Engineering for Power, Vol. 104, 1982, pp. 64-68.

11 Hussein, M. F., and Tabakoff, W., "Computation and Plotting of Solid Particle Flow in Rotating Cascades," *Computers and Fluids*, Vol. 2, 1974, pp. 1-15.

12 Tabakoff, W., and Hamed, A., "Installed Engine Performance in Dust Laden Atmosphere," AIAA Paper No. 84-2488, Nov. 1984.

13 Hamed, A., "Particle Dynamics of Inlet Flow Fields With Swirling Vanes," *Journal of Aircraft*, Vol. 19, 1982, pp. 707-712.

14 Hussein, M. F., and Tabakoff, W., "Dynamic Behavior of Solid Particles Suspended by Polluted Flow in a Turbine Stage," *Journal of Aircraft*, Vol. 10, 1973, pp. 434-440.

15 Tabakoff, W., and Malak, M. F., "Laser Measurements of Fly Ash Rebound Parameters for Use in Trajectory Calculations," ASME Paper No. 85-GT-161, Mar. 1985.

16 Tabakoff, W., Malak, M. F., and Hamed, A., "Laser Measurements of Solid Particles Rebound Parameters Impacting on 2024 Aluminum and 6A1-4V Titanium Alloys," AIAA 18th Fluid Dynamics and Plasmadynamics and Lasers Conference, Cincinnati, OH, July 1985, Paper No. 85-1570.

17 Katsanis, T., "Fortran Program for Calculating Transonic Velocities on a Blade-to-Blade Stream Surface of a Turbomachine," NASA TND-2809, May 1965.

18 Katsanis, T., and McNally, W. D., "Revised Fortran Program for Calculating Velocities and Streamlines on the Hub-Tip Mid Channel Stream Surface of an Axial, Radial, or Mixed Flow Turbomachine or Annular Duct, Vols. 1 and 2," NASA TND-8430 and NASA TND-8431, 1977.

19 Roelke, R. J., Stabe, R. G., and Evans, D. G., "Cold-Air Performance Evaluation of Scale Model Oxidizer Pump-Drive Turbine for the M-1 Hydrogen-Oxygen Rocket Engine—II. Overall Two-Stage Performance," NASA TND-3368, 1966.

A New Experimental Technique to Simulate Secondary Erosion in Turbine Cascades

P. J. Singh

J. L. Dussourd

Ingersoll-Rand Research, Inc.,
Princeton, NJ 08542

In refineries, power-recovery turbines are widely used in the fluid catalytic cracking process to extract power from particle-laden gases. The gas particles impinging on the blades cause blade and platform erosion. This erosion can be broadly classified into primary and secondary erosion according to the dynamics of the particle/flow interactions and whether the damage is caused by direct inertial impingement or by recirculation of fine particles (1–2 μm) through the blade secondary flows, by the vortices induced by these flows. This paper reports on a new experimental method devised to simulate the secondary erosion patterns without the use of a dust-laden stream. In this method, blades coated with a sublimating material such as naphthalene are tested in a wind tunnel. The secondary flow vortices tend to increase the local rate of sublimation in those areas where surface momentum gradients are high. This simulates the condition of preferential erosion induced by the dust loading present in the vortices. Tests show the induced patterns to be quite akin to secondary erosion seen on field run blades especially in the critical erosion patterns seen near the blade roots. Design modifications were then successfully developed to minimize this secondary erosion. These were shown to have a capability of reducing the erosion by 50 to 75 percent, by utilizing platform step control and naturally induced boundary layer suction. Conversely, many other features were found surprisingly ineffective. The method was also shown to be a very effective surface flow visualization technique for internal and external surfaces. Of the approaches found to be successful in minimizing erosion damage, control of the geometry of the stator to rotor steps along the hub flow path blade platforms was critical. Steps in general have the effect of making erosion worse. The most successful approach is the introduction of an inherent suction slot and the suction flow passage between individual blade platforms.

1.0 Introduction

Much attention in recent years has been given to the problem of turbine blade erosion in processes where high-pressure and usually high-temperature contaminated gas streams are to be expanded through turbomachinery in an effort to recover the energy. Among these the pressurized fluidized bed combustion system has received much support from government and private organizations such as the DOE, EPRI, and BCR, a good share of which is dedicated to solving the problem of erosion of the turbine blades from the dust in the stream. The longest time of successful operation in such an environment can actually be found in power recovery, from fluid catalytic cracking (FCC) processes and from blast furnaces, which together have the longest record of successful performance in oil refineries and in the steel industry over the past 25 years.

This paper deals with expanders used for power recovery from the hot stream generated in the catalyst regeneration pro-

Fig. 1 Typical primary erosion characterized by thinning of the trailing edges

---

Contributed by the Gas Turbine Division of The American Society of Mechanical Engineers and presented at the 31st International Gas Turbine Conference and Exhibit, Düsseldorf, Federal Republic of Germany, June 8–12, 1986. Manuscript received at ASME Headquarters January 20, 1986. Paper No. 86-GT-107.

Fig. 2 Secondary erosion on an expander blade; most of the erosion is concentrated at the suction surface of the blade root aft of the midcord

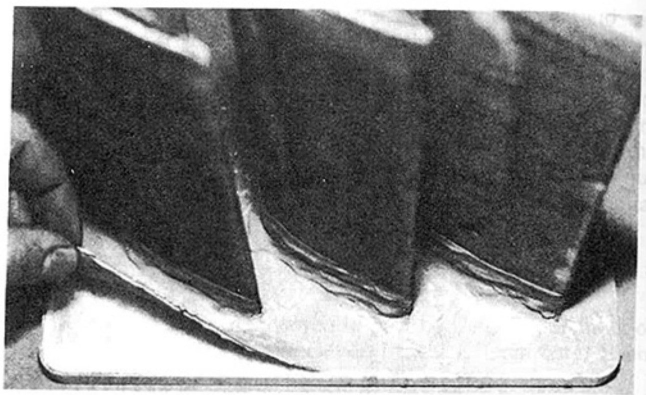

Fig. 3 Replica being peeled off a test piece; the replicating material sets in about two hours

cess, increasingly in common usage with catalytic refining. In this application the stream of hot gas is produced from pressurized combustion of the carbon contaminant on the catalyst surface, before returning it to the main process. The authors' company is the world's largest supplier of equipment for FCC applications with 30 installations throughout the world operating as power-recovery devices in an oil refinery environment, around the clock and for periods of several years between turnarounds. This research was carried out in support of these commercial applications.

In the fluid catalytic cracking (FCC) process [1-4], the hot exhaust gases laden with spent catalyst go through three stages of dynamic cleanup before entering the expander. Depending on the separator efficiency, the gases at the expander inlet have a typical particle size distribution in the range of 0 to 20 μm and a mass loading around 120 ppm. These particles interact with expander stator and rotor blades causing erosion damage. Generally as a result of the larger particles, the most damage is sustained on the rotor blades' trailing edges near the tip since the heavier particles with high inertia tend to centrifuge outward and do not readily turn with the flows. This kind of particle motion and damage potential has been widely studied and reported in the literature, for example [5-7], and is generally referred to as primary erosion (Fig. 1).

More recently, some FCC expander turbines have encountered a new type of highly localized and severe erosion near the root of rotor blades (Fig. 2). This localized erosion appears in the form of deep, sharp-edged narrow grooves, gouges, and tunnels at the root midchord of the blade's suction surface and at the platform. This erosion was first thought and later verified experimentally to be caused by secondary flow vortices. The finer particles (1-2 μm) tend to follow the cascade secondary flows and become energized in secondary flow vortices. These vortices have a high concentration of solids, because the inward-moving secondary flows transport toward the hub the heavily dust-laden flow found in the boundary layer of the blade pressure side. They are deemed to be the cause of the secondary erosion. In general expanders suffering from such erosion are using newer, high-activity catalyst which tend to have a higher percentage of finer particles. Investigation of secondary flow through turbulent blade passages has received considerable attention recently, for example [8-15].

A field evaluation of the factors causing this erosion and ways to investigate it is a very difficult and long process. Similarly the idea of using a scaled expander in a particle-laden gas test loop suffers from high cost of design and operation and long turnaround times. Instead, a new experimental method was devised capable of simulating the secondary erosion patterns without the use of a dust-laden stream.

This method postulates that the intense local mass momentum at the vortices induces high local scouring and mass transfer phenomena on the flow surfaces in the same manner it produces the high local erosion phenomena, also caused by the intense scouring of these vortices. While this phenomenon is postulated without analytical justification, it may be intuitively sensed that the rapid spinning motion of a vortex near the surface would be capable of producing high local heat and mass transfer phenomena as well as erosion, if abrasive particles are entrained by the vortex. In fact the observed results offer the best evidence of support of this thesis. Accordingly, blade cascades coated with a sublimating material such as naphthalene and subjected to typical secondary flow patterns will sublimate preferentially at places where erosion would be the highest. Care has to be exercised to maintain equivalent Reynolds number and a constant temperature. The method has been named ESN (erosion simulation using naphthalene). The observed mass loss on blades using ESN greatly resembles the erosion seen on the blades in actual service in terms of location, appearance, and sharp-edged surfaces. In addition, the secondary flow on the surface is made evident from fine vortex streaks seen on the naphthalene surface. Thus the method can also be used as a very effective surface flow-visualization technique for internal and external surfaces.

Naphthalene sublimation techniques have been used earlier by several investigators [16-18] to estimate surface heat/mass transfer rates and studies of boundary layer transition. These investigators found that the consistency of test data depended a great deal on the naphthalene crystal structure and surface finish. In the present study considerable time and effort were spent to develop techniques which can yield consistently smooth and adherent naphthalene coating on a wide range of base materials. The accurate measurement of localized mass loss also poses a significant problem which was resolved by identifying effective material for industrial surface replication.

This paper describes the techniques for applying naphthalene over different base materials, recording and quantifying the amount of material loss. Also described are the results of a sequence of validating tests using well-understood basic geometries such as cylinders, and then progressing to turbine blade shapes. Finally cascade design features have been identified that are capable of greatly weakening the intensity of the secondary flows with consequent major decreases in the observed erosion.

2.0 Experimental Method Description

The ESN method essentially consists of:

(*a*) Application of a thick naphthalene coating of the basic geometry to be investigated. Through the use of techniques to be described later, virtually any shape and basic material can be successfully coated and finished.

(*b*) Exposure of the coated object to a gas stream, with correct boundary and correct dynamic conditions for a given time period, three to six hours, at constant stream temperature, since sublimation rate is a strong function of temperature.

(*c*) Quantify the material loss globally as well as locally in the critical regions on the test object. Map the material loss profile from permanent records and correlate with the flow patterns from the flow lines etched on the surface.

2.1 Naphthalene Application

The goal for each test object is to produce a smooth, crack-free surface with as small a grain or crystal size as possible. To achieve this end, different techniques must be used for different base materials and shapes. In general the naphthalene cooling rate must be closely controlled. These techniques will be described as follows in some detail since good coating is absolutely essential to the success of the test.

2.1.1 Rolling. A 3.8 cm dia × 20 cm long aluminum cylinder is rolled in a tray filled with molten naphthalene at 120°C, the cylinder being preheated to 70°C. The preheating avoids sudden cooling at the surface, a major source of surface and internal flaws or cracks. A coating of up to 4 mm can be applied in this manner using multiple passes. The coating can then easily be machined. Smaller cylinders must be handled differently. Small thermal mass is apt to induce slow cooling and nonuniform grain growth which tends to sublimate preferentially.

2.1.2 Castings. Naphthalene can be mold-cast virtually on any object, such as on a 15 cm dia aluminum flat plate, undercut by 5 mm except at the edge to hold and protect the coating. A thick steel ring placed around the circumference acts as a mold. The plate and ring assembly must be judiciously water cooled.

2.1.3 Painting. It is difficult to use the above techniques for irregular shapes such as turbine blades. For such shapes, coating to any desired thickness can be built up by painting thin layers of naphthalene with a brush, which can be used on unvarnished mahogany blades as well as aluminum plates. The paint brush technique can also be used to sculpt fillets at the blade root as well as to generate small alterations to the basic airfoil such as built-up sharp leading edges.

2.1.4 Multi-Layer Deposition. None of the above methods worked successfully on stainless steel because of poor bonding. The problem is resolved by deposition of an intermediate layer of Facsimile material (manufactured by Flexbar Corp.) and casting naphthalene over it, forming a strong bond with the Facsimile. There may be some migration of Facsimile into naphthalene which can be compensated for by adding 1 mm to the nornal coating thickness.

2.1.5 Finishing. Naphthalene coating is easily machined, milled, or finished with sandpaper. For irregular shapes, the coating is finished with 180 grit sandpaper followed by wet-sanding, with acetone and 220 grit sandpaper. The final surface has a smooth finish of 0.5 μm or less and a marblelike appearance. One of the critical aspects for getting a good coating is the need for high-purity naphthalene. Although reagent-grade naphthalene from different manufacturers was tried, best results were obtained with the high-purity Fisher Co. naphthalene.

3.0 Validation Tests

As a first step, ESN was tried on a cylinder between end walls. Both the primary and secondary flows (in the presence of a boundary layer) around a cylinder are well established, for example [19–21]. A 3.8-cm aluminum cylinder was coated with 2 mm naphthalene coating and tested in our wind tunnel for two to three hours at a Reynolds number of 10^5.

The IRRI wind tunnel is a low-turbulence, subsonic tunnel with a wind speed of 70 m/s in the 22.5 cm wide × 40 cm high test section. The test section was equipped with single-hole and three-hole pitot tubes and hot-wire/hot-film anemometers to measure mean velocity profiles and turbulence levels.

The primary flow around a cylinder away from end effects in the test Reynolds number range is characterized by two symmetrically located separation points, the location of which varies slightly according to the Reynolds number. The test results showed clear evidence of such separation points and the location of these points correlated within ± 1 deg with the measurements reported in [21], as seen from the observed sharp ridges along the cylinder's length.

Likewise the classical horsehoe pattern seen near the base of a cylinder normal to a flat surface can easily be produced by building up such a cylinder upon a flat surface and observing the characteristic depression from the sublimated naphthalene. A similar depression can be produced on the end walls for a cascade of compressor vanes.

Th real validation test, however, was attained when actual turbine blades using ESN and subjected to flow conditions similar to those in the actual turbines were found to exhibit erosion patterns at the same location and very similar in character and intensity as the real blades in the real turbines. The realization of this effect will be described later.

4.0 Flow Visualization

ESN can also serve as a flow-visualization technique, particularly on three-dimensional surfaces. The best results are obtained with a surface grain size of the order of 1 mm. Although an extremely fine grain, because of its homogeneity, is desirable for the ESN technique, it also makes flow lines more difficult to distingish.

Several other flow visualization techniques were also tried to determine how ESN compares with other known methods of flow visualization. The ammonia-ozalid technique [22], in which a fine stream of NH_3 injected upstream of the blades left traces on the ozalid or blueprint paper, was successful but it was hard to control the location of the traces. Best success was achieved with the oil-dot matrix [23] technique. In this method, a Mylar film is fastened on the wall, on which a matrix or ink dots are marked around the traced blade profiles covering the area of interest. Just before turning the wind tunnel on, the dried ink dots are sprayed with a thin layer of wintergreen oil (synthetic methyl salicylate), which dissolved the ink. When the wind tunnel was turned on, ink dots produced streaklines along the flow path.

Comparing the above methods with ESN, it is judged that the ink-dot method is the more convenient for a flat wall or two-dimensional surfaces. However, ESN seemed to be much superior for complicated three-dimensional surfaces.

5.0 Determination of Material Loss

While the ESN technique proved encouraging in terms of flow visualization and secondary erosion determination, ways have to be devised to quantify the material loss in the pronounced gouges and craters and only there, since in this case this is the relevant index of critical damage rather than an overall material loss. Also permanent records of the surface must be made before sublimation further distorts the patterns. The surfaces are generally too rough and complex to permit convenient tracing by profilometer. A solution is to create a permanent replica of the surface and secure weight and volume measurements from it.

The best replicating results were obtained with vinyl polysilixane materials, sold under brand names Reprosil and

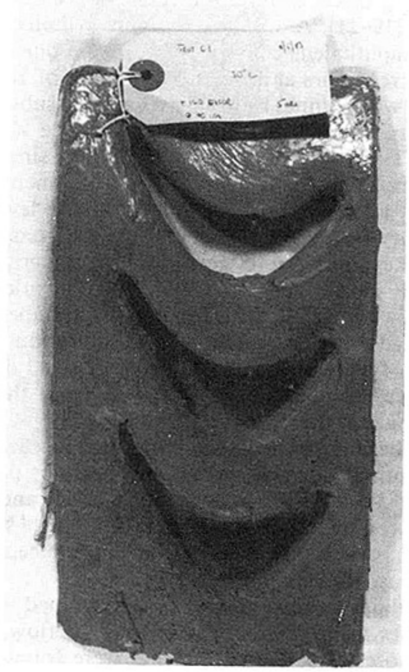

Fig. 4 Negative replica of blade coating after test

Fig. 5 A closeup of the "erosion" at the midchord on the negative replica

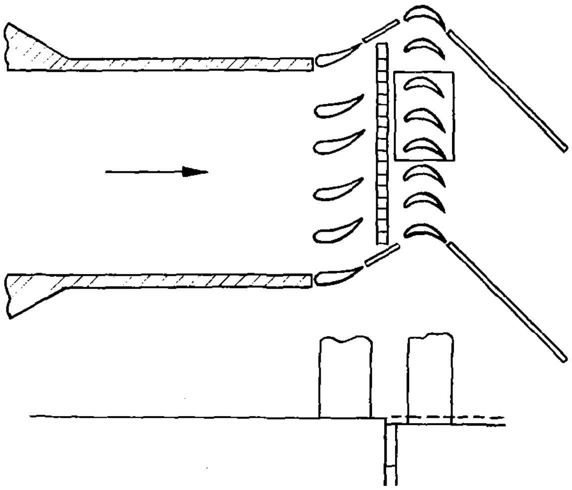

Fig. 6 Schematic of the wind tunnel test section

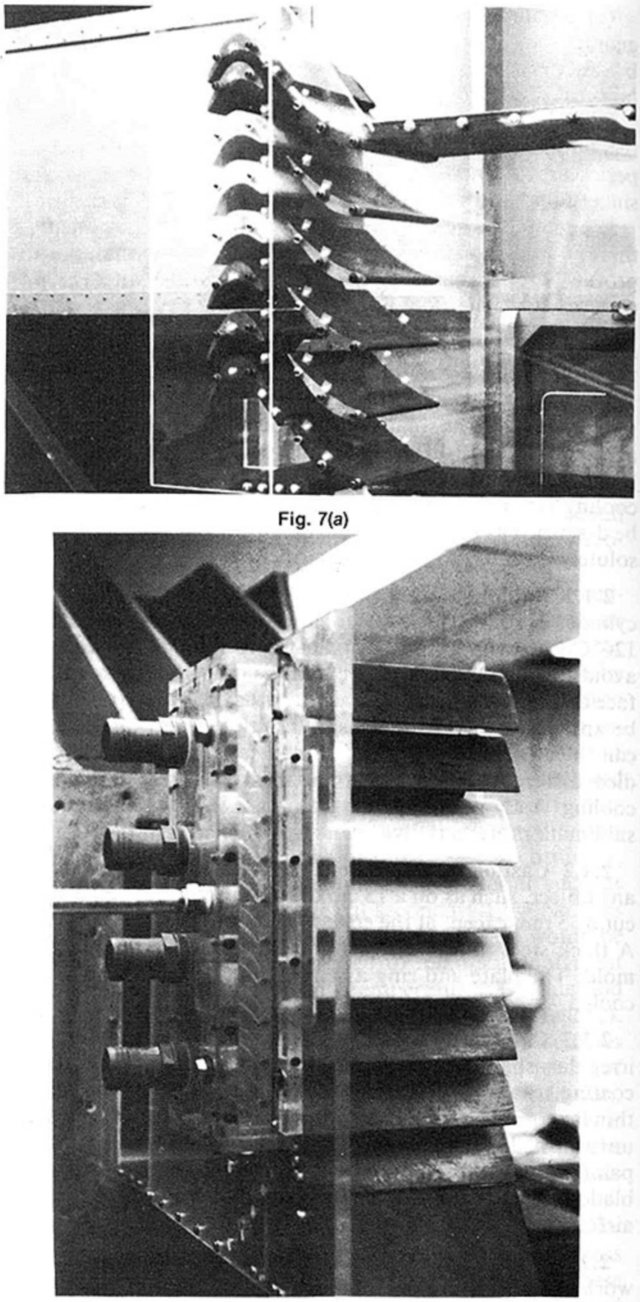

Fig. 7(a)

Fig. 7(b)

Fig. 7 Two views of the test section: (*a*) front view with tail boards removed; middle three blades of the rotor cascade are coated; (*b*) end view with front face removed as seen from the exit; on the left is the dual plenum, chamber, one for injecting air to simulate steam injection, the other to control the amount of suction through the slots; the assembly as shown is disconnected from the air supply source

Permagum among others, commonly used for making dental impressions. It is a two-part material which when painted on the surface flows easily into small features such as cracks and cavities and yields a flexible layer that can be easily removed. It does not interact with naphthalene, just peels off and leaves the naphthalene surface intact. It can be used to replicate a negative of the replica itself thus recreating the original surface.

This second replication was used to obtain erosion weight losses at the pits and gouges by smoothing the craters with a filler, the weight of which was subsequently recorded before and after. This method supplemented an earlier procedure for which a qualitative relative erosion index on a scale from 0 to 10 was used by visual observations. This method, although subjective, was found of consistent and reliable comparison.

Figure 3 shows the replica being peeled off following a test. Figures 4 and 5 show some examples of erosion damage as recorded on a negative replica. These replicas are dimensionally stable and can be stored for a long time.

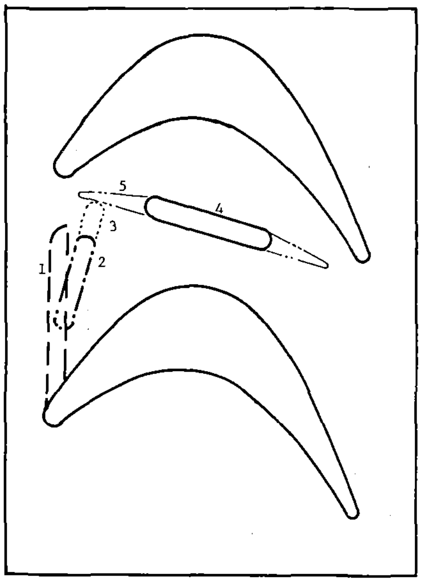

Fig. 8 Various flow fences designed to upset the secondary flow did not appear promising. Fence geometries as follows; (1) 5.7 cm long × 6 mm radius quarter circle cross section; (2) 2.5 cm long × 6 mm × 6 mm rectangular cross section; (3) same as (2) except 3.8 cm long; (4) 3.7 cm long × 6 mm × 6 mm rectangular cross section; (5) 7.6 cm long × 6 mm high varying width.

6.0 Expander Blade Tests

A set of two-dimensional stationary expander stator-rotor cascades of actual size is mounted in the wind tunnel as shown in Figs. 6 and 7. The profile of the stator blades is modified by reducing the turning angle so as to maintain the design incidence angle on the rotor blades. In the actual turbine, the stator blades are two dimensional but the rotor blades have a varying reaction and turning angle from root to tip. Tunnel blade chord Reynolds number was 3.5×10^5 as compared to 10^6 in the industrial expander.

Since the secondary erosion at the blade's root is of primary consideration in the wind tunnel the rotor cascade blades are built two dimensionally with the profile of the turbine blade root section. Three middle blades are coated with naphthalene, mounted on a coated rectangular end plate and finished with properly sized fillets at the blade–plate juncture. The coated blades, made of unvarnished mahogany, were originally undercut so as to have the correct profile after a 4-mm-thick coating is applied. The base plate simulating the blade platforms is made of aluminum and has a 5-mm-thick coating. The three coated blades are set in such a way as to have the middle blade aligned with the wake of one of the stator blades while the other two blades are staggered according to pitch relationships.

In the actual expander, the rotor disk and blades are cooled with externally injected steam. In the test setup, this steam injection is simulated by injecting 1 m^3/min of air through vaned slots in the interstage gap as shown in Fig. 7. The amount of air injected and its velocity match the momentum ratio of the injected steam to the primary gas in the real expander.

Calculations indicated that the steam injected against the rotor disk acquires only about half the tip velocity of the rotor at the blade entrance. Thus, the air is injected in the test section at 73 deg from tangential direction to match the effect of the relative steam tangential velocity in the expander. The injected air is filtered, its flow rate measured with a rotameter, and then fed to a plenum chamber for uniform entry to the test section.

A series of tests, starting with the base condition and ending with several modifications of the rotor blade profile and platform regions, to reduce the strength of the secondary flow at the blade root, were run in succession. Significant tests were repeated to assure consistency. It typically required 2–3 days to prepare the test pieces, run and evaluate a test. The test results are summarized as follows:

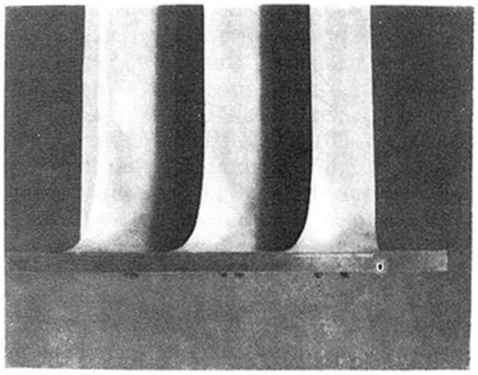

Fig. 9 Coated blades with 2.5-mm radius leading edge fillets at the base

6.1.1 The base tests using the existing expander configuration reproduced the major secondary erosion pattern observed in the field. The results indicated a strong passage vortex from pressure to suction surface at the platform, a weak horseshoe vortex at the leading edge, and curling up of the flow at about midchord of the suction surface where the suction leg of the horseshoe vortex merges with the pressure leg from the adjoining blade. The main feature was that the test results reproduced all the significant erosion patterns at and aft of the midchord as seen in the field. The characteristic features of the erosion such as localized deep pits with sharp edges were also seen on the test blades. In Fig. 5, the sharp-edged ridges represent the erosion pits in the naphthalene coating. Having shown that secondary flows are the main cause of the root erosion, several techniques to upset the surface boundary layer and the secondary flows were investigated. These included flow fences, modified leading edge fillets and suction slots. These modifications, however, had to be compatible with existing expander design and be commercially practical.

6.1.2 A number of flow fences as shown in Fig. 8 designed to upset the secondary flow were tested individually. The fences, made of steel, were uncoated and attached to the coated plate. All fences were 6 mm high and typically 6 mm thick. The leading and trailing edges were generally rounded. None of the fences tested showed any significant reduction in secondary flow strength or in erosion. The flow had a tendency to curl around or over the fence. In addition, the trailing wakes from the fences caused considerable damage of their own.

6.1.3 The leading edge fillet at the platform was enlarged to 2.5 cm radius as shown in Fig. 9. It was hoped that the larger fillet would reduce the strength of the horseshoe vortex, and therefore, the midchord secondary flow. This change had only a minor beneficial effect on the secondary erosion. Moore et al. [24] had also shown that change in the leading edge had little effect on the secondary flow in a turbine cascade.

6.1.4 The next variable tested was the study of steps between rotor and stator platforms. In fact, the base configuration has a 4-mm backward facing step (rotor platform lower than stator platform) after differential thermal growth between stator and rotor. A number of stepped configurations varying from a 6-mm forward facing step, to zero step, to 5-mm and 8-mm backward facing steps were tested. The results indicated that the zero step case or level stator and rotor platforms exhibits the least erosion. There was no major change in the character of the secondary flow as observed from flow visualization. The observed improvement for the zero step configuration is in this case the result of subjective

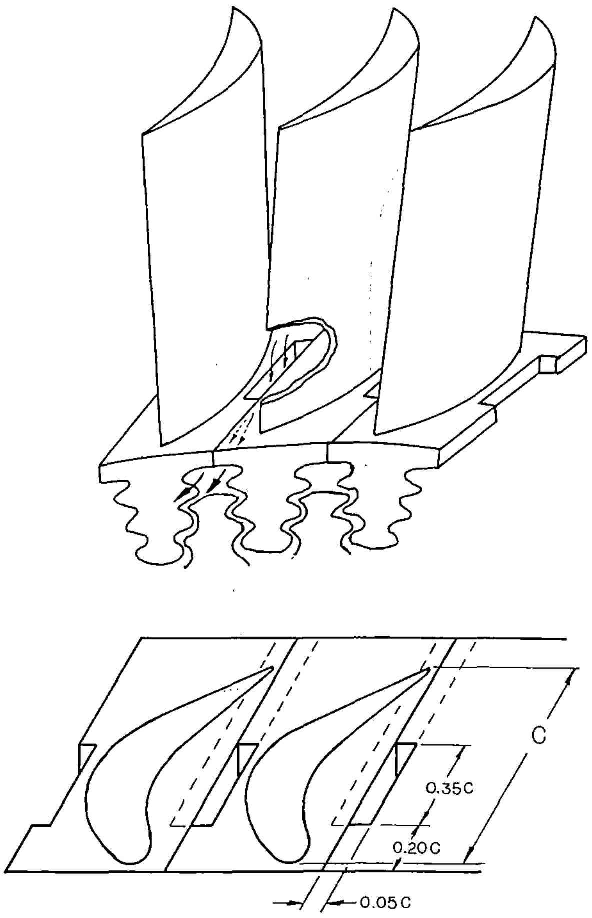

Fig. 10 Conceptual slot arrangement for operating expander

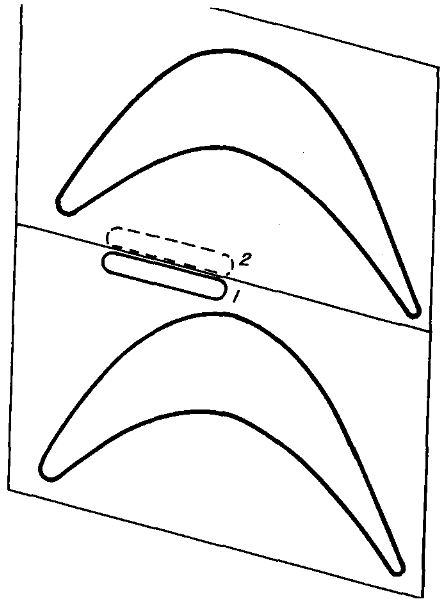

Fig. 11 Schematic of suction slot arrangement: slot No. 1 was found to be more effective than slot No. 2 in reducing erosion for a given amount of suction flow

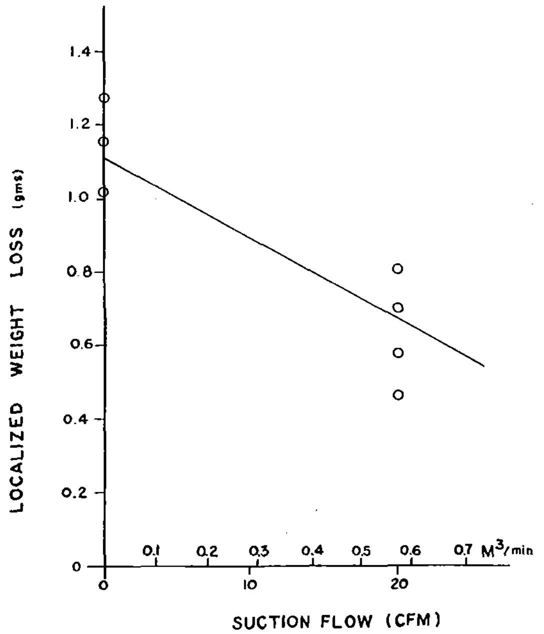

Fig. 12 Measured blade erosion for the case of the suction slot near the blade suction side and for a 4-mm backward facing step; multiple points at a given suction flow are repeat tests

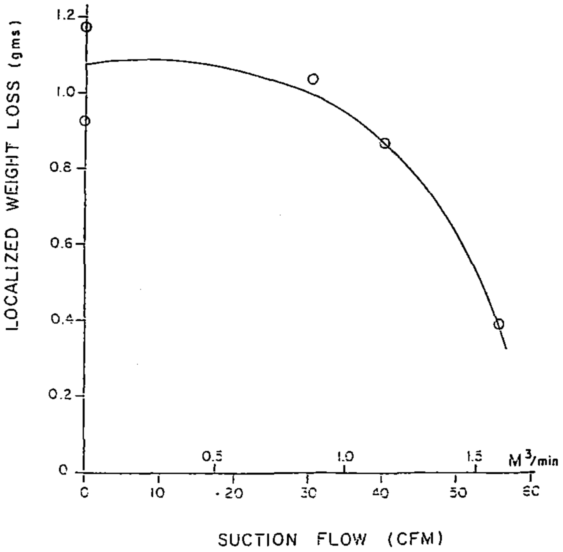

Fig. 13 Measured blade erosion for the case of the suction slot near the blade pressure side and for zero step

evaluation only, which was in use for these earlier runs as described in Section 5. Consequently, no data plots are presented.

7.0 Investigation of Suction Slots Through The Rotor Platform

Having recognized that secondary flows are difficult to upset and are capable of negotiating major obstacles, and that their curling up in vortices inflicts the damage one wishes to eliminate, more powerful techniques must be resorted to to control them.

One promising technique would be removal of the boundary layer by suction. The suction can be provided intrinsically by taking advantage of the low pressure at the discharge of the rotor. Suction slots can be built at the edge of the blade platforms and a communicating passage may be established in appropriate locations between the platform and the rotor discharge. Such a configuration is described on Fig. 10 in conceptual form.

From a series of static pressure taps in the end wall between adjacent rotor blades, it can be determined that a suitable suction flow can be removed through a reasonable size slot communicating with the rotor discharge pressure. Two configurations of suction slots were tested in the wind tunnel each positioned in a location where visualization streaks on the end walls show them to be across the path of the secondary flow streamlines. These are shown on Fig. 11. Tests were carried out by venting the slots to a variable pressure chamber and by varying the flow rate over a range compatible with the available pressure differentials in a real expander. The main results for slot location and for a reasonable slot width and length are shown in Fig. 12. It can be anticipated that for a slot located near the suction surface and with a length equal to approximately 35 percent of the chord and with a 7/1 aspect ratio, passing a flow equal to approximately 0.5 percent of the main flow (or approximately 30 cfm in the wind tunnel), the observed erosion rate is about one third of the erosion rate for the base case. Other slot locations were found to decrease with increasing suction rate. The 0.5 percent bleed quantity appears to be compatible with an acceptable erosion rate and can be obtained in practice.

Figures 12 and 13 show the wind tunnel quantitative results. For the better performing slot configuration near the suction side (Fig. 12) a consistent trend is indicated for a geometry using the same backward facing step as the base case and the actual expander. The performance could be improved with greater suction flow rates.

Figure 13 shows the case of the much less effective suction slot near the blade pressure side, in conjunction with a zero step configuration. This arrangement appears to require much larger suction flows to have an effect on erosion rate.

It is likely that still more optimum slot configurations are possible, the tests having been restricted to slots that can be fitted along the contact line of two adjacent blade platforms.

While these results appear quite adequate on a preliminary basis, the data are still somewhat lacking in quantity and consistency. Additional tests will aid in further optimization of the slot location and suction flow rates as well as provide a better grip on erosion rate measurement and reduction. In certain cases for example, rapid material loss of naphthalene along the slot perimeter was encountered. This problem can be minimized by rounding or supporting the slot edges, and by running a large number of tests to obtain statistical damage data.

Although this blade suction control would seem to offer an attractive commercial solution to the problem of blade root secondary erosion, its application is not without difficulties. New blade and disk tooling is required to accommodate the suction passages and the presence of the slot in the vicinity of a critical structural area could induce stress problems, especially if unanticipated slot erosion tends to enlarge passages. Besides, there is the possibility of slot plugging from dust accumulation. Simultaneously the authors' company has developed coatings and other metallurgical improvements of the blade. At this point in time, the blade life has been extended satisfactorily through the use of improved materials and coatings. It would appear therefore that the aerodynamic and structural design modifications suggested there would be mainly items for future improvements.

8.0 Conclusions

From these results the following conclusions may be drawn:

1 The process of erosion of complex shapes such as turbine blades can be simulated in the laboratory rapidly and inexpensively by constructing naphthalene-coated test bodies in the desired configuration and subjecting them to a wind tunnel stream without particles. The type of erosion thereby simulated is that from a secondary type of erosion for which large particles are absent, but for which small particles, which respond readily to turbulence and viscous forces, are mostly responsible for the erosion process. The observed "erosion" damage for the naphthalene-coated blade is similar in appearance, location, and character to the real damage seen on operating dust-eroded blades.

2 This technique was refined in detail for the preparation of the samples, application of the naphthalene coating, establishment of test consistency standards and data collection, the recording, measuring, and preservation of the "eroded" surfaces so as to permit securing permanent records.

3 Elimination, blocking, or upsetting the secondary flow proved to be a very difficult task. Techniques such as the use of fences, alteration of the blade, fillets, and leading edge changes did not prove to be successful.

4 Control of the steps in the platforms between the stator and the rotor however proved to be helpful with the line-to-line arrangement showing the least amount of damage from secondary flows near the root of the blades.

5 The other method which was found to weaken the secondary flow considerably near the root was through the use of a suction slot in the blade platforms allowing for removal of the cross flow boundary layers. This suction slot can be easily conceived as a gap between adjacent blade platforms communicating to a passageway over the top of the disk fir trees and discharging to the downstream end of the rotor blade row. This arrangement is seen as capable of generating sufficient suction and was shown to produce a major improvement in the observed erosion damage. It suffers however from the necessity of major retooling for the turbine disk and blades and leaves open the possibility of erosion damage internally to the suction slots themselves.

9.0 Acknowledgments

The authors wish to thank the senior management of Ingersoll-Rand Company for permission to publish this paper, for their review and approval. Also, special recognition is to be made to Messrs. Jeffrey Miller and Kim Horten. To them fell the responsibility for the tedious and exacting work of designing and constructing the test apparatus, devising the techniques for the construction and coating of the test blades and carrying out the many test configurations with care, consistency and ingenuity. Their contributions were essential to the success of the test program and are hereby gratefully acknowledged. Mrs. Vicki Phillips was especially dedicated to the task of putting everything together, and taking care of all the typing and the many other indispensable items. Her help is hereby gratefuly acknowledged.

References

1 Stettenbenz, L. M., "Benefits of the Power Recovery Gas Expander," *Chemical Engineering*, Jan. 10, 1972.

2 Krueding, A. P., "Power Recovery Techniques as Applied to Fluid Catalytic Cracking Units Regenerator Flue Gas," AIChE 79th Annual Meeting, Mar. 16, 1975.

3 Aakend, L., "FCC Problems: Erosion and Catalyst Attrition, " *Oil & Gas Journal*, Mar. 31, 1975.

4 Balfoort, J. P., "Power Recovery Systems and Hot Gas Expanders," Third Turbomachinery Symposium, Texas A&M, 1974.

5 Dussourd, J. L., "A Simple One-Dimensional Model for Primary Turbine Blade Erosion Prediction," ASME Paper No. 83-GT-164.

6 Grant, G., and Tabakoff, W., "Erosion Prediction in Turbomachinery Resulting From Environmental Solid Particles," *Journal of Aircraft*, Vol. 12, No. 5, May 1975.

7 Beacher, B., and Tabakoff, W., "Trajectories of Ash Particles Through a Coal-Burning Gas Turbine," ASME Paper No. 84-GT-122.

8 Sieverding, C. H., "Recent Progress in the Understanding of Basic Aspects of Secondary Flow in Turbine Blade Progress," ASME Paper No. 84-FT-78.

9 Langston, L. S., "Crossflows in a Turbine Cascade Passage," ASME JOURNAL OF ENGINEERING FOR POWER, Vol. 102, No. 4, Oct. 1980.

10 Langston, L. S., Nice, M. L., and Hooper, R. M., "Three-Dimensional Flow Within a Turbine Blade Passage," ASME JOURNAL OF ENGINEERING FOR POWER, Vol. 99, No. 1, Jan. 1977.

11 Sieverding, C. H., and Van den Bosch, P., "The Use of Coloured Smoke to Visualize Secondary Flows in a Turbine Blade Cascade," *Journal of Fluid Mechanics*, Vol. 134, Sept. 1983.

12 Gregory-Smith, D. G., and Graves, C. P., "Secondary Flows and Losses in a Turbine Cascade," *Viscous Effects in Turbomachines*, AGARD, 1983.

13 Marchal, P., and Sieverding, C. H., "Secondary Flows Within Turbomachinery Blading," *Secondary Flows in Turbomachines*, AGARD CP 214, 1977.

14 Hah, C., "A Navier-Stokes Analysis of Three-Dimensional Turbulent Flows Inside Turbine Blade Rows at Design and Off-Design Conditions," ASME JOURNAL OF ENGINEERING FOR GAS TURBINES AND POWER, Vol. 106, 1984, pp. 421-429.

15 Ulke, A., and Rouleau, W. T., "The Effects of Secondary Flows on Turbine Blade Erosion," ASME Paper No. 76-GT-74.

16 Kreith, F., Taylor, J. H., and Chong, J. P., "Heat and Mass Transfer From a Rotating Disk," ASME *Journal of Heat Transfer*, May 1959.

17 Tien, C. L., and Campbell, D. T., "Heat and Mass Transfer From Rotating Cones," ASME *Journal of Heat Transfer*, 1963.

18 Goldstein, R. J., and Kerni, L., "The Effect of a Wall Boundary Layer on Local Mass Transfer From a Cylinder in Crossflow," ASME *Journal of Heat Transfer*, Vol. 106, May 1984.

19 Sogin, H. H., and Subramanian, V. S., "Local Mass Transfer From Circular Cylinders in Cross Flow," ASME *Journal of Heat Transfer*, Vol. 83, 1961.

20 Lowery, G. W., and Vachon, R. I., "The Effect of Turbulence on Heat Transfer From Heated Cylinders," *Int. J. Heat Mass Transfer*, Vol. 18, 1975.

21 Coder, D. W., "Location of Separation on a Circular Cylinder in Crossflow as a Function of Reynolds Number," Naval Ship Research and Development Center, Report No. 3647.

22 Dring, R. D., Joslyn, H. D., and Hardin, "An Investigation of Axial Compressor Rotor Aerodynamics," ASME JOURNAL OF ENGINEERING FOR POWER, Vol. 103, Jan. 1981.

23 Langston, L. S., and Bayle, M. T., "A New Surface-Streamlike Flow Visualization Technique," *Journal of Fluid Mechanics*, Vol. 125, 1974.

24 Moore, J., and Ransmayr, A., "A Flow in a Turbine Cascade, Part 1: Losses and Leading Edge Effects," ASME JOURNAL OF ENGINEERING FOR GAS TURBINES AND POWER, Vol. 106, 1984, pp. 400-408.